Michael Rath

Signal Processing for Radio Positioning and Environment Mapping

Doctoral Thesis

to achieve the university degree of
Doctor of Technical Sciences

submitted to
Graz University of Technology

Supervisor
Assoc.-Prof. Dipl-Ing. Dr. Klaus Witrisal

Institute for Signal Processing and Speech Communication
Head: Univ.-Prof. Dipl-Ing. Dr.techn. Gernot Kubin

Graz, March 2021

This work has been performed within the LEAD project “Dependable Internet of Things in Adverse Environments” funded by Graz University of Technology. This work was also partially funded by the Christian Doppler Research Association.

Abstract

The upcoming 5G mobile radio standard and the concept of the Internet of Things establish the demand of location awareness for radio devices. From a signal processing perspective, this interest involves the analysis of (device) position information present in radio signals. In this context, this thesis builds on parameterized models for the radio channel response in order to fulfill three tasks.

First, (i) radio positioning systems are established, which are applicable for low-cost ultra-wideband (UWB) devices employing directional antennas. It is shown that the trade-off between simplicity and robustness hits a spot where sub-meter accuracy is achievable in real environments using a single base station, only.

Next, (ii) fundamental (lower) position error bounds are derived, applicable to the UWB positioning system from (i) and to the upcoming mm-wave radio systems. Numerical evaluation of the error bounds shows that directional antennas can compete with conventional (omni-directional) antenna arrays, whereas the former do not require phase coherency.

On the basis of a simplified formulation of the error bounds, (iii) a multipath-resolved radio environment map is formulated and applied to adaptable radio front-ends. An example application is given by extension of the presented positioning system to reduce the number of required measurements while achieving a comparable estimator performance.

Kurzfassung

Mit der Einführung des 5G-Mobilfunkstandards und des Konzepts des Internets-der-Dinge steigt das Interesse an Ortungsinformation zur Optimierung von Funknetzen. Aus Sicht der Signalverarbeitung bedeutet dieses Interesse die Analyse von Positionsinformation, die in Funksignalen vorhanden ist. In diesem Zusammenhang baut diese Arbeit auf parametrischen Modellen für die Radiokanalantwort auf, um drei Aufgaben zu erfüllen.

Zunächst werden (i) Funkortungssysteme mathematisch beschrieben, mit der Blickrichtung auf kostengünstige Ultra-wideband (UWB) Systeme mit Richtantennen. Es wird gezeigt, dass der Trade-off zwischen Systemkomplexität und Schätzerrobustheit einen Punkt erreicht, an dem in realen Umgebungen mit nur einer einzelnen Basisstation eine Submeter-Genauigkeit erreicht werden kann.

Als nächstes werden (ii) theoretische Schranken des Positionsfehlers hergeleitet, die auf das Positionierungssystem aus (i) und auf zukünftige mm-Wellen-Funksysteme anwendbar sind. Die numerische Auswertung der Fehlerschranken zeigt, dass durch den Einsatz von Richtantennen eine Genauigkeit erreicht werden kann, die vergleichbar ist mit herkömmlichen Antennenarrays, ohne dass dabei Phasenkohärenz zwischen den Richtantennen erforderlich ist.

Auf der Grundlage einer vereinfachten Formulierung dieser Fehlerschranken wird (iii) eine mehrwegeaufgelöste Kartierung der Funkumgebung (“radio environment map”) formuliert und auf adaptierbare Radio-Frontends angewendet. Als Anwendungsbeispiel wird das vorgestellte Positionierungssystem aus (i) erweitert, um die Anzahl der erforderlichen Messungen zu reduzieren und gleichzeitig eine vergleichbare Positionsgenauigkeit zu erzielen.

Acknowledgments

I would like to extend my gratitude to all the colleagues that assisted in the works included in this thesis.

First I thank my supervisor Klaus Witrisal for the support over the years, providing essential guidance for all the conducted research. Next I would like to thank the members of the LEAD project for the inspiring co-work spanning a diverse breadth of fields. Of special mention are the members of the wireless sub-project 1, Kay Römer, Carlo Boano and Mustafa Bakr for their contributions to the included papers. A heartfelt thanks goes to my LEAD office roommate and top co-author Bernhard Großwindhager for the work on SALMA, the fun conference trips and extensive philosophizing.

I would like to thank the (current as well as former) members of the SPSC for all the brisk conversations and (boozy) activities over the years. Of special mention are the mentoring (and *taverning*) performed by Erik Leitinger, Stefan Grebien and Sepp Kulmer. Thanks also to my most recent office room mates, Anh Nguyen, Thomas Wilding, Alex Venus, Ahmed Alterkawi and Michi Stocker for suffering through the occasional bad joke.

A final thanks goes again to my parents for all their support through the (even more numerous) years of my studies.

Contents

List of Figures

List of Acronyms

5G fifth generation. 4

AoA angle-of-arrival. 4, 12, 21, 22, 27, 38, 40
AoD angle-of-departure. 21, 40, 43, 46
AWGN additive white Gaussian noise. 14, 17, 18, 26, 35, 55, 61

BLE Bluetooth low energy. 29

CIR channel impulse response. 30, 32–35, 38
CRLB Cramér-Rao lower bound. 37, 39, 44

DMC dense multipath component. 12–15, 18–20, 26, 31–34, 36, 40, 41, 55
DPS delay power spectrum. 19, 41

FIM Fisher information matrix. 38–41, 46, 47

IoT Internet of Things. 3–6, 61

LLH log-likelihood. 30–35, 55, 56
LOS line-of-sight. 20, 29, 32, 35, 41, 42, 59, 68

MIMO multiple-input multiple-output. 4, 37
ML maximum likelihood. 30, 32, 36
MPC multipath component. 3, 11, 12

ODC our deliberate choice. 47, 48, 55

PEB position error bound. 37, 40–43, 45, 46, 48, 59, 61
PL path loss. 22

RC raised-cosine. 33
REM radio environment map. 45–49, 51–57, 59, 61, 62, 67–69
RF radio frequency. 6, 29, 61
RSS received signal strength. 4, 6, 29, 46

SALMA single-anchor localization using multipath assistance. 29, 30, 34, 35, 41, 44, 45, 47, 55–57, 59, 62
SINR signal-to-interference-and-noise-ratio. 26, 39–41, 46–48, 50–54, 56–60, 62, 67–69
SLAM simultaneous localization and mapping. 30
SMC specular multipath component. ix, 3, 12–17, 20–23, 25–27, 30, 31, 33, 37–44, 46–48, 51, 56, 59
SNR signal-to-noise-ratio. 26, 41

ToF time-of-flight. 4, 38

US uncorrelated scattering. 13, 15
UWB ultra-wideband. 4, 6, 29, 30, 33–37, 41, 44, 61

VA virtual anchor. 20–26, 30, 41, 42, 46–50, 59, 60

Affidavit

I declare that I have authored this thesis independently, that I have not used other than the declared sources/resources, and that I have explicitly indicated all material which has been quoted either literally or by content from the sources used. The text document uploaded to TUGRAZonline is identical to the present doctoral thesis.

Date	Signature

Part I.

Overview of Researched Topics

1. Introduction

In the upcoming years we face the reality of everyday objects becoming connected to a large network, the Internet of Things (IoT). In the same vein as our worldly fauna, this system of things encompasses a myriad of beings, ranging from simple amoeba-like devices such as low-power sensor nodes up to behemoths of complexity such as autonomously driving cars. Where the IoT differs from the animal kingdom is in a strong desire of its participants to actively communicate. While the foundation of communication for the classic internet is a large web of wires, locking its participants into place, objects in the IoT require the freedom of mobility which necessitates a form of wireless communication. Ever since the dawn of mobile phones, infrastructure and mechanisms have been put in place to enable users to communicate wirelessly. However, for the IoT with its significantly higher number of diverse participants, an evolution of existing solutions is necessary to tackle the challenges arising.

No matter how you look at it, the challenges of wireless communication come down to the *wireless channel*, which describes how the source signal changes when traveling from sender to receiver. In this regard, the channel of communicating radios is influenced by two major factors: First, we have the *physical* radio channel which incorporates signal reflections (multipath propagation) and scattering effects considering the surroundings (i.e., the environment) of the involved radios. In the context of the IoT, where things can be virtually everywhere, the arising challenges stem from cluttered environments exhibiting severe multipath propagation, e.g., indoor and industrial environments. The second major influencing factor is any form of *man-made* interference, be it competing transmissions, unintended radiations or system attacks (e.g., jamming, eavesdropping).

The focus of this thesis and collection of works lies on the first influencing factor, where the radio channel is analyzed on a signal processing level to outline information present in received radio signals. To this end, the channel can be decomposed into modular entities, the multipath components (MPCs), which will pose as the main actors of the contained works. The most impactful of the MPCs are related to strong reflections in the environment, which behave similar to specular reflections where incidence and reflection angles are equal, hence these MPCs are called specular multipath components (SMCs). The SMCs are observed and thus described in *angle* and *delay* domains, which is equivalent to space and time behavior. In blunt terms, an observer of radio signals should ask the following about the SMCs: “From where do they come?” and “When do they come?”. The answers to these questions are directly related to the *positions* of the sender and receiver relative to the environment they are in and knowing the answers enables them to adapt their radio front-ends.

The keyword here is the *environment*, which for the thesis is comprised of room geometry and a base station acting as transmitter, referred to as *anchor* due to its fixed position. To set the stage for position-aware or environment-aware things, we propose the formulation of a *radio environment map*. This map relates each position in the environment to a quality measure which indicates how “good” the radio link is. Communicating things that have knowledge of such a map can use it as a guidance system, either to guide their movement or to adapt their “feelers”. For IoT devices this concerns their radio frontends and antennas. This readies nodes of the IoT to turn into dependable cognitive systems.

1.1. Context of Work

Now, with the focal points laid out, we look at the landscape of radio technologies, highlighting the present challenges and where to place the contributions of this thesis. For that purpose, in the book chapter [S6] we created a taxonomy of communication and positioning systems, demonstrating the open challenges for IoT devices. Adjusted graphs from this work are shown in Figure 1.1 and Figure 1.2, which provide a categorization of radio technologies according to design spaces. For both worlds (communication and positioning), we see the dimensions of varying *bandwidth* on the one hand and *adaptability to the environment* on the other hand.

Starting with the communication domain, the main challenge involves data recovery in presence of fading effects, i.e., dealing with variations of the channel due to multipath interference caused by movement and / or changes in the environment. Towards the origin of the design space, we see well established, if not to say ancient, methods such as matched filters, energy detectors and rake receivers, all of which are described in various textbooks about wireless communications [24, 77, 88] and digital communications [6, 37, 83]. Moving towards the top right, we increase the bandwidth, number of employed antennas and prior knowledge in order to cover younger technologies, some of which are still of a more conceptual nature. This is also where fifth generation (5G) radio networks are situated, which are expected to employ massive multiple-input multiple-output (MIMO) array antenna systems [4, 13] due to the dramatic increase in energy efficiency and capacity, achieved by aggressive spatial multiplexing [51, 92]. Array antennas also open the gate towards millimeter-wave (mm-wave) systems [85, 87, 113], achieving a high array gain which compensates the pathloss present in these frequency bands (30-300 GHz). Towards the top right of the space, we have recent technologies that are, at the time of writing this thesis, conceptual and not common in realized systems like time reversal processing [12, 30] and cognitive radio [36, 76]. The latter is also where the concept of “environment” knowledge comes into play, which in this context refers to interference of competing users, the knowledge of which, e.g. via spectral cartography, enables systems to reach certain levels of cognition. This is also the place where the author of this thesis makes the bold choice to put his works, since, at higher bandwidths, the physical environment can be taken into consideration and multipath-resolved environment maps can be realized.

However, as we are examining location-aware devices that leverage environment maps, the meat of this thesis is concerned with positioning systems. For this, a taxonomy of positioning approaches is found in Figure 1.2, showing a design space that again spans the domains of signal/system bandwidth over the adaptability of the system. Towards the origin we see “old-school” systems where no prior knowledge is leveraged. Depending on the available bandwidth, they are categorized into carrier phase, received signal strength (RSS) or time-of-flight (ToF) in order to perform range estimates to obtain the position via a trilateration approach. Additionally, over all bandwidths the angle-of-arrival (AoA) can be estimated to determine the position via a triangulation approach. A detailed overview over these methods can be found in the habilitation thesis by Mautz [68], which provides a comprehensive survey of (indoor) positioning methods and technologies, including optical- and audio-based systems as well as GNSS. Walking towards the right of the design space, we reach the relevant systems for this thesis, with RSS maps and fingerprinting, and ultra-wideband (UWB) based multipath assisted methods like the MINT system [122]

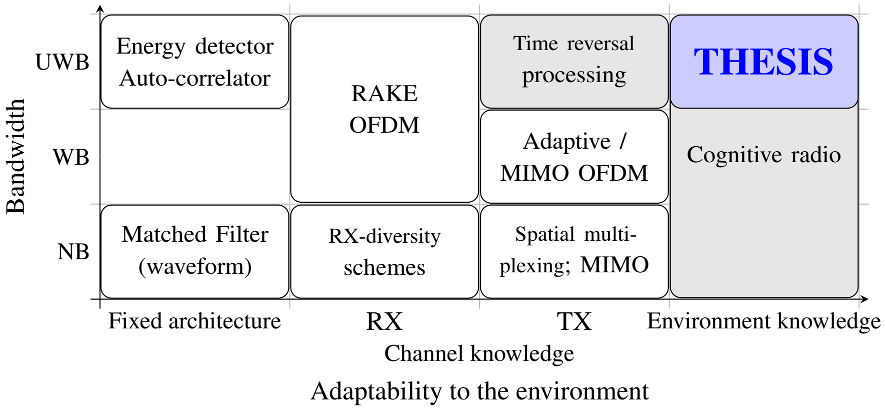

Figure 1.1.: Design space for radio (communication) systems to mitigate fading in wireless propagation channels.

(multipath-assisted indoor navigation and tracking)[1], then reaching once again systems employing cognitive concepts. For all involved methods, in order to reach a certain position accuracy, there is a general trade-off between bandwidth, diversity branches [121] and antenna directivity [118]. The contributions of this thesis reside also in this space, as indicated by three boxes, each dedicated to one of the research hypotheses to be elaborated in the following.

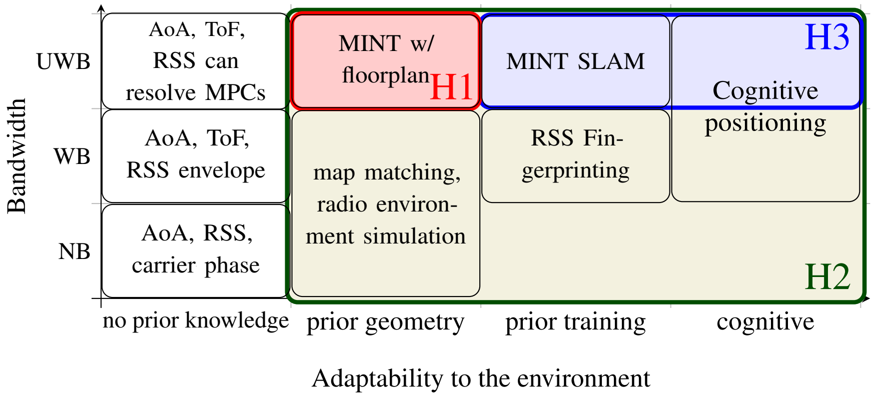

Figure 1.2.: Design space for dependable radio positioning systems.

1.2. Research Hypotheses

On the basis of the established research context, three research topics can be extracted, each tackling one aspect of dependable positioning systems for IoT devices. In the following, each topic is outlined and a corresponding research hypothesis is formulated.

---

[1] A detailed overview of related work for these subjects is given in Chapter 3.

Resource-efficient robust UWB Radio Positioning

In the first topic, it is considered how resource-efficient radio positioning systems are realized, also when taking dense multipath propagation into account. This topic builds on top of established multipath-assisted positioning methods with partial prior knowledge of the environment, such as a given floorplan, as illustrated in Figure 1.2. The keyword *resource-efficient* refers to reduced employed infrastructure such as a low number of anchors, while *robust* refers to sufficient accuracy (sub-meter) and low probability of outliers. In order to fulfill both requirements, the combination of accurate ranging via UWB signals and application of directional antennas is leveraged to formulate algorithms that can be implemented in real time on low-cost (IoT) devices where the number of participating anchor / base station devices is minimized. The corresponding hypothesis reads:

Hypothesis 1 (H1) *For challenging environments with severe multipath propagation (such as indoors), accurate (sub-meter) position estimates are possible with a single base-station, by using UWB radio signals observed with directional antennas.*

Fundamental Limits on the Accuracy of Radio Positioning

The second topic takes a theoretical perspective on radio positioning by evaluation of accuracy bounds for IoT radio devices with regards to resources such as bandwidth and antenna characteristics. Note that this topic covers most of the design space, as bandwidth and antenna parameters are tunable in the mathematical analysis, which is a pre-requisite for adaptability. Of particular interest in the analysis are non-coherent measurements (obtained from directive antennas) and the performance difference compared to conventional coherent antenna array processing. Hence, the corresponding hypothesis reads:

Hypothesis 2 (H2) *Fundamental accuracy limits of radio positioning systems can be formulated to quantify the influence of radio system parameters onto the achieved performance of these systems. The key parameters are signal bandwidth and antenna directivity, the latter can be given either by coherent array processing, or alternatively using observations from multiple directional antennas non-coherently.*

Multipath-resolved Radio Environment Maps

With the third and final topic, the realm of radio environment maps is entered. Opposed to conventional RSS-based maps, it is desired to include multipath-related features. To this end, UWB signals and directional antennas are applied to obtain a multipath-resolved radio channel for both time and angle domains. In the design space, we are situated in the very top right also tapping into the field of cognitive positioning and control. A first concept of a multipath-resolved map is established based on the bounds developed in the previous topic. We want to explore how such a map may be used in adaptable radio frequency (RF) front-ends and multi-antenna systems to improve the accuracy and robustness of radio positioning systems. The intended objectives are summarized in the following hypothesis:

Hypothesis 3 (H3) *Resolving multipath components in the time and angle domains allows the construction of radio environment maps which can be used to improve the performance of radio positioning systems.*

1.3. Organization and Contributions

This thesis is structured into one chapter that covers the basic background and then one chapter for each formulated research question. Each of these chapters contains a section about related work to put the contributions into perspective with existing literature. In the following, each chapter and an overview of its contents is outlined.

Chapter 2: Background. As a starting point, a fundamental framework in terms of radio signal models is provided. First, a formulation of the used propagation channel models and received radio signal models is established, describing the main actors, i.e. specular and dense multipath components of the radio channel. In particular, three antenna setups for the received signal model are be described (single omni, multiple coherent omni and multiple non-coherent directional) to enable later comparisons. In the same fashion, two noise models are introduced (additive white Gaussian noise, with and without dense multipath). The second part of this chapter deals with the modeling of specular multipath components, in terms of geometric features (relating to a plan of the environment) and in terms of amplitude quality models (evaluating the strength of reflections).

Chapter 3: Resource-efficient Radio Positioning Systems. This chapter deals with H1. Positioning algorithms are formulated based on the signal and noise models from Chapter 2 and then selected results from two measurements campaigns are shown. The first campaign used high-fidelity measurement equipment, the second one low-cost devices.

Chapter 4: Fundamental Limits of Radio Positioning. This chapter deals with H2 by means of a mathematical analysis of the established signal models to derive provable bounds on the positioning accuracy. An overview of different error bounds is given and the derivation of the thesis-relevant bound is outlined, which describes the influence of bandwidth and antenna patterns. Selected simulation results are discussed for a non-trivial indoor environment.

Chapter 5: Multipath-resolved Radio Environment Maps. This chapter deals with H3. The formulation of a radio environment map on the basis of the error bounds from Chapter 4 is proposed and its application to the positioning methods from Chapter 3 is described and analyzed based on simulations. Selected results from a related measurement campaign (parking garage environment) are described.

Chapter 6: Conclusions. A summary of the described contents is provided with reference to possible future work.

In the following, two lists of publications are provided. The first list shows all papers included in this thesis (see Part II). The second list shows further papers that the author of this thesis has participated in as co-author. These works are also referenced throughout the thesis showing their relevance to the covered subjects.

List of included papers

[T1] B. Großwindhager, M. Rath, J. Kulmer, M. S. Bakr, C. A. Boano, K. Witrisal, and K. Römer. "SALMA: UWB-based Single-Anchor Localization System Using Multipath Assistance." In: *Proceedings of the 16th ACM Conference on Embedded Networked Sensor Systems*. SenSys '18. Shenzhen, China, Nov. 2018, pp. 132–144.

[T2] M. Rath, J. Kulmer, E. Leitinger, and K. Witrisal. “Single-Anchor Positioning: Multipath Processing With Non-Coherent Directional Measurements.” In: *IEEE Access* 8 (2020), pp. 88115–88132.

[T3] M. Rath, J. Kulmer, M. S. Bakr, B. Großwindhager, and K. Witrisal. “Indoor Localization and Communication Enhanced by Directional UWB Antennas.” In: *Workshop on Dependable Wireless Communications and Localization for the IoT*. Graz, Austria, Sept. 2017.

[T4] M. Rath, J. Kulmer, M. S. Bakr, B. Großwindhager, and K. Witrisal. “Multipath-assisted Indoor Positioning Enabled by Directional UWB Sector Antennas.” In: *IEEE 18th International Workshop on Signal Processing Advances in Wireless Communications (SPAWC)*. Sapporo, Japan, July 2017, pp. 1–5.

[T5] M. Rath, E. Leitinger, A. Nguyen, and K. Witrisal. “Directionally Resolved UWB Channel Modeling for Environment-Aware Positioning.” In: *14th European Conference on Antennas and Propagation (EuCAP)*. Mar. 2020, pp. 1–5.

List of co-authored papers related to the thesis

[S1] M. S. Bakr, B. Großwindhager, M. Rath, J. Kulmer, I. C. Hunter, R. A. Abd-Alhameed, K. Witrisal, C. A. Boano, K. Römer, and W. Bösch. “A Compact Broadband Frequency Selective Microstrip Antenna and Its Application to Indoor Positioning Systems for Wireless Networks.” In: *IET Microwaves, Antennas and Propagation* (July 2019).

[S2] B. Großwindhager, C. A. Boano, M. Rath, and K. Römer. “Concurrent Ranging with Ultra-Wideband Radios: From Experimental Evidence to a Practical Solution.” In: *IEEE 38th International Conference on Distributed Computing Systems (ICDCS)*. Vienna, Austria, July 2018, pp. 1460–1467.

[S3] B. Großwindhager, C. A. Boano, M. Rath, and K. Römer. “Enabling Runtime Adaptation of Physical Layer Settings for Dependable UWB Communications.” In: *IEEE 19th International Symposium on ”A World of Wireless, Mobile and Multimedia Networks” (WoWMoM)*. Chania, Greece, June 2018, pp. 01–11.

[S4] B. Großwindhager, M. S. Bakr, M. Rath, F. Gentili, W. Bösch, K. Witrisal, C. A. Boano, and K. Römer. “Poster: Switchable Directional Antenna System for UWB-based Internet of Things Applications.” In: *Proceedings of the 2017 International Conference on Embedded Wireless Systems and Networks*. EWSN ’17. Uppsala, Sweden, Feb. 2017, pp. 210–211.

[S5] B. Großwindhager, C. A. Boano, M. Rath, and K. Römer. “Poster Abstract: Runtime Adaptation of PHY Settings for Dependable UWB Communications.” In: *Proceedings of the 17th ACM/IEEE International Conference on Information Processing in Sensor Networks*. IPSN ’18. Porto, Portugal, Apr. 2018, pp. 128–129.

[S6] B. Großwindhager, M. Rath, M. S. Bakr, P. Greiner, C. A. Boano, K. Witrisal, F. Gentili, J. Grosinger, W. Bösch, and K. Römer. “Dependable Wireless Communication and Localization in the Internet of Things.” In: *Mission-Oriented Sensor Networks and Systems: Art and Science: Volume 2: Advances*. Ed. by H. M. Ammari. Cham: Springer International Publishing, 2019, pp. 209–256.

[S7] B. Großwindhager, M. Rath, J. Kulmer, M. S. Bakr, C. A. Boano, K. Witrisal, and K. Römer. “Dataset: single-anchor indoor localization with decawave DW1000 and directional antennas.” In: *Proceedings of the First Workshop on Data Acquisition To Analysis*. DATA ’18. Shenzhen, China, Nov. 2018, pp. 21–22.

[S8] B. Großwindhager, M. Rath, J. Kulmer, S. Hinteregger, M. Bakr, C. A. Boano, K. Witrisal, and K. Römer. “UWB-based Single-anchor Low-cost Indoor Localization System.” In: *Proceedings of the 15th ACM Conference on Embedded Network Sensor Systems*. SenSys ’17. Delft, Netherlands, Nov. 2017, 34:1–34:2.

[S9] B. Großwindhager, M. Stocker, M. Rath, C. A. Boano, and K. Römer. “SnapLoc: An Ultra-fast UWB-based Indoor Localization System for an Unlimited Number of Tags.” In: *Proceedings of the 18th ACM/IEEE International Conference on Information Processing in Sensor Networks*. IPSN ’19. Montreal, Quebec, Canada, Apr. 2019, pp. 61–72.

[S10] A. N. Hong, M. Rath, J. Kulmer, S. Grebien, K. N. Van, and K. Witrisal. “Gaussian Process Modeling of UWB Multipath Components.” In: *IEEE Seventh International Conference on Communications and Electronics (ICCE)*. Hue City, Vietnam, July 2018, pp. 291–296.

[S11] A. N. Hong, M. Rath, E. Leitinger, S. Hinteregger, K. N. Van, and K. Witrisal. “Channel Capacity Analysis of Indoor Environments for Location-Aware Communications.” In: *IEEE Global Telecommunications Conference (GLOBECOM)*. Washington D.C., USA, Dec. 2016, pp. 1–6.

[S12] J. Kulmer, S. Grebien, M. Rath, and K. Witrisal. “On the unimportance of phase-coherent measurements for beampattern-assisted positioning.” In: *Proceedings of the IEEE Wireless Communications and Networking Conference (WCNC’18)*. Barcelona, Spain, Apr. 2018, pp. 1–6.

[S13] J. Kulmer, S. Hinteregger, B. Großwindhager, M. Rath, M. S. Bakr, E. Leitinger, and K. Witrisal. “Using DecaWave UWB transceivers for high-accuracy multipath-assisted indoor positioning.” In: *IEEE International Conference on Communications (ICC)*. Paris, France, May 2017, pp. 1239–1245.

[S14] A. H. Nguyen, M. Rath, E. Leitinger, K. V. Nguyen, and K. Witrisal. “Gaussian Process Modeling of Specular Multipath Components.” In: *Applied Sciences* 10.15 (July 2020), p. 5216.

2. Background

In this chapter, various models are defined for radio signals and the most significant terms and acronyms are introduced, which poses as the foundation for the remainder of the thesis. The model definitions follow closely the ones in [T2], with some extensions to provide further insight. In essence, all included papers use equivalent signal models with the same setup. The second part of this chapter deals with the main “actors” of this thesis, the specular multipath components and how to model their geometry-related parameters and their power-related parameters.

The starting point in Section 2.1 is a propagation channel model in its most general form, followed by the introduction of assumptions to abstract specific signal models cumulatively. This differs from the included papers, which start with a reduced, simplified signal model due to space constraints and also to focus on the most relevant aspects of the respective hypotheses. The rational behind the choice of a more detailed description is to provide a transparent, thorough elaboration on all involved quantities, i.e., to reduce any unclear implications to a minimum. The reader may skip the earlier subsections depending on the desired level of detail in the elaborations.

2.1. Signal and System Models

The central element of this thesis is the wireless channel between two nodes. These two “protagonists” will be called *anchor* and *agent* throughout this thesis[1]. The anchor is situated at a fixed, known position denoted by $\boldsymbol{a}$, whereas the agent can move around freely and its (current) position is denoted by $\boldsymbol{p}$. We are interested in how a signal exchanged between anchor and agent changes due to the wave propagation within the environment, which is described by the *radio channel*.

2.1.1. Multipath Channel Models

The static[2] radio channel between agent and anchor is described by the spreading function

$$\tilde{h}(\Omega,\Psi,\tau;\boldsymbol{p}) = \sum_{\kappa=1}^{\infty} \tilde{\alpha}_\kappa(\boldsymbol{p})\,\delta\big(\Omega-\tilde{\Omega}_\kappa(\boldsymbol{p})\big)\delta\big(\Psi-\tilde{\Psi}_\kappa(\boldsymbol{p})\big)\,\delta\big(\tau-\tilde{\tau}_\kappa(\boldsymbol{p})\big) \tag{2.1}$$

where $\delta(\cdot)$ denotes the Dirac delta function. In further elaborations, the agent acts as transmitter, without loss of generality. Equation (2.1) describes the superposition of infinitely many MPCs that originate from reflections by objects in the environment. From the perspective of the anchor, one individual MPC, referred to by index κ, is described by

---

[1] Common alternative terms found in the literature are *base station* for the anchor, and *mobile station*, *terminal* or *user equipment* for the agent.

[2] Static in this sense means that there are no (absolute) time variations, hence the time dependence is omitted.

its complex amplitude $\tilde{\alpha}_\kappa$, its direction of arrival $\tilde{\Omega}_\kappa$, its direction of departure $\tilde{\Psi}_\kappa$ and its (relative) delay $\tilde{\tau}_\kappa$. The directions $\tilde{\Omega}_\kappa$ and $\tilde{\Psi}_\kappa$ may be defined by an azimuth and elevation angle tuple, e.g., $\tilde{\Omega}_\kappa = \left(\tilde{\phi}_\kappa, \tilde{\theta}_\kappa\right)$. In the literature, this model is commonly referred to as *double-directional radio channel* [105]. It should be emphasized that this model is rather generic and thus suited to describe any multipath channel. It can, e.g., also be used when audio signals are considered. The main restriction is a static environment, i.e., no changes in the physical surroundings and stationarity in the frequency domain are assumed.

In the following, assumptions are introduced, which are related to the used antennas to measure the channel. The assumptions are cumulative, i.e., each assumption builds on top of the previous one. After the formulation of each assumption, a short description of its application to (2.1) is given.

- The MPC directions are restricted to horizontal propagation (azimuth plane), i.e., the direction parameters are specified solely by azimuth angles and the position vectors are defined in $\mathbb{R}^2$. The elevation angle is then considered to be constant with $\tilde{\theta}_\kappa = \frac{\pi}{2}$ for all κ. In many works, such as the included ones, this assumption is justified by application of antennas at the anchor that exhibit a narrow elevation pattern, resulting in negligible effect of MPCs arriving from elevation angles other than $\frac{\pi}{2}$. An extension to three dimensional scenarios with horizontal and vertical propagation is straightforward, but it would lead to cumbersome notations without bringing significant additional insights.
  Application to (2.1)*: The directions $\tilde{\Omega}_\kappa$ and $\tilde{\Psi}_\kappa$ are replaced with azimuth angles $\tilde{\phi}_\kappa$ and $\tilde{\varphi}_\kappa$.*
- The simplest form of agents are considered, equipped with a single omni-directional antenna in the azimuth plane (e.g., a dipole antenna). Hence, we may use the equivalent of the angle-of-departure integrated channel [105], i.e. a single-directional channel, considering the direction of arrival domain from the perspective of the anchor only.
  Application to (2.1)*: The angle-of-departure $\tilde{\varphi}_\kappa$ vanishes as an argument and the respective delta function is omitted.*
- Radio measurements are conducted with a finite observation aperture in space and frequency. As a result, separated MPCs are collected into a set of $k = 1 \dots K$ SMCs and all unresolvable MPCs originating for example from diffuse scattering are described by a dense multipath component (DMC) [21, 90].
  Application to (2.1)*: New summation over k and corresponding replacement of MPC parameters with SMCs and inclusion of the DMC.*

Applying these assumptions as stated, we obtain the simplified (2D) radio channel model, described by the spreading function

$$h(\phi,\tau;\boldsymbol{p}) = \sum_{k=1}^{K} \alpha_k(\boldsymbol{p}) e^{j\zeta_k(\boldsymbol{p})}\, \delta\big(\phi - \phi_k(\boldsymbol{p})\big)\, \delta\big(\tau - \tau_k(\boldsymbol{p})\big) + \nu(\phi,\tau;\boldsymbol{p}). \tag{2.2}$$

Each SMC is described by amplitude α_k, phase rotation ζ_k, AoA ϕ_k and delay τ_k[3]. The latter two parameters (angle and delay) can be directly related to the agent position via a geometric model of the environment, as will be explained in Section 2.2.2. Amplitude and phase parameters are more delicate in terms of position-related modeling and will hence be described in terms of quality-related quantities in Section 2.2.3.

---

[3] Note that we separated the (previously) complex-valued amplitude into its absolute value and its phase to obtain only real-valued SMC parameters.

Reflections that are either too weak to be of use or result from scattering are captured by the DMC $\nu(\phi,\tau;\boldsymbol{p}) \in \mathbb{C}$. The DMC is modeled as a complex circular (i.e. zero-mean) Gaussian random process [41, 90]. Assuming uncorrelated scattering (US) in the delay and angular domains, the auto-correlation function of $\nu(\phi,\tau;\boldsymbol{p})$ is given by

$$R_{\nu\nu}(\phi,\phi',\tau,\tau';\boldsymbol{p}) = S_{\nu}(\phi,\tau;\boldsymbol{p})\,\delta(\phi-\phi')\,\delta(\tau-\tau') \tag{2.3}$$

where $S_{\nu}(\phi,\tau;\boldsymbol{p})$ describes the azimuth-delay power spectrum [21] at the anchor position. Essentially, $S_{\nu}(\phi,\tau;\boldsymbol{p})$ captures and characterizes the DMC for a particular environment. Later, we will look at further refinements, e.g., treating the domains separately, which will allow us to account for the DMC in practical applications.

With the model from (2.2) at hand, we established our main protagonists, the SMCs, which open the door to use knowledge about the physical environment, as well as our antagonist, the DMC, which represents faced challenges that arise in, e.g., indoor environments with rich multipath scattering. In the next step, we examine what is seen by the anchor when the agent instigates an actual signal transmission.

2.1.2. Received Signal Models

As a short recap, the designated propagation channel model in (2.2) was established, where the agents are restricted to employ omni-directional antennas operating in the azimuth plane. In order to establish a model of the signal as it is received at the anchor, we specify the setup at the anchor to employ an antenna array that consists of $m = 1 \ldots M$ antennas. When referring to the general anchor position, we use $\boldsymbol{a}$ which is defined to be the mass point of the antenna array. Then, the position of the mth antenna element is denoted by $\boldsymbol{a}^{(m)}$. This position is determined by the distance to the array center denoted by $d^{(m)}$ and the azimuth angle $\phi^{(m)}$. An example is shown in Figure 2.1.

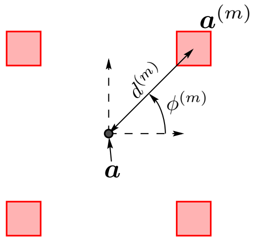

Figure 2.1.: Antenna array at anchor (in azimuth plane). As an example, the angle and distance parameters of one array element are shown.

Now, for the transmission taking place, there are multiple ways how to treat the signal as received at the anchor with regards to the spatial and time domains. It is common to use equivalent image domains obtained via Fourier transforms. There is a duality from the spatial to the angle domain and from the time to the frequency domain. In this thesis, the choice is to treat the domains separately. First the angle domain, where we look at the azimuth-beampattern of the mth antenna, denoted by $b_m(f,\phi)$. Then, in terms of the time domain, the agent transmits a lowpass-equivalent signal $s(t)$ modulated by carrier frequency f_c. To obtain the received signal at antenna m denoted by $r_m(t)$, the linear channel given by the spreading function in (2.2) has to be convolved with the transmitted signal $s(t)$ taking beampattern $b_m(f,\phi)$ into consideration. However, certain further assumptions may be used to simplify this process and to specify the scenario arriving at a compact description. Analogously to Section 2.1.1, we outline assumptions cumulatively and note the mathematical application.

- For the antennas at the anchor, in frequency domain, we assume identical beampatterns over all relevant frequencies. This is a basic antenna design requirement to enable many applications. In terms of antenna polarization properties, we assume a single (matched) polarization state at anchor and agent. That is, co- and cross-polarization effects are not considered, however their inclusion is straight-forward.
  Application to (2.2)*: In further reference of anchor antenna m, we use* $b_m(f,\phi) = b_m(\phi)$ *for the complex-valued azimuth antenna gains.*
- For the time-domain description of radio waves impinging at the antenna elements, we make use of the far-field *plane-wave assumption*, i.e., we assume planar wave fronts instead of spherical ones. This assumption is used in the majority of array processing works, since a treatment of spherical wave fronts significantly increases the complexity of mathematical models with insignificant gain in insights.
  Application to (2.2)*: Treatment of the transmitted signal* $s(t)$ *can be performed completely in the delay domain, i.e., the angle-domain of channel* $h(\phi,\tau;\boldsymbol{p})$ *does not affect the transmitted signal directly, but only the beampatterns.*
- Introduced time delays at antenna elements in relation to the delay of the mass point will be only considered in terms of (angle-dependent) phase changes, i.e., the time delay of the signal envelope will be neglected. This is usually referred to as the *narrowband / wideband* assumption, where it is assumed that the delay and angle domains are separated, i.e., space-frequency cross-product terms are zero [19, Ch. 4.2]. This assumption is fair to use because the envelope information is negligible with respect to the phase information in practical situations [31, 117, 118].
  Application to (2.2)*: We introduce the antenna element phase change* $e^{j\zeta^{(m)}(\phi)}$*, which is multiplied by the beampatterns* $b_m(\phi)$ *to obtain the antenna response of one array element.*

Taking these assumptions into consideration, we get the received signal at antenna m when we convolve the spreading function in (2.2) with the transmitted signal $s(t)$ and antenna response $b_m(\phi)e^{j\zeta^{(m)}(\phi)}$ as follows

$$\begin{aligned} r_m(t) &= \iint b_m(\phi)e^{j\zeta^{(m)}(\phi)}s\big(t-\tau\big)\,h(\phi,\tau)\,\mathrm{d}\phi\,\mathrm{d}\tau + w_m(t) \\ &= \sum_{k=1}^{K}\alpha_k e^{j\left(\zeta_k+\zeta^{(m)}(\phi_k)\right)}\,b_m(\phi_k)s(t-\tau_k) + r_m^{\mathrm{DM}}(t) + w_m(t) \end{aligned} \tag{2.4}$$

where we dropped the position dependence for the sake of legibility, i.e., all SMC-related parameters (with subscript k) are written as $x_k \triangleq x_k(\boldsymbol{p})$. (Later, for the DMC-related part, the position dependence is dropped as well.) Similarly to the simplified channel from (2.2), the received signal from (2.4) can be separated into three distinct parts: The first part contains the position-related SMC parameters $\{\alpha_k,\zeta_k,\phi_k,\tau_k\}$ which scale and shift the transmitted signal. The second part $r_m^{\mathrm{DM}}(t)$ is a stochastic process characterizing the self-interference due to the DMC. Finally, measurement noise $w_m(t)$ is modeled as additive white Gaussian noise (AWGN) with double-sided power spectral density of $\frac{N_0}{2}$.

The SMC-related part poses as the foundation of all following chapters and will be discussed in detail in Section 2.2. However, now we shed light onto the DMC-related part, which is a challenging feat and hence, in most works, any signal components equivalent to DMC are treated as AWGN. We may write the second part of (2.4) as

$$r_m^{\mathrm{DM}}(t) = \iint b_m(\phi)e^{\zeta^{(m)}(\phi)}s(t-\tau)\,\nu(\phi,\tau)\,\mathrm{d}\phi\,\mathrm{d}\tau.$$

Since we have the stochastic quantity $\nu(\phi,\tau)$, we examine correlation properties of this signal for a pair of antennas (m,m') with

$$\begin{aligned}\mathbb{E}\left\{r_m^{\mathrm{DM}}(t)(r_{m'}^{\mathrm{DM}}(t'))^*\right\} &= \iiiint b_m(\phi)\, b_{m'}^*(\phi') e^{j(\zeta^{(m)}-\zeta^{(m')})} s(t-\tau)\, s(t'-\tau') \\ &\qquad \times \mathbb{E}\left\{\nu(\phi,\tau)\nu^*(\phi',\tau')\right\} \mathrm{d}\phi\, \mathrm{d}\phi'\, \mathrm{d}\tau\, \mathrm{d}\tau' \\ &= \iint S_\nu(\phi,\tau) b_m(\phi)\, b_{m'}^*(\phi) e^{j(\zeta^{(m)}-\zeta^{(m')})} \\ &\qquad \times s(t-\tau)\, s(t'-\tau)\, \mathrm{d}\phi\, \mathrm{d}\tau. \end{aligned} \tag{2.5}$$

Here, we included the azimuth-delay power spectrum from (2.3), where we applied the US assumption. It should be noted that this assumption also allows us to use the same stochastic process $\nu(\phi,\tau)$ for all antenna elements, because the assumption implies homogeneity in spatial domain [80, Ch. 2.4], thus the correlation between m and m' due to spatial separation is effectively covered. Obviously, with (2.5) we are still deep in analytic territory without a closed-form solution. However, entering the discrete-time domain will allow us to resolve this issue with familiar treatable quantities such as covariance matrices. In the following, we will enter this domain and arrive at multiple discrete-time system models, each suited for particular applications handled in the later chapters of the thesis.

2.1.3. Discrete-time System Models

In the previous section, we established a generic received signal model in (2.4) and outlined the challenging characterization of the DMC in (2.5). In the following, we establish multiple system models, each suited to tackle different research hypotheses, by entering the discrete-time domain via sampling. Hence, we will use vector notation for signals and parameters, e.g., $\boldsymbol{y} = [y_1,\dots,y_N]^{\mathrm{T}} \in \mathbb{R}^{N\times 1}$.

In any practical system, the anchor acquires N_s samples of the received signal using the mth antenna element sampled with frequency $f_{\mathrm{s}} = 1/T_{\mathrm{s}}$ to write the samples as $[\boldsymbol{r}_m]_i = r_m([i-1]\cdot T_{\mathrm{s}}), i = 1\dots N_s$. All sampled antenna element signals are then stacked into the observation vector $\boldsymbol{r} = [\boldsymbol{r}_1^T,\dots,\boldsymbol{r}_M^T]^T \in \mathbb{C}^{MN_s\times 1}$ given as

$$\boldsymbol{r} = \boldsymbol{x}(\boldsymbol{\theta}) + \boldsymbol{n}. \tag{2.6}$$

Here, we have again on the one hand the SMC-related term $\boldsymbol{x}(\boldsymbol{\theta})$ as a function of the SMC parameters

$$\boldsymbol{\theta} = \left[\boldsymbol{\phi}^{\mathrm{T}}, \boldsymbol{\tau}^{\mathrm{T}}, \boldsymbol{\alpha}^{\mathrm{T}}, \boldsymbol{\zeta}^{\mathrm{T}}\right]^{\mathrm{T}} \tag{2.7}$$

and on the other hand the DMC and noise related term $\boldsymbol{n}$. The size of each individual parameter vector is $\mathbb{R}^{K\times 1}$ e.g., $\boldsymbol{\alpha} = [\alpha_1,\dots,\alpha_K]^{\mathrm{T}}$. An exception is the phase parameter $\boldsymbol{\zeta}$, which differs depending on the amplitude phase processing at the anchor, hence it will be specified later.

In the following, we outline different anchor setups and their respective signal models, first for the SMC-related part and then for the noise-related part. The setups are denoted as (I), (II) and (III), and they will be referred to as such throughout the thesis. Each model provides the finalized foundation for the tasks described in the upcoming chapters.

Setup (I): simple anchor

For this setup, the anchor uses the same system as the agents, i.e, it is equipped with a single omni-directional antenna situated at (known) position $\boldsymbol{a}$. Hence, we have for the number of antenna elements $M = 1$ and for the beampattern $b_1(\phi) = 1$[4]. With this setup, we have the deterministic part of each observation

$$\boldsymbol{x}^{(\mathrm{I})}\left(\boldsymbol{\theta}^{(\mathrm{I})}\right) = \left[\boldsymbol{s}(\tau_1) \quad \dots \quad \boldsymbol{s}(\tau_K)\right] \begin{bmatrix} \alpha_1 e^{j\zeta_1} \\ \vdots \\ \alpha_K e^{j\zeta_K} \end{bmatrix} \qquad \in \mathbb{C}^{N_s \times 1} \tag{2.8}$$

with

$$\boldsymbol{s}(\tau_k) = \left[s(0 \cdot T_\mathrm{s} - \tau_k), \dots, s([N-1] \cdot T_\mathrm{s} - \tau_k)\right]^\mathrm{T} \qquad \in \mathbb{R}^{N_s \times 1}.$$

This compact model enables the treatment of single-antenna radio channel measurements and it has been used in multiple multipath-assisted positioning applications [70]. However, with only a single antenna and no directional beampattern, SMC angles can not be explored and hence we have the parameter vector

$$\boldsymbol{\theta}^{(\mathrm{I})} = \left[\boldsymbol{\tau}^\mathrm{T}, \boldsymbol{\alpha}^\mathrm{T}, \boldsymbol{\zeta}^\mathrm{T}\right]^\mathrm{T} \qquad \in \mathbb{R}^{3K \times 1}. \tag{2.9}$$

Setup (II): conventional antenna array processing

We extend (I), by adding additional omni-directional antennas situated at positions $\boldsymbol{a}^{(m)}$, thus forming an array of M elements with known geometry and fixed orientation; an example is shown in Figure 2.1. For this setup, we describe the SMC-related signal model with

$$\boldsymbol{x}^{(\mathrm{II})}\left(\boldsymbol{\theta}^{(\mathrm{II})}\right) = \begin{bmatrix} \boldsymbol{s}(\tau_1) e^{j\zeta^{(1)}(\phi_1)} & \dots & \boldsymbol{s}(\tau_K) e^{j\zeta^{(1)}(\phi_K)} \\ \vdots & \ddots & \vdots \\ \boldsymbol{s}(\tau_1) e^{j\zeta^{(M)}(\phi_1)} & \dots & \boldsymbol{s}(\tau_K) e^{j\zeta^{(M)}(\phi_K)} \end{bmatrix} \begin{bmatrix} \alpha_1 e^{j\zeta_1} \\ \vdots \\ \alpha_K e^{j\zeta_K} \end{bmatrix} \quad \in \mathbb{C}^{MN_s \times 1} \tag{2.10}$$

with parameter vector

$$\boldsymbol{\theta}^{(\mathrm{II})} = \left[\boldsymbol{\phi}^\mathrm{T}, \boldsymbol{\tau}^\mathrm{T}, \boldsymbol{\alpha}^\mathrm{T}, \boldsymbol{\zeta}^\mathrm{T}\right]^\mathrm{T} \qquad \in \mathbb{R}^{4K \times 1}. \tag{2.11}$$

We have the distance of the antenna elements (situated at $\boldsymbol{a}_1^{(m)}$) relative to the mass point at $\boldsymbol{a}_1$, which introduces a time delay and corresponding phase change determined by

$$\zeta^{(m)}\left(\phi_k\right) = 2\pi f_\mathrm{c} \tfrac{d^{(m)}}{c} \cos\left(\phi_k - \phi^{(m)}\right). \tag{2.12}$$

---

[4] One might use $b_1(\phi) = 1/\sqrt{2\pi}$ in order to have the energy-normalized case with $\int_{-\pi}^{\pi} |b_1(\phi)|^2 \, \mathrm{d}\phi = 1$.

Having multiple antennas allows the system to resolve the angle domain, i.e., each element sees a different angle-dependent phase at impinging SMCs. We refer to this as the *coherent processing* case, where the SMC phase ζ_k can be estimated from the measured signal by accounting for the relative phase change $\zeta^{(m)}(\phi)$ at the antenna elements, which requires the array geometry and orientation to be known. Then, the phase parameter is described by $\boldsymbol{\zeta} = [\zeta_1, \ldots, \zeta_k]^{\mathrm{T}} \in \mathbb{R}^{K \times 1}$, which is in line with the other parameters.

Setup (III): non-coherent directional antennas

The third setup presents an alternative to (II), in that the SMC angles are accessed via directional antennas instead of array processing. That is, there are again M array elements with directional beampatterns $b_m(\phi)$. The corresponding SMC-related signal model is given by

$$\boldsymbol{x}^{(\mathrm{III})}\left(\boldsymbol{\theta}^{(\mathrm{III})}\right) = \begin{bmatrix} b_1(\phi_1)\, s(\tau_1) e^{j\tilde{\zeta}_{1,1}} & \ldots & b_1(\phi_K)\, s(\tau_K) e^{j\tilde{\zeta}_{K,1}} \\ \vdots & \ddots & \vdots \\ b_M(\phi_1)\, s(\tau_1) e^{j\tilde{\zeta}_{1,M}} & \ldots & b_M(\phi_K)\, s(\tau_K) e^{j\tilde{\zeta}_{K,M}} \end{bmatrix} \begin{bmatrix} \alpha_1 \\ \vdots \\ \alpha_K \end{bmatrix} \in \mathbb{C}^{MN_s \times 1} \tag{2.13}$$

with parameter vector

$$\boldsymbol{\theta}^{(\mathrm{III})} = \left[\boldsymbol{\phi}^{\mathrm{T}}, \boldsymbol{\tau}^{\mathrm{T}}, \boldsymbol{\alpha}^{\mathrm{T}}, \tilde{\boldsymbol{\zeta}}^{\mathrm{T}}\right]^{\mathrm{T}} \qquad \in \mathbb{R}^{K(M+3) \times 1}. \tag{2.14}$$

This model is referred to by the *non-coherent processing* case, where we can not separate the SMC phase ζ_k and the relative phase changes $\zeta^{(m)}(\phi_k)$, i.e., the antenna elements can have arbitrary position offsets from the reference position $\boldsymbol{a}$. These phase effects are combined to the parameter $\tilde{\zeta}_{k,m}$ and the corresponding parameter vector is of the form

$$\tilde{\boldsymbol{\zeta}} = [\tilde{\zeta}_{1,1}, \ldots, \tilde{\zeta}_{K,1}, \tilde{\zeta}_{1,2}, \ldots, \tilde{\zeta}_{K,2}, \ldots, \tilde{\zeta}_{1,M}, \ldots, \tilde{\zeta}_{K,M}]^{\mathrm{T}} \qquad \in \mathbb{R}^{KM \times 1}.$$

This concludes the outline of three different SMC-related signal models which will be accessed later in order to formulate positioning algorithms (using (I) and (III) in Chapter 3), determine position accuracy bounds (for all setups in Chapter 4) and formulate radio environment maps (using (III) in Chapter 5). Next, we move to the noise-related (i.e., stochastic) part of the signal model denoted by $\boldsymbol{n}$.

Noise model I: only measurement noise

The most common way to include uncertainties in signal models is by means of AWGN. This is motivated by thermal noise being present in every (electric) measurement system and AWGN has been used to accurately model it. Hence, we describe the noise-related parts via

$$\boldsymbol{n}^{(\mathrm{AWGN})} = \boldsymbol{w} \qquad \in \mathbb{C}^{MN_s \times 1} \tag{2.15}$$

using the complex Gaussian $\boldsymbol{w} \sim \mathcal{CN}(\boldsymbol{0}, \boldsymbol{C}_{\boldsymbol{w}})$. Here, the covariance matrix is given by

$$\boldsymbol{C}_{\boldsymbol{w}} = \sigma_w^2 \boldsymbol{I}_{MN_s} \qquad \in \mathbb{R}^{MN_s \times MN_s} \tag{2.16}$$

where σ_w^2 is the sample-based noise variance, which can be related to the AWGN power spectral density from (2.4) via $\sigma_w^2 = N_0/T_\mathrm{s}$. This model is simple, without environment specific assumptions, and is thus the to-go choice in most positioning algorithms, especially when implementations on low-cost devices are considered, where there are many additional hardware-related noise sources present. In this thesis, this model is also used for most of the maximum-likelihood based positioning methods and we use directly the noise vector $\boldsymbol{w}$. There are manifold ways to generate realizations of this noise vector given a set variance σ_w^2, a difficulty arises only in setting this variance to fulfill certain criteria, e.g., channel quality.

Noise model II: including dense multipath

The second proposal to treat uncertainties is the more sophisticated choice of respecting the dense multipath propagation as it is characterized in (2.5). To start, we consider the most general model with multiple array elements with arbitrary beampatterns. We have

$$\boldsymbol{n}^{(\mathrm{DM})} = \boldsymbol{\nu} + \boldsymbol{w} \qquad \in \mathbb{C}^{MN_s \times 1} \tag{2.17}$$

representing the stochastic process characterizing the DMC $\boldsymbol{\nu}$ and the measurement noise $\boldsymbol{w}$ (as described before). We describe these quantities again by a Gaussian process $\boldsymbol{n}^{(\mathrm{DM})} \sim \mathcal{CN}(\boldsymbol{0}, \boldsymbol{C}_{\boldsymbol{n}})$ with covariance matrix

$$\boldsymbol{C}_{\boldsymbol{n}} = \boldsymbol{C}_{\boldsymbol{\nu}} + \boldsymbol{C}_{\boldsymbol{w}} \tag{2.18}$$

where we made the trivial assumption that DMC and measurement noise are independent. The measurement noise covariance matrix $\boldsymbol{C}_{\boldsymbol{w}}$ is defined in (2.16), whereas for the DMC covariance matrix $\boldsymbol{C}_{\boldsymbol{\nu}}$ there are additionally correlations between antenna elements to be taken into account. For this, we separate $\boldsymbol{C}_{\boldsymbol{\nu}}$ into blocks of size $N_s \times N_s$, each describing the correlations between one pair of antennas indexed as (m, m'). On the basis of (2.5), we may write one block of the DMC covariance matrix as

$$\boldsymbol{C}_{\boldsymbol{\nu}}^{(m,m')} = \iint S_\nu(\phi,\tau)\, b_m(\phi)\, b_{m'}^*(\phi)\, e^{j(\zeta^{(m)}(\phi) - \zeta^{(m')}(\phi))} \boldsymbol{s}(\tau) \boldsymbol{s}(\tau)^\mathrm{H}\, \mathrm{d}\phi\, \mathrm{d}\tau. \tag{2.19}$$

We simplify this covariance matrix by consideration of antennas adhering the following assumption.

- The DMC is uncorrelated between antennas, i.e., $\boldsymbol{C}_{\boldsymbol{\nu}}$ is block-diagonal. For each of the previously described anchor antenna setups, there are different arguments supporting this assumption: For (II) (conventional array), the DMC becomes approximately uncorrelated for an antenna-spacing of $\lambda/2$ and a uniform angular power spectrum [80]. For (III) (directional antennas), it can be argued that each antenna at the anchor covers a different sector in the azimuth plane due to differently aligned beampatterns. As a result, the shapes of the beampatterns are approximately orthogonal such that

$$\int S_\nu(\phi,\tau)\, b_m(\phi)\, b_{m'}^*(\phi)\, \mathrm{d}\phi \ll \int S_\nu(\phi,\tau)\, |b_m(\phi)|^2\, \mathrm{d}\phi. \tag{2.20}$$

This expression shows that the angle-delay power spectrum has to be considered for this assumption to be fulfilled exactly.

Taking this assumption into account, the mth DMC covariance matrix on the main diagonal is written as

$$\boldsymbol{C}_{\boldsymbol{\nu}}^{(m)} \triangleq \boldsymbol{C}_{\boldsymbol{\nu}}^{(m,m)} = \iint S_{\nu}(\phi,\tau)\,|b_m(\phi)|^2\,\boldsymbol{s}(\tau)\boldsymbol{s}(\tau)^{\mathrm{H}}\,\mathrm{d}\phi\,\mathrm{d}\tau \tag{2.21}$$

whereas all off-diagonal matrices vanish, i.e.,

$$\boldsymbol{C}_{\boldsymbol{\nu}}^{(m,m')} = \mathbf{0}_{N_s} \qquad\qquad \forall m \neq m'.$$

Further restrictions are needed to make this noise model suitable for performance analysis and algorithm development. First, we introduce the following assumption:

- The DMC angle-delay power spectrum is shaped such that its domains are independent, i.e., both angle and delay domain can be treated separately. Hence, we write

  $$S_{\nu}(\phi,\tau) = S_{\nu}^{(\phi)}(\phi)\cdot S_{\nu}^{(\tau)}(\tau) \tag{2.22}$$

  where $S_{\nu}^{(\phi)}(\phi)$ is the angle power spectrum and $S_{\nu}^{(\tau)}(\tau)$ is the delay power spectrum (DPS). The latter will play an important role later, as the delay domain yields the most accurate position information.

With this, we can separate the double integral from (2.21) to write the DMC-related matrix as

$$\boldsymbol{C}_{\boldsymbol{\nu}}^{(m)} = \int S_{\nu}^{(\phi)}(\phi)\,|b_m(\phi)|^2\,\mathrm{d}\phi\cdot\int S_{\nu}^{(\tau)}(\tau)\,\boldsymbol{s}(\tau)\boldsymbol{s}(\tau)^{\mathrm{H}}\,\mathrm{d}\tau \tag{2.23}$$

The DMC angle power spectrum is difficult to treat, hence we formulate the general matrix

$$\boldsymbol{C}_{\phi} = \begin{bmatrix} \int S_{\nu}^{(\phi)}(\phi)\,|b_1(\phi)|^2\,\mathrm{d}\phi & \dots & 0 \\ \vdots & \ddots & \vdots \\ 0 & \dots & \int S_{\nu}^{(\phi)}(\phi)\,|b_M(\phi)|^2\,\mathrm{d}\phi \end{bmatrix} \qquad \in \mathbb{R}^{M\times M} \tag{2.24}$$

which collects the angle-related DMC contributions for each antenna. Furthermore, we approximate the remaining integral with a sum to write

$$\begin{aligned} \int S_{\nu}^{(\tau)}(\tau)\,\boldsymbol{s}(\tau)\boldsymbol{s}(\tau)^{\mathrm{H}}\,\mathrm{d}\tau &\approx \sum_{j=0}^{N_s-1} S_{\nu}^{(\tau)}(j\cdot T_{\mathrm{s}})\,\boldsymbol{s}(\tau)\boldsymbol{s}(j\cdot T_{\mathrm{s}})^{\mathrm{H}}\,T_{\mathrm{s}} \\ &= \boldsymbol{S}_{\mathrm{c}}\boldsymbol{C}_{\tau}\boldsymbol{S}_{\mathrm{c}}^{\mathrm{H}} \end{aligned} \tag{2.25}$$

with

$$\boldsymbol{S}_{\mathrm{c}} = [\boldsymbol{s}(0\cdot T_{\mathrm{s}}), \boldsymbol{s}(1\cdot T_{\mathrm{s}}), \dots, \boldsymbol{s}([N_s-1]\cdot T_{\mathrm{s}})] \qquad \in \mathbb{R}^{N_s\times N_s} \tag{2.26}$$

$$\boldsymbol{C}_{\tau} = \begin{bmatrix} S_{\nu}^{(\tau)}(0\cdot T_{\mathrm{s}}) & \dots & 0 \\ \vdots & \ddots & \vdots \\ 0 & \dots & S_{\nu}^{(\tau)}([N-1]\cdot T_{\mathrm{s}}) \end{bmatrix}\cdot T_{\mathrm{s}} \qquad \in \mathbb{R}^{N_s\times N_s}. \tag{2.27}$$

The matrix $\boldsymbol{S}_{\mathrm{c}}$ is used to perform the circular *convolution* with respect to the signal vectors. Combining all introduced matrices, the full DMC covariance matrix is written as

$$\boldsymbol{C}_{\boldsymbol{\nu}} = \boldsymbol{C}_{\phi} \otimes (\boldsymbol{S}_{\mathrm{c}} \boldsymbol{C}_{\tau} \boldsymbol{S}_{\mathrm{c}}^{\mathrm{H}}) \qquad \in \mathbb{R}^{MN_s \times MN_s} \tag{2.28}$$

where $\otimes$ denotes the Kronecker product. To specify the DMC covariance matrix, we need to choose a model for $S_{\nu}^{(\tau)}(\tau)$, where commonly (and in this thesis) single- and double-exponential decay models are used. Then, the matrix $\boldsymbol{C}_{\phi}$ contains weighting factors for each antenna, depending on the directionality of the DMC from the perspective of the anchor. There is no straight-forward method to properly model this matrix, hence an alternative approach used in this thesis as well as in many publications is to assume a uniform DMC angle power spectrum, which simplifies the respective matrix to

$$\hat{\boldsymbol{C}}_{\phi} = \boldsymbol{I}_{M}. \tag{2.29}$$

To obtain a realization of the DMC $\boldsymbol{\nu}^{(i)}$, given a specified covariance matrix $\boldsymbol{C}_{\boldsymbol{\nu}}$, the Cholesky decomposition can be used to obtain

$$\boldsymbol{C}_{\boldsymbol{\nu}} = \boldsymbol{L}_{\boldsymbol{\nu}} \boldsymbol{L}_{\boldsymbol{\nu}}^{\mathrm{H}} \tag{2.30}$$

where $\boldsymbol{L}_{\boldsymbol{\nu}}$ is a lower triangular matrix. Then one can draw a standard complex Gaussian $\boldsymbol{w}^{(i)} \sim \mathcal{CN}(\boldsymbol{0}, \boldsymbol{I}_{MN_s})$ and get a DMC realization via

$$\boldsymbol{\nu}^{(i)} = \boldsymbol{L}_{\boldsymbol{\nu}} \boldsymbol{w}^{(i)}. \tag{2.31}$$

2.2. Modeling Specular Multipath Components

The previous section has established models for the signals exchanged between agent and anchor, which poses as a foundation for this thesis. For all analyzed signals, the main source of position and environment information lies within the SMCs, hence this section is dedicated to models putting SMCs into context with the considered scenarios.

In the first part of this section, we look at time and angle-resolved models for the SMCs, the second part describes the underlying geometric models, and in the third part we look at models for the amplitudes, more specifically, how to evaluate the quality of SMC amplitudes for the posed hypotheses.

2.2.1. SMC Parameters

Each SMC is characterized by the parameters established in (2.7). These parameters in turn are related to the agent position $\boldsymbol{p}$ via the geometry of the environment. In this regard, we want to make clear that we have K SMCs, which includes the line-of-sight (LOS) component labeled with $k = 1$ and $K - 1$ reflections labeled with $k = 2 \ldots K$. Hence for $k > 1$, each SMC involves the reflection on flat surfaces such as wall segments of a room.

In the following, we define each geometry-related SMC parameter as a function of the agent position $\boldsymbol{p}$ and the virtual anchor (VA) position $\boldsymbol{a}_k$. The latter represents a virtual source [49, 123] that is determined using a geometric floorplan model as is defined in Section 2.2.2. From this floorplan model, we also need the geometry-related quantities of

SMC order $O(k)$ (number of wall bounces), wall segment angle ϕ_l^{seg} (orientation of the lth wall segment) and propagation path index $g_k(j)$ (segments index of the jth bounce).

From the parameter set (2.7), a direct relation to the geometry can be established for delay and angle, whereas for amplitudes and phases, there are merely partial relations and proposed models. More treatment of the latter is provided in Section 2.2.3.

We start with the SMC path length and the corresponding delay (time-of-flight) defined as

$$d_k(\boldsymbol{p}) = \|\boldsymbol{a}_k - \boldsymbol{p}\| \tag{2.32}$$

$$\tau_k(\boldsymbol{p}) = \tfrac{1}{c}\, d_k(\boldsymbol{p}) \tag{2.33}$$

where c is the propagation speed (unless stated otherwise, vacuum speed of light approximated with $c \approx 3 \cdot 10^8$ m/s is used). With this, the VAs enable a simple and compact computation of SMC delays for reflections of arbitrary order. The complexity arises only in determining high-order VA positions and their visibility properties.

Next, we move into angle domain and define the angle-of-departure (AoD) from the perspective of the agent. For further usage, we write the unit vector associated with AoD $\varphi_k(\boldsymbol{p})$ as

$$\boldsymbol{e}\big(\varphi_k(\boldsymbol{p})\big) = \tfrac{1}{d_k(\boldsymbol{p})}(\boldsymbol{a}_k - \boldsymbol{p}) \tag{2.34}$$

where we note that, even though the AoD is used as an argument directly, its relation arises from the association to the corresponding VA. Then, the AoD is obtained by

$$\varphi_k(\boldsymbol{p}) = \measuredangle\Big(\boldsymbol{e}\big(\varphi_k(\boldsymbol{p})\big)\Big) \tag{2.35}$$

where the angle function $\measuredangle(\,\cdot\,)$ can be realized in several ways on the basis of trigonometric functions, one possibility is outlined in the segment angle description (2.45).

For SMC order $O(k)$, the AoD is related to the AoA (from the perspective of the anchor) using the angles of all involved wall segments as

$$\phi_k(\boldsymbol{p}) = (-1)^{O(k)}\big(\varphi_k(\boldsymbol{p}) - \pi\big) - 2\sum_{j=1}^{O(k)} (-1)^j\, \phi_{g_k(j)}^{\text{seg}}. \tag{2.36}$$

Here, $g_k(j)$ is used to access the corresponding segment angle in the propagation path.

For the treatment of first and second-order VAs, simplified computations of the AoAs may be written as

$$\phi_k(\boldsymbol{p}) = \pi - \varphi_k(\boldsymbol{p}) + 2\phi_{k-1}^{\text{seg}} \qquad O(k) = 1 \tag{2.37}$$

$$\phi_k(\boldsymbol{p}) = \varphi_k(\boldsymbol{p}) - \pi + 2(\phi_{k-1}^{\text{seg}} - \phi_{g_k(2)}^{\text{seg}}) \qquad O(k) = 2. \tag{2.38}$$

It should be noted that the simple segment indexing $g_k(1) = k - 1$ was used. Furthermore, all derived angles in this section can assume values outside the interval $[0, 2\pi]$, hence it might be necessary to obtain an equivalent angle via $(\phi_k(\boldsymbol{p}) \bmod 2\pi)$, e.g., to access antenna pattern values from a codebook.

What remains are SMC amplitudes and phases, which depend on the materials of the reflected surfaces and therefore a generalized modeling process is difficult. However, we may formulate position-related models of SMC amplitudes and phases as

$$\alpha_k(\boldsymbol{p}) = \mathrm{PL}\big(d_k(\boldsymbol{p})\big)\,\big|\Gamma_k\big(\varphi_k(\boldsymbol{p})\big)\big| \tag{2.39}$$

$$\zeta_k(\boldsymbol{p}) = \tfrac{2\pi}{\lambda_c} d_k(\boldsymbol{p}) + \arg\Big(\Gamma_k\big(\varphi_k(\boldsymbol{p})\big)\Big) \tag{2.40}$$

where $\arg(\cdot)$ denotes the complex argument. Furthermore, $\mathrm{PL}(\cdot)$ describes the path loss (PL) for the respective propagated distance $d_k(\boldsymbol{p})$, $\Gamma_k(\cdot)$ is the reflection coefficient of the corresponding VA for a given incidence angle $\varphi_k(\boldsymbol{p})$ and λ is the wavelength at f_c. There are various ways to model the PL for narrow-band systems where SMC separation is not possible. However, in our case, we use the simple free space model with $\mathrm{PL}(d) = 1/d$. The reflection coefficient covers amplitude losses and carrier phase rotations, both related to the materials and incidence angles of each bounced surface, hence we have the AoA dependence. This physical process can turn highly complex for higher-order reflections. A simplified model can be used by dropping the angle dependence and assuming a halving of the amplitude power per surface bounce, i.e, $|\Gamma_k| = (1/\sqrt{2})^{O(k)}$, which means that for the phase there is no relation to the agent position considered.

Due to the difficult reflection effects, in the later parts of Chapter 3 and Chapter 4, SMC amplitudes and phases are treated as nuisance parameters for the position estimation problem. A better way to examine the SMC amplitudes is by looking at their statistics, which is done in Section 2.2.3 in terms of second-order statistics that represent the amplitude "quality".

2.2.2. Geometry-related Modeling

As each SMC involves the reflection on flat surfaces from the environment, a detailed description thereof is required. In the following, we define the geometry of an environment mathematically as a combination of wall segments forming a *floorplan*.

Floorplan definition

In general, each reflective surface of a floorplan can be defined by a plane, using one (base) position on the plane and the plane normal. However, in this thesis, azimuth plane operation is considered, thus the environment is described by $l = 1 \dots L$ line segments and the lth segment is defined by a pair of points $(\boldsymbol{w}_l^{(1)}, \boldsymbol{w}_l^{(2)})$ which represent the segment *start* and *end* coordinates. We stack these segment coordinates to get the floorplan matrix

$$\boldsymbol{W} = \begin{bmatrix} \boldsymbol{w}_1^{(1)} & \cdots & \boldsymbol{w}_L^{(1)} \\ \boldsymbol{w}_1^{(2)} & \cdots & \boldsymbol{w}_L^{(2)} \end{bmatrix} \qquad \in \mathbb{R}^{4\times L} \tag{2.41}$$

i.e., each column contains the 2D coordinates of one (wall) segment. For later use, we use a simple matrix multiplication to obtain the direction matrix

$$\boldsymbol{V} = [\boldsymbol{v}_1 \dots \boldsymbol{v}_L] = \begin{bmatrix} -1 & 0 & 1 & 0 \\ 0 & -1 & 0 & 1 \end{bmatrix} \boldsymbol{W} \qquad \in \mathbb{R}^{2\times L} \tag{2.42}$$

where the lth column $\boldsymbol{v}_l$ contains the direction vector of the corresponding segment. Another multiplication results in the matrix of normal vectors

$$\boldsymbol{N} = [\boldsymbol{n}_1 \dots \boldsymbol{n}_L] = \boldsymbol{R}_{\pi/2} \boldsymbol{V} \qquad \in \mathbb{R}^{2\times L} \tag{2.43}$$

where $\boldsymbol{R}_{\pi/2}$ is the azimuth rotation matrix defined by

$$\boldsymbol{R}_\alpha = \begin{bmatrix} \cos\alpha & -\sin\alpha \\ \sin\alpha & \cos\alpha \end{bmatrix} \tag{2.44}$$

that rotates a 2D vector by the angle α when multiplied from the left.

With the direction vectors, we can write the lth segment azimuth angle as

$$\phi_l^{\text{seg}} = \measuredangle(\boldsymbol{v}_l) \bmod \pi \tag{2.45}$$

where the angle function $\measuredangle(\,\cdot\,)$ can be implemented in various ways using inverse trigonometric functions. To this end, a useful function for implementations is the double-argument inverse tangent function applied onto the unit vector of the wall segment written as $\operatorname{atan2}([\boldsymbol{v}_l]_y, [\boldsymbol{v}_l]_x)$, where $[\cdot]_x$ and $[\cdot]_y$ are used to access the corresponding coordinates of the vector. This function can determine the angle in the complete interval of $[0, 2\pi]$ and a detailed description is given in Appendix A. Finally, the modulo operator is used to get consistent segment angles regardless of the order of segment start- and end-point to fulfill $\phi_l^{\text{seg}} \in [0, \pi]$.

As a summary, we define $l = 1 \dots L$ sets

$$\mathcal{F}_l = \left\{ \boldsymbol{w}_l^{(1)}, \boldsymbol{w}_l^{(2)}, \boldsymbol{v}_l, \boldsymbol{n}_l, \phi_l^{\text{seg}} \right\} \tag{2.46}$$

each of which collects all characterizing quantities for the wall segment l. From an application perspective, it is sufficient to provide the segment matrix $\boldsymbol{W}$, then via (2.42)-(2.45) the remaining parts of the segment set can be derived. With the segment sets at hand, we now introduce the concept of VAs, which enables compact geometric models for the SMC parameters, as shown in Section 2.2.1.

Virtual anchors (VAs)

Each VA is associated with one SMC and thus the VA position is written as $\boldsymbol{a}_k$, where we include the physical anchor as the first VA with $\boldsymbol{a}_1 \triangleq \boldsymbol{a}$. Further VA positions are obtained via mirroring operations of the physical anchor $\boldsymbol{a}_1$ by all involved wall segment surfaces in the propagation path. Such a path is determined by the sequence of interacting segments, which can be described by an ordered array of indices among the L dedicated wall segments. One particular segment is accessed via $g_k(j)$ which indicates the index of the jth reflective surface for the kth SMC. The number of bounced surfaces determines the order of SMC and VA. For the kth SMC, the reflection order is denoted by $O(k)$. In this thesis, we consider reflections up to order 2, for which we will outline the VA derivation in the following.

We start with first-order VAs, which are obtained by mirroring the physical anchor position $\boldsymbol{a}_1$ at each wall segment as

$$\boldsymbol{a}_k = \operatorname{mirr}(\boldsymbol{a}_1, \mathcal{F}_{k-1}) \qquad\qquad \forall k \in [2, L+1] \tag{2.47}$$

with the mirroring operation defined by

$$\operatorname{mirr}(\boldsymbol{x}, \mathcal{F}_i) = \boldsymbol{x} + 2\Big((\boldsymbol{w}_i^{(1)} - \boldsymbol{x})^{\mathrm{T}} \tfrac{\boldsymbol{n}_i}{\|\boldsymbol{n}_i\|}\Big)\boldsymbol{n}_i \tag{2.48}$$

where the bracket-term corresponds to the Hessian normal form of the segment line equation[5]. It should be noted that for any wall segment labeled by l, the corresponding first-order VA index is $k = l + 1$, making the segment-to-VA association straight forward ($g_k(1) = k - 1$ for the propagation path).

---

[5] The Hessian normal form is used to obtain the distance of any position $\boldsymbol{x}$ to the corresponding line of the ith segment. The used position $\boldsymbol{w}_i^{(1)}$ could be replaced by any position on the segment line.

In the next step, to determine second-order VAs, further mirroring operations are performed, this time using the established first-order VAs. Let $k' \in [2, L+1]$ determine the index of one first-order VA and $l \in [1, L] \setminus k'-1$ is the index of the wall segment causing the second interaction (the segment associated with the picked first-order VA is excluded). Then, the corresponding second-order VA is obtained via

$$\boldsymbol{a}_k = \operatorname{mirr}(\boldsymbol{a}_{k'}, \mathcal{F}_l) \qquad \forall k \in [L+2, L^2+1]. \tag{2.49}$$

For a picked first-order VA k' and segment l, the index of the resulting second-order VA is determined by

$$k = 2 + (k'-1)(L-1) + l - u(l - k' + 1) \tag{2.50}$$

where $u(\cdot)$ is the unit-step function, which is used to take the rejected cases where $l = k'-1$ into account. This indexing leads to a sequential numbering, cycling through the wall segments for each first-order VA. A demonstration is given in Figure 2.2 showing a simple floorplan with $L = 3$ segments, where, if we take e.g. VA $\boldsymbol{a}_3$ ($k' = 3$) and mirror it at the wall segment with $l = 3$, we get the second-order VA with $k = 8$ and corresponding path $g_8(1) = 2, g_8(2) = 3$.

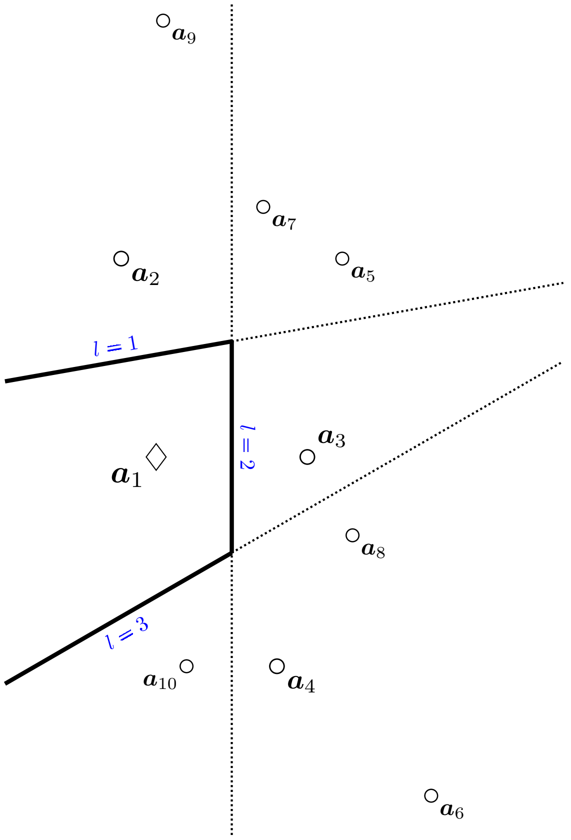

Figure 2.2.: Example floorplan showing first- and second-order VAs and the corresponding indexing according to (2.50).

For arbitrary higher VA orders $O(k)$, the process in (2.49) has to be repeated, whereas the used VAs $\boldsymbol{a}_{k'}$ have $O(k') = O(k) - 1$ and the considered wall segment is chosen via

$g_k(O(k))$. Following this method, the total number of considered SMCs amounts to

$$K = 1 + \sum_{i=0}^{\max_k\{O(k)\}-1} L(L-1)^i \tag{2.51}$$

where $\max_k\{\cdot\}$ describes the maximum operator for all possible values of k. In Chapter 3 and Chapter 5 we have $K = L+1$ (use only SMCs of order 1), whereas in Chapter 4 we have $K = L^2+1$ (use SMCs up to order 2).

SMC visibility

To determine if a specific SMC is usable at agent position $\boldsymbol{p}$, visibility conditions have to be considered, i.e., there has to be an uninterrupted path from anchor at $\boldsymbol{a}_1$ to agent at $\boldsymbol{p}$ including all reflection surfaces. In simple terms, we may describe the visibility condition as $\mathrm{vis}(\boldsymbol{p},k) \in \{0,1\}$. The visibility is then easily considered in the models from Section 2.1.3 by replacing all amplitudes via $\alpha_k(\boldsymbol{p}) \to \alpha_k(\boldsymbol{p})\mathrm{vis}(\boldsymbol{p},k)$, i.e., non-visible SMCs are basically "deleted".

For general reflection orders, a visibility condition test can be performed with the method of *ray launching*. In this method, the propagation path is traversed starting at the physical anchor and going through all involved VAs with ascending order until the agent is reached. For each pair of VAs (or VA and agent) on the path, intersection tests are performed, first, with the corresponding wall segment to determine if a reflection is geometrically possible, and second, with all other wall segments to determine if the reflection is blocked by a different part of the floorplan.

While this procedure is computationally demanding, it is possible to perform significantly more efficient visibility tests when simpler floorplans and lower reflection orders are considered. When the (start- and end-) points of the wall segments form a convex polygon[6] and only first-order reflections are considered, the visibility of each SMC can be determined via

$$\begin{aligned} \mathrm{vis}(\boldsymbol{p},k) &= \tfrac{1}{2}\,\mathrm{sgn}\big((\boldsymbol{p}-\boldsymbol{a}_k)^{\mathrm{T}}\tilde{\boldsymbol{n}}_k^{(1)}\big) - \tfrac{1}{2}\,\mathrm{sgn}\big((\boldsymbol{p}-\boldsymbol{a}_k)^{\mathrm{T}}\tilde{\boldsymbol{n}}_k^{(2)}\big) \\ \tilde{\boldsymbol{n}}_k^{(i)} &= \boldsymbol{R}_{\pi/2}\big(\boldsymbol{w}_{k-1}^{(i)} - \boldsymbol{a}_k\big). \end{aligned} \tag{2.52}$$

Essentially, this method performs two half-plane tests for $\boldsymbol{p}$ using the lines from VA to both segment start- and end-point. The intersection of these half-planes forms a "visibilty cone" and $\boldsymbol{p}$ is part of this cone when the signs of the half-plane test values differ.

In implementations, this test can be optimized defining normal form equivalent vectors and stacking multiple agent positions in a matrix as

$$\begin{aligned} \bar{\boldsymbol{n}}_k^{(i)} &= \begin{bmatrix} \tilde{\boldsymbol{n}}_k^{(i)} \\ -\boldsymbol{a}_k^{\mathrm{T}}\tilde{\boldsymbol{n}}_k^{(i)} \end{bmatrix} && \in \mathbb{R}^{3\times 1} \\ \boldsymbol{P} &= \begin{bmatrix} \boldsymbol{p}_1 & \dots & \boldsymbol{p}_{N_p} \\ 1 & \dots & 1 \end{bmatrix} && \in \mathbb{R}^{3\times N_p}. \end{aligned} \tag{2.53}$$

Then, it is possible to perform the following element-wise test to obtain a visibility vector for all positions

$$\boldsymbol{p}_{\mathrm{vis},k} = \neg(\boldsymbol{P}^{\mathrm{T}}\bar{\boldsymbol{n}}_k^{(1)} \ominus \boldsymbol{P}^{\mathrm{T}}\bar{\boldsymbol{n}}_k^{(2)}) \qquad \in \{0,1\}^{N_p\times 1} \tag{2.54}$$

---

[6] In a convex polygon, the path between each possible pair of inside points (agent positions) does not intersect with any of the polygon segments.

where $\neg$ is the logical not operator and $\ominus$ is the element-wise (logical) equality. Then, to include this visibility vector in the signal models, we perform an element-wise multiplication $\boldsymbol{\alpha}_k \odot \boldsymbol{p}_{\mathrm{vis},k}$ using a stacked vector containing the amplitudes α_k for all agent positions, i.e., we obtain $\alpha_k = 0$ for non-visible SMCs.

As a final geometry-related remark, it should be noted that, for a floorplan with perpendicular wall segments, there can be multiple VAs with identical positions (for VAs with order 2 or higher) and hence the SMC parameters are also identical. However, only one of these overlapping VAs is visible at any agent position, i.e., the visibility regions of the VAs are disjoint.

2.2.3. Amplitude Quality Modeling

While delay and angle parameters can be directly modeled using the environment geometry, for the SMC amplitudes the position-relation poses a difficult task, as described in Section 2.2.2. For more sophisticated elaborations, we have to fall back to statistical models, i.e., we look at power-related quantities on the basis of the noise models described in Section 2.1.3.

In this regard, we may examine the signal-to-interference-and-noise-ratio (SINR) defined by

$$\mathrm{SINR}_{k,m}(\boldsymbol{p}) = \frac{|\alpha_k(\boldsymbol{p})|^2}{\sigma_w^2} \|s(\tau_k(\boldsymbol{p}))\|^2_{\mathcal{H}_m} \tag{2.55}$$

where we have again the variance of the measurement noise σ_w^2 and $\|\cdot\|^2_{\mathcal{H}_m}$ denotes the squared norm in the Hilbert space $\mathcal{H}_m$ defined by

$$\langle \boldsymbol{x}, \boldsymbol{y} \rangle_{\mathcal{H}_m} = \sigma_w^2 \boldsymbol{x}^{\mathrm{H}} \big(\boldsymbol{C}_{\boldsymbol{n}}^{(m)}\big)^{-1} \boldsymbol{y} \tag{2.56}$$

$$\|\boldsymbol{x}\|^2_{\mathcal{H}_m} = \langle \boldsymbol{x}, \boldsymbol{x} \rangle_{\mathcal{H}_m}. \tag{2.57}$$

This space describes the effect of self interference by the DMC at antenna m which is accounted for via the covariance matrix of the noise model. The weighted inner product and weighted norms are used to account for the inverse of $\boldsymbol{C}_{\boldsymbol{n}}^{(m)}$ as a whitening operation [115, 121]. Clearly, we can use the covariance matrices from the described assumptions to put the SINR in the context of certain setups, e.g.,

$$\mathrm{SNR}_k(\boldsymbol{p}) = \frac{|\alpha_k(\boldsymbol{p})|^2}{\sigma_w^2} \|s(\tau_k(\boldsymbol{p}))\|^2 \qquad (\textsc{awgn})\ \boldsymbol{C}_{\boldsymbol{n}}^{(m)} = \sigma_w^2 \boldsymbol{I}_{N_s} \tag{2.58}$$

$$\mathrm{SINR}_k(\boldsymbol{p}) = \frac{|\alpha_k(\boldsymbol{p})|^2}{\sigma_w^2} \|s(\tau_k(\boldsymbol{p}))\|^2_{\mathcal{H}} \qquad (\textsc{dm})\ \boldsymbol{C}_{\boldsymbol{n}}^{(m)} = \boldsymbol{S}_{\mathrm{c}} \boldsymbol{C}_{\tau} \boldsymbol{S}_{\mathrm{c}}^{\mathrm{H}} + \sigma_w^2 \boldsymbol{I}_{N_s}. \tag{2.59}$$

where, in the AWGN case, we obviously have an SMC signal-to-noise-ratio (SNR). The different SINRs act as SMC quality measures for various methods by putting directly the "strength" of one SMC into context with the considered noise model.

We look at one more important assumption regarding overlapping SMCs:

- All SMCs are orthogonal to one another, i.e., there is no path-overlap in the resolvable angle-and-delay domain. Formally, this means that for any two SMCs k and k', we have

$$\sum_{m=1}^{M} b_m^*(\phi_k) b_m(\phi_{k'}) \langle \boldsymbol{s}(\tau_k), \boldsymbol{s}(\tau_{k'}) \rangle_{\mathcal{H}_m} \ll \sum_{m=1}^{M} |b_m(\phi_k)|^2 \|\boldsymbol{s}(\tau_k)\|_{\mathcal{H}_m}. \tag{2.60}$$

For the case of directional antennas covering non-overlapping sectors in the azimuth plane in (iii), the left-hand side expression of (2.60) is always close to zero, except for the case of two SMCs arriving at the same time while also having the same AoA, which occurs whenever the agent is very close to a reflective surface. This means for (iii), a "distance-to-wall" requirement for the agent is sufficient to fulfill this assumption. E.g., a required distance can be chosen equivalent to a path length of $1.5\,T_\mathrm{p} \cdot c$, which amounts to 0.5 m for a bandwidth of 1 GHz.

3. Resource-efficient Radio Positioning Systems

In this chapter, we outline positioning methods for the signal models from Chapter 2. Likelihood based algorithms are formulated using (I) and (III). For the latter, both noise models are considered. Two selected results are discussed, one based on high-fidelity measurements to analyze the likelihoods evaluated over the whole environment, and another result based on low-cost UWB transceivers to evaluate the positioning performance for selected regions in the environment. The latter as a complete system is named single-anchor localization using multipath assistance (SALMA) and a holistic description is provided in [T1]. The algorithm descriptions summarize [T2] and [T1]. The likelihood analysis is taken from [T4], whereas in [T3] an analysis on the channel response level is provided. The algorithm performance results are also found in [T1].

In the following, we put the presented positioning system into context with other existing works (Section 3.1), explain the positioning algorithms (Section 3.2) and show selected results (Section 3.3).

3.1. Related Work

The gist of the presented indoor positioning method and realized system (SALMA) is that it is *low-cost*, *UWB*-based, *multipath assisted* with a *single anchor*. In the following, we will relate each of these attributes to other existing works.

In terms of accurate low-cost positioning systems, there are various realizations of optical (LED-based) systems [3, 50, 60, 64, 127], which usually exhibit a high LOS condition requirement and strong accuracy degradation with increased range. Realizations based on acoustic systems [52, 63, 69, 81, 82, 137] usually struggle when dealing with multipath propagation. In the context of RF systems, our specific system is based on UWB signals. There are many other narrowband technologies that have been considered using RSS fingerprints such as Wi-Fi [28, 97, 107, 124, 126], Bluetooth low energy (BLE) [20, 103, 128], and low-power narrowband adhering to IEEE 802.15.4, e.g., the ZigBee platform [7, 61]. Furthermore, for BLE, there are systems based on beacon networks with occupancy detection [62, 79]. With lower available bandwidth, the common requirement of all these RF systems is a high number of available anchors with corresponding setup / training phase, which ultimately results in high deployment efforts.

UWB technology gained wide spread popularity first around 2005-2010, due to, among others, its beneficial ranging capabilities [18, 134]. Almost a decade later, most high-accurate (decimeter level) positioning systems were still based on UWB as was shown in the yearly Microsoft localization competitions [65]. Similar to SALMA, many UWB systems have also been implemented by using the low-cost DecaWave transceiver chip [32, 43–45, 53, 102, 112]. Compared to SALMA, these systems require a high number of anchors, typically between eight [53, 112] and fifteen [45], while reaching comparable accuracies. While

SALMA is snapshot based, in [119], a DecaWave-based platform for multi-target tracking is described. A detailed generalized description of the applied algorithms is provided in [74]. Großwindhager, a co-author of several included papers, worked also on runtime adaptation of physical layer settings to improve UWB communications in [S3, S5], as well as a DecaWave-based UWB platform named SnapLoc which realizes concurrent ranging (any number of agents may range to multiple anchors without the need of synchronization) in [S2, S9]. Related to the latter are also the works of Corbalán [15, 16] providing an alternative approach to enable concurrent ranging with UWB radios. One open question of the SALMA system, the best placement of the anchor, was addressed in [95]. The channel impulse response (CIR) was analyzed in terms of path overlap over the whole environment (dense agent position grid) using multiple anchor positions to determine an "effective length" of the CIR, which can be used as a fitness value for potential anchor positions.

Several works have exploited electronically steerable or switchable antenna systems to enable single-anchor localization using narrowband technologies [14, 93], or even UWB-based systems [84, 108, 133], albeit either only based on simulations or lacking a thorough performance analysis. The antennas employed to conduct the directional measurements used in this chapter are described in detail in [S1], also with reference to potential positioning applications.

In terms of multipath-assisted radio positioning, the foundation for the methods described in this thesis was laid by the works of Meissner and Leitinger, starting with the early works [71, 72], extended in [57] and developed into a simultaneous localization and mapping (SLAM) method in [59]. Similar to the latter multipath-assisted radio SLAM method are the works of Gentner in [23, 114]. In parallel to the works of this thesis, Kulmer extended the multipath-assisted methods to cooperative positioning (i.e., without fixed anchors) in [48].

3.2. Problem Formulation

The tackled objective of this chapter is estimation of the agent position $\boldsymbol{p}$ using measured observation signals $\boldsymbol{r}$, i.e., we may write this process as $\hat{\boldsymbol{p}} = f(\boldsymbol{r})$. For the systems used to obtain the observation $\boldsymbol{r}$, we consider (I) and (III) from Chapter 2, which means we describe single-anchor positioning enabled by consideration of multipath propagation. For this purpose, we do not estimate SMC parameters (angle and delay) from the measurements. Instead, for efficiency purposes, we follow a maximum likelihood (ML) approach where we derive log-likelihood (LLH) functions. The LLHs are solely parameterized by hypothesized agent positions. The basis for the LLH models is the simple (AWGN) noise model given in (2.16). In terms of system models, we use both the simple system with a single omni-directional antenna (I) given in (2.8) and the system with multiple directional antennas (III) given in (2.13). All described positioning systems use only the L first-order SMCs characterized by the VAs from (2.47). The reason for this is on the one hand the significantly reduced signal strength of higher-order reflections, and on the other hand the difficult geometric treatment of higher-order reflections in terms of visibility, which will be explained later. In the following, we summarize the LLH-based methods described in [T1, S12, S13, T2].

To start off, we return to our general observation model from (2.6), which can be written as a circular complex Gaussian random variable

$$\boldsymbol{r} \sim \mathcal{CN}\big(\boldsymbol{x}(\boldsymbol{\theta}), \boldsymbol{C_n}\big) \tag{3.1}$$

for which the likelihood-function is written as

$$p(\boldsymbol{r}|\boldsymbol{\theta}) = \pi^{-MN_s}\det\{\boldsymbol{C_n}\}^{-1}\exp\Big\{-\big(\boldsymbol{r}-\boldsymbol{x}(\boldsymbol{\theta})\big)^{\mathrm{H}}\boldsymbol{C_n}^{-1}\big(\boldsymbol{r}-\boldsymbol{x}(\boldsymbol{\theta})\big)\Big\}. \tag{3.2}$$

We apply the natural logarithm and neglect all terms that do not depend on $\boldsymbol{\theta}$ to obtain

$$L(\boldsymbol{r}|\boldsymbol{\theta}) = -\big(\boldsymbol{r}-\boldsymbol{x}(\boldsymbol{\theta})\big)^{\mathrm{H}}\boldsymbol{C_n}^{-1}\big(\boldsymbol{r}-\boldsymbol{x}(\boldsymbol{\theta})\big). \tag{3.3}$$

Although this term is only proportional to the LLH $\log p(\boldsymbol{r}|\boldsymbol{\theta})$, we will refer to $L(\boldsymbol{r}|\boldsymbol{\theta})$ as LLH for the sake of brevity. Since the objective is to determine the agent position $\boldsymbol{p}$, we have to use the position-dependent models for the parameters in $\boldsymbol{\theta}$. This works for $\boldsymbol{\tau}$ and $\boldsymbol{\phi}$ with the geometric modeling as described in Section 2.2.2, whereas the amplitude-related parameters $\boldsymbol{\alpha}$ and $\boldsymbol{\zeta}$ are assumed unrelated to the agent position and thus treated as nuisance parameters. Hence, for the LLHs of specific models, we will use agent positions and nuisance parameters as given variables.

We first assume (I) with (AWGN), i.e., we have $\boldsymbol{r} \in \mathbb{C}^{N_s \times 1}$ and we use (2.8) for $\boldsymbol{x}(\boldsymbol{\theta})$, (2.9) for $\boldsymbol{\theta}$ and (2.16) for $\boldsymbol{C_n}$ to obtain

$$L^{(\mathrm{I})}(\boldsymbol{r}|\boldsymbol{p}) = -\big\|\boldsymbol{r}-\boldsymbol{S}(\boldsymbol{\tau})\tilde{\boldsymbol{\alpha}}\big\|^2 \tag{3.4}$$

where we used the auxiliary variables

$$\boldsymbol{S}(\boldsymbol{\tau}) = \begin{bmatrix}\boldsymbol{s}(\tau_1) & \dots & \boldsymbol{s}(\tau_K)\end{bmatrix} \tag{3.5}$$

$$\tilde{\boldsymbol{\alpha}} = \begin{bmatrix}\alpha_1 e^{j\zeta_1} & \dots & \alpha_K e^{j\zeta_K}\end{bmatrix}^{\mathrm{T}}. \tag{3.6}$$

Note that for $\boldsymbol{\tau}$, there is a dependence on $\boldsymbol{p}$ which is determined by (2.33), but we leave out the dependence in the notation to improve legibility. To set the nuisance parameters, we follow a least-squares equivalent approach to maximize the right-hand side of (3.4) with respect to $\tilde{\alpha}_k = \alpha_k e^{j\zeta_k}$, resulting in

$$\begin{aligned}\tilde{\boldsymbol{\alpha}} &= (\boldsymbol{S}^{\mathrm{H}}(\boldsymbol{\tau})\boldsymbol{S}(\boldsymbol{\tau}))^{-1}\boldsymbol{S}^{\mathrm{H}}(\boldsymbol{\tau})\boldsymbol{r}\\ &\approx \boldsymbol{S}^{\mathrm{H}}(\boldsymbol{\tau})\boldsymbol{r}.\end{aligned} \tag{3.7}$$

The second line assumes that the SMCs are orthogonal in delay domain as described in (2.60). While this assumption is stronger here due to the lack of directional antennas, its application results in a simplification with the merit of efficient computation.

Next, we consider (III) where we have $\boldsymbol{r} \in \mathbb{C}^{MN_s \times 1}$, we use (2.13) for $\boldsymbol{x}(\boldsymbol{\theta})$ and (2.14) for $\boldsymbol{\theta}$. We formulate two variants depending on the used noise model, one where we use (AWGN) with (2.16) for $\boldsymbol{C_n}$ and another for (DM) with (2.18) and (2.28) for $\boldsymbol{C_n}$. For the latter, we also assume a uniform DMC angle power spectrum following (2.29). Then, two LLH variants are written as

$$L^{(\mathrm{III,AWGN})}(\boldsymbol{r}|\boldsymbol{p}) = -\sum_{m=1}^{M}\big\|\boldsymbol{r}_m-\boldsymbol{X}_m(\boldsymbol{\phi},\boldsymbol{\tau},\tilde{\zeta}_m)\boldsymbol{\alpha}\big\|^2 \tag{3.8}$$

$$L^{(\mathrm{III,DM})}(\boldsymbol{r}|\boldsymbol{p}) = -\sum_{m=1}^{M}\big\|\boldsymbol{r}_m-\boldsymbol{X}_m(\boldsymbol{\phi},\boldsymbol{\tau},\tilde{\zeta}_m)\boldsymbol{\alpha}\big\|^2_{\mathcal{H}} \tag{3.9}$$

with auxiliary variables

$$\boldsymbol{X}_m(\boldsymbol{\phi}, \boldsymbol{\tau}, \tilde{\boldsymbol{\zeta}}_m) = \begin{bmatrix} b_m(\phi_1)\boldsymbol{s}(\tau_1)e^{j\tilde{\zeta}_{1,m}} & \dots & b_m(\phi_K)\boldsymbol{s}(\tau_K)e^{j\tilde{\zeta}_{K,m}} \end{bmatrix} \tag{3.10}$$

$$\tilde{\boldsymbol{\zeta}}_m = \begin{bmatrix} \tilde{\zeta}_{1,m} & \dots & \tilde{\zeta}_{K,m} \end{bmatrix}^{\mathrm{T}} \tag{3.11}$$

$$\boldsymbol{\alpha} = \begin{bmatrix} \alpha_1 & \dots & \alpha_K \end{bmatrix}^{\mathrm{T}}. \tag{3.12}$$

Again, we have a (not explicitly shown) dependence on $\boldsymbol{p}$ for $\boldsymbol{\phi}$ and $\boldsymbol{\tau}$ which is determined by (2.36) and (2.33), respectively. In (3.9), the DMC delay power spectrum is applied in the Hilbert norm following (2.59). A generalized LLH, using different noise covariance matrices for each antenna, is described in [T2, Section VI.A]. To determine the nuisance parameters, we follow the approach introduced in [S12] to obtain

$$\hat{\alpha}_{k,m} = \frac{1}{b_m(\phi_k)} \frac{\langle \boldsymbol{s}(\tau_k), \boldsymbol{r}_m \rangle_{\mathcal{H}}}{\|\boldsymbol{s}(\tau_k)\|_{\mathcal{H}}} \tag{3.13}$$

$$\tilde{\zeta}_{k,m} = \arg\{\hat{\alpha}_{k,m}\} \tag{3.14}$$

$$\alpha_k = \frac{\sum_{m=1}^{M} |b_m(\phi_k)|^2 |\hat{\alpha}_{k,m}|}{\sum_{m=1}^{M} |b_m(\phi_k)|^2}. \tag{3.15}$$

In short, these equations can be seen as a beampattern-weighted amplitude estimate whereas the noise phase is retained.

To conclude the ML estimation method, using any of the LLHs from (3.4), (3.8) or (3.9), a position estimate is determined via

$$\hat{\boldsymbol{p}} = \underset{\boldsymbol{p} \in \mathcal{P}}{\operatorname{argmax}} \, L^{(\cdot)}(\boldsymbol{r}|\boldsymbol{p}) \tag{3.16}$$

where the set $\mathcal{P}$ contains selected candidate positions within communication range to the anchor. A straight-forward choice for the positions in $\mathcal{P}$ would be a dense grid spanning over the considered environment, i.e., a full LLH evaluation as was done exemplarily in [T4] (see Section 3.3). In implementations from the included papers, a more efficient choice for $\mathcal{P}$ was used, following the approach introduced in [S13] where candidate positions are limited to a circle around $\boldsymbol{a}$ with radius $\hat{d}_1$ (the LOS distance estimate obtained, e.g., via a two-way ranging approach).

3.3. Selected Results

In this section, we highlight some evaluation results that are based on the described ML methods applied onto measured CIR data that represent the observation vector $\boldsymbol{r}$. The indoor environment of choice is an office-like lab room shown in Figure 3.1. The wall materials consist of plaster board (on the left and right) and there are glass windows on the top. On the bottom there is a metal white board which poses as a beneficial reflection surface. We look at two evaluations in the room, both of which use one physical anchor in the bottom right corner and slightly different furniture setup.

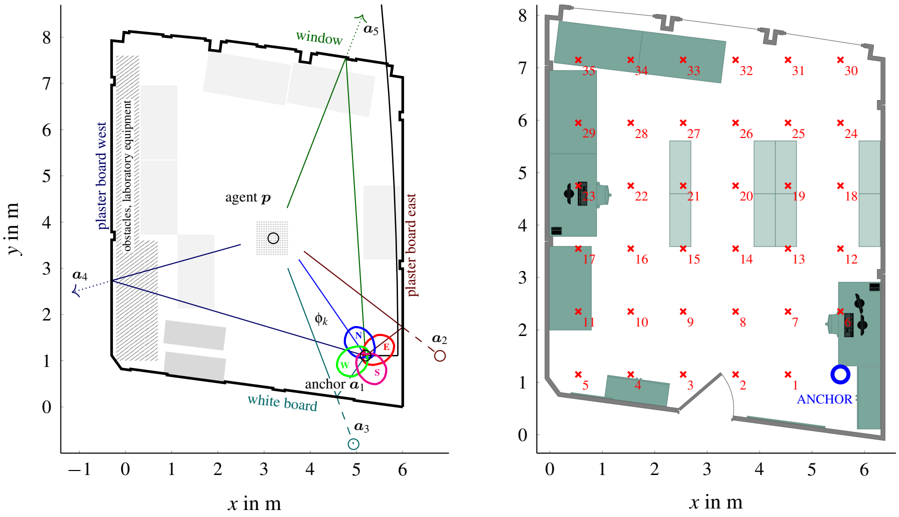

(a)

(b)

Figure 3.1.: Floorplan of the evaluation environment, showing (a) the directional antennas at the anchor, the virtual antenna array at the agent and various furniture, and (b) a different furniture setup including shelves (light-shaded near room center) with 35 evaluation positions distributed evenly over the room.

3.3.1. Evaluation I: High-fidelity Measurement Equipment

In the first evaluation, the agent was placed on a regular 15 × 14 grid with a spacing of 5 cm (see Figure 3.1a near the center), resulting in a measurement set of 210 CIRs. For measurement equipment, the Ilmsens Correlative Channel Sounder was used [132] with an omni-directional UWB coin antenna [47, Chapter B.3] at the agent. At the anchor either the same coin antenna was used to represent (I), or a switchable antenna system with four directional UWB antennas exhibiting about 90° half-power beamwidth [S1] was used to represent (III). While the source signal used by the channel sounder covers the whole UWB spectrum from 3 to 10 GHz, we convolve this signal with our desired transmitted signal, being a raised-cosine (RC) pulse at $f_c = 5.4$ GHz with a pulse width of $T_p = 2.4$ ns (equivalent to a bandwidth of about 500 MHz) and a roll-off factor of $R = 0.9$. This choice of bandwidth and roll-off factor leads to a signal that matches the IEEE 802.15.4 (2011) compliant DecaWave DW1000 UWB transceiver signal, as was shown in [S13]. The choice of center frequency was due to the operating frequency band of the directional antennas, but it deviates from the UWB channels defined in the IEEE 802.15.4 (2011) standard [38]. However, the main determining factors for positioning performance are bandwidth and antenna directivity (cf. Chapter 4), hence the choice of center frequency has insignificant impact. The close spacing of the agent positions allows various examinations such as angle-resolved amplitude models and statistical analysis of the DMC. The latter is necessary to access the noise model (DM), in order to make use of the full LLH in (3.9).

For our first highlighted result, we look at the likelihood based on one measurement taken at the center of the agent array evaluated over the complete room. The results are shown in Figure 3.2a for (I), evaluating (3.4) and in Figure 3.2b for (III), evaluating (3.8). Using (I) results in a flatter likelihood where ambiguities remain due to SMCs that are unresolvable in delay domain only, whereas (III) enables accessing the angle domain to obtain a likelihood with one clear maximum.

Next, a summary of the quantitative results is provided in Figure 3.3 which shows the cumulative frequency of position errors obtained. Some dotted lines are shown, verticals to indicate certain error values and horizontals to indicate certain percentiles. For each result curve, the corresponding paper describing the evaluation in detail is written in the legend. Position error results are shown for agent positions in a small region in the center of the room to compare the performance of (I) using (3.4), indicated by a black line, and (III) using (3.8), indicated by a red line with disc markers. Due to the directivity of the antennas in (III) we see a significant improvement of the accuracy with the 90% error decreasing from 60 cm to 25 cm. Furthermore, the robustness is increased where an error of 25 cm is achieved only by 55% of the cases with (I) compared to 90% with (III). To conclude the results of Evaluation I, we look at application of (III) with noise model (DM) based on the LLH in (3.9), which is indicated by a blue line with square markers. Here, respecting the DMC results in a significant improvement when looking at difficult cases at the 90% error, which is improved from 25 cm to 17 cm and the amount of estimates that achieve an error of less than 10 cm goes up from 50% to 72%.

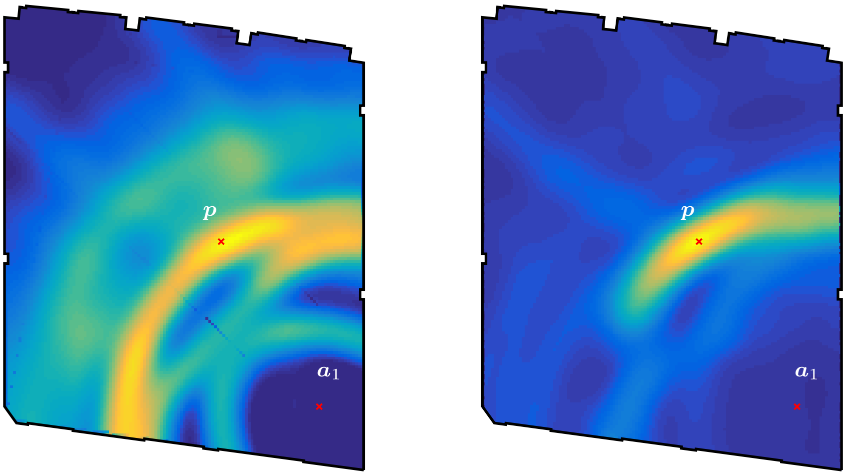

(a)

(b)

Figure 3.2.: Likelihood evaluated over the lab room environment using (a) Setup (I) with (3.4) and (b) Setup (III) with (3.8).

3.3.2. Evaluation II: Low-cost Devices

The second evaluation uses a set of 35 agent positions spread over the whole room to represent both simple and challenging parts of indoor environments (see Figure 3.1b). At each agent position 100 CIRs were measured. The lighter shaded areas indicate racks that were filled with books and bottle crates, to increase the difficulty to obtain accurate position estimates at certain parts of the room. The system that was used for this evaluation was implemented on low-cost devices based on the DecaWave UWB transceiver, which we named SALMA[1]. Again, there exist both setups. SALMA-light represents (I) using

---

[1] This system was first conceptualized in [S4] and then realized into a demonstrator system with a live presentation in [S8].

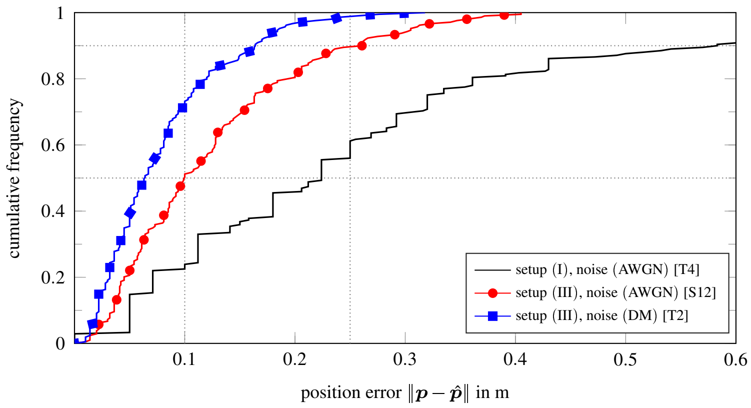

Figure 3.3.: Cumulative frequency of position error for lab room considering different anchor setups using the channel sounder.

a single omni-directional antenna at the anchor, and SALMA-full represents (III) using switchable directional antennas. The SALMA system always uses noise model (AWGN), because among the objectives of the system are timeliness with a reasonable update rate and consistent performance over the whole environment. Hence, the AWGN LLHs given in (3.4) and (3.8) are used. A key difference to the other evaluation is the (effective) bandwidth. SALMA uses channel 7 of the IEEE 802.15.4 (2011) UWB PHY standard [38, Section 14.4] with a claimed bandwidth of 1081.6 MHz at center frequency 6489.6 GHz. Compared to the channel sounder measurements, the higher bandwidth is required here to guarantee consistent performance and to remedy the hardware shortcomings. The conducted measurements are part of a publicly available dataset[2] which is described in [S7].

The positioning results for the considered room are shown in Figure 3.4a, where for each of the 35 evaluation positions, the average position estimates are shown connected to the ground truth position (indicating estimation bias) and error ellipses indicating the 3-fold standard deviation, on the basis of 100 CIR measurements. Overall, the radial position errors are in the centimeter range, due to the good ranging capabilities with UWB signals. The tangential position error stays in reasonable bounds with outliers for higher ranges and for positions where the LOS is blocked by the racks (light shaded areas). However the majority of the estimates assumes errors in the decimeter range.

Again, we consider quantitative results in terms of cumulative frequency of the position error using all 3500 estimates, shown in Figure 3.4b. The resulting performance is shown for two furniture setups of the racks, one where they were kept empty (purple, cross markers), and one were the racks were filled, as mentioned, with books and bottle crates (black, no markers). Obviously, since this evaluation considers many positions with higher distances and with LOS obstruction, the performance degrades compared to Evaluation I, albeit a median error of 45 cm and a 90% error of 55 cm (considering filled racks) are respectable errors regarding the spectrum of currently available indoor positioning systems. Also, having stronger LOS obstruction with filled racks seems to only marginally decrease the performance, which is also a benefit compared to non-radio positioning technologies.

---

[2] See `https://www.tugraz.at/en/institutes/iti/salma/database/`.

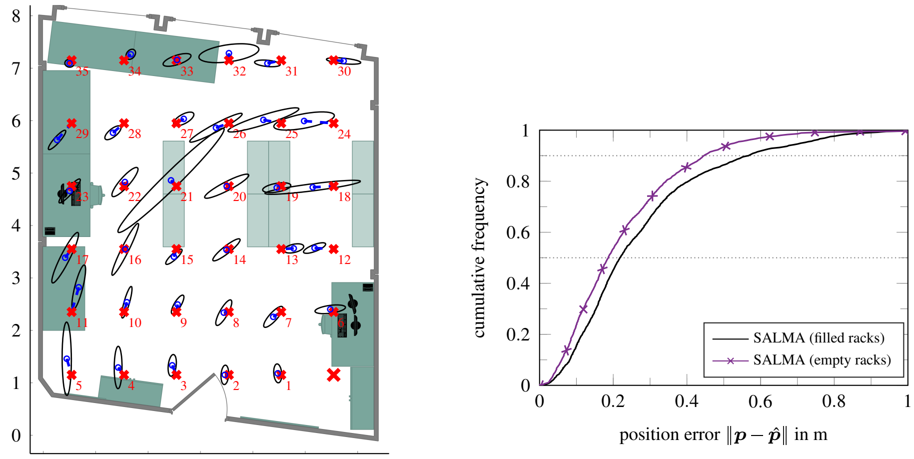

(a) (b)

Figure 3.4.: Results for lab room showing (a) average of estimates and error ellipses (b) cumulative frequency of position error for different furniture setup using either empty or filled racks (light shaded area in (a)).

3.4. Concluding Remarks

In this chapter, we used the established signal models to derive positioning methods that may be implemented on low-cost UWB radios. Our aim was to tackle Hypothesis 1, i.e. to outline how non-coherent directional measurements can be used at a single anchor to obtain accurate agent positions. Our derivations revealed the following insights:

- The presented ML-based multipath assisted positioning methods enable single-anchor systems sub-meter position estimates in almost real time on low-cost UWB compliant devices.
- Application of directional antennas at the anchor tackles challenging regions in the environment.
- The consideration of DMC enables further improvements.

4. Fundamental Limits of Radio Positioning

In this chapter, we analyze the position error of a single-anchor positioning system exploiting SMCs with varying antenna setups at the anchor. The analysis is based on all system and noise models described in Chapter 2, with a special focus on (III). The derivation of the Cramér-Rao lower bound (CRLB) on the position error, which is also known as position error bound (PEB) [99], is outlined in order to evaluate the theoretical performance limit of this positioning system, in comparison to a conventional antenna-array system (II) and a single-antenna setup (I). The contents of this chapter summarize and contextualize the derivations and results from [T2] with some selected parts from [T4].

In the following, we put the presented error bound analysis into context with other existing works (Section 4.1), derive the bound (Section 4.2) and show selected results (Section 4.3).

4.1. Related Work

The origins of the CRLB, i.e., lower bounds on the variance of statistical parameter estimates, go back to the namesakes of the bound, first with the early (1945) paper of Rao [86] and then, in parallel published a year later, in the textbook of Cramér [17, Chapter 33]. First applications of these bounds towards localization were conducted in the 1970s for acoustic signal sources on the basis of range estimates [9, 46], even considering array signals [29]. At this time, in parallel, the GPS community developed a related position accuracy bound for the trilateration methods used therein, called *dilution of precision* [54, 104], which was later shown to be in close relation to the CRLB [11].

Greater interest in performance bounds of radio positioning systems arose at the dawn of the 21st century, with UWB radio systems getting into focus, granting availability to high time resolution [10] and resilience to dense multipath [120]. CRLB derivations of UWB channel parameters were conducted [39, 56], and a compact framework to evaluate the limits of wideband localization was created by Shen and Win [99–101], including elaborations on the effect of pathoverlap [98]. These works where extended for array localization by Han [31].

In the years leading up to the 2020s, with the advent of realizable mm-wave systems, antenna arrays have been upscaled towards massive MIMO systems, which raised the interest in localization limits of these systems. With their high angle resolution, the position information carried by multipath components has been analyzed for MIMO systems [73, 96], and in turn, position and orientation error bounds [2, 27, 96] have been developed. On the basis of these works, specific treatment of bounds for single-anchor mm-wave systems have been derived in [1, 40].

A detailed derivation of the CRLB is provided in the textbooks by Van Trees [115, Chapter 2.4.2] for general continuous-time systems and by Kay [42, Chapter 3] for discrete-time systems, the latter containing also closely related examples such as range estimation. While these books pose as the foundation for most of the referenced works, the specific radio channel approach used in this chapter is largely based on the thesis of Richter [90] as a starting point, and then in more detail (for the multipath-assisted positioning paradigm) by the works of Leitinger [58] and Witrisal [121, 123], where the former also treats anchor-to-agent synchronization effects. On the basis of the latter works, in parallel to the included paper [T2], Wilding derived error bounds for antenna arrays [117, 118], with a focus on the analysis of the impact of the signal bandwidth on the ToF and AoA estimation performance in dense multipath channels.

4.2. Problem Formulation

We are interested in the achievable position accuracy of systems that aquire measurements described by our established signal models (I)-(III), considering the noise models (AWGN) and (DM), i.e., dense multipath is taken into account for the analysis. This analysis reveals *what is possible* with our positioning systems from the previous chapter. Our means of obtaining lower bounds on the position error follow a two-step process: first we outline the derivation of the Fisher information matrix (FIM) for the SMC parameters in Section 4.2.1, second we use the established FIM to get quantifiable bounds on the agent position accuracy in Section 4.2.2, where we also reveal which SMC parameters carry the most position information.

4.2.1. Fisher Information of Model Parameters

On the basis of the established signal models, we can examine the useful information present in observed signals. To this end, we will determine the FIM. The elements of this matrix quantify the amount of information that observed radio signals carry about unknown position-related model parameters.

For our general signal model describing the CIR observations (2.6), the FIM is well known when using a Gaussian noise model described by covariance matrix $\boldsymbol{C}_{\boldsymbol{n}}$. It is defined as [42, Chapter 15.7]

$$\boldsymbol{I}_{\boldsymbol{\theta}} = 2\Re\left\{\boldsymbol{J}_{\boldsymbol{\theta}}^{\mathrm{H}}\boldsymbol{C}_{\boldsymbol{n}}^{-1}\boldsymbol{J}_{\boldsymbol{\theta}}\right\} \tag{4.1}$$

where $\boldsymbol{J}_{\boldsymbol{\theta}}$ denotes the Jacobian of the signal model with respect to the elements of a length-N_θ parameter vector

$$\boldsymbol{J}_{\boldsymbol{\theta}} = \left[\left(\tfrac{\partial}{\partial\theta_1}\boldsymbol{x}(\boldsymbol{\theta})\right) \;\cdots\; \left(\tfrac{\partial}{\partial\theta_{N_\theta}}\boldsymbol{x}(\boldsymbol{\theta})\right)\right] \qquad \in \mathbb{R}^{MN_s \times N_\theta}. \tag{4.2}$$

The number of parameters N_θ is determined by the respective setup used, which can be seen in (2.9), (2.11) and (2.14). Also, it should be emphasized that the FIM in (4.1) is valid for a *known* $\boldsymbol{C}_{\boldsymbol{n}}$, i.e., the noise covariance matrix does not depend on the SMC parameters. The columns of (4.2) are the main building blocks of the FIM. We therefore outline these columns for each signal model in the following

$$\tfrac{\partial}{\partial\theta_i}\boldsymbol{x}^{(\mathrm{I})}(\boldsymbol{\theta}^{(\mathrm{I})}) = \tfrac{\partial}{\partial\theta_i}\left(\alpha_i e^{j\zeta_i}\boldsymbol{s}(\tau_i)\right) \tag{4.3}$$

$$\tfrac{\partial}{\partial\theta_i}\boldsymbol{x}^{(\mathrm{II})}(\boldsymbol{\theta}^{(\mathrm{II})}) = \tfrac{\partial}{\partial\theta_i}\left(\alpha_i e^{j\zeta_i}\boldsymbol{s}(\tau_i)\otimes\left[e^{j\zeta^{(1)}(\phi_i)} \quad \ldots \quad e^{j\zeta^{(M)}(\phi_i)}\right]^{\mathrm{T}}\right) \tag{4.4}$$

$$\tfrac{\partial}{\partial\theta_i}\boldsymbol{x}^{(\mathrm{III})}(\boldsymbol{\theta}^{(\mathrm{III})}) = \tfrac{\partial}{\partial\theta_i}\left(\alpha_i\boldsymbol{s}(\tau_i)\otimes\left[b_1(\phi_i)e^{j\tilde{\zeta}_{i,1}} \quad \ldots \quad b_m(\phi_i)e^{j\tilde{\zeta}_{i,M}}\right]^{\mathrm{T}}\right) \tag{4.5}$$

where $\otimes$ denotes the Kronecker product. While derivatives towards amplitudes and phases are straight-forward, for angles and delays it is required to specify / determine the corresponding beampattern and (pulse) signal derivatives described by $\dot{\boldsymbol{b}}(\phi) = \partial \boldsymbol{b}/\partial\phi$ and $\dot{\boldsymbol{s}}(\tau) = \partial \boldsymbol{s}/\partial\tau$. From (4.3)-(4.5) it is clear that the entries of the FIM (4.1) are related to inner-products using shifted pulses weighted by the inverse of the noise covariance matrix, hence the Hilbert space definition from (2.56) and (2.57) may be used for a compact description. Entries on the main diagonal, which act as the main contribution to parameter information, are related to the SMC SINR values from (2.58) for (AWGN) and (2.59) for (DM). A detailed description of FIM entries for model (III) is provided in [T2, Appendix A]. An equivalent description of FIM entries for model (I) is given in [58] and for model (II) it is given in [118].

To establish a position relation, we separate the SMC parameters into two parts with $\boldsymbol{\theta} = [\boldsymbol{\theta}_{\text{used}}^{\mathrm{T}}, \boldsymbol{\theta}_{\text{nuis}}^{\mathrm{T}}]^{\mathrm{T}}$ where $\boldsymbol{\theta}_{\text{used}}$ contains all parameters that are related to the agent position (i.e., SMC delays $\boldsymbol{\tau}$ and angles $\boldsymbol{\phi}$) and $\boldsymbol{\theta}_{\text{nuis}}$ contains all remaining *nuisance* parameters (we denote its length by N_{nuis}). The latter includes the amplitudes $\boldsymbol{\alpha}$ and phases $\boldsymbol{\zeta}$ in all three setups, but by choice, it may also include delays and angles, whereas the respective other is then the sole position-related parameter contained in $\boldsymbol{\theta}_{\text{used}}$ in order to examine how much position information is contained therein.

To obtain a position-related FIM, a transformation is required to analyze a new parameter vector

$$\boldsymbol{\psi} = \left[\boldsymbol{p}^{\mathrm{T}}, \boldsymbol{\theta}_{\text{nuis}}^{\mathrm{T}}\right]^{\mathrm{T}} \qquad \in \mathbb{R}^{(2+N_{\text{nuis}})\times 1} \tag{4.6}$$

where a transformation is performed via

$$\boldsymbol{I}_{\boldsymbol{\psi}} = \boldsymbol{J}_{\boldsymbol{\psi}}^{\mathrm{T}} \boldsymbol{I}_{\boldsymbol{\theta}} \boldsymbol{J}_{\boldsymbol{\psi}} \qquad \in \mathbb{R}^{(2+N_{\text{nuis}})\times(2+N_{\text{nuis}})} \tag{4.7}$$

with the corresponding Jacobian

$$\boldsymbol{J}_{\boldsymbol{\psi}} = \begin{bmatrix} \frac{\partial}{\partial \boldsymbol{p}^{\mathrm{T}}} \boldsymbol{\theta}_{\text{used}} & \boldsymbol{0}_{(N_\theta - N_{\text{nuis}})\times N_{\text{nuis}}} \\ \boldsymbol{0}_{N_{\text{nuis}}\times 2} & \boldsymbol{I}_{N_{\text{nuis}}} \end{bmatrix}. \tag{4.8}$$

Here in the top left of the Jacobian, we have the derivative of the position-related SMC parameters with respect to the agent position, which is also called *spatial gradients*. These gradients are obtained by computing the corresponding derivative of (2.33) for delays and (2.36) for angles,

$$\tfrac{\partial}{\partial \boldsymbol{p}}(\tau_k) = -\tfrac{1}{c}\,\boldsymbol{e}(\varphi_k) \tag{4.9}$$

$$\tfrac{\partial}{\partial \boldsymbol{p}}(\phi_k) = \tfrac{1}{d_k}(-1)^{O(k)}\boldsymbol{e}(\varphi_k - \tfrac{\pi}{2}) \tag{4.10}$$

where the unit vectors as introduced in (2.34) are used. Note that to compute (4.10), the partial derivatives (of the atan2 function) described in (A.2) and (A.3) may be used.

4.2.2. Cramér-Rao Lower Bound on Position Estimate

The established FIM $\boldsymbol{I}_{\boldsymbol{\psi}}$ on the parameter vector $\boldsymbol{\psi}$ is used to obtain the CRLB [42, 115] for an estimated parameter vector of $\hat{\boldsymbol{\psi}}$ via

$$\mathbb{E}\left\{\|\boldsymbol{\psi} - \hat{\boldsymbol{\psi}}\|^2\right\} \geqslant \operatorname{tr}\left\{\boldsymbol{I}_{\boldsymbol{\psi}}^{-1}\right\}. \tag{4.11}$$

Note that we might use $\boldsymbol{\theta}$ here instead to determine the lower bound on one of the SMC parameters directly. While (4.11) determines the lower bound on all parameters $\boldsymbol{\psi}$, the main focus lies on the agent positions, hence we consider the upper left part of the inverse of the FIM to define the PEB as

$$\mathrm{PEB}_{\boldsymbol{p}} = \sqrt{\mathrm{tr}\left\{\left[\mathcal{I}_{\boldsymbol{\psi}}^{-1}\right]_{2\times 2}\right\}}. \tag{4.12}$$

While in the upcoming result section, a PEB analysis is presented for the full FIM, it is possible to write a closed-form solution for the PEB by application of the concept of equivalent FIM [101]. Hereby, only FIM sub-matrices related to angles $\boldsymbol{\phi}$ and delays $\boldsymbol{\tau}$ are used to formulate a 2×2 position-related equivalent FIM, which is then used in (4.12). This application is possible by neglecting parameter cross-dependency sub-matrices of the FIM, justified by assumptions (2.20) and (2.60). The obtained equivalent FIM results for the three signal models are given by

$$\widetilde{\mathcal{I}_{\boldsymbol{p}}}^{(\mathrm{I})} = 8\pi^2 \sum_{k=1}^{K} \frac{\beta_0^2}{c^2} \widetilde{\mathrm{SINR}}_k \, \boldsymbol{D}_r(\varphi_k) \tag{4.13}$$

$$\widetilde{\mathcal{I}_{\boldsymbol{p}}}^{(\mathrm{II})} = 8\pi^2 \sum_{k=1}^{K} \left(\frac{\beta_0^2}{c^2} \widetilde{\mathrm{SINR}}_k \, \boldsymbol{D}_r(\varphi_k) + \frac{D_\lambda^2(\phi_k)}{d_k^2} M \, \mathrm{SINR}_k \, \boldsymbol{D}_r\left(\varphi_k - \tfrac{\pi}{2}\right) \right) \tag{4.14}$$

$$\widetilde{\mathcal{I}_{\boldsymbol{p}}}^{(\mathrm{III})} = 8\pi^2 \sum_{k=1}^{K} \left(\frac{\beta_0^2}{c^2} \|\boldsymbol{b}(\phi_k)\|^2 \, \widetilde{\mathrm{SINR}}_k \, \boldsymbol{D}_r(\varphi_k) + \frac{D_b^2(\phi_k)}{d_k^2} M \, \mathrm{SINR}_k \, \boldsymbol{D}_r\left(\varphi_k - \tfrac{\pi}{2}\right) \right) \tag{4.15}$$

where $\boldsymbol{D}_r(\varphi) = \boldsymbol{e}(\varphi)\boldsymbol{e}^{\mathrm{T}}(\varphi)$ is the ranging direction matrix [101] which indicates the direction of the obtained information gain.

In this regard, we see for all three setups an information gain due to the estimated SMC delays τ_k. It is oriented towards the AoA (in radial direction) of each SMC and scaled by the (mean-square) bandwidth of the signal $\boldsymbol{s}(\tau_k)$

$$\beta_k^2 = \frac{\|\dot{\boldsymbol{s}}(\tau_k)\|_{\mathcal{H}}^2}{4\pi^2 \, \|\boldsymbol{s}(\tau_k)\|_{\mathcal{H}}^2} \tag{4.16}$$

$$\beta_0^2 = \frac{\|\dot{\boldsymbol{s}}(\tau)\|^2}{4\pi^2 \, \|\boldsymbol{s}(\tau)\|^2} \tag{4.17}$$

where, on the one hand in (4.16), we have the Hilbert norm accounting for a whitening operation for noise model (DM) and on the other hand, we have (4.17) representing the case of noise model (AWGN), where an Euclidean norm is used and the k dependency drops. As a second quantity to scale the radial position information, there is the effective SINR defined as

$$\widetilde{\mathrm{SINR}}_k = \mathrm{SINR}_k \, \gamma_k \, \xi_k^{\text{delay}} \tag{4.18}$$

where $\gamma_k = \beta_k^2/\beta_0^2$ is interpreted as a *whitening gain*. The factor $\xi_k^{\text{delay}} \in [0, 1]$ is interpreted as an information loss due to the cross-dependency between the delay and amplitude estimation in presence of DMC. This information loss is explained in [T2, Appendix A]. Moreover, for (III), the beampatterns in AoA direction also affect the information gain.

For (II) and (III), due to the possibility to measure the AoA via array processing or directional antennas, we also see an information gain perpendicular to the AoD (in tangential direction) for each SMC. This gain scales with the number of antennas and the SINR associated with each SMC, and it decreases with the SMC path length. Additionally, we have normalized squared aperture functions affected by array geometry for (II), and by the beampattern shapes for (III). The aperture functions are given by

$$D_{\lambda}^{2}(\phi) = \frac{1}{M} \sum_{m=1}^{M} \left(\frac{d^{(m)}}{\lambda} \right)^{2} \sin^{2}\left(\phi - \phi^{(m)}\right) \tag{4.19}$$

$$D_{b}^{2}(\phi) = \frac{1}{4\pi^{2} M} \sum_{m=1}^{M} |\dot{b}_{m}(\phi)|^{2}. \tag{4.20}$$

As a concluding remark, in order to consider noise model (AWGN) for the equivalent FIMs in (4.13)-(4.15), one has to merely replace β_k with β_0 and all SINRs with SNRs obtained using (2.58).

4.3. Selected Results

In this section, representative PEB results from [T2] are outlined to compare the signal models and to analyze contributions of different SMC parameters. The PEB from (4.12) is evaluated numerically using the full FIM for a specific (artificial) environment, the "L-shaped" room depicted in Figure 4.1. This geometry was chosen due to a reasonably high amount of surfaces, leading also to a region without LOS visibility. Each SMC is associated to one of the shown VAs and a position information gain is contributed by each visible SMC. There are certain selected agent positions spread over the environment (shown as blue crosses) which will be used in the following PEB evaluations to provide a direction-resolved PEB visualization.

For the transmitted signal $s(t)$, a root-raised-cosine pulse with roll-off $\beta = 0.6$ and bandwidth $1/T_p = 1$ GHz at carrier frequency $f_c = 7$ GHz was chosen. This choice matches with the transmitted signal of SALMA (see Section 3.3.2), only with a deviation of roughly 500 MHz for the carrier frequency (SALMA uses $f_c = 6489.6$ GHz). In terms of DMC, the (diagonal) matrix $\boldsymbol{C}_\tau$ is specified according to (2.27) with the DPS $S_\nu^{(\tau)}(\tau)$ defined as a double exponential via

$$S_{\nu}^{(\tau)}(\tau) = \Omega_1 \frac{\gamma_1 + \gamma_{\text{rise}}}{\gamma_1(\gamma_1 + \gamma_{\text{rise}}(1-\chi))} \left(1 - \chi e^{-\tau/\gamma_{\text{rise}}}\right) e^{-\tau/\gamma_1} \tag{4.21}$$

where γ_{rise} and γ_1 define the "rise" and "decay" times (in other literature, γ_1 is denoted by γ_{dec}) which establish the shape of the double-exponential, $\chi \in [0,1]$ is used to tweak between single ($\chi = 0$) and double-exponential ($\chi = 1$) shape and Ω_1 is the normalized power, i.e., it is used to set a certain self-interference level for the used SINRs. Equation (4.21) is taken from [41], where it is used to describe the power-delay-profile of the UWB channel contribution by the non-LOS component. The parameter values chosen for the DPS in our analysis are $\gamma_1 = 20$ ns, $\gamma_{\text{rise}} = 5$ ns and $\chi = 0.98$ which are the same values as used in [58]. The thereby established DPS resembles statistics from measurements taken in mid-sized office environments. The normalized DPS power Ω_1 was set such that $|\alpha_1^{(1\text{m})}|^2/\Omega_1 = 10$ dB is achieved, i.e., the LOS component energy at a distance of 1 m from the anchor is set in relation to the DMC power. With the signal and noise quantities set, the PEB is evaluated over the whole environment using a uniformly sampled grid of agent positions with a spacing of 2 cm. To obtain a PEB value from (4.12), the FIM is evaluated numerically using (4.3)-(4.5) for the respective setup, whereby the SMC parameters are set using the VA model following (2.36) for angles, (2.33) for delays, (2.39) for amplitudes and (2.40) for phases. For the latter two, the free space model with simplified $|\Gamma_k| = (1/\sqrt{2})^{O(k)}$ is used.

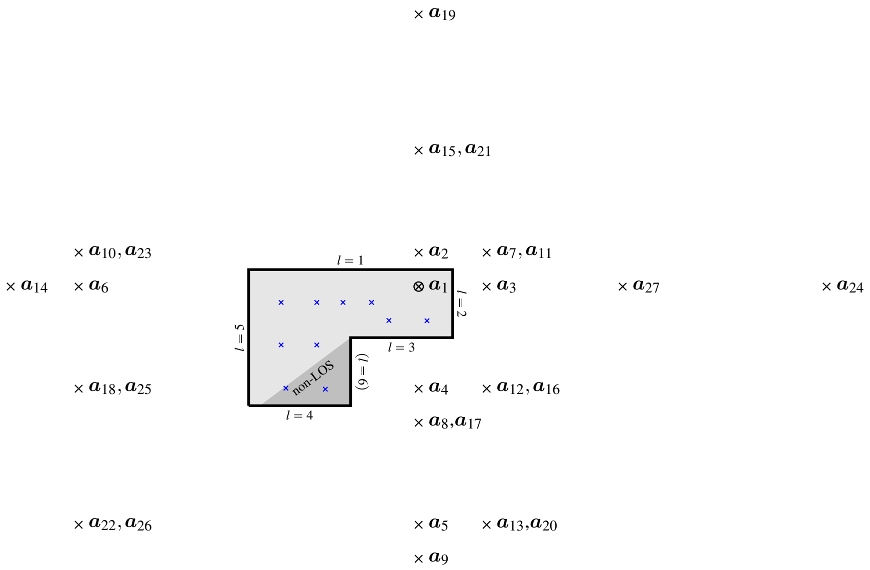

Figure 4.1.: Floorplan of environment used for the PEB evaluation. VAs up to order 2 are shown, the wall segment indices are depicted as $l = i$ and the region with non-visible LOS is indicated. The VA indices follow (2.50), whereas there are multiple VAs with shared positions due to perpendicular wall segments. Of special mention is the segment $(l = 6)$ which contributes to only a single SMC associated with $\boldsymbol{a}_{27}$ (propagation path $g_{27}(1) = 6, g_{27}(2) = 5$), all other possible SMCs involved with this segment are never visible.

4.3.1. Comparison of System Setups

In the first evaluation, we compare the achieved PEB values between the setups (I)-(III). For (II) and (III), we consider small antenna arrays with $M = 4$, where the elements are placed evenly on a circle with $d^{(m)} = 1.52$ cm (resulting in an inter-antenna spacing of $\lambda_c/2$) and $\phi^{(m)} = \frac{\pi}{2} \cdot m$, for $m = 1 \dots 4$. For the antenna patterns in (III), we use

$$b_m(\phi) = \frac{1}{2} \sum_{\ell} e^{j\ell(m\frac{\pi}{2}+\phi)}, \qquad \ell \in \{-1.5, -0.5, 0.5, 1.5\} \tag{4.22}$$

which corresponds to a Dirichlet kernel function (see (28) in [T2]) and generates a beampattern that covers one sector of the azimuth plane for each cardinal direction. The antennas used for the measurements presented in [T3] and [T1] exhibit comparable beampatterns. In terms of nuisance parameters, we only consider amplitudes and phases, i.e., we use $\boldsymbol{\theta}_{\text{nuis}} = [\boldsymbol{\alpha}^{\mathrm{T}}, \boldsymbol{\zeta}^{\mathrm{T}}]^{\mathrm{T}}$ ($\tilde{\boldsymbol{\zeta}}$ for (III)) in the derivations after (4.6) to explore the full potential of geometry-related SMC parameters.

The PEB evaluated over the environment is shown in Figure 4.2 for the three models and, for selected agent positions, the bound is also visualized in terms of radial (directed towards anchor) and tangential (perpendicular to radial) error. First, considering (I) in Figure 4.2a, we see overall good PEB values below half a meter even in the non-LOS region, which is made possible by the position information from multipath components. However, in certain regions there is a large drop due to overlapping multipath, which deteriorates the information that can be gained from the respective SMC. Considering the results of the other two setups shown in Figure 4.2b and Figure 4.2c, this drop is reduced significantly because the overlap can be resolved by accessing information from the angle-domain, either via array processing in (II), or via application of directional antennas in (III). With (II), slightly better values are achieved than with (III), albeit coherent processing of the antenna measurements is necessary to achieve this. With (III) instead, a simpler processing without inter-antenna coherent measurements is possible, which was also put into practice in [T1] (see Section 3.3.2).

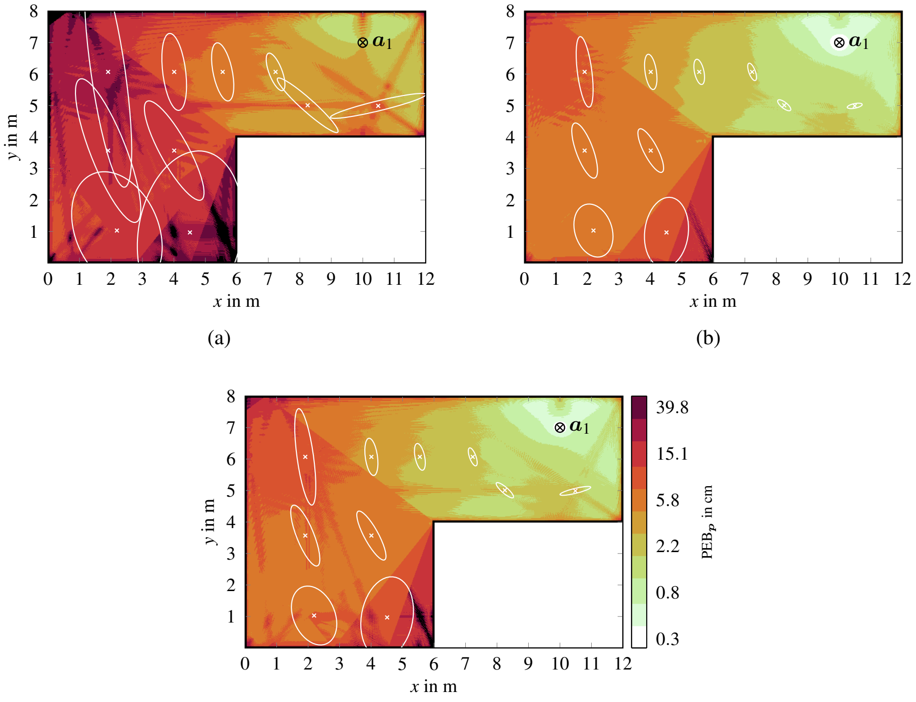

(a)

(b)

(c)

Figure 4.2.: Position error bound using (a) setup (I), (b) setup (II), and (c) setup (III), the latter two with $M = 4$ antennas.

4.3.2. Comparison of Angle and Delay Information

For (III), our main model of interest, we look at the contributions to the PEB in terms of position information when only one of the geometry-related parameters (either $\boldsymbol{\phi}$ or $\boldsymbol{\tau}$) is used. For this purpose, the PEB is evaluated while treating one of the parameters as nuisance parameter, i.e., it is considered to be unrelated to the agent position. That is, we use $\boldsymbol{\theta}_{\text{nuis}} = [\boldsymbol{\phi}^{\mathrm{T}}, \boldsymbol{\alpha}^{\mathrm{T}}, \tilde{\boldsymbol{\zeta}}^{\mathrm{T}}]^{\mathrm{T}}$ to evaluate the amount of delay information, as well as $\boldsymbol{\theta}_{\text{nuis}} = [\boldsymbol{\tau}^{\mathrm{T}}, \boldsymbol{\alpha}^{\mathrm{T}}, \tilde{\boldsymbol{\zeta}}^{\mathrm{T}}]^{\mathrm{T}}$ to evaluate the angle information in (4.6). The evaluated PEB results are shown in Figure 4.3. Considering the usage of delay information only, shown in Figure 4.3a, we se a strong resemblance to the full PEB shown in Figure 4.2c. This clearly identifies the SMC delays as the main contributor to position information. Only using angle information, as shown in Figure 4.3b, achieves worse PEB values by about a factor of 100 (note the different colorbar scaling). It is clear that mainly the tangential error is decreased by angle information, i.e., the error in direction perpendicular to the AoD from the perspective of the agent is smaller. The conclusion to draw from this is that the main purpose of directional antennas is to assist in the SMC overlap resolution, whereas SMC angle estimation alone is not suited for positioning with this low number of antennas. In [T2], the same evaluation is performed using $M = 16$, showing more pronounced accuracy improvements in tangential direction, which illustrates that with pencil-beam antennas, eventually angle information will become as relevant as delay information, reinforcing the present trade-off between signal bandwidth and antenna directionality.

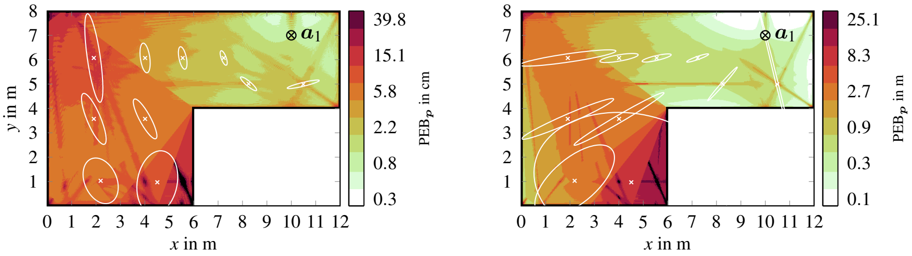

(a) (b)

Figure 4.3.: Position error bound using setup (III) with $M = 4$ antennas, whereas only (a) delay information, (b) angle information is used.

4.4. Concluding Remarks

In this chapter, we analyzed the established signal models to derive the CRLB on the position error. Our aim was to tackle Hypothesis 2, i.e., to gain insights about the position information contained in (UWB) signals, comparing single antenna measurements with multi-antenna systems, processing measurements coherently and non-coherently whereas directional antennas are used. Our analysis revealed the following insights:

- Application of multi antenna systems tackles challenging environments by opening up the angle domain to avoid SMC path overlap.
- Achieved bounds by non-coherent directional measurements resemble bounds using coherent (omni-directional) arrays.
- For systems with smaller arrays (such as SALMA), the main contributor to position information lies in SMC delays.

5. Multipath-resolved Radio Environment Maps

In this chapter, a radio environment map is formulated to leverage a multipath-resolved channel model (from Chapter 2) in order to improve the robustness of a multipath assisted positioning system. The simplified PEB from Chapter 4 is used as a basis for the map formulation. As an example application, a modified version of the algorithm used in the SALMA system is presented and evaluated with simulated measurements. This algorithm uses the environment map to guide an antenna selection process, in order to reduce the number of used measurements. Both, map formulation and algorithm are conceptual and, at the submission time of the thesis, there have not been related publications from the author yet.

In the following, we examine radio maps in literature in context with the formulated concepts of this chapter (Section 5.1), describe a problem formulation for the radio map (Section 5.2), conceptualize the titular radio environment map (Section 5.3), describe and evaluate a modified SALMA system using the map (Section 5.4), and show other related results from one of the papers included in the thesis (Section 5.5).

5.1. Related Work

In essence, radio maps as described in this thesis are born out of two related concepts: *cognitive radio* and *location awareness*. The former involves the first actual formulations of radio environment maps (REMs), with the cognitive radio concept that was originally proposed 1999 by Mitola [75, 76], where a map may indicate the available (spectrum) resources for users to be shared efficiently in a game theoretic approach. These publications spawned a new cognitive radio and dynamic spectrum access community with a wide breadth of works. Summarizing surveys are found in [116, 135]. Among the many publications that followed, the works of Haykin are of note, providing a holistic view of the concept [35, 36] and a corresponding textbook [34]. While many works are of conceptual nature, especially considering the ambitious task of handling heterogeneous user networks, a first standard applying the concept was developed with IEEE 802.22, which enables spectrum sharing for TV broadcast bands [106]. Considering the term radio *environment* map itself, it first appeared in [136], albeit the REM formulated in the mentioned work is a multi-layered structure where available radio resources are just one part next to, e.g., service and policy aspects, and without deeper consideration of the physical environment. Further detailed elaborations on REMs for cognitive radio are provided in [130].

Looking at the second influencing concept of *location awareness*, it describes the notion of radio network participants to have knowledge about their pose and how to leverage this information. Main motivator to use this information is a potential increase of channel throughput by utilizing, among others, the regularity of human motion patterns [25] or (dense) multipath spatial profiles of industrial environments [67, 109]. This made the concept of location awareness to one of the main innovations intended for 5G [110], as the upcoming technologies were deemed capable to provide the necessary position estimation accuracy [8]. This capability is given, on the one hand, by a high density of connected devices and base stations, and on the other hand by higher bandwidths and antenna numbers intended to be usable by a single device. While the latter poses as the basis for the map concept given in this chapter, the former (device density) facilitated the application of REMs on the basis of narrowband signals in the form of RSS or power spectrum maps. Construction of these radio maps may be performed, among others, by using spectral cartography [91, 111], or by crowd-sensing [5, 94]. Potential radio map applications have been outlined such as channel prediction [66], which may be efficiently performed using Gaussian processes [22, 78], or used by robot guidance systems [129] (see [125] for a survey on robot coordination systems). For positioning systems, next to the fingerprinting applications (see Section 3.1), RSS maps have been used for position tracking systems [55, 131].

Additionally to the results shown in Section 5.5, the author of this thesis worked together with Nguyen on the analysis of SINRs related to SMCs in multiple works. In [S11], SINRs of SMCs are analyzed with respect to the contribution to the channel capacity of the wireless link. It is concluded that each SMC adds to the channel capacity and thus the robustness of the link, i.e., redundancy is provided by each SMC resulting in a robustness gain. In [S10] and [S14], Gaussian process regression (GPR) is used to obtain an angle-dependent model for the SMC amplitudes using AoDs from the perspective of the corresponding VAs. The goal is to model the reflection coefficients of the involved walls, essentially to obtain an amplitude model as is formulated by (2.39) in Chapter 2. The GPR is evaluated on the same data that is used in this chapter (Section 5.3), resulting in angle-resolved SINR models for SMCs. The results indicate angle regions, and thus wall regions, with beneficial reflection properties, which may be taken advantage of by, e.g., an adaptive antenna system similar to what is presented in this chapter.

5.2. Problem Formulation

A general REM can be formulated as a generic spatial field function $f(\boldsymbol{p})$ over the (agent) position $\boldsymbol{p}$ [5]. For narrowband systems, this function describes the power spectral density or received signal strength at $\boldsymbol{p}$, where a high number of physical anchors are considered as transmitters (for examples from literature, see the previous section). In contrast, we consider REMs based on systems with high bandwidths and antenna arrays following setups (I)-(III), allowing us to leverage multipath resolved models with close relation to geometric properties of the environment. For this matter, we propose to apply the PEB from (4.12) considering the FIMs from (4.13)-(4.15) to formulate a *multipath-resolved* REM as

$$f(\boldsymbol{p}) = \mathrm{tr}\left\{\widehat{\boldsymbol{I}_{\boldsymbol{p}}}^{-1}\right\}. \tag{5.1}$$

For the estimate of the equivalent FIM, we first look at the simplest case of (I) with

$$\widehat{\boldsymbol{I}_{\boldsymbol{p}}}^{(\mathrm{I})} = \sum_{k=1}^{K} \widehat{\mathrm{SINR}}_k(\boldsymbol{p})\, \boldsymbol{D}_r\left(\varphi_k(\boldsymbol{p})\right) \tag{5.2}$$

where we use estimated SINRs to quantify the FIM for the actual radio environment. The SINRs may be obtained from measured channel responses taken in the environment, as is described in Section 5.3. The idea behind this formulation is related to the concept of *cognitive radio*, more precisely in cognitive control [36] where agents use an entropic reward function as a guidance system. Hence, in (5.2), we only consider quantities related to the agent position. Furthermore, we neglected whitening gain and information loss as described in (4.18), i.e., $\widetilde{\mathrm{SINR}}_k(\boldsymbol{p}) \approx \mathrm{SINR}_k(\boldsymbol{p})$.

Of greater interest is (III), for which, on the basis of (4.15), the simplified equivalent FIM may be written as

$$\widehat{\boldsymbol{I}_{\boldsymbol{p}}}^{(\mathrm{III})} = \sum_{k=1}^{K} \widehat{\mathrm{SINR}}_k(\boldsymbol{p}) \Big(\frac{\beta_0^2}{c^2} \left\| \boldsymbol{b}(\phi_k(\boldsymbol{p})) \right\|^2 \boldsymbol{D}_r\left(\varphi_k(\boldsymbol{p})\right) + \frac{D_b^2(\phi_k)}{d_k^2} \boldsymbol{D}_r\left(\varphi_k(\boldsymbol{p}) - \tfrac{\pi}{2}\right) M \Big) \tag{5.3}$$

$$\approx \sum_{m=1}^{M} \sum_{k=1}^{K} \left| b_m(\phi_k(\boldsymbol{p})) \right|^2 \widehat{\mathrm{SINR}}_k(\boldsymbol{p})\, \boldsymbol{D}_r\left(\varphi_k(\boldsymbol{p})\right). \tag{5.4}$$

In the second line, we used the observation from Section 4.3.2 which identifies the delay information as main contributor, hence the angle information part is neglected. On top of that, we separate the individual antenna contributions in order to write REMs for each antenna as

$$f^{(m)}(\boldsymbol{p}) = \mathrm{tr}\left\{ \left[\sum_{k=1}^{K} \left| b_m(\phi_k(\boldsymbol{p})) \right|^2 \widehat{\mathrm{SINR}}_k(\boldsymbol{p})\, \boldsymbol{D}_r\left(\varphi_k(\boldsymbol{p})\right) \right]^{-1} \right\}. \tag{5.5}$$

This REM formulation allows adaptable antenna systems to choose which antenna to use for radio observations. A corresponding antenna selection criterion may be formulated as the following

$$m_t = \operatorname*{argmin}_{m} \{ f^{(m)}(\boldsymbol{p}_t) \}. \tag{5.6}$$

Among others, an application of this selection rule is to guide positioning systems, either based on state space filters [33] or snapshot estimates. For the latter we present an evaluation of an enhanced SALMA system based on simulated measurements in Section 5.4.

5.3. REM Concept Evaluation

On the basis of the measurement data described in [S14], which was recorded once again in the lab room (see Chapter 3), we evaluate the directional multipath-resolved REM as described in (5.5). The data is comprised of 595 channel measurements taken along a trajectory spanning significant parts of the room (see Figure 5.1). To estimate the SINR values of specific SMCs, we adhere to the following process:

- Determine potential VAs up to a certain order (our deliberate choice (ODC): order 2) on the basis of an available floorplan, using all segments that surpass a certain length and thus provide a sufficiently large surface (ODC: 50 cm). The VA positions are then computed via mirroring operations as described in Section 2.2.2. The floorplan with used segments and corresponding VAs is shown in Figure 5.1.
- For each VA, determine the set of visible trajectory positions, denoted by $\mathcal{P}_k$. This procedure contains a geometric visibility test (e.g., with a ray launching procedure) and a path-overlap test, where for each pair of VAs, it is examined if their corresponding SMC delays are more than T_p apart, i.e.

$$|\tau_k(\boldsymbol{p}) - \tau_{k'}(\boldsymbol{p})| > T_\mathrm{p} \qquad \forall k \neq k', \mathrm{vis}(\boldsymbol{p}, k) \wedge \mathrm{vis}(\boldsymbol{p}, k') = 1. \tag{5.7}$$

If this condition is violated by a VA-pair (k,k'), both VAs are assumed to be non-visible, otherwise $\boldsymbol{p}$ is added to $\mathcal{P}_k$. If the thereby established set contains less positions than a certain threshold (ODC: require $|\mathcal{P}_k| > 50$ to make the SINR estimator reliable enough), the VA is outright neglected and will not be used in further processing.

- Form trajectory position clusters using the sets $\mathcal{P}_k$ described in the previous step. To this end, the K-means algorithm is applied iteratively to obtain cluster point sets $\mathcal{C}_k^{(i)}, i = 1 \ldots K_{\text{means}}$, starting with a significantly high enough number for the cluster centers (ODC: $K_{\text{means}} = 12$) and reducing this number until the smallest cluster contains enough points to make the SINR estimator reliable (again, ODC: $\min_i(|\mathcal{C}_k^{(i)}|) > 50$ points). Examples for two VAs are shown in Figure 5.2.
- For each cluster and corresponding VA $\{\mathcal{C}_k^{(i)}, \boldsymbol{a}_k\}$, perform a calibration procedure, where a position grid is spanned to cover the vicinity of the VA position, and from this grid array the best candidate is chosen according to

$$\hat{\boldsymbol{a}}_k^{(i)} = \underset{\bar{\boldsymbol{a}}_k}{\operatorname{argmax}} \Big\{ - \sum_{\boldsymbol{p} \in \mathcal{C}_k^{(i)}} \big\| \boldsymbol{r}(\boldsymbol{p}) - \hat{\alpha}_k(\boldsymbol{p}) \boldsymbol{s}\big(\tfrac{1}{c} \|\bar{\boldsymbol{a}}_k - \boldsymbol{p}\|\big) \big\| \Big\} \tag{5.8}$$

  where $\boldsymbol{r}(\boldsymbol{p})$ denotes the channel response for the corresponding trajectory position and the amplitudes $\hat{\alpha}_k(\boldsymbol{p})$ are estimated via (3.7). This procedure is equivalent to a least-squares estimation method considering independent measurements. The calibration is repeated multiple times with smaller grids spanned over the found VA position from the previous iteration to determine a local maximum. For the result shown below, this calibration process was performed with three repetitions using square grids with uniform spacing of (ODC) $[5, 1, 0.2]$ cm.
- Estimate the SINR using all amplitudes of one cluster in a method-of-moments approach. The amplitudes are obtained again via (3.7) with calibrated VAs $\hat{\boldsymbol{a}}_k^{(i)}$ for $\boldsymbol{p} \in \mathcal{C}_k^{(i)}$. Then, the first- and second-order moments of all amplitudes $(|\hat{\alpha}_k^{(i)}|)$ associated with one cluster are determined (e.g., denoted by $m_{k,1}^{(i)}$ and $m_{k,2}^{(i)}$) and the SINR is computed via $\text{SINR}_k^{(i)} = \Big(\frac{m_{k,1}^{(i)}}{\sqrt{(m_{k,1}^{(i)})^2 - m_{k,2}^{(i)}}} - 1 \Big)^{-1}$ [26].
- Option 1, *global* SINR: for each SMC k, obtain a single SINR by averaging over all $\text{SINR}_k^{(i)}$.
- Option 2, *clustered* SINR: for any agent position $\boldsymbol{p}$ of interest for the REM, take the estimated SINRs of the closest cluster centers. Example estimates are shown at the top of Figure 5.2 for the corresponding VAs.
- The REM $f^{(m)}(\boldsymbol{p})$ is obtained via (5.5) evaluated over an agent position grid spanning the whole environment, using the estimated SINRs from the previous step. The directional antennas are simulated using the same method as in Chapter 4, applying (4.22) to obtain beampatterns covering the four cardinal directions. The SMC angles are obtained via the geometric model using (2.35) and (2.36).

Example results of this evaluation are shown in Figure 5.3 for a physical anchor placed in the top right corner of the room, where SINRs on the basis of position clusters are used. Analogously, Figure 5.4 shows the results for a physical anchor in the bottom right corner, whereas global SINRs estimates are used. The REM values were scaled to be in accordance with the PEB values from Chapter 4. Also, the trajectory of agent positions is indicated for which measurements were taken and error ellipses are shown for selected agent points. The shown REMs illustrate the benefit of activating certain

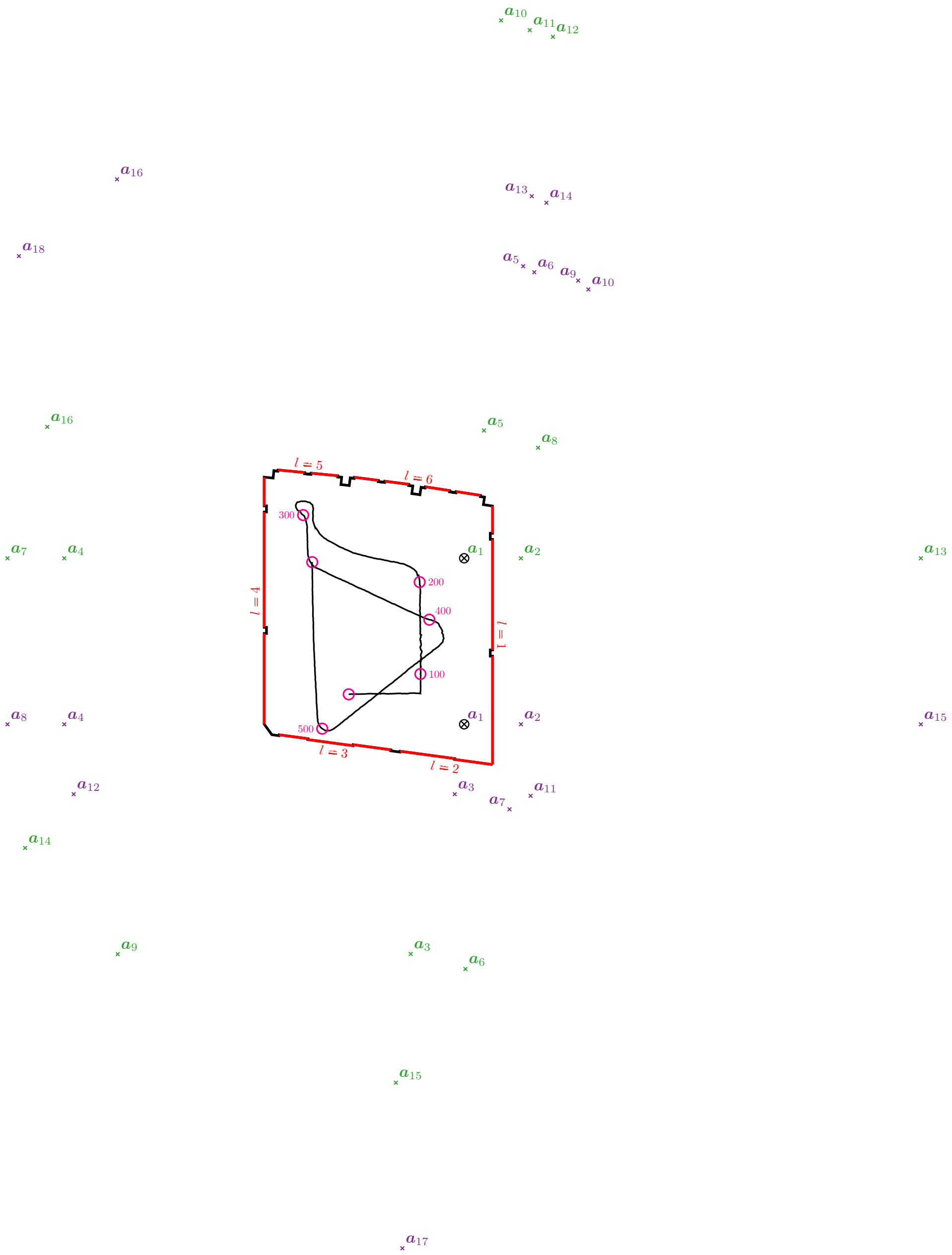

Figure 5.1.: Floorplan of environment used for the REM evaluation. VAs up to order 2 are shown, the wall segment indices are depicted as $l = i$ (note that parallel segments are merged for the indices). The VAs are labeled with consecutive indices, non-visible VAs are excluded and overlapping VAs are merged. VAs for physical anchor 1 (top right) are colored brightly (green) and VAs for physical anchor 2 (bottom right) are colored darker (purple). Sample positions on the trajectory and their indices are indicated (in magenta).

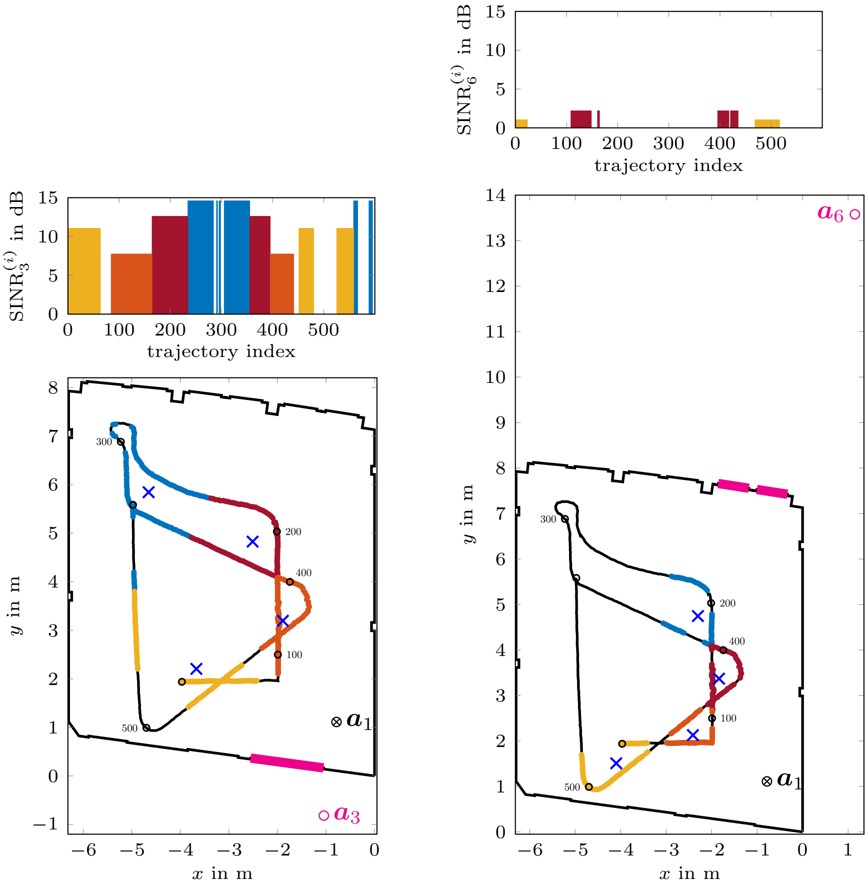

(a)

(b)

Figure 5.2.: Example of trajectory position clustering, shown for two VAs with their respective wall segments (in magenta). The corresponding trajectory positions $\mathcal{P}_k$ are indicated in different colors for each cluster and blue crosses indicate the cluster centers determined by the K-means algorithm. Note that there are gaps in the trajectory positions due to the path overlap criterion (5.7). On the top, the SINR values for each cluster are indicated (using $\boldsymbol{a}_6$, some clusters have SINR$= -\infty$).

directional antennas, when looking at the width of the ellipses in direction of the anchor (radial information) and in perpendicular direction (tangential information). In cases where SMCs overlap, it can be beneficial to use antennas that point towards reflection surfaces, since more position information is present in some direction. As examples, in Figure 5.3, for center-left positions at $(x \approx -5, y \approx 5)$ the “left” antenna (b), pointing towards the agent does have good radial values, but the “up” antenna (a), pointing towards the windows, has better tangential values and might thus be a good choice. Similar observations can be made in Figure 5.4 at $(x \approx -5, y \approx 5)$, comparing the antennas (a) facing the agent and (c) facing the south wall.

The corresponding evaluation of the antenna selection rule (5.6) is illustrated in Figure 5.5 for these two REM examples, showing for each agent position which antenna achieves the highest REM value and should thus be selected by an adaptive positioning method. Similar to the made REM observations, it can be seen how there are large regions where the best antenna is not directly facing the agent because of beneficial SMC visibility conditions. E.g, the antenna facing to the right is the best match towards the bottom in Figure 5.5a and towards the top right in Figure 5.5b along the trajectory. In Appendix B, further results are shown where the SINR estimation basis is switched, i.e., global SINRs for top right shown in Figure B.1 and clustered SINRs for bottom right shown in Figure B.2 with the corresponding antenna selection shown in Figure B.3.

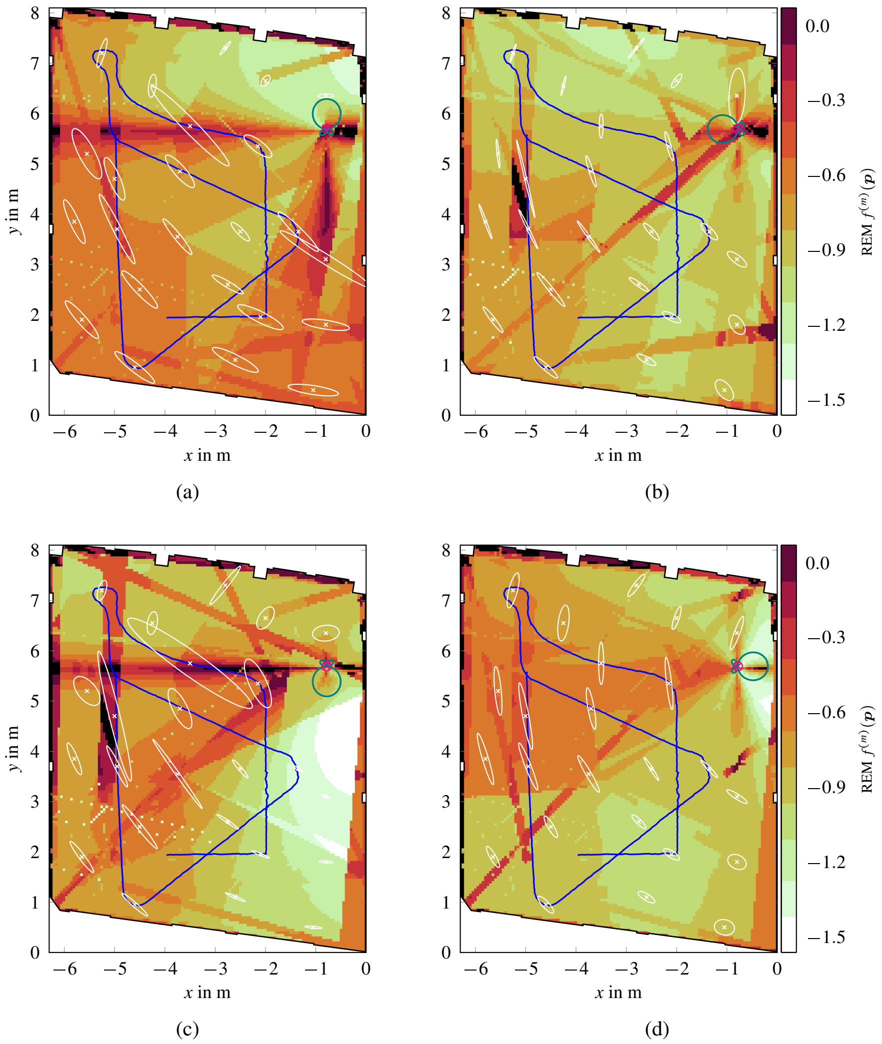

(a)

(b)

(c)

(d)

Figure 5.3.: REM evaluation of (5.5) for the **top** right anchor, using **clustered** SINR estimates and a directional antenna facing (a) up (b) left (c) down (d) right.

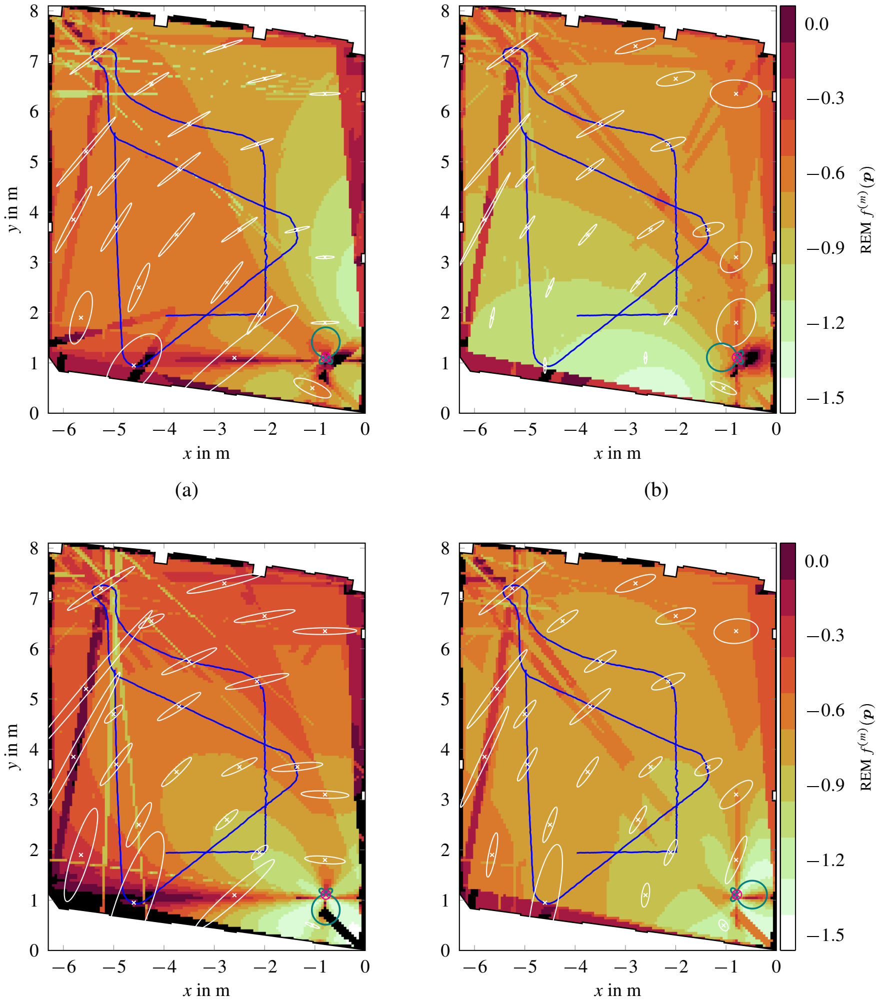

(a) (b) (c) (d)

Figure 5.4.: REM evaluation of (5.5) for the **bottom** right anchor, using **global** SINR estimates and a directional antenna facing (a) up (b) left (c) down (d) right.

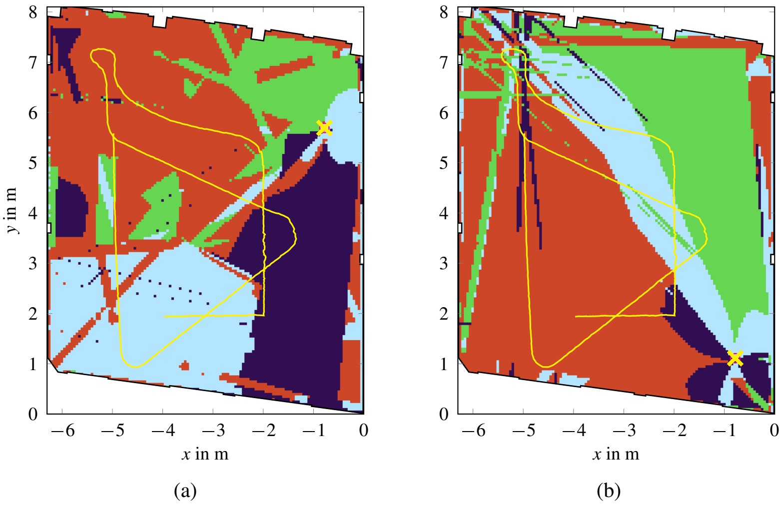

(a) (b)

Figure 5.5.: Antenna selection via (5.6) based on the REM for (a) the top right anchor using clustered SINR estimates (see Figure 5.3) and for (b) the bottom right anchor using global SINR estimates (see Figure 5.4).
Color coding: **Up**, **Left**, **Down**, **Right**

5.4. Example Application: Adaptive SALMA

To put the formulated map concept into practice, we extend the SALMA system from Chapter 3 to include any REM as just defined. The objective of this extension is to use the REM for feedback control in order to reduce the number of antenna measurements needed to obtain a position estimate, without significantly reducing the accuracy. The main controlling quantity that should influence the algorithm is a selection similar to (5.6), however, we want to respect the REMs of all antennas, hence, we define the selection vector

$$\boldsymbol{m}_t = \operatorname*{sort}_{m} \left(f^{(m)}(\hat{\boldsymbol{p}}_{t-1}) \right) \qquad t \in [1, N_t] \tag{5.9}$$

where sort_i is a sort function that stacks the corresponding values for all i into a vector in ascending order and we have t as a discrete time index for up to N_t time steps. The subscript $t-1$ indicates that the position estimate from the last time step is used to determine the used REM values and, for the evaluation, we use the ground truth position in the first time step ($\hat{\boldsymbol{p}}_0 = \boldsymbol{p}_1$).

With this selection vector, the algorithm from Chapter 3 is adapted in the LLH evaluation from (3.8) by not using all antennas with $m = 1 \dots M$, but rather using the selector from (5.9). Hence, we define

$$\bar{L}_{\hat{M}}^{(\mathrm{III,AWGN})}(\boldsymbol{r}|\boldsymbol{p}) = - \sum_{m \in \left[\boldsymbol{m}_t\right]_1^{\hat{M}}} \left\| \boldsymbol{r}_m - \boldsymbol{X}_m(\boldsymbol{\phi}, \boldsymbol{\tau}, \tilde{\zeta}_m)\boldsymbol{\alpha} \right\|^2 \tag{5.10}$$

where we have the parameter $\hat{M}$ that determines how many of the antennas should be selected using the REM values. This already allows the algorithm to reduce the number of used antennas, guided by the REM. However, to make the algorithm truly adaptive, we introduce a mechanism that varies this parameter depending on the previous position estimate. For this, we have a time-dependent selection that starts with $\hat{M}(t) = 1$ and is then sequentially changed based on the following criteria

$$\mathrm{if}\left(\|\hat{\boldsymbol{p}}_{t-1} - \hat{\boldsymbol{p}}_t^{(\hat{M}(t))}\| > d_{\mathrm{thresh}} \right) \text{ then } \hat{M}(t) = \hat{M}(t) + 1 \tag{5.11}$$

where we have $\hat{\boldsymbol{p}}_{t-1}$ as the final estimate from the last step (for the first estimate, all antennas are used, i.e. $\hat{M}(1) = M$) and the current estimate $\hat{\boldsymbol{p}}_t^{(\hat{M}(t))}$ is obtained using $\hat{M}(t)$ antennas. The threshold value d_{thresh} is set accordingly to detect outliers, i.e., "jumps" in the estimate. For concept evaluation purposes, we use a constant threshold (ODC: $d_{\mathrm{thresh}} = 0.33$ m), whereas a dependency on a velocity estimate or measurement may be a reasonable further extension.

To evaluate the application of the REM, measurements for four directional antennas as they would be conducted by SALMA were simulated for the 595 trajectory positions. For the noise model, we used the same parameters as in Chapter 4 for the AWGN and DMC (representing the corresponding indoor environment; for details see Section 4.3). For each position, 100 realizations of the channel response measurements were created. These measurements were used in the standard SALMA methods described in Chapter 3 and using (5.10) with $\hat{M} = 1 \dots 3$, which we named correspondingly "solo", "duo", and "trio". Lastly, the adaptive selection from (5.11) was used and the respectively determined $\hat{M}(t)$ values were stored to see the average numbers of required antennas. The used REMs for the selection vector are the ones shown in Figure 5.3 for anchor 1 (top right, using clustered SINR) and Figure 5.4 for anchor 2 (bottom right, using global SINR).

The results of the position error for all realizations are shown in Figure 5.6. Comparing the number of antennas used, it is clear that a single directional antenna can not compete with the omni-directional antenna used in SALMA-light, which is caused by the fact that a single directional antenna is likely to attenuate some useful SMCs to a large degree such that the likelihood becomes multi-modal, just as with the omni antenna. Using two or three antennas remedies this effect, whereas the latter seems to be sufficient to reach the SALMA-full results (especially for anchor 2). The most valuable result however, is the application of the adaptive method, which comes very close to SALMA-full for the outliers (higher percentiles), albeit with decreased accuracy (slope of curves) due to reduced position information present with overall fewer measurement used.

Figure 5.7 shows position error results to compare the adaptive SALMA methods (solid lines) to slight variations thereof (dashed lines). In these altered versions, the selection vector $\boldsymbol{m}_t$ is randomized with a random permutation of $1 \ldots M$. The idea behind this simulation is to show that the REM guidance is effectively improving the results compared to "blindly" reducing the number of used antennas. These results show that the REM clearly improves the results for all cases were more than one antenna is used. However, this observation is more pronounced with anchor 1. Of special note is the duo case, where a random selection of the two used antennas leads to a significantly worse performance (on the level of SALMA-light). Curiously, when examining the solo case, a random selection performs slightly better than the REM-guided one. It seems that, for the cases where we have a strong reduction of most SMCs, the REM is no longer a reliable selection criteria to get the "best" LLH for the algorithm.

Further analysis of the adaptive method is seen in Figure 5.8, which shows the average needed number of antennas. It is clear that for the majority (around 60%) of agent positions, it is sufficient to use a single antenna. Only in challenging regions it is necessary to switch on additional antennas, where the full setup is only needed in around 15% of the cases. The average used antenna numbers are 1.8 for anchor 1 and 1.73 for anchor 2, i.e., less directional observations are needed than with the "duo" method. However, we do note that it may require multiple estimates, i.e., LLH evaluations have to be computed whenever more antennas (in around 40% of the cases) are needed. The average needed numbers are also depicted in Figure 5.9, albeit shown over the trajectory positions. This presents a clear picture of challenging regions, e.g., for the region in the top left (index 300 and also towards the end of the trajectory) the system commonly needs 3 or more antennas, regardless of what anchor is used.

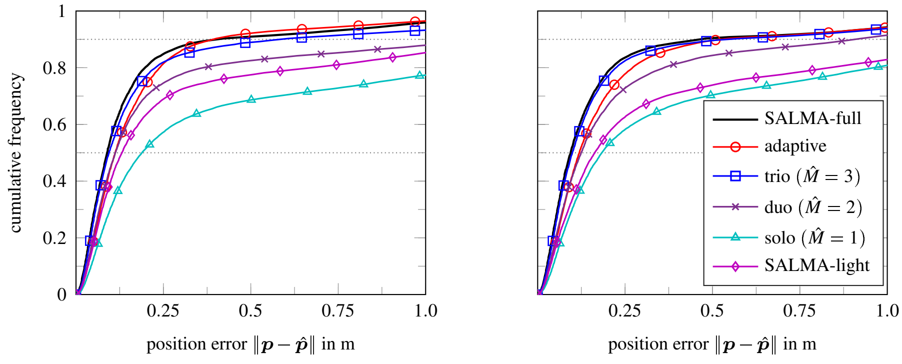

(a) (b)

Figure 5.6.: Positioning evaluation for (a) anchor 1 (top right, clustered SINR), (b) anchor 2 (bottom right, global SINR) along trajectory using the standard SALMA methods and enhanced versions with varying antenna numbers selected by application of the REM.

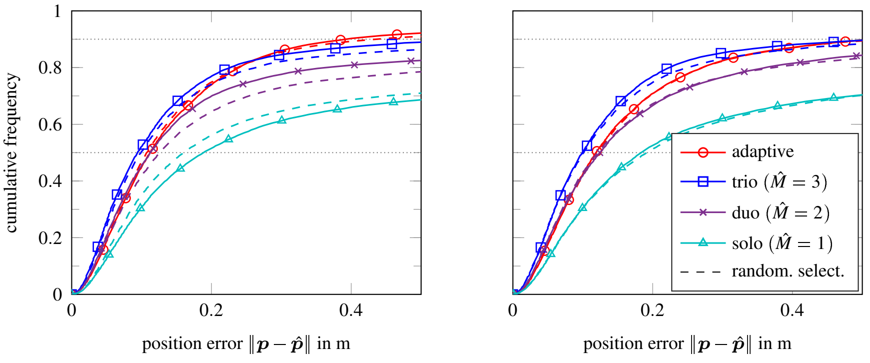

(a) (b)

Figure 5.7.: Positioning evaluation for (a) anchor 1 (top right, clustered SINR), (b) anchor 2 (bottom right, global SINR) analogous to Figure 5.6. Comparison between the REM-based selection and a variation of the method where the antenna selection is randomized.

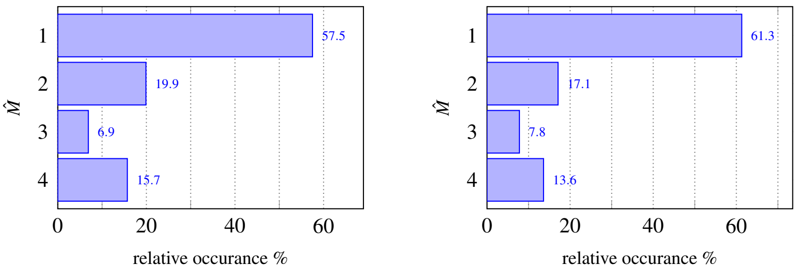

(a) (b)

Figure 5.8.: Distribution of needed antennas for the adaptive SALMA method using (a) anchor 1 (top right, clustered SINR), (b) anchor 2 (bottom right, global SINR).

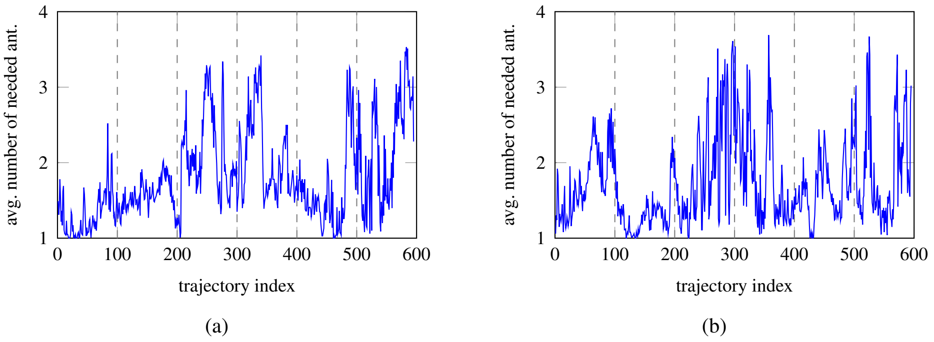

(a)

(b)

Figure 5.9.: Average number of needed antennas for each trajectory position for (a) anchor 1 (top right, clustered SINR), (b) anchor 2 (bottom right, global SINR).

5.5. Selected Related Results

A close resemblance to the basis of the formulated REMs is provided in [T5], where a similar measurement campaign was performed in a parking garage using the SALMA positioning system described in Chapter 3 and [T1]. Figure 5.10a shows the environment with considered VAs and agent trajectory. Many of the VAs result from reflecting surfaces at the ceiling (metal beams). The system was mounted on a moving car and channel responses were measured over the shown trajectory switching between four directional antennas. An SINR evaluation was performed, again considering an anchor calibration step similar to (5.8), with agent position clusters along the trajectory denoted by $\boldsymbol{p}_C^{(i)}$. The resulting SINR estimates are shown in Figure 5.10b, evaluated over the trajectory position clusters. Naturally, the LOS component is the strongest SMC, however there are regions around index 15, which is at the center of the U-turn, where a strong SMC from the left wall ($\hat{\alpha}_2$) is present. Further elaborations of this kind are found in [T5]. More analysis of the environment geometry and measurements is needed to calculate an REM and apply the positioning method described in this chapter, which is open for future work [89].

5.6. Concluding Remarks

In this chapter, we proposed the concept of a *directional, multipath-resolved radio environment map* on the basis of the simplified PEB described in the previous chapter. Our aim was to create a bridge to the cognitive radio concept in terms of cognitive control, to consider delay- / angle-resolved models in order to tackle Hypothesis 3. Our analysis revealed the following insights:

- A database of radio channel observations can be used to obtain an insightful environment map which takes geometric aspects into account.
- The formulated environment map can be created for radio systems equipped with multiple directional antennas, thereby obtaining one map for each antenna. The maps are intended to be used for adaptive systems to provide a fitness value for each antenna.
- An application of the map was verified via inclusion in the previously presented positioning system (SALMA). In particular, when the system uses multiple directional antennas, the map acts as a guide to select which antenna to use. The results for the four-antenna system show that, on average, less than two antennas are needed to achieve results close to the original (SALMA-full) system with four antennas.

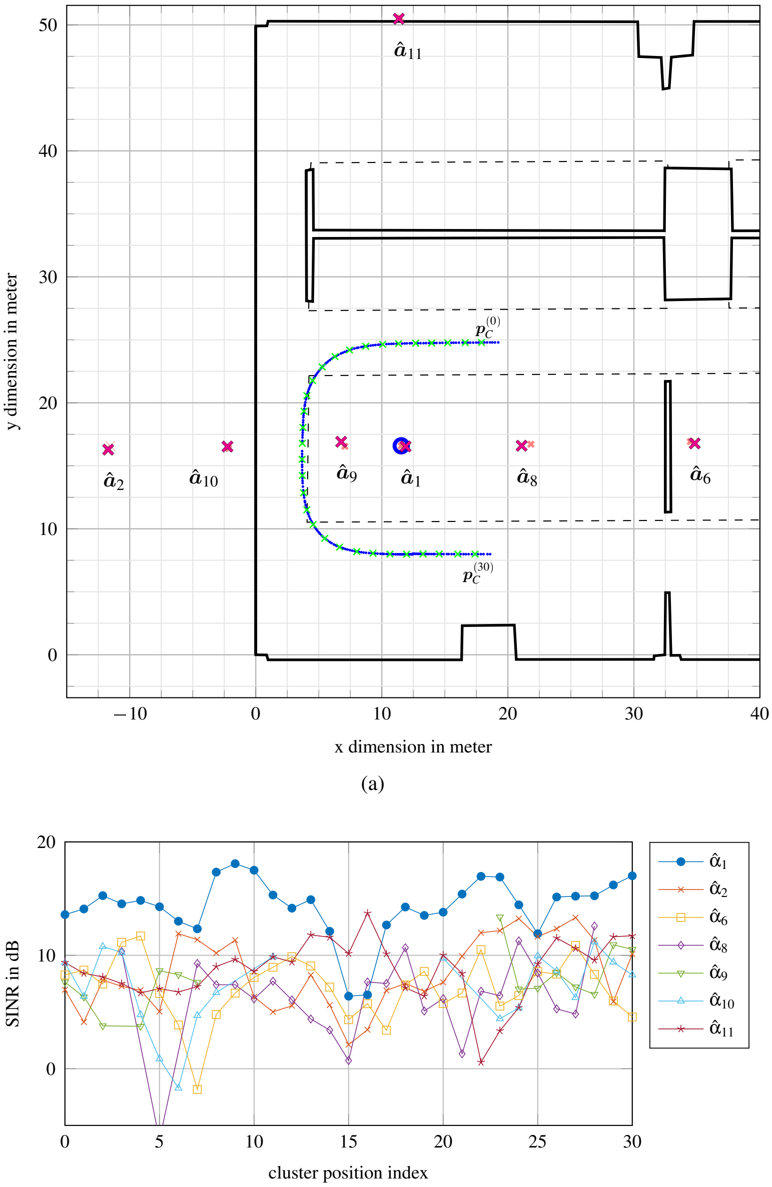

(a)

(b)

Figure 5.10.: Amplitude quality evaluation in parking garage environment showing (a) the floorplan with the used (calibrated) VAs and (clustered) trajectory, (b) the estimated SINR values for the position clusters over the trajectory.

6. Conclusions and Outlook

The objective of this thesis has been to enable agents of radio networks to become location-aware. To this end, a radio environment map (REM) is formulated providing a picture of position information present in the environment. The REM is used to drive adaptive RF front-ends in order to improve the dependability of wireless links between *Internet of Things* (IoT) nodes.

As a foundation for REMs, Chapter 2 provides a signal processing framework for single-link scenarios involving radio signals exchanged between a mobile agent and a static base station (anchor). Varying degrees of complexity are considered for the system at the anchor side to support simple IoT nodes such as sensor nodes, as well as more sophisticated systems such as mobile phones or cars. Three systems are formulated using (i) one omni-directional antenna, (ii) multiple omni-directional antennas coherently and (iii) multiple directional antennas non-coherently. The provided framework has been used in the main body of this work as a basis to tackle three research questions, formulated as hypotheses, namely (H1) the design of resource-efficient positioning systems, (H2) fundamental limits of positioning accuracy and (H3) formulation of multipath-resolved REMs. The hypotheses are tackled in Chapters 3–5 which are summarized in the following, also with reference to the included papers.

In Chapter 3, single-anchor positioning methods are described on the basis of UWB signals and a corresponding implementation using low-cost DecaWave DWM1000 hardware is outlined [T1]. Analysis of position likelihoods considering UWB signals indicates the benefits of directional antennas to resolve ambiguities [T4]. Evaluations in office-like environments exemplify an improvement of positioning performance, where outliers are significantly diminished. Additionally, dense multipath is included in the noise model (on top of simple AWGN), which improves the positioning performance, as is shown in evaluations based on simulations [T2].

Moving to a more theoretical side of things, Chapter 4 deals with the fundamental limits on position accuracy of estimators using signals from the established framework. The position error bound (PEB) is calculated on the basis of the well established Cramér-Rao lower bound and Fisher information for the three system setups defined in Chapter 2. An evaluation over a challenging environment (including non line-of-sight regions) is given via numerical analysis where it is shown that using directional measurements non-coherently has the potential to compete with conventional array processing setups using omni-directional antennas coherently [T2]. The trade-off between bandwidth and directionality is highlighted when using the non-coherent setup. In contrast to many other works (e.g., [2, 27, 31]), dense multipath components are respected in the noise model on top of a simple AWGN model, enabling an analysis of different environments with varying multipath propagation.

In Chapter 5 a *multipath-resolved* REM is formulated, which uses channel response signals and geometry to inform agents about available position information. The given map uses the simplified PEB described in Chapter 4 and map values may be used as feedback control driving, e.g., an adaptive (switchable) antenna system. Determination of map values is performed using SINR values associated with specular multipath components, originating from strong reflections in the environment. An evaluation of such SINRs was performed in a challenging parking garage environment [T5]. An addition to the SALMA system is formulated making use of the REM values in order to select which antennas to use. Evaluation of this *adaptive* SALMA method on the basis of simulated data shows that a performance close to the original system is achievable, while the average number of used antennas is reduced from 4 down to less than 2. For future work, it is intended to perform the REM and adaptive algorithm evaluation using real data from a harsh environment, such as the parking garage described in [T5].

Appendix

A. Four Quadrant Inverse Tangent

The inverse tangent function with two arguments can be used to determine the angle of a two-dimensional vector $[x, y]^\mathrm{T}$, whereby the image covers the complete angle range $[0, 2\pi]$ and the poles of the involved $\operatorname{atan}(\cdot)$ function are taken care of. The function is written $\operatorname{atan2} : \mathbb{R}^2 \mapsto \mathbb{R}$ defined as

$$\operatorname{atan2}(x, y) \triangleq \begin{cases} \operatorname{atan}(\frac{y}{x}) & x > 0 \\ \operatorname{atan}(\frac{y}{x}) + \pi & x < 0, y > 0 \\ \pi & x < 0, y = 0 \\ \operatorname{atan}(\frac{y}{x}) - \pi & x < 0, y < 0 \\ \frac{\pi}{2} & x = 0, y > 0 \\ -\frac{\pi}{2} & x = 0, y < 0. \end{cases} \tag{A.1}$$

The partial derivatives are written as

$$\frac{\partial}{\partial x}\operatorname{atan2}(x, y) = \begin{cases} 0 & x = 0, y = 0 \\ -\frac{y}{x^2+y^2} & \text{else} \end{cases} \tag{A.2}$$

$$\frac{\partial}{\partial y}\operatorname{atan2}(x, y) = \begin{cases} 0 & x = 0, y = 0 \\ \frac{x}{x^2+y^2} & \text{else.} \end{cases} \tag{A.3}$$

B. Additional REMs for Lab Room

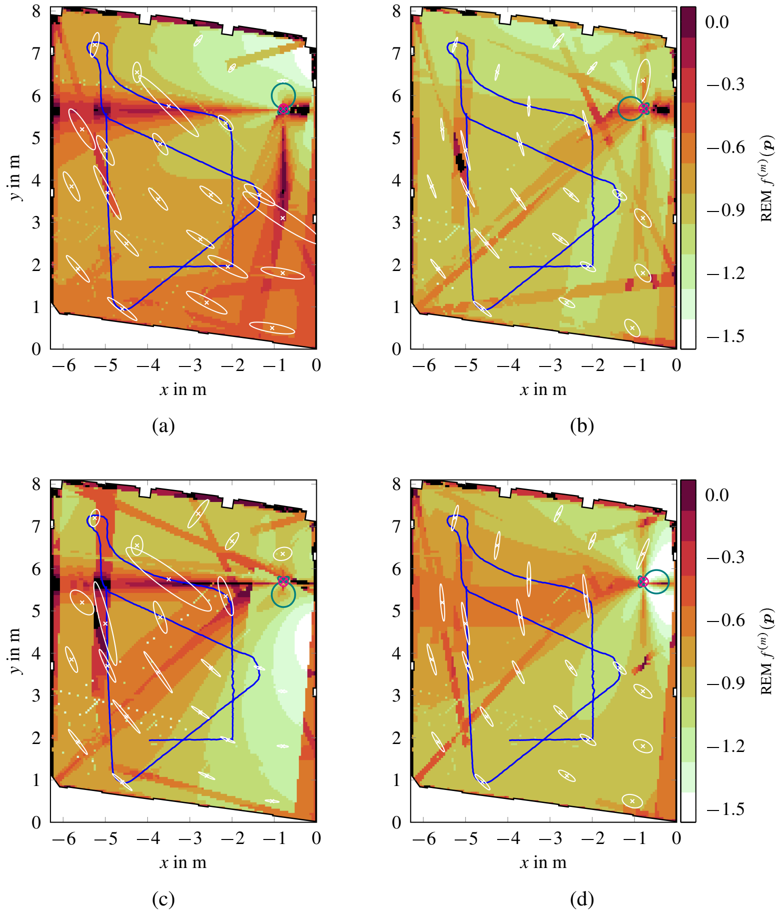

(a)

(b)

(c)

(d)

Figure B.1.: REM evaluation of (5.5) for the **top** right anchor, using **global** SINR estimates and a directional antenna facing (a) up (b) left (c) down (d) right.

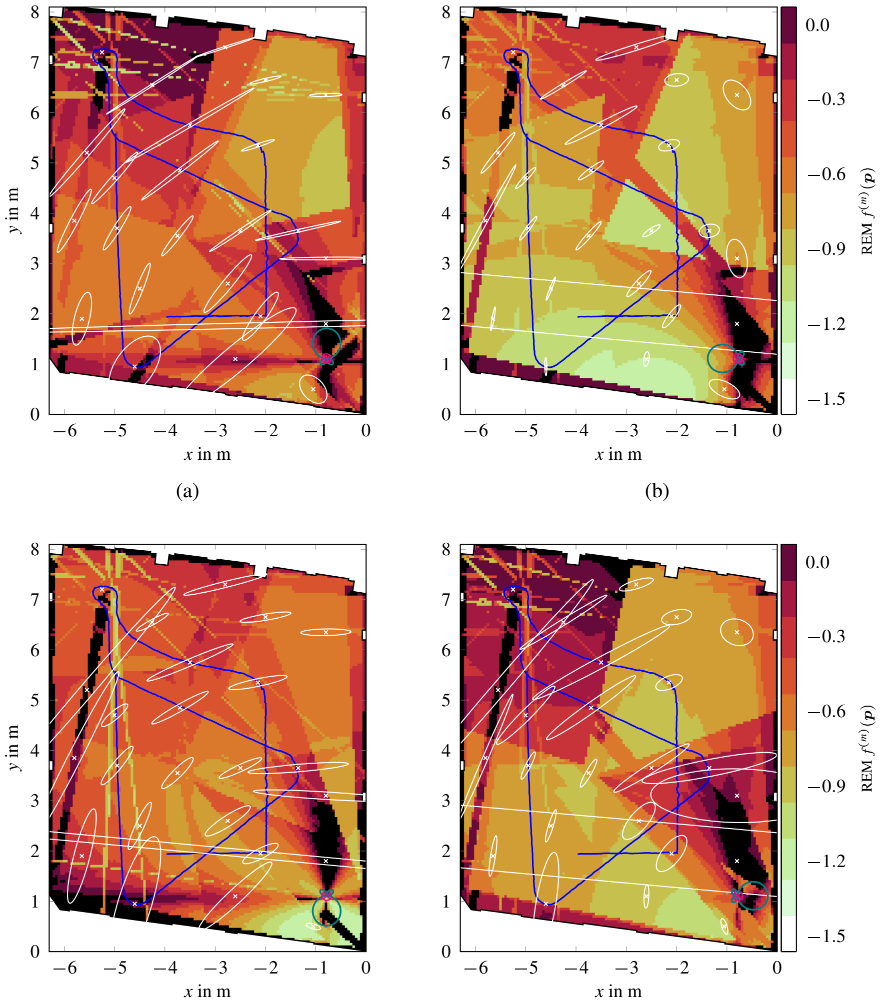

(a) (b)

(c) (d)

Figure B.2.: REM evaluation of (5.5) for the **bottom** right anchor, using **clustered** SINR estimates and a directional antenna facing (a) up (b) left (c) down (d) right. Note that there are regions where the REM assumes very bad (i.e., very high) values close to the anchor. The reason for this degradation is that, for measurements associated with this region, only the LOS is visible due to the directivity of the antennas and hence a position estimate is not feasible.

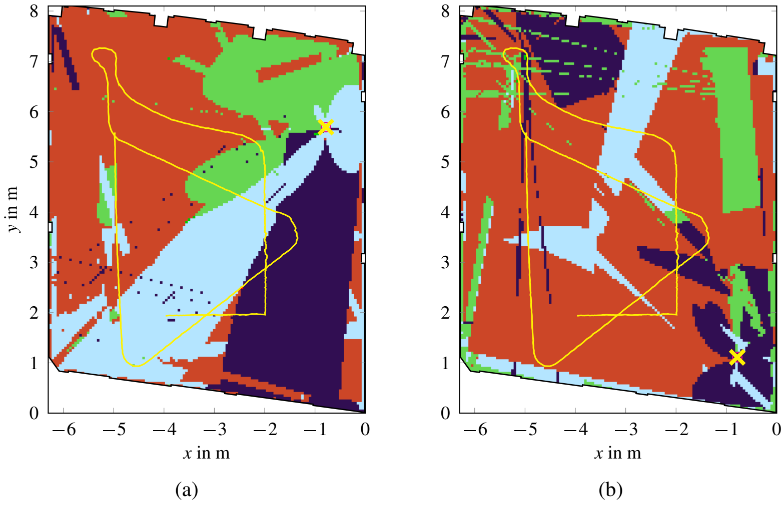

Figure B.3.: Antenna selection via (5.6) based on the REM for (a) the top right anchor using global SINR estimates and for (b) the bottom right anchor using clustered SINRs estimates.
Color coding: **Up**, **Left**, **Down**, **Right**

Bibliography

[1] Z. Abu-Shaban, H. Wymeersch, T. Abhayapala, and G. Seco-Granados. “Single-Anchor Two-Way Localization Bounds for 5G mmWave Systems.” In: *IEEE Transactions on Vehicular Technology* 69.6 (June 2020), pp. 6388–6400.

[2] Z. Abu-Shaban, X. Zhou, T. Abhayapala, G. Seco-Granados, and H. Wymeersch. “Error Bounds for Uplink and Downlink 3D Localization in 5G Millimeter Wave Systems.” In: *IEEE Transactions on Wireless Communications* 17.8 (Aug. 2018), pp. 4939–4954.

[3] F. Alam, M. T. Chew, T. Wenge, and G. S. Gupta. “An Accurate Visible Light Positioning System Using Regenerated Fingerprint Database Based on Calibrated Propagation Model.” In: *IEEE Transactions on Instrumentation and Measurement* 68.8 (Aug. 2019), pp. 2714–2723.

[4] J. G. Andrews, S. Buzzi, W. Choi, S. V. Hanly, A. Lozano, A. C. K. Soong, and J. C. Zhang. “What Will 5G Be?” In: *IEEE Journal on Selected Areas in Communications* 32.6 (June 2014), pp. 1065–1082.

[5] E. Arias-de-Reyna, P. Closas, D. Dardari, and P. M. Djuric. “Crowd-Based Learning of Spatial Fields for the Internet of Things: From Harvesting of Data to Inference.” In: *IEEE Signal Processing Magazine* 35.5 (Sept. 2018), pp. 130–139.

[6] J. R. Barry, E. A. Lee, and D. G. Messerschmitt. *Digital communication*. 3rd ed. Springer Science & Business Media, 2004.

[7] V. Bianchi, P. Ciampolini, and I. De Munari. “RSSI-Based Indoor Localization and Identification for ZigBee Wireless Sensor Networks in Smart Homes.” In: *IEEE Transactions on Instrumentation and Measurement* 68.2 (Feb. 2019), pp. 566–575.

[8] F. Boccardi, R. W. Heath, A. Lozano, T. L. Marzetta, and P. Popovski. “Five disruptive technology directions for 5G.” In: *IEEE Communications Magazine* 52.2 (Feb. 2014), pp. 74–80.

[9] G. C. Carter. “Variance bounds for passively locating an acoustic source with a symmetric line array.” In: *The Journal of the Acoustical Society of America* 62.4 (Oct. 1977), pp. 922–926.

[10] D. Cassioli, M. Z. Win, and A. F. Molisch. “The ultra-wide bandwidth indoor channel: from statistical model to simulations.” In: *IEEE Journal on Selected Areas in Communications* 20.6 (Aug. 2002), pp. 1247–1257.

[11] J. Chaffee and J. Abel. “GDOP and the Cramer-Rao bound.” In: *Proceedings of IEEE Position, Location and Navigation Symposium (PLANS’94)*. Apr. 1994, pp. 663–668.

[12] Y. Chen, B. Wang, Y. Han, H. Q. Lai, Z. Safar, and K. J. R. Liu. “Why Time Reversal for Future 5G Wireless? [Perspectives].” In: *IEEE Signal Processing Magazine* 33.2 (Mar. 2016), pp. 17–26.

[13] W. H. Chin, Z. Fan, and R. Haines. “Emerging technologies and research challenges for 5G wireless networks.” In: *IEEE Wireless Communications* 21.2 (Apr. 2014), pp. 106–112.

[14] A. Cidronali, S. Maddio, G. Giorgetti, and G. Manes. "Analysis and performance of a smart antenna for 2.45-GHz single-anchor indoor positioning." In: *IEEE Transactions on Microwave Theory and Techniques* 58.1 (Jan. 2010), pp. 21–31.

[15] P. Corbalán, G. P. Picco, and S. Palipana. "Chorus: UWB Concurrent Transmissions for GPS-like Passive Localization of Countless Targets." In: *Proceedings of the 18th ACM/IEEE International Conference on Information Processing in Sensor Networks*. IPSN '19. Apr. 2019, pp. 133–144.

[16] P. Corbalán and G. P. Picco. "Concurrent Ranging in Ultra-Wideband Radios: Experimental Evidence, Challenges, and Opportunities." In: *Proceedings of the 2018 International Conference on Embedded Wireless Systems and Networks*. EWSN '18. Madrid, Spain: Junction Publishing, Feb. 2018, pp. 55–66.

[17] H. Cramér. *Mathematical methods of statistics*. Princeton University Press, 1946.

[18] D. Dardari, A. Conti, U. Ferner, A. Giorgetti, and M. Z. Win. "Ranging With Ultrawide Bandwidth Signals in Multipath Environments." In: *Proceedings of the IEEE* 97.2 (Feb. 2009), pp. 404–426.

[19] G. Durgin. *Space-time Wireless Channels*. Prentice Hall Press, 2002.

[20] R. Faragher and R. Harle. "Location Fingerprinting With Bluetooth Low Energy Beacons." In: *IEEE Journal on Selected Areas in Communications* 33.11 (Nov. 2015), pp. 2418–2428.

[21] B. H. Fleury. "First- and second-order characterization of direction dispersion and space selectivity in the radio channel." In: *IEEE Transactions on Information Theory* 46.6 (Sept. 2000), pp. 2027–2044.

[22] M. Fröhle, T. Charalambous, I. Nevat, and H. Wymeersch. "Channel Prediction With Location Uncertainty for Ad Hoc Networks." In: *IEEE Transactions on Signal and Information Processing over Networks* 4.2 (June 2018), pp. 349–361.

[23] C. Gentner, T. Jost, W. Wang, S. Zhang, A. Dammann, and U. C. Fiebig. "Multipath Assisted Positioning with Simultaneous Localization and Mapping." In: *IEEE Transactions on Wireless Communications* 15.9 (Sept. 2016), pp. 6104–6117.

[24] A. Goldsmith. *Wireless Communications*. Cambridge University Press, 2005.

[25] M. C. González, C. A. Hidalgo, and A.-L. Barabási. "Understanding individual human mobility patterns." In: *Nature* 453.7196 (June 2008), pp. 779–782.

[26] L. J. Greenstein, D. G. Michelson, and V. Erceg. "Moment-method estimation of the Ricean K-factor." In: *IEEE Communications Letters* 3.6 (June 1999), pp. 175–176.

[27] A. Guerra, F. Guidi, and D. Dardari. "Single-Anchor Localization and Orientation Performance Limits Using Massive Arrays: MIMO vs. Beamforming." In: *IEEE Transactions on Wireless Communications* 17.8 (Aug. 2018), pp. 5241–5255.

[28] X. Guo, N. R. Elikplim, N. Ansari, L. Li, and L. Wang. "Robust WiFi Localization by Fusing Derivative Fingerprints of RSS and Multiple Classifiers." In: *IEEE Transactions on Industrial Informatics* 16.5 (May 2020), pp. 3177–3186.

[29] W. Hahn and S. Tretter. "Optimum processing for delay-vector estimation in passive signal arrays." In: *IEEE Transactions on Information Theory* 19.5 (Sept. 1973), pp. 608–614.

[30] F. Han, Y. Yang, B. Wang, Y. Wu, and K. J. R. Liu. "Time-Reversal Division Multiple Access over Multi-Path Channels." In: *IEEE Transactions on Communications* 60.7 (July 2012), pp. 1953–1965.

[31] Y. Han, Y. Shen, X. Zhang, M. Z. Win, and H. Meng. “Performance Limits and Geometric Properties of Array Localization.” In: *IEEE Transactions on Information Theory* 62.2 (Feb. 2016), pp. 1054–1075.

[32] F. Hartmann, F. Pistorius, A. Lauber, K. Hildenbrand, J. Becker, and W. Stork. “Design of an Embedded UWB Hardware Platform for Navigation in GPS Denied Environments.” In: *Proceedings of the IEEE Symposium on Communications and Vehicular Technology in the Benelux (SCVT)*. Nov. 2015, pp. 1–6.

[33] S. Haykin, Y. Xue, and P. Setoodeh. “Cognitive Radar: Step Toward Bridging the Gap Between Neuroscience and Engineering.” In: *Proceedings of the IEEE* 100.11 (Nov. 2012), pp. 3102–3130.

[34] S. Haykin. *Cognitive dynamic systems: perception-action cycle, radar and radio*. Cambridge University Press, 2012.

[35] S. Haykin. “Cognitive Radio: Brain-Empowered Wireless Communications.” In: *IEEE Journal on Selected Areas in Communications* 23.2 (Feb. 2005), pp. 201–220.

[36] S. Haykin and J. M. Fuster. “On Cognitive Dynamic Systems: Cognitive Neuroscience and Engineering Learning From Each Other.” In: *Proceedings of the IEEE* 102.4 (Apr. 2014), pp. 608–628.

[37] S. S. Haykin. *Digital communications*. John Wiley & Sons, 1988.

[38] IEEE. *Standard for Low-Rate Wireless Networks*. 802.15.4-2011. 2011.

[39] D. B. Jourdan, D. Dardari, and M. Z. Win. “Position error bound for UWB localization in dense cluttered environments.” In: *IEEE Transactions on Aerospace and Electronic Systems* 44.2 (Apr. 2008), pp. 613–628.

[40] A. Kakkavas, M. H. Castañeda García, R. A. Stirling-Gallacher, and J. A. Nossek. “Performance Limits of Single-Anchor Millimeter-Wave Positioning.” In: *IEEE Transactions on Wireless Communications* 18.11 (Nov. 2019), pp. 5196–5210.

[41] J. Karedal, S. Wyne, P. Almers, F. Tufvesson, and A. F. Molisch. “A Measurement-Based Statistical Model for Industrial Ultra-Wideband Channels.” In: *IEEE Transactions on Wireless Communications* 6.8 (Aug. 2007), pp. 3028–3037.

[42] S. Kay. *Fundamentals of Statistical Signal Processing: Estimation Theory*. Prentice Hall Signal Processing Series, 1993.

[43] B. Kempke, P. Pannuto, B. Campbell, and P. Dutta. “SurePoint: Exploiting Ultra Wideband Flooding and Diversity to Provide Robust, Scalable, High-Fidelity Indoor Localization.” In: *Proceedings of the 14th International Conference on Embedded Network Sensor Systems (SenSys)*. Nov. 2016, pp. 137–149.

[44] B. Kempke, P. Pannuto, and P. Dutta. “Harmonium: Asymmetric, Bandstitched UWB for Fast, Accurate, and Robust Indoor Localization.” In: *Proceedings of the 15th ACM/IEEE International Conference on Information Processing in Sensor Networks*. IPSN ’16. Vienna, Austria, Apr. 2016.

[45] B. Kempke, P. Pannuto, and P. Dutta. “PolyPoint: Guiding Indoor Quadrotors with Ultra-Wideband Localization.” In: *Proceedings of the 2nd International Workshop on Hot Topics in Wireless (HotWireless)*. Sept. 2015, pp. 16–20.

[46] C. Knapp and G. Carter. “The generalized correlation method for estimation of time delay.” In: *IEEE Transactions on Acoustics, Speech, and Signal Processing* 24.4 (Aug. 1976), pp. 320–327.

[47] C. Krall. “Signal processing for ultra wideband transceivers.” PhD thesis. Graz University of Technology, Austria, 2008.

[48] J. Kulmer, E. Leitinger, S. Grebien, and K. Witrisal. “Anchorless Cooperative Tracking Using Multipath Channel Information.” In: *IEEE Transactions on Wireless Communications* 17.4 (Apr. 2018), pp. 2262–2275.

[49] J. Kunisch and J. Pamp. “An Ultra-Wideband space-variant Multipath Indoor Radio Channel Model.” In: *IEEE Conference on Ultra Wideband Systems and Technologies*. Nov. 2003, pp. 290–294.

[50] Y.-S. Kuo, P. Pannuto, K.-J. Hsiao, and P. Dutta. “Luxapose: Indoor Positioning with Mobile Phones and Visible Light.” In: *Proceedings of the 20th Annual International Conference on Mobile Computing and Networking*. MobiCom ’14. Maui, Hawaii, USA, Sept. 2014, pp. 447–458.

[51] E. G. Larsson, O. Edfors, F. Tufvesson, and T. L. Marzetta. “Massive MIMO for next generation wireless systems.” In: *IEEE Wireless Communications Magazine* 52.2 (Feb. 2014), pp. 186–195.

[52] P. Lazik and A. Rowe. “Indoor Pseudo-Ranging of Mobile Devices using Ultrasonic Chirps.” In: *Proceedings of the 10th International Conference on Embedded Network Sensor Systems (SenSys)*. Nov. 2012, pp. 99–112.

[53] A. Ledergerber, M. Hamer, and R. D’Andrea. “A Robot Self-Localization System using One-Way Ultra-Wideband Communication.” In: *Proceedings of the International Conference on Intelligent Robots and Systems (IROS)*. Sept. 2015, pp. 3131–3137.

[54] H. B. Lee. “Accuracy Limitations of Hyperbolic Multilateration Systems.” In: *IEEE Transactions on Aerospace and Electronic Systems* AES-11.1 (Jan. 1975), pp. 16–29.

[55] S. Lee, S. W. Choi, C. Laoudias, and S. Kim. “Heterogeneous Device Tracking With RSS Variation Mitigation Over a Radio Map.” In: *IEEE Wireless Communications Letters* 5.5 (Oct. 2016), pp. 552–555.

[56] Lei Huang and Chi Chung Ko. “Performance of maximum-likelihood channel estimator for UWB communications.” In: *IEEE Communications Letters* 8.6 (June 2004), pp. 356–358.

[57] E. Leitinger, M. Fröhle, P. Meissner, and K. Witrisal. “Multipath-Assisted Maximum-Likelihood Indoor Positioning using UWB Signals.” In: *IEEE International Conference on Communications (ICC)*. June 2014, pp. 170–175.

[58] E. Leitinger, P. Meissner, C. Rudisser, G. Dumphart, and K. Witrisal. “Evaluation of Position-Related Information in Multipath Components for Indoor Positioning.” In: *IEEE Journal on Selected Areas in Communications* 33.11 (Nov. 2015), pp. 2313–2328.

[59] E. Leitinger, F. Meyer, F. Hlawatsch, K. Witrisal, F. Tufvesson, and M. Z. Win. “A Belief Propagation Algorithm for Multipath-Based SLAM.” In: *IEEE Transactions on Wireless Communications* 18.12 (Dec. 2019), pp. 5613–5629.

[60] L. Li, P. Hu, C. Peng, G. Shen, and F. Zhao. “Epsilon: A Visible Light Based Positioning System.” In: *11th USENIX Symposium on Networked Systems Design and Implementation (NSDI 14)*. Seattle, WA, Apr. 2014, pp. 331–343.

[61] Z. Li, T. Braun, X. Zhao, Z. Zhao, F. Hu, and H. Liang. “A Narrow-Band Indoor Positioning System by Fusing Time and Received Signal Strength via Ensemble Learning.” In: *IEEE Access* 6 (2018), pp. 9936–9950.

[62] Y.-W. Lin and C.-Y. Lin. “An interactive real-time locating system based on bluetooth low-energy beacon network.” In: *Sensors* 18.5 (May 2018), p. 1637.

[63] K. Liu, X. Liu, and X. Li. “Guoguo: Enabling Fine-Grained Smartphone Localization via Acoustic Anchors.” In: *IEEE Transactions on Mobile Computing* 15.5 (May 2016), pp. 1144–1156.

[64] S. Liu and T. He. “SmartLight: Light-weight 3D Indoor Localization Using a Single LED Lamp.” In: *Proceedings of the 15th ACM Conference on Embedded Network Sensor Systems*. SenSys ’17. Delft, Netherlands, Nov. 2017.

[65] D. Lymberopoulos and J. Liu. “The Microsoft Indoor Localization Competition: Experiences and Lessons Learned.” In: *IEEE Signal Processing Magazine* 34.5 (Sept. 2017), pp. 125–140.

[66] M. Malmirchegini and Y. Mostofi. “On the Spatial Predictability of Communication Channels.” In: *IEEE Transactions on Wireless Communications* 11.3 (Mar. 2012), pp. 964–978.

[67] F. Mani, F. Quitin, and C. Oestges. “Directional Spreads of Dense Multipath Components in Indoor Environments: Experimental Validation of a Ray-Tracing Approach.” In: *IEEE Transactions on Antennas and Propagation* 60.7 (July 2012), pp. 3389–3396.

[68] R. Mautz. “Indoor positioning technologies.” Habilitation thesis. ETH Zurich, 2012.

[69] R. Mautz. “The Challenges of Indoor Environments and Specification on some Alternative Positioning Systems.” In: *Proceedings of the 6th Workshop on Positioning, Navigation and Communication (WPNC)*. Mar. 2009, pp. 29–36.

[70] P. Meissner. “Multipath-Assisted Indoor Positioning.” PhD thesis. Graz University of Technology, 2014.

[71] P. Meissner, C. Steiner, and K. Witrisal. “UWB Positioning with Virtual Anchors and Floor Plan Information.” In: *Proceedings of the 7th Workshop on Positioning, Navigation and Communication (WPNC)*. Mar. 2010, pp. 150–156.

[72] P. Meissner and K. Witrisal. “Multipath-Assisted Single-Anchor Indoor Localization in an Office Environment.” In: *19th International Conference on Systems, Signals and Image Processing (IWSSIP)*. Vienna, Austria, Apr. 2012.

[73] R. Mendrzik, H. Wymeersch, G. Bauch, and Z. Abu-Shaban. “Harnessing NLOS Components for Position and Orientation Estimation in 5G Millimeter Wave MIMO.” In: *IEEE Transactions on Wireless Communications* 18.1 (Jan. 2019), pp. 93–107.

[74] F. Meyer, T. Kropfreiter, J. L. Williams, R. Lau, F. Hlawatsch, P. Braca, and M. Z. Win. “Message Passing Algorithms for Scalable Multitarget Tracking.” In: *Proceedings of the IEEE* 106.2 (Feb. 2018), pp. 221–259.

[75] J. Mitola III. “Cognitive radio: An integrated agent architecture for software defined radio.” PhD thesis. KTH Royal Institute of Technology, 2000.

[76] J. Mitola III and G. Q. Maguire Jr. “Cognitive Radio: Making Software Radios More Personal.” In: *IEEE Personal Communications* 6.4 (Aug. 1999), pp. 13–18.

[77] A. F. Molisch. *Wireless Communications*. John Wiley & Sons, 2005.

[78] L. S. Muppirisetty, T. Svensson, and H. Wymeersch. “Spatial Wireless Channel Prediction under Location Uncertainty.” In: *IEEE Transactions on Wireless Communications* 15.2 (Feb. 2016), pp. 1031–1044.

[79] P. C. Ng, J. She, and S. Park. “High Resolution Beacon-Based Proximity Detection for Dense Deployment.” In: *IEEE Transactions on Mobile Computing* 17.6 (June 2018), pp. 1369–1382.

[80] A. Paulraj, R. Nabar, and D. Gore. *Introduction to space-time wireless communications*. Cambridge University Press, 2003.

[81] C. Peng, G. Shen, and Y. Zhang. "BeepBeep: A High-Accuracy Acoustic-Based System for Ranging and Localization Using COTS Devices." In: *ACM Transactions on Embedded Computing Systems* 11.1 (Apr. 2012).

[82] N. B. Priyantha, A. Chakraborty, and H. Balakrishnan. "The Cricket Location-Support System." In: *Proceedings of the 6th Annual International Conference on Mobile Computing and Networking*. MobiCom '00. Boston, Massachusetts, USA: Association for Computing Machinery, Aug. 2000, pp. 32–43.

[83] J. G. Proakis. *Digital Communications*. McGraw-Hill, 2007.

[84] X. Qing, Z. N. Chen, and T. S. P. See. "Sectored Antenna Array for Indoor Mono-Station UWB Positioning Applications." In: *Proceedings of the 3rd European Conference on Antennas and Propagation*. Berlin, Germany, Mar. 2009, pp. 822–825.

[85] S. Rangan, T. S. Rappaport, and E. Erkip. "Millimeter-Wave Cellular Wireless Networks: Potentials and Challenges." In: *Proceedings of the IEEE* 102.3 (Mar. 2014), pp. 366–385.

[86] C. R. Rao. "Information and the accuracy attainable in the estimation of statistical parameters." In: *Bulletin of the Calcutta Mathematical Society* 37.3 (1945), pp. 81–91.

[87] T. S. Rappaport, S. Sun, R. Mayzus, H. Zhao, Y. Azar, K. Wang, G. N. Wong, J. K. Schulz, M. Samimi, and F. Gutierrez. "Millimeter Wave Mobile Communications for 5G Cellular: It Will Work!" In: *IEEE Access* 1 (2013), pp. 335–349.

[88] T. S. Rappaport. *Wireless Communications: Principles and Practice*. Prentice Hall PTR, 1996.

[89] M. Rath, K. Witrisal, et al. "Map-based Antenna Adaptation for Multipath-assisted Positioning." paper under preparation. 2021.

[90] A. Richter. "Estimation of Radio Channel Parameters: Models and Algorithms." PhD thesis. Ilmenau University of Technology, 2005.

[91] D. Romero, S. Kim, G. B. Giannakis, and R. López-Valcarce. "Learning Power Spectrum Maps From Quantized Power Measurements." In: *IEEE Transactions on Signal Processing* 65.10 (May 2017), pp. 2547–2560.

[92] F. Rusek, D. Persson, B. K. Lau, E. G. Larsson, T. L. Marzetta, O. Edfors, and F. Tufvesson. "Scaling Up MIMO: Opportunities and Challenges with Very Large Arrays." In: *IEEE Signal Processing Magazine* 30.1 (Jan. 2013), pp. 40–60.

[93] M. Rzymowski, P. Woznica, and L. Kulas. "Single-Anchor Indoor Localization Using ESPAR Antenna." In: *IEEE Antennas and Wireless Propagation Letters* 15 (Nov. 2016), pp. 1183–1186.

[94] I. Santos, J. J. Murillo-Fuentes, and P. M. Djurić. "Recursive Estimation of Dynamic RSS Fields Based on Crowdsourcing and Gaussian Processes." In: *IEEE Transactions on Signal Processing* 67.5 (Mar. 2019), pp. 1152–1162.

[95] S. O. Schmidt, M. Cimdins, and H. Hellbrück. "On the Effective Length of Channel Impulse Responses in UWB Single Anchor Localization." In: *International Conference on Localization and GNSS (ICL-GNSS)*. Nuremberg, Germany, June 2019, pp. 1–6.

[96] A. Shahmansoori, G. E. Garcia, G. Destino, G. Seco-Granados, and H. Wymeersch. “Position and Orientation Estimation Through Millimeter-Wave MIMO in 5G Systems.” In: *IEEE Transactions on Wireless Communications* 17.3 (Mar. 2018), pp. 1822–1835.

[97] G. Shen, Z. Chen, P. Zhang, T. Moscibroda, and Y. Zhang. “Walkie-Markie: Indoor Pathway Mapping Made Easy.” In: *10th USENIX Symposium on Networked Systems Design and Implementation (NSDI 13)*. Lombard, IL, Apr. 2013, pp. 85–98.

[98] Y. Shen and M. Z. Win. “Effect of Path-Overlap on Localization Accuracy in Dense Multipath Environments.” In: *IEEE International Conference on Communications (ICC)*. May 2008, pp. 4197–4202.

[99] Y. Shen and M. Z. Win. “Fundamental Limits of Wideband Localization; Part I: A General Framework.” In: *IEEE Transactions on Information Theory* 56.10 (Oct. 2010), pp. 4956–4980.

[100] Y. Shen and M. Z. Win. “On the Use of Multipath Geometry for Wideband Cooperative Localization.” In: *IEEE Global Telecommunications Conference (GLOBECOM)*. Honolulu, Hawaii, USA, Dec. 2009, pp. 1–6.

[101] Y. Shen, H. Wymeersch, and M. Z. Win. “Fundamental limits of wideband localization - part II: cooperative networks.” In: *IEEE Transactions on Information Theory* 56.10 (Oct. 2010), pp. 4981–5000.

[102] B. Silva, Z. Pang, J. Åkerberg, J. Neander, and G. Hancke. “Experimental Study of UWB-based High Precision Localization for Industrial Applications.” In: *IEEE International Conference on Ultra-WideBand (ICUWB)*. Sept. 2014, pp. 280–285.

[103] S. Sou, W. Lin, K. Lan, and C. Lin. “Indoor Location Learning Over Wireless Fingerprinting System with Particle Markov Chain Model.” In: *IEEE Access* 7 (2019), pp. 8713–8725.

[104] J. J. Spilker Jr. “GPS signal structure and performance characteristics.” In: *Navigation* 25.2 (1978), pp. 121–146.

[105] M. Steinbauer, A. F. Molisch, and E. Bonek. “The double-directional radio channel.” In: *IEEE Antennas and Propagation Magazine* 43.4 (Aug. 2001), pp. 51–63.

[106] C. R. Stevenson, G. Chouinard, Z. Lei, W. Hu, S. J. Shellhammer, and W. Caldwell. “IEEE 802.22: The first cognitive radio wireless regional area network standard.” In: *IEEE Communications Magazine* 47.1 (Jan. 2009), pp. 130–138.

[107] W. Sun, J. Liu, C. Wu, Z. Yang, X. Zhang, and Y. Liu. “MoLoc: On Distinguishing Fingerprint Twins.” In: *IEEE 33rd International Conference on Distributed Computing Systems (ICDCS)*. Philadelphia, PA, USA, July 2013, pp. 226–235.

[108] X. Sun, Y. Ma, J. Xu, J. Zhang, and J. Wang. “A high Accuracy Mono-Station UWB Positioning System.” In: *IEEE International Conference on Ultra-WideBand (ICUWB)*. Sept. 2008, pp. 201–204.

[109] E. Tanghe, D. P. Gaillot, M. Liénard, L. Martens, and W. Joseph. “Experimental Analysis of Dense Multipath Components in an Industrial Environment.” In: *IEEE Transactions on Antennas and Propagation* 62.7 (July 2014), pp. 3797–3805.

[110] R. D. Taranto, S. Muppirisetty, R. Raulefs, D. Slock, T. Svensson, and H. Wymeersch. “Location-Aware Communications for 5G Networks: How location information can improve scalability, latency, and robustness of 5G.” In: *IEEE Signal Processing Magazine* 31.6 (Nov. 2014), pp. 102–112.

[111] Y. Teganya, D. Romero, L. M. L. Ramos, and B. Beferull-Lozano. “Location-Free Spectrum Cartography.” In: *IEEE Transactions on Signal Processing* 67.15 (Aug. 2019), pp. 4013–4026.

[112] J. Tiemann, F. Eckermann, and C. Wietfeld. “ATLAS - An Open-Source TDOA-based Ultra-Wideband Localization System.” In: *International Conference on Indoor Positioning and Indoor Navigation (IPIN)*. Oct. 2016, pp. 1–6.

[113] E. Torkildson, U. Madhow, and M. Rodwell. “Indoor Millimeter Wave MIMO: Feasibility and Performance.” In: *IEEE Transactions on Wireless Communications* 10.12 (Dec. 2011), pp. 4150–4160.

[114] M. Ulmschneider, S. Zhang, C. Gentner, and A. Dammann. “Multipath Assisted Positioning With Transmitter Visibility Information.” In: *IEEE Access* 8 (2020), pp. 155210–155223.

[115] H. L. Van Trees. *Detection, Estimation and Modulation Theory, Part I: Detection, Estimation, and Linear Modulation Theory*. John Wiley & Sons, 1968.

[116] B. Wang and K. J. Liu. “Advances in Cognitive Radio Networks: A Survey.” In: *IEEE Journal of Selected Topics in Signal Processing* 5.1 (Feb. 2011), pp. 5–23.

[117] T. Wilding, S. Grebien, E. Leitinger, U. Mühlmann, and K. Witrisal. “Single-Anchor, Multipath-Assisted Indoor Positioning with Aliased Antenna Arrays.” In: *52nd Asilomar Conference on Signals, Systems, and Computers*. Pacific Grove, CA, USA, Oct. 2018, pp. 525–531.

[118] T. Wilding, S. Grebien, U. Mühlmann, and K. Witrisal. “Accuracy Bounds for Array-Based Positioning in Dense Multipath Channels.” In: *Sensors* 18.12 (Dec. 2018), p. 4249.

[119] M. Z. Win, F. Meyer, Z. Liu, W. Dai, S. Bartoletti, and A. Conti. “Efficient Multisensor Localization for the Internet of Things: Exploring a New Class of Scalable Localization Algorithms.” In: *IEEE Signal Processing Magazine* 35.5 (Sept. 2018), pp. 153–167.

[120] M. Z. Win and R. A. Scholtz. “On the robustness of ultra-wide bandwidth signals in dense multipath environments.” In: *IEEE Communications Letters* 2.2 (Feb. 1998), pp. 51–53.

[121] K. Witrisal, E. Leitinger, S. Hinteregger, and P. Meissner. “Bandwidth Scaling and Diversity Gain for Ranging and Positioning in Dense Multipath Channels.” In: *IEEE Wireless Communications Letters* 5.4 (Aug. 2016), pp. 396–399.

[122] K. Witrisal and P. Meissner. “Performance bounds for multipath-assisted indoor navigation and tracking (MINT).” In: *IEEE International Conference on Communications (ICC)*. Ottawa, ON, Canada, June 2012, pp. 4321–4325.

[123] K. Witrisal, P. Meissner, E. Leitinger, Y. Shen, C. Gustafson, F. Tufvesson, K. Haneda, D. Dardari, A. F. Molisch, A. Conti, and M. Z. Win. “High-Accuracy Localization for Assisted Living: 5G systems will turn multipath channels from foe to friend.” In: *IEEE Signal Processing Magazine* 33.2 (Mar. 2016), pp. 59–70.

[124] C. Wu, Z. Yang, Z. Zhou, Y. Liu, and M. Liu. “Mitigating Large Errors in WiFi-Based Indoor Localization for Smartphones.” In: *IEEE Transactions on Vehicular Technology* 66.7 (July 2017), pp. 6246–6257.

[125] Y. Wu, X. Ren, H. Zhou, Y. Wang, and X. Yi. “A Survey on Multi-Robot Coordination in Electromagnetic Adversarial Environment: Challenges and Techniques.” In: *IEEE Access* 8 (2020), pp. 53484–53497.

[126] Z. Xiao, H. Wen, A. Markham, and N. Trigoni. “Lightweight map matching for indoor localisation using conditional random fields.” In: *Proceedings of the 13th ACM/IEEE International Symposium on Information Processing in Sensor Networks*. IPSN ’14. Berlin, Germany, Apr. 2014, pp. 131–142.

[127] B. Xie, G. Tan, and T. He. “SpinLight: A High Accuracy and Robust Light Positioning System for Indoor Applications.” In: *Proceedings of the 13th ACM Conference on Embedded Networked Sensor Systems*. SenSys ’15. Seoul, South Korea, Nov. 2015, pp. 211–223.

[128] L. Xie, X. Jin, M. Zhou, Y. Wang, and Z. Tian. “Cost-efficient BLE fingerprint database construction approach via multi-quadric RBF interpolation.” In: *EURASIP Journal on Wireless Communications and Networking* 50 (Feb. 2019), pp. 1–15.

[129] Y. Yan and Y. Mostofi. “To Go or Not to Go: On Energy-Aware and Communication-Aware Robotic Operation.” In: *IEEE Transactions on Control of Network Systems* 1.3 (Sept. 2014), pp. 218–231.

[130] H. B. Yilmaz, T. Tugcu, F. Alagöz, and S. Bayhan. “Radio environment map as enabler for practical cognitive radio networks.” In: *IEEE Communications Magazine* 51.12 (Dec. 2013), pp. 162–169.

[131] F. Yin and F. Gunnarsson. “Distributed Recursive Gaussian Processes for RSS Map Applied to Target Tracking.” In: *IEEE Journal of Selected Topics in Signal Processing* 11.3 (Apr. 2017), pp. 492–503.

[132] R. Zetik, J. Sachs, and R. S. Thomä. “UWB short-range radar sensing - The architecture of a baseband, pseudo-noise UWB radar sensor.” In: *IEEE Instrumentation & Measurement Magazine* 10.2 (Apr. 2007), pp. 39–45.

[133] H. Zhang, X. Cui, B. An, and T. A. Gulliver. “A Distance and Angle Estimated Method based on Single UWB Station.” In: *Proceedings of the International Conference on Signal Processing, Communication and Computing (ICSPCC)*. Aug. 2013, pp. 1–6.

[134] J. Zhang, P. V. Orlik, Z. Sahinoglu, A. F. Molisch, and P. Kinney. “UWB Systems for Wireless Sensor Networks.” In: *Proceedings of the IEEE* 97.2 (Feb. 2009), pp. 313–331.

[135] Q. Zhao and B. M. Sadler. “A Survey of Dynamic Spectrum Access.” In: *IEEE Signal Processing Magazine* 24.3 (May 2007), pp. 79–89.

[136] Y. Zhao, B. Le, and J. H. Reed. “Chapter 11 - Network Support: The Radio Environment Map.” In: *Cognitive Radio Technology*. Ed. by B. A. Fette. Burlington: Newnes, 2006, pp. 337–363.

[137] B. Zhou, M. Elbadry, R. Gao, and F. Ye. “BatTracker: High Precision Infrastructure-Free Mobile Device Tracking in Indoor Environments.” In: *Proceedings of the 15th ACM Conference on Embedded Network Sensor Systems*. SenSys ’17. Delft, Netherlands: Association for Computing Machinery, Nov. 2017.

Part II.

Included Papers

SALMA: UWB-based Single-Anchor Localization System using Multipath Assistance

Bernhard Großwindhager*, Michael Rath*, Josef Kulmer, Mustafa S. Bakr,
Carlo Alberto Boano, Klaus Witrisal, and Kay Römer

published in the 16th ACM Conference on Embedded Networked Sensor Systems
(SenSys 2018)

Abstract

Setting up indoor localization systems is often excessively time-consuming and labor-intensive, because of the high amount of anchors to be carefully deployed or the burdensome collection of fingerprints. In this paper, we present SALMA, a novel low-cost UWB-based indoor localization system that makes use of only one anchor and that does neither require prior calibration nor training. By using only a crude floor plan and by exploiting multipath reflections, SALMA can accurately determine the position of a mobile tag using a single anchor, hence minimizing the infrastructure costs, as well as the setup time. We implement SALMA on off-the-shelf UWB devices based on the Decawave DW1000 transceiver and show that, by making use of multiple directional antennas, SALMA can also resolve ambiguities due to overlapping multipath components. An experimental evaluation in an office environment with clear line-of-sight has shown that 90% of the position estimates obtained using SALMA exhibit less than 20 cm error, with a median below 8 cm. We further study the performance of SALMA in the presence of obstructed line-of-sight conditions, moving objects and furniture, as well as in highly dynamic environments with several people moving around, showing that the system can sustain decimeter-level accuracy with a worst-case average error below 34 cm.

---

[*] authors contributed equally to this work

1 Introduction

Localizing people and objects in a precise and accurate way is a key requirement for future location-aware Internet of Things (IoT) applications such as assisted living [1], health care [2], and robot navigation [3, 4]. As of today, achieving an accurate position estimation is still a grand challenge especially *indoors*, where global navigation satellite systems such as GPS, Galileo, GLONASS, and Beidou are not applicable due to the limited signal reception [5].

Challenges of indoor positioning. When estimating the position of a device indoors, one needs to deal with severe *attenuation, multipath, and scattering* of signals due to walls, furniture, or other surrounding objects. This is, for example, a major challenge for localization systems making use of narrowband RF technologies: solutions based on IEEE 802.15.4 [6, 7], Bluetooth [8, 9], and Wi-Fi [10, 11] are indeed highly susceptible to multipath fading, and can hardly achieve a sub-meter accuracy in these settings [12].

Indoor environments are also *highly dynamic*: moving people and objects may obstruct the line-of-sight (LOS) path between a source and a receiver. This is, for example, particularly challenging for localization systems based on optical technologies. Furthermore, the unpredictable presence of interference sources (e.g., co-located wireless devices using the same frequency band) can cause loss of information and fluctuations in the received signal strength that drastically affect the accuracy of positioning algorithms.

A practical localization system needs to achieve a high positioning accuracy despite these inherent properties of indoor environments. This task is further complicated by the fact that an ideal indoor localization system should maximize the accuracy, efficiency, and responsiveness of position estimation, while *minimizing deployment efforts and costs.* Although a plethora of distinct approaches has been proposed in the literature, none of them can yet achieve a high accuracy at minimal costs and is thus widely accepted [13].

Deployment overhead still too high. After comparing the performance of more than 100 state-of-the-art indoor localization systems under the same settings, Lymberopoulos and Liu [13] have concluded that the set-up procedure of existing solutions is excessively *time-consuming* and *labor-intensive.* As a consequence, the use of most systems is still impractical in real-world deployments.

This state of affairs represents a serious problem, because recent solutions based on Ultra-wideband (UWB) could easily achieve accuracies in the order of decimeters [4, 14]. However, one cannot fully exploit this outstanding positioning accuracy, because of the high overhead in deploying the required infrastructure. These systems employ indeed multiple anchors (e.g., at least 8 [15], 9 [16], or 15 [4]), each of which needs to be carefully placed [17] in order to maximize the system's performance – a burden that is not sustainable on a large scale. Similarly, localization systems based on RSS profiling [11, 18] require a laborious offline data collection process before deployment to acquire the radio maps (fingerprints). Even worse, fingerprinting needs to be frequently repeated to cope with environmental changes, such as furniture setup and human motion: this makes the installation costs prohibitively high.

Minimizing the deployment effort of localization systems while still allowing to sustain a high positioning accuracy is hence a long-due fundamental step towards the creation of solutions that are viable for real-world IoT applications.

Contributions. In this paper we present SALMA, a novel UWB-based indoor localization system that can sustain a decimeter-level accuracy despite the use of only a *single* anchor. SALMA removes the need of multiple anchors by exploiting multipath propagation, i.e., specular reflections originating from static objects. The system works out of the box without any time-consuming setup phase, as it does not require any prior calibration, training, or position estimates (i.e., SALMA is based on neither fingerprinting nor other learning algorithms). All that is needed is a crude floor plan showing the geometry of the building in which the system is installed. The map includes static objects such as walls and windows only, to avoid adaptations if furniture or other objects are moved.

Starting from this floor plan and the known location and orientation of the anchor, SALMA models the theoretical multipath propagation and compares it with the estimated channel impulse response (CIR) derived by the anchor node, as shown in Sect. 3. Exploiting the position-related information embedded in the CIR allows to unambiguously determine the position of a tag using a single anchor with an accuracy comparable to the one achieved by common multi-anchor UWB systems. This way, SALMA reduces the infrastructure costs and setup time, hence addressing the omnipresent trade-off between accuracy and deployment costs.

We implement SALMA on off-the-shelf UWB devices based on the popular Decawave DW1000 transceiver, building – to the best of our knowledge – the *first* low-cost single-anchor UWB-based indoor localization system. In particular, as shown in Sect. 4, we support multiple tags simultaneously and shift the burden of position estimation to the anchor node. This allows to keep the design of the mobile tag simple, so to preserve its limited battery capacity.

We specifically implement SALMA for two-dimensional settings in order to support map-based navigation and tracking applications such as locating patients in hospitals [19], assistance for visually impaired, disabled, and elderly people [1,20–22], as well as monitoring sport events [23,24]. The applicability to three-dimensional settings and the resulting challenges are discussed in Sect. 8.

We further show how overlapping multipath components (MPCs) may limit the performance of SALMA when using a single omni-directional antenna. To alleviate this problem, we illustrate in Sect. 5 how to improve the robustness of SALMA using *multiple directional antennas*. The latter enable the exploration of the angular information of MPCs to enhance the system's performance remarkably.

In Sect. 6, we carry out a thorough experimental evaluation[1] of the performance of SALMA in an office environment with clear LOS conditions. Among others, our results reveal that 90% of position estimates obtained with SALMA exhibit less than 20 cm error, with a median below 8 cm. This performance was obtained with a single measurement snapshot from four directional antennas. We further simulate how the accuracy of SALMA can be improved with a higher number of antennas with narrower bandwidth.

In Sect. 7, we study the performance of SALMA in the presence of *obstructed LOS*, showing that 90% of position estimates exhibit less than 30 cm error, with a median below 15 cm. Furthermore, we evaluate SALMA in a challenging setting (stockroom) reaching a 90% error of 44.5 cm, and show that moving objects and furniture has a limited effect on the performance. We also deploy SALMA in an office crowded with tens of people moving in/out across 24-hours, and show that – even in such a highly dynamic environment – SALMA sustains a worst-case average error below 34 cm. Therefore, by exploiting the redundancy offered by multipath reflections, SALMA achieves a high accuracy even with obstructed LOS, addressing an inherent vulnerability of traditional systems.

In summary, this paper makes the following contributions:

---

[1] All datasets are publicly accessible under `http://www.iti.tugraz.at/SALMA` [25].

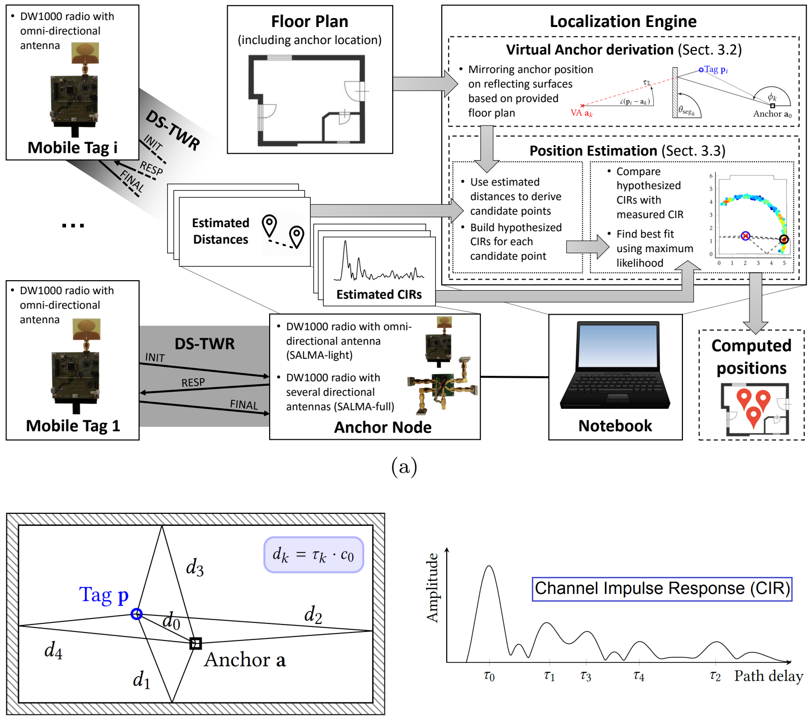

(a)

(b)

Figure 1: Overview of SALMA's design (a): the system makes use of the multipath propagation between a single anchor and a tag i. The multipath propagation is characterized by the estimated CIR containing position-related information (b).

- We present SALMA, a UWB-based indoor localization system making use of only a single anchor and requiring neither prior profiling nor calibration (Sect. 3);
- We implement SALMA on off-the-shelf UWB devices and support multiple tags simultaneously (Sect. 4);
- We increase the robustness of the system to overlapping MPCs by using multiple directional antennas (Sect. 5);
- We evaluate the performance of SALMA experimentally in different scenarios with clear LOS and show that 90% of position estimates exhibit less than 20 cm error (Sect. 6);
- We show that SALMA is resilient to obstructed LOS situations and that it sustains a high accuracy even in dynamic environments with objects and people moving around (Sect. 7).

2 SALMA: Overview

Fig. 1a shows a sketch of SALMA's design. The system consists of a single anchor (fixed infrastructure) and multiple battery-powered mobile tags (devices to be localized). The anchor is connected to and powered by a central notebook running a *localization engine* that computes the position of each tag.

Every tag initiates a double-sided two-way ranging (DS-TWR) with the anchor node, following a time division multiple access scheme. The two-way ranging process allows the anchor to estimate the distance $d_0 = \|\mathbf{p} - \mathbf{a}\|$, with $\mathbf{p}$ and $\mathbf{a}$ being the tag and the anchor location, respectively (Fig. 1b). Upon completion of the DS-TWR process, the anchor records the estimated distance $\hat{d_0}$, as well as an estimate of the channel impulse response (CIR) provided by the UWB transceiver, and forwards this info to the localization engine.

Exploiting multipath propagation. The CIR embeds information about the multipath propagation consisting of reflections from walls. Traditional UWB localization systems employ the CIR to estimate the distance d_0, which is related to the path delay τ_0 as follows: $d_0 = \tau_0 \cdot c_0$, with c_0 being the speed of light. Therefore, these systems only use the path delay τ_0, and forgo remaining multipath components (MPCs). SALMA, instead, additionally uses delays of reflected multipath components, which contain additional geometric information (cf. τ_k and d_k in Fig. 1b for $k = 1, \ldots, 4$).

Localization engine. Starting from a floor plan showing the geometry of the building in which the system is installed[2], and the known location of the anchor, SALMA models the theoretical multipath propagation by employing the concept of virtual anchors [26] and by building a hypothesized CIR for several candidate positions. The latter are selected on a circle of radius $\hat{d_0}$ centered in $\mathbf{a}$, with $\hat{d_0}$ being the estimated distance derived from the DS-TWR. The localization engine then compares the hypothesized CIR of each candidate point with the one measured through the DS-TWR process, and returns the best fit using maximum likelihood estimation.

As we will show in the next sections, exploiting the position-related information encoded in the MPCs allows to unambiguously and accurately determine the position of a tag using a single anchor.

3 SALMA: design principles

We describe next the mathematical principles behind the functional stages of SALMA, showing how the system can leverage the information that is contained in the observed CIR to accurately narrow down the tag position. First, we present a model of the observed CIR including the multipath component (MPC) parameters in Sect. 3.1. We then explain in Sect. 3.2 how to use the known anchor position and floor plan to determine *virtual anchors* that can relate the tag position to parameters embedded in the CIR. Third, we describe in Sect. 3.3 how these parameters are used in combination with the observed CIR to obtain a position estimate. Sect. 4 then outlines how these methods are implemented on off-the-shelf hardware.

3.1 Signal model

Taking advantage of multipath propagation requires its proper modeling. In the following, we introduce the signal model relating the effective system response

---

[2] While furniture and other objects do affect the performance of the system, the impact stays in reasonable bounds as demonstrated in Sect. 6 and 7. Thus, there is no need to keep track of whether tables, shelves, or other furniture have moved.

(i.e., the observed CIR) and the parameters of multipath components. We assume that a tag is equipped with a single omni-directional antenna, while the anchor can carry M antennas. Each antenna with index $m = 1, \dots, M$ is characterized with its beampattern $b_m(\phi)$. The observed CIR $r_m(t)$ between a single tag and the anchor's m^{th} antenna can be modeled as:

$$r_m(t) = \sum_{k=0}^{K} \alpha_k b_m(\phi_k) s_{\text{DW}}(t - \tau_k) + w_m(t). \tag{1}$$

The first term on the right-hand-side describes K specular MPCs, i.e., dominant reflections, of the transmitted signal $s_{\text{DW}}(t)$. The latter includes de-spreading and filtering at the receiver. Each MPC is characterized by its complex-valued amplitude α_k, angle of departure ϕ_k and delay τ_k. These MPCs are resulting from reflections at flat surfaces such as walls, windows or doors and will be further discussed in Sect. 3.2. The last term $w_m(t)$ denotes zero-mean white Gaussian measurement noise with variance σ_w^2. Note that the proposed signal model in (1) can model single omni-directional as well as multiple directional antenna measurements.

The signal $r_m(t)$ is sampled with frequency $f_{\text{s}} = 1/T_{\text{s}}$ and N_s samples are acquired. Hence, we use vector notation [27, 28] to compactly describe the signal model in (1) as:

$$\boldsymbol{r} = \boldsymbol{X}(\boldsymbol{\tau}, \boldsymbol{\phi})\boldsymbol{\alpha} + \boldsymbol{w} \tag{2}$$

with

$$\begin{bmatrix} \boldsymbol{r}_1 \\ \vdots \\ \boldsymbol{r}_M \end{bmatrix} = \begin{bmatrix} \boldsymbol{X}_1(\boldsymbol{\tau}, \boldsymbol{\phi}) \\ \vdots \\ \boldsymbol{X}_M(\boldsymbol{\tau}, \boldsymbol{\phi}) \end{bmatrix} \boldsymbol{\alpha} + \begin{bmatrix} \boldsymbol{w}_1 \\ \vdots \\ \boldsymbol{w}_M \end{bmatrix} \tag{3}$$

and

$$\begin{aligned} \boldsymbol{r}_m &= [r_m(0 \cdot T_{\text{s}}), \dots, r_m([N_s - 1] \cdot T_{\text{s}})]^{\text{T}} \\ \boldsymbol{X}_m(\boldsymbol{\tau}, \boldsymbol{\phi}) &= [b_m(\phi_0)\boldsymbol{s}(\tau_0) \dots b_m(\phi_K)\boldsymbol{s}(\tau_K)] \\ \boldsymbol{s}(\tau_k) &= [s_{\text{DW}}(0 \cdot T_{\text{s}} - \tau_k), \dots, s_{\text{DW}}([N_s - 1] \cdot T_{\text{s}} - \tau_k)]^{\text{T}} \\ \boldsymbol{w}_m &= [w_m(0 \cdot T_{\text{s}}), \dots, w_m([N_s - 1] \cdot T_{\text{s}})]^{\text{T}} \\ \boldsymbol{\phi} &= [\phi_0, \dots, \phi_K]^{\text{T}};\ \boldsymbol{\tau} = [\tau_0, \dots, \tau_K]^{\text{T}};\ \boldsymbol{\alpha} = [\alpha_0, \dots, \alpha_K]^{\text{T}}. \end{aligned}$$

Thus, the proposed signal model connects the MPC parameters $(\alpha_k, \phi_k, \tau_k)$ with the expected CIR. In Sect. 3.2, we relate these parameters to the tag position.

3.2 Geometric model and virtual anchors

The MPC parameters of the CIR contain position-related information regarding the tag location as well as the environment [29]. Following Euclidean geometry, simple relations can be obtained for ϕ_k and τ_k. In particular, we employ the concept of virtual anchors (VAs) [26] in order to relate MPC parameters to the tag positions (see Fig. 2). To obtain the positions of the virtual anchors $\mathbf{a}_k$ $(k > 0)$, the position of the physical anchor $\mathbf{a}_0 \triangleq \mathbf{a}$ is mirrored at each reflective flat surface. Fig. 2 illustrates the top-view of a single reflection. A specular MPC (black solid) originates at the wall segment. Assignment of the specular MPC to a virtual anchor (red cross) enables an efficient calculation of the MPC parameters, delay, and angle.

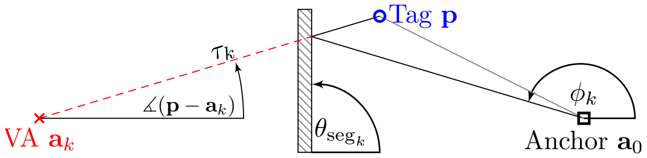

Figure 2: The concept of virtual anchors (VA) and its use in calculating the angle of departure ϕ_k and delay τ_k.

The delay τ_k follows as geometric distance between tag and VA, divided by the speed of light c_0, according to

$$\tau_k = \frac{1}{c_0}\|\mathbf{p}-\mathbf{a}_k\|. \tag{4}$$

We describe the angle of departure ϕ_k via the azimuth angle between tag and VA $\measuredangle(\mathbf{p}-\mathbf{a}_k)$ according to

$$\phi_k = 2\,\theta_{\text{seg}_k} - \measuredangle(\mathbf{p}-\mathbf{a}_k). \tag{5}$$

Here, θ_{seg_k} denotes the angle of the involved reflective surface that was used to generate the VA $\mathbf{a}_k$ (see Fig. 2).

Note that, in this work, we limit the multipath propagation to *single-bounce* reflections, i.e., only a single reflective object is bounced during the path's propagation. Hence, the number of considered surfaces also determines the number of used MPCs K and VAs, e.g., for the floorplan shown in Fig. 1b we set $K = 4$ resulting in four VAs. In principle, the virtual anchor model can be extended to cover higher-order reflections as well. However, higher-order reflections are attenuated strongly, due to their increased path length and additional reflection losses. It should be also noted that, for each tag position $\mathbf{p}$, the visibility of the VAs has to be taken into account. This means that we have to check the direct path from $\mathbf{p}$ to the VA position $\mathbf{a}_k$ for intersections with any obstacles or wall segments. Only if there is a single involved intersection with the correct wall segment, we can use the k-th MPC in the signal model.

While the parameters τ_k and ϕ_k can be directly derived from the geometric model using the known VAs, a proper model for the MPC amplitudes α_k is difficult to obtain [28]. Hence, we propose to treat α_k as nuisance parameter, estimated directly from the observation $\boldsymbol{r}$.

3.3 Position estimation

In the following, we present a position estimator based on the CIR measurements. We aim for a maximum likelihood (ML) estimator, derived from the signal model in (2). To allow efficient computations, we assume complex-valued white Gaussian measurement noise $\boldsymbol{w}$. The likelihood $p(\boldsymbol{r}|\mathbf{p})$ of observation $\boldsymbol{r}$ conditioned on tag position $\mathbf{p}$ follows as:

$$p(\boldsymbol{r}|\mathbf{p}) = \left(\tfrac{1}{\pi\sigma_w^2}\right)^{MN_s} \exp\left\{-\tfrac{1}{\sigma_w^2}\|\boldsymbol{r}-\boldsymbol{X}(\boldsymbol{\tau},\boldsymbol{\phi})\boldsymbol{\alpha}\|^2\right\} \tag{6}$$

where $\boldsymbol{\tau}$ and $\boldsymbol{\phi}$ are related to the tag position via (4) and (5). Taking the log of (6) results in the log-likelihood function

$$\log p(\boldsymbol{r}|\mathbf{p}) = -MN_s\log(\pi\sigma_w^2) - \tfrac{1}{\sigma_w^2}\|\boldsymbol{r}-\boldsymbol{X}(\boldsymbol{\tau},\boldsymbol{\phi})\boldsymbol{\alpha}\|^2. \tag{7}$$

This function depends on MPC amplitudes $\boldsymbol{\alpha}$. We propose to estimate $\boldsymbol{\alpha}$ as least squares solution [28] according to

$$\hat{\boldsymbol{\alpha}} = (\boldsymbol{X}^{\mathrm{H}}(\boldsymbol{\tau},\boldsymbol{\phi})\boldsymbol{X}(\boldsymbol{\tau},\boldsymbol{\phi}))^{-1}\boldsymbol{X}^{\mathrm{H}}(\boldsymbol{\tau},\boldsymbol{\phi})\boldsymbol{r} \tag{8}$$

with $(\cdot)^{\mathrm{H}}$ denoting the conjugate and transposed. The position estimate $\hat{\mathbf{p}}$ maximizing the log-likelihood function can be formulated as a non-linear optimization problem:

$$\hat{\mathbf{p}} = \underset{\mathbf{p}\in\mathcal{P}}{\operatorname{argmax}} \log p(\boldsymbol{r}|\mathbf{p}) = \underset{\mathbf{p}\in\mathcal{P}}{\arg\min} \|\boldsymbol{r} - \boldsymbol{X}(\boldsymbol{\tau},\boldsymbol{\phi})\hat{\boldsymbol{\alpha}}\|^2. \tag{9}$$

The parameters $\boldsymbol{\tau}$ and $\boldsymbol{\phi}$ are determined via the geometry, and these parameters in turn build the hypothesized CIR $\boldsymbol{X}(\boldsymbol{\tau},\boldsymbol{\phi})\hat{\boldsymbol{\alpha}}$, which is compared to the observed CIR $\boldsymbol{r}$. The position for which the hypothesis comes closest to the observation (and thus maximizes the likelihood) is chosen as the position estimate $\hat{\mathbf{p}}$. Searching for a global maximum requires to evaluate (9) at each feasible tag position $\mathcal{P}$, i.e., all positions within the communication range to the anchor. As shown in [27], this exhaustive search can be limited to potential candidate points that are located along a circle around $\mathbf{a}$ with radius $\hat{d}_0$. We consider N_C candidate points $\mathcal{P} = \{\mathbf{p}^{(j)}\}_{j=1}^{N_C}$ where each point is drawn independently with Gaussian distributed radius $d^{(j)} \sim \mathcal{N}(\hat{d}_0, \sigma^2_{\mathrm{DW}})$ and uniformly distributed angle $\phi^{(j)} \sim \mathcal{U}(0, 2\pi)$ [27]. Candidate points lying outside of the room are discarded. These can be determined with simple line equation tests using the given floor plan. The number of candidate points N_C has a direct impact on the accuracy of the found estimate (9) and will be studied in Sect. 6.3.

4 Implementation on Off-the-Shelf Devices

We implement SALMA on off-the-shelf UWB devices. After introducing the hardware in Sect. 4.1, we sketch the scheme used to derive the distance between the tag and anchor as well as the CIR $\boldsymbol{r}_m$ in Sect. 4.2. We then illustrate how the system can support multiple tags in Sect. 4.3 and describe the implementation of the position estimation in Sect. 4.4.

4.1 Hardware

The system consists of Decawave EVB1000 platforms used for both anchor and tags (Fig. 3a). These platforms employ the low-cost IEEE 802.15.4-compliant UWB transceiver DW1000 [30]. The tags are battery-powered and can be moved around freely. The anchor, instead, is located at a fixed position $\mathbf{a}$ and is connected to a notebook running MATLAB. The antenna at the tag is a self-made linearly polarized omni-directional dipole antenna (Fig. 3b), but any off-the-shelf omni-directional UWB antenna is suitable. At the anchor, instead, we employ either a single omni-directional antenna (Sect. 4.4) or multiple directional antennas (Sect. 5.2).

Transmitted pulse shape. The proposed signal model in (1) requires a known transmitted pulse shape $s_{\mathrm{DW}}(t)$. The IEEE 802.15.4-2015 standard allows the generation of an arbitrary pulse shape, as long as it fulfills certain requirements on its cross-correlation with a standard reference signal, a root raised cosine pulse with a roll-off factor of $\beta = 0.5$ [31]. Decawave follows the IEEE 802.15.4-2015 standard, but does not provide information regarding the transmitted signal of the

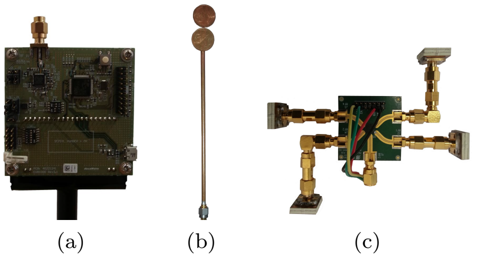
(a) (b) (c)

Figure 3: Decawave EVB1000 node (a) with self-made omni-directional dipole antenna (b) and switchable directional antenna system employed in Sect. 5.2 (c).

DW1000. Therefore, we identify $s_{\text{DW}}(t)$ in a measurement campaign. We place a transmitter and receiver 1 m apart from each other in clear LOS conditions. The receiver logs 1000 CIRs. In a post-processing step, we separate the LOS from the CIR and calculate an average over these signals, which defines the transmitted pulse shape $s_{\text{DW}}(t)$ of the DW1000.

4.2 Acquiring CIR and ranging

As shown in Fig. 1a, the localization engine of SALMA requires to estimate the distance $\hat{d}_0$ between the tag and the anchor, and to derive information about the multipath propagation by acquiring the CIR provided by the DW1000.

Two-way ranging. Due to the missing synchronization between anchor and tags, we employ a double-sided two-way ranging scheme (DS-TWR) to estimate the distance $\hat{d}_0 = \|\mathbf{p} - \mathbf{a}\|$ between each tag and the anchor (see Fig. 4). The DS-TWR scheme consists of three messages, each of which contains an 11-byte MAC header embedding source and destination address, as well as a 16-bit checksum. The payload of the first message (*INIT*) and the second message (*RESP*) is 1 byte long (`MSG_ID`). The last message (*FINAL*) is 16 bytes long and contains the message ID as well as three 5-byte timestamps [32]. The uncalibrated distance $\hat{d}_{\text{TWR}}$ is calculated in the DS-TWR scheme with [33, pp. 213]:

$$\hat{d}_{\text{TWR}} = \frac{T_{round1} \cdot T_{round2} - T_{reply1} \cdot T_{reply2}}{T_{round1} + T_{round2} + T_{reply1} + T_{reply2}} \tag{10}$$

To calibrate the distance estimate, we perform 5000 DS-TWR trials between the anchor and a tag placed 2 m apart from each other. The derived variance and mean of the difference between the reported distance $\hat{d}_{\text{TWR}}$ and the true distance $d_0 = 2\,\text{m}$ is $\sigma^2_{\text{DW}} = (0.054\,\text{m})^2$ and $\mu = 0.26\,\text{m}$, respectively. Hence, the calibrated distance estimate follows as $\hat{d}_0 = \hat{d}_{\text{TWR}} - \mu$. The distance $\hat{d}_0$ and the variance σ^2_{DW} define the distribution of the candidate points around the anchor, as shown in Sect. 3.3.

Acquisition of CIR. Besides deriving the distance $\hat{d}_0$ between anchor and tag, the anchor acquires the CIR $\boldsymbol{r}_m$ from the *FINAL* message received from the tag. Fig. 1b illustrates an exemplary $\boldsymbol{r}_m$. The sampling period is set to $T_{\text{s}} = 1/f_{\text{s}} = 1/(2 \cdot 499.2\,\text{MHz}) = 1.0016\,\text{ns}$. Each sample consists of a 16-bit real integer and a 16-bit imaginary integer resulting in a total size of 4048 Bytes. To reduce the amount of data read via SPI from the DW1000, we limit the length of the CIR to $N_s = 100$ samples.

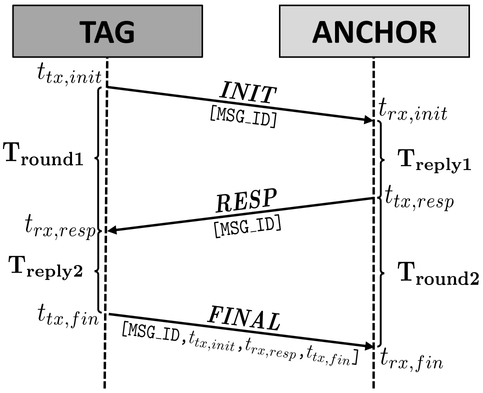

Figure 4: Double-sided two-way ranging scheme.

Having the tags initiate the DS-TWR lets the anchor receive the required information to run the localization algorithm (i.e., the *INIT* and *FINAL* message). At the same time, it also allows to shift the burden on the anchor, which is typically static and much more powerful than tags, as it is line-powered and connected to a backbone localization engine that performs the CPU-intensive calculations. This is advantageous in real-world deployments, as tags are able to control the position update rate based on their energy budget. For example, by equipping a tag with an accelerometer, one can initiate a position update only in case of a movement, and remain in low-power mode otherwise.

4.3 Supporting multiple tags

We have so far considered only a single tag placed at an unknown position $\mathbf{p}$. SALMA can support up to N_t tags placed at positions $\mathbf{p}_i$ (with $i = 1...N_t$) by employing a slotted ALOHA scheme. The duration of a time-slot is related to the computation time necessary to obtain a position estimate (evaluated experimentally in Sect. 6.4) plus a guard interval of 1 ms at the start/end of each time-slot to overcome mis-alignments due to clock drifts.

In our current implementation, the anchor periodically broadcasts beacon messages embedding information about the time-slots' occupancy every 30 seconds[3]. Tags are not assigned to specific time-slots, but have instead the freedom to use any of the unoccupied ones: this enables a tag to use several time-slots in case it requires a higher update rate. In principle, this scheme may lead to collisions if two tags pick the same time-slot. This is, however, a well-known issue that has been largely studied in RFID systems where the reader sends a request and tags pick a random slot to answer [34, 35]. Existing anti-collision schemes can be readily applied also in SALMA. For example, the anchor can monitor the number of occupied slots and adjust their number accordingly, or adapt the slot duration by changing the number of candidate points.

---

[3] Due to the stable clock of the EVB1000 board (10 ppm), an even higher interval between beacon messages can be safely selected.

4.4 SALMA-light: Position estimation using omni-directional antennas

After the anchor has acquired the estimated distance $\hat{d}_0$ and the CIR $\boldsymbol{r}_m$, SALMA needs to carry out the position estimation as described in Sect. 3.3. We provide a first implementation of such a position estimation by equipping the anchor node with a single omni-directional antenna: we call this implementation *SALMA-light*. When using a single antenna, only a single CIR observation is available, which greatly simplifies the signal model from (3) with $M = 1$.

Obtaining a position estimate. We use $\hat{d}_0$ to obtain candidate points, as described in Sect. 3.3. At each candidate point, only the MPC delays τ_k are calculated using (4), since the beampattern has no effect on the estimate. The amplitude estimate from (8) requires a computationally demanding matrix inversion, and, in the case of overlapping MPCs, the matrix might not even be invertible. Hence, we approximate the log-likelihood value from (9) iteratively [27]:

$$\begin{aligned} \text{init} : \boldsymbol{r}^{(0)} &= \boldsymbol{r} \\ \text{for } k = 1 \dots K : \alpha_k &= \boldsymbol{s}^{\mathrm{H}}(\tau_k)\boldsymbol{r}^{(k-1)} && (11) \\ \boldsymbol{r}^{(k)} &= \boldsymbol{r}^{(k-1)} - \alpha_k \boldsymbol{s}(\tau_k) && (12) \end{aligned}$$

Essentially, we take the observed CIR $\boldsymbol{r}$ and sequentially subtract sub-hypotheses $(\alpha_k \boldsymbol{s}(\tau_k))$ by using pulses shifted to the respective τ_k and weighted by single amplitude estimates α_k. The resulting $\boldsymbol{r}^{(K)}$ is then the left-over ‘residual’ signal. The latter represents how similar the hypothesized and measured CIRs are, and is thus used as an approximation of the log-likelihood. This procedure is repeated for each candidate point and the one with highest log-likelihood value is chosen to be the tag position estimate $\hat{\mathbf{p}}$.

Limitation: multipath ambiguities. While this method is simple, the non-accessible beampattern restricts the algorithm to delay information only. This restriction makes the algorithm sensitive to overlapping MPCs, as well as to ambiguities in the delay times of MPCs, which may degrade the positioning performance significantly, as shown in Sect. 6.2.

5 Tackling multipath ambiguities

As discussed in Sect. 4.4, SALMA-light uses measurements from a single antenna only, which makes the algorithm sensitive to overlapping MPCs and ambiguities. In this section, we introduce *SALMA-full*: an enhanced version of the system in which the anchor makes use of multiple switchable directional antennas[4]. Hence, we may now take advantage of the full signal model from (3), where each antenna m is characterized by its beampattern $b_m(\phi)$ covering one sector of the azimuth plane.

The combined observations of the antennas enable the system to separate closely-arriving MPCs in the spatial domain. However, the combination of several antenna measurements requires phase-coherency between the measurements, which is not given by low-cost transceivers. In the following, we tackle the phase-coherency issue (Sect. 5.1), describe how to carry out position estimation using directional antennas (Sect. 5.2), and highlight the key differences in the employed hardware compared to SALMA-light (Sect. 5.3).

---

[4] This system was showcased at SenSys’17 [36].

5.1 Non-phase-coherent amplitude estimates

Phase-coherency demands accurate radio clocks, which are not provided by off-the-shelf UWB transceivers like the DW1000. In our case, this affects the implementation of the presented amplitude estimates in (8). Inaccurate clocks between consecutive measurements are perceived as a phase change in the baseband-equivalent CIR. Thus, amplitude estimates from consecutive measurements differ in their complex-valued phase $\alpha_{k,m} \approx e^{j\varphi}\alpha_{k,m'}$, where φ denotes the unknown phase offset. However, the unkown phase offset φ is required for the position estimate in (9).

To overcome the necessity of phase coherency, we follow the approach presented in [28]. Assuming non-overlapping MPCs ($\boldsymbol{s}(\tau_k)^H\boldsymbol{s}(\tau_k) \approx 0$), an MPC amplitude α_k can be estimated independently as projection of the normalized signal $\frac{\boldsymbol{s}^{\mathrm{H}}(\tau_k)}{\boldsymbol{s}^{\mathrm{H}}(\tau_k)\boldsymbol{s}(\tau_k)}$ onto the m-th measurement $\boldsymbol{r}_m$ according to

$$\alpha_{k,m} = \frac{\boldsymbol{s}^{\mathrm{H}}(\tau_k)\,\boldsymbol{r}_m}{\boldsymbol{s}^{\mathrm{H}}(\tau_k)\boldsymbol{s}(\tau_k)}. \tag{13}$$

Furthermore, the amplitude estimate in (8) can be written as complex-valued average. Relaxing the complex-valued weighted average by an absolute-valued average [37] results in an estimate of the k-th MPC amplitude α_k^{avg} according to

$$\alpha_k^{\mathrm{avg}} = \frac{\sum\limits_{m=1}^{M} |\alpha_{k,m}| \cdot |b_m(\phi_k)|^2}{\sum\limits_{m'=1}^{M} |b_{m'}(\phi_k)|^2}. \tag{14}$$

The remaining phase $\angle\alpha_{k,m}$ is extracted from the individual antenna measurements and the amplitude estimate $\hat{\alpha}_{k,m}^{\mathrm{avg}}$ of the m-th antenna and k-th MPC results in

$$\hat{\alpha}_{k,m}^{\mathrm{avg}} = \alpha_k^{\mathrm{avg}} \exp(j\angle\alpha_{k,m}). \tag{15}$$

This approximation combines MPC amplitudes from non-phase-coherent measurements, taking into account the directivity of the M antennas.

5.2 SALMA-full: position estimation using directional antennas

In contrast to SALMA-light, SALMA-full collects observations from M directional antennas. The antennas are physically separated (see Fig. 3c), which results in different range estimates from tag to each antenna. Since this difference is smaller than the standard deviation of the DW1000 ranging, this error can be neglected. However, to create the candidate points as described in Sect. 3.3, we use the mean value of all ranges.

For each candidate point, the MPC parameters $\boldsymbol{\tau}$ and $\boldsymbol{\phi}$ are calculated using the VA positions in (4) and (5), respectively. For the amplitude estimates, the same iterative approach is followed as in Sect. 4.4, but it is adapted to use the stacked observed CIRs $\boldsymbol{r} = [\boldsymbol{r}_1^{\mathrm{T}}, \ldots, \boldsymbol{r}_M^{\mathrm{T}}]^{\mathrm{T}}$ and to take the non-coherent amplitude estimates from the previous section into account. For this, in the iteration step (11), we use α_k^{avg} from (14), and for step (12), we use

$$\boldsymbol{r}_m^{(k)} = \boldsymbol{r}_m^{(k-1)} - b_m(\phi_k)\hat{\alpha}_{k,m}^{\mathrm{avg}}\boldsymbol{s}(\tau_k).$$

This gives us a (stacked) residual $\boldsymbol{r}^{(K)} = \left[(\boldsymbol{r}_1^{(K)})^{\mathrm{T}}, \ldots, (\boldsymbol{r}_M^{(K)})^{\mathrm{T}}\right]^{\mathrm{T}}$ representing the similarity between the hypothesized and measured CIR that is used as an approximation for the log-likelihood. The final estimate $\hat{\mathbf{p}}$ is obtained by evaluating the log-likelihood for each candidate point and by picking the one achieving the maximum.

Two aspects are worth of note regarding the beampatterns $b_m(\phi)$ of the antennas: first, we use 36 sampled values $b_m(i \cdot \Phi_s)$ with a spacing of $\Phi_s = 10°$ obtained from a measurement campaign. Second, when the anchor is employed, it can be oriented with $\Phi_o = j \cdot 10°$, where j might be chosen as desired. For the implementation, this value has to be known. SALMA then uses $b_m\big(\lfloor \frac{\phi_k+\Phi_o+5}{10} \rfloor \bmod 36\big)$ to approximate $b_m(\phi_k)$, also taking the orientation into account.

5.3 Hardware differences

In contrast to SALMA-light, in SALMA-full we exploit four self-made and low-cost directional antennas with a half-power beamwidth of about 150° (see Fig. 3c). The antennas are mounted such that each one points in a different cardinal direction. The evaluation in Sect. 6.2 shows that, even with this wide beamwidth, SALMA achieves an error below 20 cm for 90% of the estimated positions. The higher number of antennas increases the acquisition time of CIRs and distance estimates. Hence, the acquisition duration is higher than that of SALMA-light, as discussed in Sect. 6.4.

6 Evaluation

We evaluate the positioning capabilities of SALMA in challenging indoor environments: an office (Room A, see Fig. 5a and 6a), and a stockroom (Room B, see Fig. 5b and 6b). After describing the experimental setup in Sect. 6.1, we answer the following questions:

- What is the benefit of using SALMA-full over SALMA-light? (Sect. 6.2);
- What is the *accuracy* achieved by SALMA, and at which computational costs? (Sect. 6.3);
- How long does it take to estimate a position, and what are the implications on *scalability*? (Sect. 6.4);
- Do more (and better) antennas improve the performance of SALMA? (Sect. 6.5).

We answer all these questions in Room A under clear LOS conditions. In Sect. 7, we will then specifically evaluate how SALMA performs in more challenging environments with obstructed LOS (both rooms), and a dynamic environment due to moving objects and people (Room A).

6.1 Experimental setup

We carry out the evaluation in an office containing obstacles and scattering objects such as desks, chairs, shelves, and PC monitors, as shown in Fig. 5a and 6a (Room A). We place the tag in $N_{\text{EP}} = 35$ evenly distributed evaluation points, while fixing the anchor next to the table. We mount both anchor and tag on a tripod at a height of 1.50 m, i.e., well above the obstacles, so to have clear LOS conditions. The anchor is connected to a Lenovo ThinkPad T450s notebook running MATLAB. The tag, instead, is battery-powered and can move freely. The only pre-processing required by SALMA is to enter the anchor location and orientation as well as the

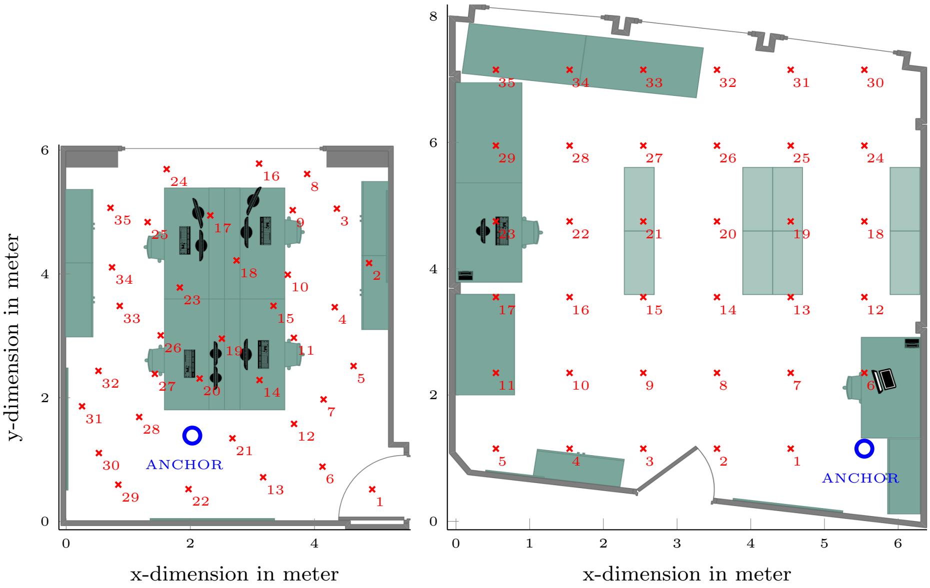

(a) Room A (office): Plan

(b) Room B (stockroom): Plan

Figure 5: Evaluation setup (2D-plan): we consider 35 evaluation points (red crosses) in two different environments.

(a) Room A (office): Picture

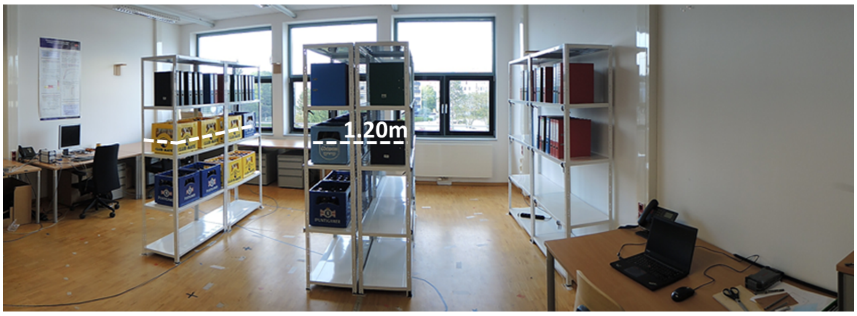

(b) Room B (stockroom): Picture

Figure 6: Evaluation setup (Picture): the white dashed line marks the measurement height under obstructed LOS.

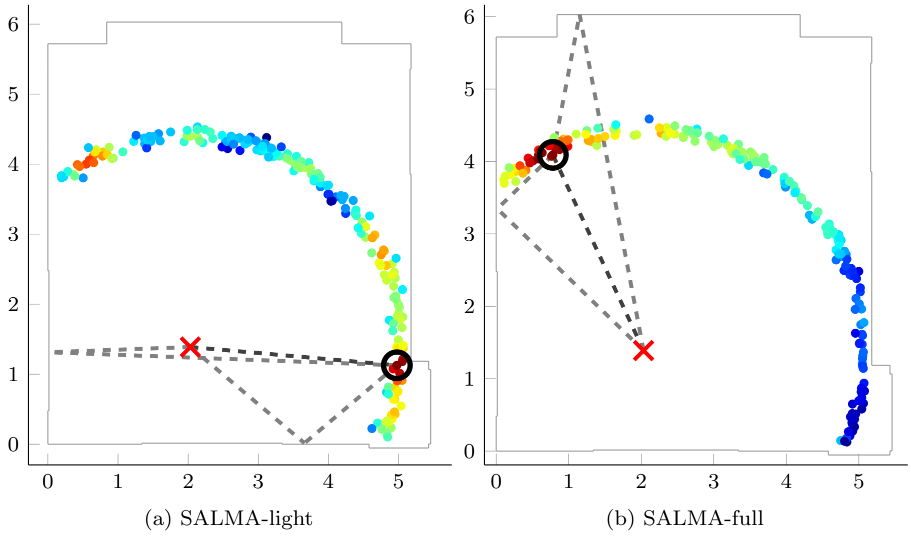

(a) SALMA-light (b) SALMA-full

Figure 7: Evidence of multipath ambiguities.

coordinates of the surrounding four wall segments. The following settings are used by the DW1000: maximum data rate (6.8 Mbps), pulse repetition frequency of 64 MHz, and a preamble symbol repetition of 1024. Channel 7 is used due to its high bandwidth (900 MHz) and since our self-made directional antennas are optimized for this band. At each evaluation point (denoted by $\mathbf{p}_{\mathrm{EP}}$), we perform 100 position estimates, hence carrying out 3500 evaluations in total for both SALMA-light and SALMA-full. We denote the i-th position estimate by $\hat{\mathbf{p}}_i$, and obtain the absolute position error with

$$\mathrm{Err}_i = \|\hat{\mathbf{p}}_i - \mathbf{p}_{\mathrm{EP}}\|. \tag{16}$$

Statistically, we look at the cumulative distribution function (CDF) over the errors Err_i using all evaluation points (i.e., 3500 estimates) for different configurations, as illustrated in the upcoming sections.

6.2 SALMA-light vs. SALMA-full

In this section we examine the performance of both SALMA implementations comparatively.

Handling ambiguities. SALMA-light relies solely on the position information contained in the arrival times of MPCs. Hence, the resulting likelihood for the positions is highly multimodal, or in other words, there are multiple regions that seem to best fit the observed signal. This is demonstrated in Fig. 7, which shows the positioning result using SALMA-light (Fig. 7a) and SALMA-full (Fig. 7b) for one estimation run on position 34 (cf. Fig. 5a). The colored dots indicate the candidate point positions, where the color represents the likelihood values (red=high, blue=low). SALMA-light has three regions showing similarly high likelihood values (red and orange dots), caused by similarly long MPC paths, which results in a completely wrong estimate. In contrast, SALMA-full can narrow the estimate down to find the true position of the tag. This is possible due to the combined directional antenna observations, where wrong candidate points have low likelihood values because amplitude values do not fit to the antenna patterns.

Quantitative comparison. We show the improvement quantitatively by accounting for all 3500 estimates via the CDF of the absolute position error. Fig. 8 shows the CDF for SALMA-light (dashed blue line) and SALMA-full (solid orange line). With SALMA-light, 67.3% of all evaluations have a position error below 25 cm. On the other hand, 21.7% of the evaluations have an error above 1 m: these outliers are caused by the multipath ambiguities, as just explained. By using directional antennas, SALMA-full can mitigate these outliers: 90% of all evaluations are below 20.17 cm, whilst 99% of the evaluations are below 29.72 cm.

We can hence conclude that SALMA-full clearly outperforms SALMA-light thanks to the additional angular information. Hence, we focus the next evaluations on SALMA-full only.

6.3 Localization accuracy

With the promising results shown in Sect. 6.2, we investigate the accuracy of SALMA in more detail, and focus also on the computational costs.

Role of candidate points. We examine the impact of the number of candidate points used by SALMA-full. To this end, we perform 3500 estimates for different number of candidate points $N_C \in \{50, 100, 200, 500, 1000\}$. Fig. 9 shows the resulting CDF: even when using only 50 candidate points (blue, star), 90% of the estimates have an error below 30 cm. However, there are outliers for about 5% of the estimates. Increasing the number of candidate points removes the outliers and improves the performance to a "saturation point" at about 200 candidate points (i.e., a higher number of points gives negligible improvements). Hence, we make N_C=200 our preferred setup and use it for all further evaluations, unless stated otherwise. The number of candidate points increases the computation time linearly, so N_C can act as a trade-off between computational costs and accuracy, as illustrated in Sect. 6.4.

Individual evaluation points. A more detailed display of the accuracy is shown in Fig. 10a. For the 100 estimates at each position of Room A, the mean (blue circle) and the 3-fold standard deviation (black error ellipse) are shown. The former indicates that there is little estimation bias (distance to ground truth). As for the standard deviation, with the good ranging precision of UWB, the ranging deviation is small (facing the LOS), while info gained by the MPCs determines the angle deviation (perpendicular to the LOS). Overall, the good performance is reinforced, while there are certain positions (e.g., 9, 16, and 18) with a slightly higher bias. Of special note is that the accuracy of SALMA does not degrade at higher ranges: pos. 8, 16, and 24 are placed more than 4 meters apart from the anchor, but their estimates are as accurate as the ones obtained at positions much closer to the anchor. This is highlighted in Fig. 11 showing the average position error with respect to the real distance between anchor and tag. This stands in contrast to many other indoor positioning techniques, where the inaccuracy increases quickly with the range, e.g., visual systems [38].

6.4 Scalability

The number of supported tags by SALMA is limited by (i) the computation time of the position estimation, (ii) the duration of the DS-TWR, as well as (iii) the time needed to stream the CIR and additional info to the notebook via USB. The duration of a DS-TWR is mainly defined by the packet length of its three packets, which is 3.49 ms. Streaming one CIR to MATLAB takes 4.62 ms.

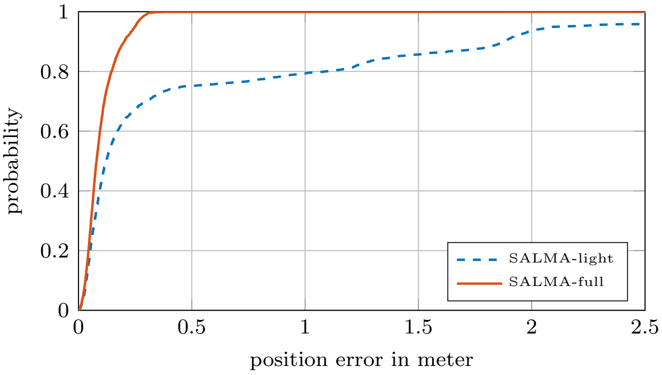

Figure 8: SALMA-light sustains an accuracy below 30 cm only in 70% of the cases due to multipath ambiguities. By exploiting the angular domain, SALMA-full exhibits an error below 30 cm in 99% of the cases (Room A).

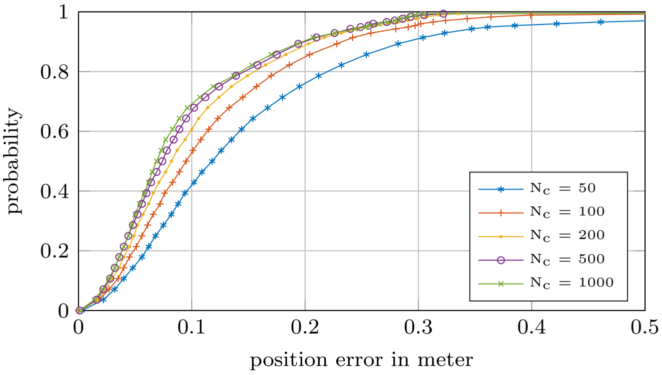

Figure 9: Impact of the number of candidate points on SALMA's accuracy: N_C=200 acts a good trade-off.

The computation time of the position estimation depends on the notebook's performance and on the number of candidate points. In the evaluations, the algorithms are performed in MATLAB on a Lenovo ThinkPad T450s with 2.59 GHz clock and 8 GB RAM. An increase in the number of candidate points scales the computation time linearly. Thus, we evaluate the time needed per candidate point. SALMA-light takes 174.77±12.2 μs and SALMA-full requires 955.13±23.5 μs per candidate point. Thus, with $N_C = 200$ candidate points, the algorithms take 34.95 ms and 191.03 ms, respectively. The overall duration of a position estimation with SALMA-light when using $N_C = 200$ is hence 43.06 ms, resulting in an update rate of 23 Hz. Using $N_C = 50$, instead, gives an update rate of 60 Hz.

When using SALMA-full, for each antenna a DS-TWR trial is performed and four CIRs are acquired: this reduces the achievable update rate. In total, SALMA-full requires 223.5 ms for $N_C = 200$ and 79.8 ms for $N_C = 50$, resulting in an update rate of about 4.5 Hz and 12.5 Hz, respectively. Thus, SALMA can easily compete with comparable solutions and outdoor positioning systems like GPS.

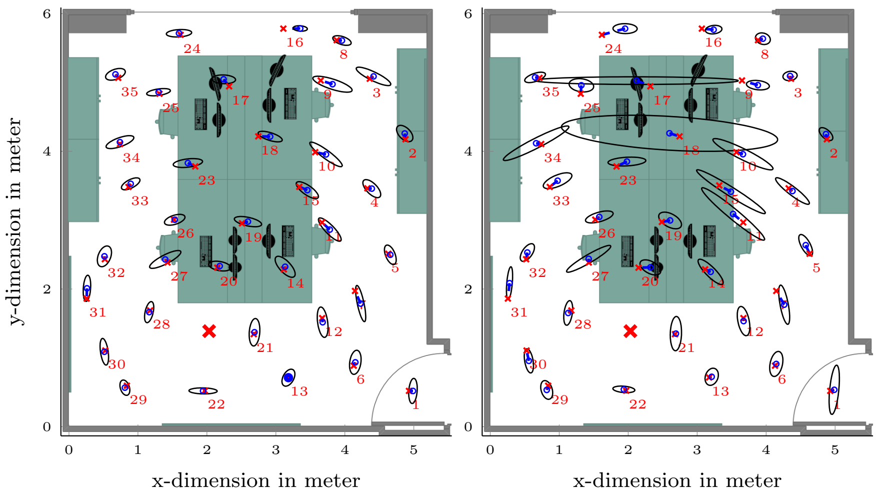

(a) Clear LOS (b) Obstructed LOS

Figure 10: Error ellipses showing position bias and three-fold standard deviation (Room A).

6.5 The role of the antenna

We examine next how SALMA would perform when using more antennas with more directive beampatterns. As such antennas are not yet commercially available, we simulate artificial CIRs ($\boldsymbol{r}$) and ranging ($\hat{d_0}$) for the same tag positions shown in Fig. 5a. For any tag position $\mathbf{p}$, we can create an artificial CIR in two steps:

1. Specular part: we shift and add pulses $s_{\mathrm{DW}}(t - \tau_k)$ weighted by beampattern $b(\phi_k)$ and amplitude α_k using the known delays τ_k and angles ϕ_k. The amplitude exhibits free-space path-loss and each reflection halves the magnitude. We consider MPCs up to order two.

2. Scattering part: we simulate diffuse multipath by drawing realizations of a Gaussian random process whose variance is defined by a double exponential power delay profile according to equation (9) from [39]. Additionally we simulate AWGN measurement noise with an SNR of 29.5 dB at 1 m.

This simulation setup allows us to adjust the half-power beamwidth (HPBW) of the antennas and to recreate the effect of clutter by setting a signal-to-interference[5] ratio (SIR). The latter is defined by the ratio between LOS and scattering energy. We determined empirically that an SIR of 3 dB properly describes the environment.

To recreate the performance behavior from the SALMA-full measurement runs described in Sect. 6.3, we set the HPBW to 150°, matching the properties of the used antennas. Additionally, we carry out simulations using six antennas with a HPBW of 90°, reflecting a higher quality implementation. Fig. 12 shows the results. On the one hand, we can see that the SALMA-full simulation (red curve) fits the measured results (purple curve) closely. A slightly better performance is achieved in the simulation, because the impact of bias due to floor plan inaccuracies is not present. On the other hand, we can notice that, when simulating six antennas (blue curve), the performance of SALMA improves significantly: the 90% error

---

[5] Interference, in this case, refers to self-interference due the scattering part.

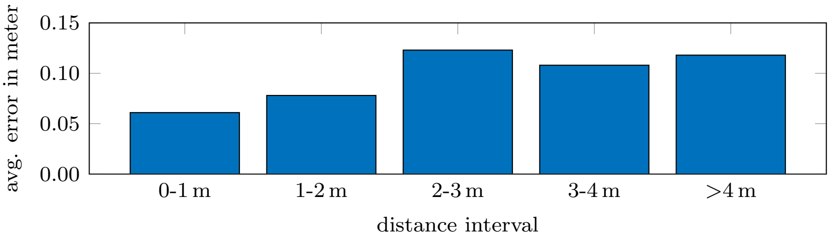

Figure 11: Average position error w.r.t. the real distance.

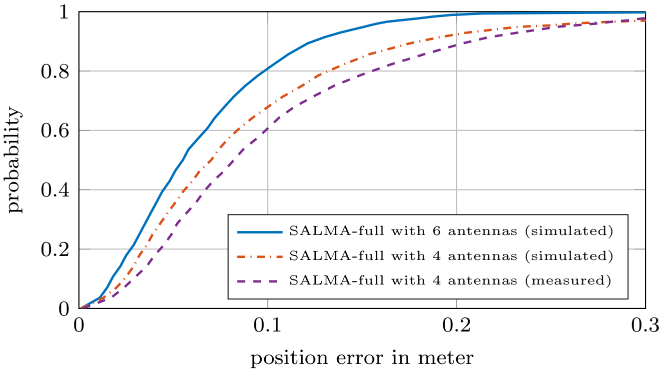

Figure 12: Simulated performance of SALMA when using multiple antennas with more directive beampatterns.

decreases by about 10 cm to almost reach the sub-decimeter mark, whilst 99% of the estimates achieve an error below 20 cm.

7 Robustness to non-line-of-sight and dynamic environments

Indoor environments are inherently highly dynamic due to moving humans and objects. Thus, the value of a localization system strongly depends on (i) its performance under obstructed LOS, (ii) its behavior in different environments and (iii) its robustness in crowded settings. In this section, we discuss the performance of SALMA under non-line-of-sight (NLOS) conditions (Sect. 7.1), when furniture is moved without updating the map (Sect. 7.2) and in the case of a highly-dynamic and crowded environment (Sect. 7.3).

7.1 Performance under NLOS conditions

In situations of a blocked LOS, range-based systems suffer from a positive bias [40]. This is either caused by the lower propagation speed in case the signal propagates through the obstacle, or, in case of a fully blocked LOS, due to the misinterpretation of a reflection as the direct path.

Distance bias. SALMA requires the distance estimate $\hat{d}_0$ between anchor and tag to distribute the candidate points on a circle around the anchor as described in Sect. 3.3. Thus, an obstructed LOS causes an increase in the radius of the

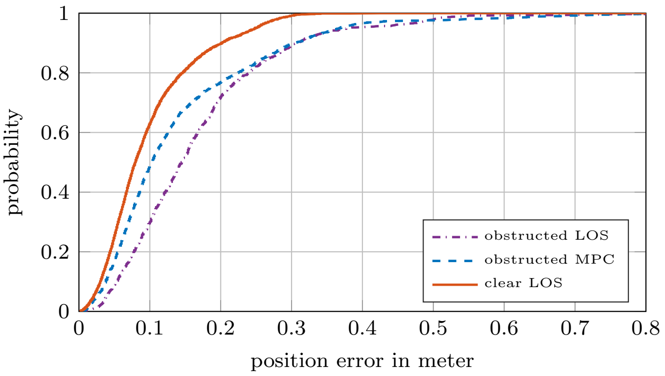

Figure 13: Performance of SALMA in clear LOS, obstructed MPC, and obstructed LOS situations in Room A.

circle. First, we analyze the impact of different objects on $\hat{d}_0$. We place tag and anchor 2 m apart from each other and perform 1000 DS-TWR trials with different objects blocking the LOS. The objects included: a metal plate (800×450×3 mm), PC monitors, and humans. The threshold-based mechanism of the DW1000 was able to detect a leading edge corresponding to the LOS in each of the trials. But, indeed, the obstructed LOS leads to a positive bias in the range estimate. Metal plate and PC monitor caused a range bias of 11 cm and 13.1 cm, respectively. Even in the case of humans blocking the LOS, the leading edge was successfully detected, but two humans blocking the LOS already led to a range bias of 41.8 cm. Further evaluations will show that SALMA is robust even in the case of a range bias.

Accuracy evaluation. SALMA is not just making use of the LOS component, but also of specular MPCs. Thus, we evaluate SALMA also in situations of blocked MPCs. We repeat the evaluation in Room A described in Sect. 6.1: this time, however, we mount the tag and the anchor at a height of 1.20 m, corresponding to the height of monitors, shelves, and people in the room. Depending on the position of the evaluation points, this results in obstructed LOS for twelve of these points $EP_{OLOS} = \{3, 8, 9, 10, 15, 16, 18, 19, 25, 26, 33, 34\}$, which results in 1200 evaluations. Note that, for all these evaluation points, there were also specular MPCs blocked by objects. For twenty points, instead, the LOS was still clear but specular MPCs were blocked $EP_{OMPC} = \{1, 2, 4-7, 11-14, 17, 20-24, 27, 28, 32, 35\}$. In total, 2000 evaluations were acquired in these situations. The remaining 300 evaluations are still in clear LOS with no blocked MPCs, thus, they are ignored. Fig. 13 (magenta dash dotted line) shows the CDF of all evaluations under blocked LOS (EP_{OLOS}). The median is at 14.5 cm and the error for 90% of the estimates is still below 30.7 cm. The blue dashed line in Fig. 13 shows the CDF just considering evaluations where significant multipath components are blocked by obstacles or humans (EP_{OMPC}). The median is at 10.25 cm and the error for 90% of the estimates is below 30.52 cm. This shows that SALMA remains robust even in the case of blocked MPCs.

Qualitative evaluation. In Fig. 10b, we see again the accuracy for individual evaluation points, now for the obstructed LOS case. While the position bias (distance blue circles to red crosses) did not increase significantly, we can see that the variance in the angular direction increases for most of the evaluation points. The error ellipses shown in Fig. 10b indicate two evaluation points with significantly

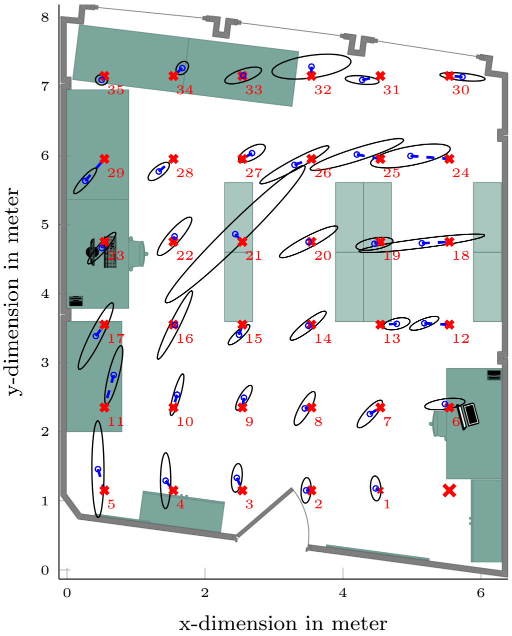

Figure 14: Error ellipses showing position bias and three-fold standard deviation with empty racks in Room B.

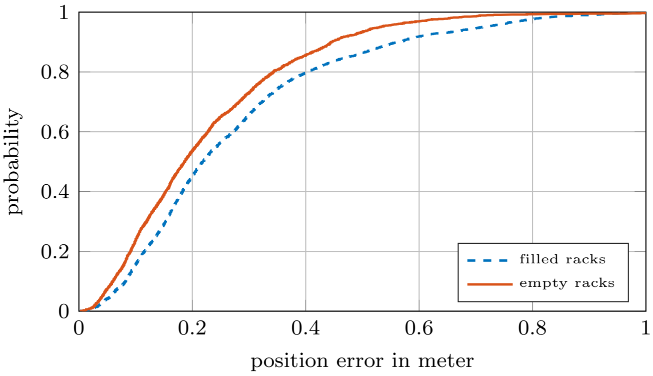

Figure 15: Performance of SALMA in Room B in the case of moving obstacles (storage racks are empty or filled).

higher variances (no. 17 and 18) as the other points. The reason is the unfortunate position of the anchors in this case. The PC monitors and obstacles at the left and right wall block the respective MPCs, thus, the position information obtained at these positions comes only from the LOS and the reflection from the window. Since these two reflections are arriving at the same angle, SALMA suffers from a poor geometric configuration. This results in ambiguities similar to the ones shown in Sect. 6.2. Due to significant MPCs from the left and right wall, this situation was not evident in the clear LOS case (see Fig. 10a).

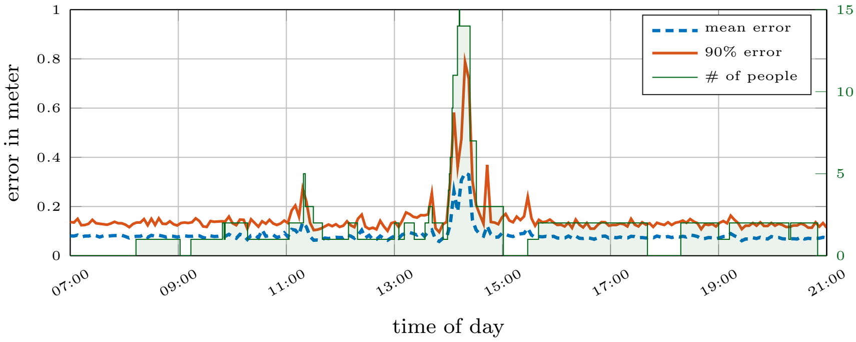

Figure 16: Snippet of a 24-hours experiment in dynamic environments. The dashed blue line depicts the mean error of 50 position estimates over time, whilst the solid orange line shows the 90% error. Despite the people moving in/out of the room (green line), SALMA can sustain a decimeter-level position accuracy.

7.2 Performance in stockroom with moving obstacles

In Sect. 6 and 7.1, we have performed all the measurements in Room A. To prove the capabilities of SALMA also in more challenging environments and in the presence of moving obstacles, we have evaluated its performance also in Room B (see Fig. 5b and 6b).

Performance in more challenging environments. To challenge SALMA, we chose a stockroom that is larger than Room A (46.7 m^2 vs. 31.6 m^2) and cluttered with desks, storage racks (bright rectangles in Fig. 5b) and several other metal objects (see Fig. 6b). We have mounted anchor and tag at a height of 1.20 m. Fig. 15 (solid orange line) shows the CDF of all evaluations in Room B. The median is at 18.6 cm and 90% of all estimates obtain an error below 44.5 cm. Thus, compared to the evaluation in Room A, the performance of SALMA is slightly worse due to the larger room with more clutter and wall materials with unfavorable reflective properties (see Sect. 8). Fig. 14 shows the accuracy for individual evaluation points. Similar to Room A (see Sect. 7.1), some positions (e.g., 4, 5, 12, 18, 24) suffer from an unfavorable anchor placement as the LOS is arriving from the same angle as strong reflections.

Moving obstacles. The performance of localization systems based on RSS profiling and fingerprinting is highly affected by moving obstacles. Thus, changing the furniture in a room often requires to update or repeat measurements. To evaluate the performance of SALMA in the case of moving obstacles or furniture, we have stocked up the storage racks in Room B with full beer crates and other objects (see Fig. 6b). As the goal of SALMA is to minimize the setup effort, we do not model reflections from obstacles such as the full storage racks. Fig. 15 shows that the position error (dashed blue line), while higher due to the range bias introduced by obstructed LOS, still stays in reasonable bounds, relatively unaffected by the additional reflections. Thus, SALMA only slightly loses accuracy in favor of practicability and setup time.

7.3 Performance in a crowded environment

For a final stress test of SALMA and to evaluate its behavior in a dynamic environment including NLOS situations, we employed our system again in the office scenario (Room A) for a non-stop 24 hours run. The system was exposed to the usual ongoing work flow that involves multiple people passing by the system, thereby blocking the LOS or MPCs, hence creating a dynamic environment. During the 24 h experiment, SALMA localized three tags at representative positions (positions 3, 15, and 33) simultaneously. The positions were deliberately chosen to be under obstructed LOS. Every five seconds we estimated the tag positions resulting in 51840 position estimates. We evaluate the performance of the system on multiple levels. Fig. 16 shows the mean error (dashed blue line) and the 90% error (solid orange line) over 50 position updates from 07:00 - 21:00 o'clock. Additionally, we track the number of present people in the room during the experiment (green stairstep graph). The figure focuses on daytime, since over night no one was in the room and the performance remained constant. It can be seen that the usual working environment (with the two designated working people present) does not impair the performance of the system providing an average error below 11.2 cm. In terms of present people, there are two events prominent in Fig. 16: at 11:00 o'clock there was a meeting with five people and at 14:00 o'clock we have presented SALMA to thirteen people making it in total fifteen people in the room simultaneously. We asked people to move around the room freely during the presentation, thus, the LOS and the MPCs were obstructed in a dynamic fashion. Even though the error increases during these periods, still, when the room was completely filled with people, the average error was below 34 cm and the 90% error below 79 cm. The latter indicates that SALMA is robust also in a highly dynamic environment and under NLOS conditions.

Comparison to other multi-anchor systems. Comparing the accuracy of SALMA with other UWB-based systems is difficult, as they are either evaluated in mobile 2D [14, 15, 41] or static 3D [4, 16] scenarios. Silva et al. [42] report a 2D static LOS mean error of 16.6 cm. SALMA instead achieves an average error of just 9.85 cm in clear LOS. Kempke et al. [4, 16] report a 90% error of 77 cm and 50 cm in static 3D, respectively. In contrast, SALMA achieves a 90% error of 50 cm between 14:00-14:30 o'clock, thus, under obstructed LOS and when up to fifteen people were walking around. Therefore, it is fair to say that SALMA can compete and even outperform existing systems, despite using just a single anchor.

8 Discussion

Our evaluation demonstrates the capabilities of SALMA to perform accurate positioning in typical indoor environments. However, it has also highlighted a number of challenges and open questions that we will elaborate in detail in this section.

Sensitivity to chosen anchor position. Due to SALMA's principle, just one anchor per room is required. In our evaluations, we examined two typical choices for anchor positions, namely, in the vicinity of the room center (Room A) and in the corner of the room (Room B). Both variants have pros and cons: in Room A we have a full candidate point circle for many ranges, which increases the risk of ambiguities, especially for SALMA-light. However, SALMA-full can take full advantage of the beampatterns in all directions to stay relatively unaffected (as we have demonstrated in Sec. 6.2). In Room B, we have, at most, a quarter circle of candidate points: on the one hand, this reduces possible ambiguities. However, on the other hand, this results in higher ranges with reduced signal strength and reduced benefit from the angular information. We also pointed out some difficult positions in both rooms where LOS and the strongest reflection come from the same direction, resulting in a plateau in the likelihood which leads to a dilution of precision. These cases exist no matter what anchor position is chosen.

The anchor orientation can be set arbitrarily, but it has to be fixed and known to correctly weight the amplitudes.

Including the third dimension. SALMA is designed specifically to perform 2D positioning. This choice is rather pragmatic: physical and algorithmic setup of the system are simplified dramatically, enabling a practical implementation with short setup time and efforts, while only using a single anchor. Also, many applications (e.g., navigation tasks) do not require any height information. In principle, the methods can be extended to the third dimension: (i) determining the VAs can be done by mirroring at plane surfaces, (ii) for the MPC angle one needs to take the elevation beampatterns into account and (iii) the candidate points are placed on a range sphere rather than circle. However, this drastically increases the computational complexity and makes the position likelihood even more multimodal. A 3D model of the environment could help to avoid ambiguities due to floor or ceiling reflections, however, our antennas exhibit a fairly narrow elevation pattern, hence, the impact of ceiling, floor, and other reflections is limited significantly.

Effect of wall materials. The main setup effort for SALMA is the determination of reflecting surfaces in the considered environment. However, additional care has to be taken with regard to the material of the surfaces. Preferably, materials such as glass and metal enable good reflectors and including them in the models enhances the position estimate. On the other hand, plaster boards or wooden surfaces, even if they are flat and smooth, give little to no contribution in terms of specular reflections and can in fact decrease the performance. For example, in Room B, the eastern wall, even though close to the anchor, is made out of plasterboard and does not contribute with a specular multipath component. Thus, it should not be included in the signal model as a source of a virtual anchor.

9 Related Work

Indoor localization technologies. Many RF technologies have been investigated for indoor localization, such as Wi-Fi [10], Bluetooth [8,9], and IEEE 802.15.4 [6,43]. However, these systems hardly achieve an accuracy below 1 m, require a high amount of reference nodes, and typically come with a high deployment effort. Optical systems are among the most accurate indoor localization systems, but cannot inherently operate in NLOS conditions [38]. SALMA, instead, reaches a median error of 15 cm and a 90% error of 30 cm even in obstructed LOS conditions. Acoustic systems can also achieve decimeter-level accuracy, but their biggest enemy – multipath propagation – is SALMA's best friend [44,45].

UWB indoor localization systems. UWB-based systems can also achieve decimeter-level accuracy [13,46]. Recently, several systems have been implemented using low-cost UWB transceivers [4,14–16,41,42]. However, these systems require a high amount of anchors, typically between eight [14,15] and fifteen [4]. SALMA, instead, uses a single anchor and – to the best of our knowledge – no comparable solution exists. In terms of accuracy, as discussed in Sect. 7.3, it is fair to say that SALMA can compete and even outperform existing systems, despite using just a single anchor.

Multipath-assisted localization systems. Theoretical works have discussed the performance bounds of multipath-assisted indoor localization via simulation [47–49] and using very expensive, bulky and wired-synchronized equipment [26, 50, 51]. Instead, with SALMA, we are the first to enable the exploitation of multipath reflections for low-cost, low-power wireless localization systems.

Directional antennas to enable single-anchor systems. Several works have exploited electronically steerable or switchable antenna systems to enable single-anchor localization using narrowband technologies [52, 53]. However, SALMA outperforms all these systems due to the exploitation of the position-related information provided by the MPCs. Sun et al. [54] presented a UWB-based system claimed to achieve decimeter-level accuracy. However, their measurement setup is vague and a thorough analysis of the system performance is missing. Quing et al. [55] and Zhang et al. [56] presented similar systems, but solely based on simulation.

Although not exploiting directional antennas, also Chronos [57] requires just a single access point to estimate the position of another device. In particular, Chronos uses an omni-directional antenna array and emulates a wideband radio on commodity Wi-Fi systems. Still, due to the position-related information provided by the MPCs, SALMA outperforms Chronos in terms of accuracy. Furthermore, by using the license-free ISM bands, Chronos interferes and is prone to the interference of other devices using the 2.4 GHz band.

10 Conclusions and Future Work

In this paper, we present SALMA, a low-cost UWB-based indoor localization system that exploits multipath reflections to tear down the position estimation to a unique solution while only using a single anchor. Besides a crude floor plan and the position of the anchor, the system does not need any prior calibration or training phase. By using directional antennas, we increased the robustness of SALMA against overlapping MPCs. We extensively evaluated the performance of SALMA under LOS and NLOS conditions, as well as during a 24 h stress-test to challenge SALMA in dynamic settings. Under LOS, SALMA achieved a median error below 8 cm and an error below 20 cm for 90% of the position estimates. Even under obstructed LOS and in a highly dynamic environment SALMA sustains a high accuracy.

Our aim in this paper was to show the outstanding capabilities of SALMA without using a tracking filter and solely utilizing single-shot single-anchor measurements. In future work, we will combine SALMA with a particle filter and an inertial measurement unit to benefit from past position estimates. Moreover, we will perform an exhaustive evaluation of SALMA in mobile environments.

Acknowledgments

This work has been performed within the LEAD project "Dependable Internet of Things in Adverse Environments" funded by Graz University of Technology. This work was also partially funded by the SCOTT project. SCOTT (`http://www.scott-project.eu`) has received funding from the Electronic Component Systems for European Leadership Joint Undertaking under grant agreement No 737422. This joint undertaking receives support from the European Unions Horizon

2020 research and innovation programme and Austria, Spain, Finland, Ireland, Sweden, Germany, Poland, Portugal, Netherlands, Belgium, Norway. SCOTT is also funded by the Austrian Federal Ministry of Transport, Innovation and Technology (BMVIT) under the program "ICT of the Future" between May 2017 and April 2020. More information at `https://iktderzukunft.at/en/`.

References

[1] K. Witrisal *et al.*, "High-Accuracy Localization for Assisted Living: 5G systems will Turn Multipath Channels from Foe to Friend," *IEEE Signal Processing Magazine*, vol. 33, no. 2, Mar. 2016.

[2] S. R. Islam *et al.*, "The Internet of Things for Health Care: a Comprehensive Survey," *IEEE Access*, vol. 3, Jun. 2015.

[3] K. Guo, Z. Qiu, C. Miao, A. H. Zaini, C.-L. Chen, W. Meng, and L. Xie, "Ultra-Wideband-Based Localization for Quadcopter Navigation," *Unmanned Systems Journal*, vol. 4, no. 1, Jan. 2016.

[4] B. Kempke, P. Pannuto, and P. Dutta, "PolyPoint: Guiding Indoor Quadrotors with Ultra-Wideband Localization," in *Proc. of the* 2^{nd} *Int. Workshop on Hot Topics in Wireless (HotWireless)*, Sep. 2015.

[5] D. Dardari, P. Closas, and P. M. Djurić, "Indoor Tracking: Theory, Methods, and Technologies," *IEEE Transactions on Vehicular Technology*, vol. 64, no. 4, Apr. 2015.

[6] J. Larranaga, L. Muguira, J. M. Lopez-Garde, and J. I. Vazquez, "An Environment Adaptive ZigBee-based Indoor Positioning Algorithm," in *Proc. of the Int. Conf. on Indoor Positioning and Indoor Navigation (IPIN)*, Sep. 2010.

[7] X. Huang, W. Zhu, and D. Lu, "Underground Miners Localization System based on ZigBee and WebGIS," in *Proc. of the* 18^{th} *Int. Conf. on Geoinformatics*, Jun. 2010.

[8] G. Conte *et al.*, "BlueSentinel: a First Approach using iBeacon for an Energy Efficient Occupancy Detection System," in *Proc. of the* 1^{st} *ACM Conf. on Embedded Systems for Energy-Efficient Buildings (BuildSys)*, Nov. 2014.

[9] M. Bargh and R. de Groote, "Indoor Localization based on Response Rate of Bluetooth Inquiries," in *Proc. of the* 1^{st} *ACM Int. Workshop on Mobile Entity Localization and Tracking in GPS-less Environments (MELT)*, Sep. 2008.

[10] S. Gansemer *et al.*, "RSSI-based Euclidean Distance Algorithm for Indoor Positioning Adapted for the use in Dynamically Changing WLAN Environments and Multi-level Buildings," in *Proc. of the 2010 IPIN Conference*, Sep. 2010.

[11] S. He and S.-H. G. Chan, "Wi-Fi Fingerprint-based Indoor Positioning: Recent Advances and Comparisons," *IEEE Comm. Surveys & Tutorials*, vol. 18, no. 1, Aug. 2016.

[12] R. Mautz, "Indoor positioning technologies," Ph.D. dissertation, ETH Zürich, Feb. 2012.

[13] D. Lymberopoulos and J. Liu, "The Microsoft Indoor Localization Competition: Experiences and Lessons Learned," *IEEE Signal Processing Magazine*, vol. 34, no. 5, Sep. 2017.

[14] A. Ledergerber, M. Hamer, and R. D'Andrea, "A Robot Self-Localization System using One-Way Ultra-Wideband Communication," in *Proc. of the Int. Conf. on Intelligent Robots and Systems (IROS)*, Sep. 2015.

[15] J. Tiemann, F. Eckermann, and C. Wietfeld, "ATLAS - An Open-Source TDOA-based Ultra-Wideband Localization System," in *Proc. of the Int. Conf. on Indoor Positioning and Indoor Navigation (IPIN)*, Oct. 2016.

[16] B. Kempke *et al.*, "SurePoint: Exploiting Ultra Wideband Flooding and Diversity to Provide Robust, Scalable, High-Fidelity Indoor Localization," in *Proc. of the* 14th *Int. Conf. on Embedded Network Sensor Systems (SenSys)*, Nov. 2016.

[17] J. T. Isaacs, D. J. Klein, and J. P. Hespanha, "Optimal Sensor Placement for Time Difference of Arrival Localization," in *Proceedings of the* 48th *IEEE Conference on Decision and Control (CDC)*, Dec. 2009.

[18] C. Nerguizian, C. Despins, and S. Affes, "Geolocation in Mines with an Impulse Response Fingerprinting Technique and Neural Networks," *IEEE Transactions on Wireless Communications*, vol. 5, no. 3, Mar. 2006.

[19] L. Jiang, L. N. Hoe, and L. L. Loon, "Integrated UWB and GPS Location Sensing System in Hospital Environment," in *Proc. of the* 5th *Int. Conf. on Industrial Electronics and Applications (ICIEA)*, Jun. 2010.

[20] T. H. Riehle, P. Lichter, and N. A. Giudice, "An Indoor Navigation System to Support the Visually Impaired," in *Proc. of the* 30th *Int. Conf. of the IEEE Engineering in Medicine and Biology Society*, Aug. 2008.

[21] R. Mirza, A. Tehseen, and A. J. Kumar, "An Indoor Navigation Approach to Aid the Physically Disabled People," in *Proc. of the* 18th *Int. Conf. on Computing, Electronics and Electrical Technologies (ICCEET)*, Mar. 2012.

[22] D. Espes, A. Daher, Y. Autret, E. Radoi, and P. Le Parc, "Ultra-Wideband Positioning for Assistance Robots for Elderly," in *Proc. of the* 10th *International Conference on Signal Processing, Pattern Recognition and Applications (SPPRA)*, Feb. 2013.

[23] B. Perrat *et al.*, "Quality Assessment of an Ultra-Wide Band Positioning System for Indoor Wheelchair Court Sports," *Proc. of the Inst. of Mechanical Engineers, Part P: Journal of Sports Eng. and Techn.*, vol. 229, no. 2, Apr. 2015.

[24] R. Leser, A. Schleindlhuber, K. Lyons, and A. Baca, "Accuracy of an UWB-based Position Tracking System used for Time-Motion Analyses in Game Sports," *European Journal of Sport Science*, vol. 14, no. 7, Feb. 2014.

[25] B. Großwindhager *et al.*, "Dataset: Single-Anchor Indoor Localization with Decawave DW1000 and Directional Antennas," in *Proc. of the 1st Workshop on Data Acquisition To Analysis (DATA'18)*, Nov 2018.

[26] P. Meissner, C. Steiner, and K. Witrisal, "UWB Positioning with Virtual Anchors and Floor Plan Information," in *Proc. of the* 7^{th} *Int. Workshop on Positioning, Navigation and Communication (WPNC)*, Mar. 2010.

[27] J. Kulmer *et al.*, "Using Decawave UWB Transceivers for High-accuracy Multipath-assisted Indoor Positioning," in *Proc. of the* 5^{th} *Int. Workshop on Advances in Network Localization and Navigation (ANLN)*, May 2017.

[28] J. Kulmer, S. Grebien, M. Rath, and K. Witrisal, "On the Unimportance of Phase-Coherent Measurements for Beampattern-Assisted Positioning," in *Proc. of the Int. Conf. on Wireless Comm. and Networking (WCNC)*, Apr. 2018.

[29] J. Kulmer, E. Leitinger, S. Grebien, and K. Witrisal, "Anchorless Cooperative Tracking using Multipath Channel Information," *IEEE Transactions on Wireless Communications*, vol. PP, no. 99, Jan. 2018.

[30] Decawave Ltd., *DW1000 Datasheet. Version 2.12*, 2016.

[31] I. C. Society, *Standard for Low-Rate Wireless Networks*, Std. 802.15.4, 2015.

[32] B. Großwindhager *et al.*, "Enabling Runtime Adaptation of Physical Layer Settings for Dependable UWB Communications," in *Proc. of the 19th IEEE Intern. Symposium on A World of Wireless, Mobile and Multimedia Networks (WoWMoM)*, 2018.

[33] Decawave Ltd., *DW1000 User Manual. Version 2.10*, 2016.

[34] K. Finkenzeller, *RFID Handbuch – Grundlagen und praktische Anwendungen von Transpondern, kontaktlosen Chipkarten und NFC.* Hanser, 2008.

[35] V. Namboodiri *et al.*, "An Extensive Study of Slotted Aloha-based RFID Anti-collision Protocols," *Computer Communications*, vol. 35, no. 16, Sep. 2012.

[36] B. Großwindhager *et al.*, "Demo Abstract: UWB-based Single-anchor Low-cost Indoor Localization System," in *Proc. of the* 15^{th} *ACM Int. Conf. on Embedded Networked Sensor Systems (SenSys), demo session*, Nov 2017.

[37] P. Mowlaee *et al.*, *Single Channel Phase-Aware Signal Processing in Speech Communication: Theory and Practice.* John Wiley & Sons, 2016.

[38] S. Liu and T. He, "SmartLight: Light-weight 3D Indoor Localization Using a Single LED Lamp," Nov. 2017.

[39] J. Karedal, S. Wyne, P. Almers, F. Tufvesson, and A. F. Molisch, "A Measurement-Based Statistical Model for Industrial Ultra-Wideband Channels," *IEEE Transactions on Wireless Communications*, vol. 6, no. 8, pp. 3028–3037, Aug. 2007.

[40] S. Maranò, W. M. Gifford, H. Wymeersch, and M. Z. Win, "NLOS Identification and Mitigation for Localization Based on UWB Experimental Data," *IEEE Journal on Selected Areas in Communications*, vol. 28, no. 7, Sep. 2010.

[41] F. Hartmann *et al.*, "Design of an Embedded UWB Hardware Platform for Navigation in GPS Denied Environments," in *Proc. of the IEEE Symposium on Communications and Vehicular Technology in the Benelux (SCVT)*, Nov. 2015.

[42] B. Silva, Z. Pang, J. Åkerberg, J. Neander, and G. Hancke, "Experimental Study of UWB-based High Precision Localization for Industrial Applications," in *Proc. of the Int. Conf. on Ultra-WideBand (ICUWB)*, Sep. 2014.

[43] C. W. Ou *et al.*, "A ZigBee Position Technique for Indoor Localization Based on Proximity Learning," in *Proc. of the International Conference on Mechatronics and Automation (ICMA)*, Aug. 2017.

[44] P. Lazik and A. Rowe, "Indoor Pseudo-Ranging of Mobile Devices using Ultrasonic Chirps," in *Proc. of the* 10^{th} *Int. Conf. on Embedded Network Sensor Systems (SenSys)*, Nov. 2012.

[45] R. Mautz, "The Challenges of Indoor Environments and Specification on some Alternative Positioning Systems," in *Proc. of the* 6^{th} *Int. Workshop on Positioning, Navigation and Communication (WPNC)*, Mar. 2009.

[46] J. Zhang, P. V. Orlik, Z. Sahinoglu, A. F. Molisch, and P. Kinney, "UWB Systems for Wireless Sensor Networks," *Proceedings of the IEEE*, vol. 97, no. 2, Feb. 2009.

[47] K. Witrisal and P. Meissner, "Performance Bounds for Multipath-Assisted Indoor Navigation and Tracking (MINT)," in *Proc. of the Int. Conf. on Comm. (ICC)*, Jun. 2012.

[48] B. Hu, Z. Shi, and Y. Wang, "Single-Sensor Based Indoor Localisation by Exploiting Multipath Propagation," *Electronics Letters*, vol. 54, no. 3, pp. 179–181, Feb. 2018.

[49] C. Gentner, T. Jost, W. Wang, S. Zhang, A. Dammann, and U. Fiebig, "Multipath assisted positioning with simultaneous localization and mapping," *IEEE Transactions on Wireless Communications*, vol. 15, no. 9, pp. 6104–6117, Sept 2016.

[50] E. Leitinger, M. Fröhle, P. Meissner, and K. Witrisal, "Multipath-Assisted Maximum-Likelihood Indoor Positioning using UWB Signals," in *Proc. of the Int. Conf. on Comm. Workshops (ICC)*, Jun. 2014.

[51] Y. Kuang, K. Åström, and F. Tufvesson, "Single Antenna Anchor-Free UWB Positioning Based on Multipath Propagation," in *Proceedings of the International Conference on Communications (ICC)*, Jun. 2013.

[52] A. Cidronali, S. Maddio, G. Giorgetti, and G. Manes, "Analysis and Performance of a Smart Antenna for 2.45-GHz Single-Anchor Indoor Positioning," *IEEE Transactions on Microwave Theory and Techniques*, vol. 58, no. 1, Jan. 2010.

[53] M. Rzymowski, P. Woznica, and L. Kulas, "Single-Anchor Indoor Localization Using ESPAR Antenna," *IEEE Antennas and Wireless Prop. Letters*, vol. 15, Nov. 2016.

[54] X. Sun, Y. Ma, J. Xu, J. Zhang, and J. Wang, "A high Accuracy Mono-Station UWB Positioning System," in *Proc. of the Int. Conf. on Ultra-WideBand (ICUWB)*, Sep. 2008.

[55] X. Qing, Z. N. Chen, and T. S. P. See, "Sectored Antenna Array for Indoor Mono-Station UWB Positioning Applications," in *Proc. of the* 3^{rd} *European Conf. on Antennas and Propagation*, Mar. 2009, pp. 822–825.

[56] H. Zhang, X. Cui, B. An, and T. A. Gulliver, “A Distance and Angle Estimated Method based on Single UWB Station,” in *Proc. of the Int. Conf. on Sig. Proc., Comm. and Computing (ICSPCC)*, Aug. 2013.

[57] D. Vasisht, S. Kumar, and D. Katabi, “Decimeter-level Localization with a Single WiFi Access Point,” in *Proc. of the* 13^{th} *Usenix Conf. on Networked Systems Design and Implementation (NSDI)*, Mar. 2016.

Single-Anchor Positioning: Multipath Processing With Non-Coherent Directional Measurements

Michael Rath, Josef Kulmer, Erik Leitinger, and Klaus Witrisal

published in IEEE Access 8 (2020)

Abstract

High-accuracy indoor radio positioning can be achieved by using (ultra) wideband (UWB) radio signals. Multiple fixed anchor nodes are needed to compute the position or alternatively, specular multipath components (SMCs) extracted from radio signals can be exploited. In this work, we study a multipath-based, single-anchor positioning system that acquires directional measurements non-coherently. These non-coherent measurements can be obtained, e.g., from a single-chain mm-wave transceiver with analog beam steering or from a low-complexity ultra-wideband transceiver with switched directional antennas. The directional antennas support the separation of SMCs and the suppression of the undesired diffuse multipath component (DMC) with the benefit that the required signal bandwidth can be drastically reduced. The paper analyzes the Cramér-Rao lower bound (CRLB) on the position estimation error to gain insight in the influence of the system design parameters as well as the impact of the DMC on the position error. The CRLB is compared between the non-coherent antenna setup, a conventional array with coherent processing, and a single-antenna setup. A maximum-likelihood position estimation algorithm is formulated. Its performance is evaluated with synthetically generated data as well as with UWB measurements. We show that the accuracy and robustness are significantly improved due to the processing of angular information. Analyzing the measured data for a line-of-sight link, the median error decreases from 22 down to 7 cm, the measurements better than 20 cm increase from 46 to 95 %, and outliers above 50 cm reduce from 12 to 0 %.

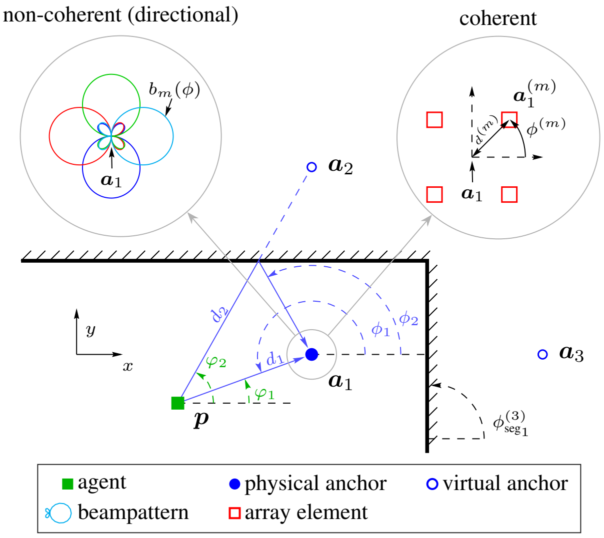

Figure 1: Exemplary environment in a room corner. There is one physical anchor at position $\boldsymbol{a}_1$, either equipped with a conventional coherent array indicated by red boxes (top right) or with directional antennas, each covering one sector of the azimuth plane (top left). Empty blue circles outside the room at $\boldsymbol{a}_2, \boldsymbol{a}_3$ indicate virtual anchors obtained by mirroring the anchor position $\boldsymbol{a}_1$ at reflective wall surfaces. The mobile agent at position $\boldsymbol{p}$ is indicated by a green filled box.

1. Introduction

1.1. Motivation and State of the Art

Fifth generation (5G) radio networks are expected to employ massive multiple-input multiple-output (MIMO) array antenna systems [1,2] due to the dramatic increase in energy efficiency and capacity, achieved by aggressive spatial multiplexing [3,4]. Array antennas in MIMO systems also open the gate to use millimeter-wave (mm-wave) based systems, since the array gain with a high number of antennas compensates the high pathloss present in these frequency bands (30-300 GHz) [5–7].

For positioning, large bandwidth enables good time resolution, whereas MIMO processing enables good angle resolution by exploiting array processing [8–14]. This conclusion has been drawn from the analysis of the Cramér-Rao lower bound (CRLB) on the position (and orientation) estimation error(s). The CRLB is a powerful tool to analyze the performance of positioning systems with regards to the impact of system parameters, such as bandwidth, carrier frequency, and antenna configuration. Additionally, the analysis of the CRLB gives insights about the impact of model-dependent multipath component (MPC) parameters, i.e., specular multipath component (SMC) and dense multipath component (DMC) parameters [10–15]. An increased signal bandwidth improves the delay resolution of SMCs and also the capability to suppress the DMC [10,12,14,15], and therefore it improves the delay information that can be extracted from received radio signals. Similarly, the angular information is enhanced by increasing the array aperture, as analyzed in detail in [11]. Here, the number of antenna elements is also related to a diversity gain in (dense) multipath channels [12–14], which reduces the bandwidth needed for a targeted performance.

Recent works [8, 15–18] build on leveraging SMCs for positioning if a sufficient signal bandwidth and/or number of antennas is accessible to enable high time and angle resolution. Each SMC carries position-related information stemming from its delay only [15] or from its delay, angle-of-departure (AoD), and angle-of-arrival (AoA) [16,17], leading to a reduced need for infrastructure (number of fixed anchors) and/or an increased redundancy (robustness). However, to exploit this information, it is necessary to model the relationship between parameters that characterize the SMCs and the position/orientation of a mobile agent. A geometric model of the environment can serve for this purpose. In the most simple case, this model consists of a set of *virtual anchors* (VAs) — mirror images of the physical anchor at flat surfaces [8, 19] — as illustrated in Fig. 1. Multipath-based positioning systems face the challenge of acquiring such maps of environment features. The works in [16, 17] consider the impact of estimating these map features on the Fisher information of the position and orientation error. In [20–24], simultaneous localization and mapping algorithms are presented that estimate the environment map from consecutive measurements, achieving accurate and robust position tracking of a mobile agent in challenging indoor environments. In [8, 25], the use of mm-wave antenna arrays was discussed for multipath-based indoor positioning.

All these references show that coherent antenna array systems are advantageous for robust high-accuracy positioning. However, their common drawback is the increased hardware complexity and the resulting (peak) power consumption. Each additional transceiver chain multiplies the hardware needed for the signal acquisition/generation and the corresponding frontend signal processing steps. This makes the use of parallel, coherent processing of all the antenna signals very expensive, in particular for ultra-wide bandwidth (UWB) signals with sampling frequencies in the GHz-range. Hybrid analog-digital architectures have been proposed as an alternative for massive-MIMO mm-wave base-stations aiming at very high antenna directivities [26–28]. In this architecture, the number of radio frequency chains is much smaller than the number of antennas [29]; potentially only one transceiver chain is implemented. The main idea is to use analog beamforming (e.g. phase shifters or directive antenna elements) to gain directivity and only process one or a few received signals coherently [30].

A similar principle has been employed in [31], where a single-anchor, multipath-based positioning system has been described for high-accuracy (indoor) positioning for low-cost Internet-of-Things applications. A switched antenna system with four directive antenna elements is used, pointing in the four cardinal directions, in order to facilitate the reliable separation of MPCs [32]. As an example, the top left of Fig. 1 illustrates the antenna configuration from [31, 32], where UWB radios are used according to the IEEE802.15.4 standard.

With the newly proposed “phase-based ranging” extension [33], accurate delay and angle estimation also becomes applicable to Bluetooth Low Energy signals. However, it remains to be investigated if a multipath-based positioning system can be realized with this technology. Furthermore, switched directive antennas were also proposed for RSS-based indoor positioning [34, 35]. In [36], the CRLB was derived for RSS-based indoor positioning using switched directive antennas.

Both analog/hybrid beamforming as well as switched antenna systems are not capable of acquiring *coherent* measurements for conventional phase-based array processing, because signals from multiple antennas are measured *consecutively* rather than in parallel. Phase coherence between such consecutive measurements is very hard to achieve, given the high demands on radio-frequency oscillators and the potential dynamics of the environment, especially with mm-wave radios [28].

1.2. Contributions of the Paper

In this work, we analyze a single-anchor positioning system exploiting SMCs, which is capable of acquiring channel impulse response measurements with a set of different directive antennas. Potentially, these measurements are not phase-coherent with respect to one another. We derive the CRLB on the position error to evaluate the theoretical performance limit of this positioning system, in comparison to a conventional antenna-array system and a single-antenna setup. An illustration of both antenna setups is shown in Fig. 1. For conventional coherent processing, the anchor is equipped with an array of antennas of known geometry radiating in an isotropic manner (shown on the right for a rectangular constellation). For so-called "non-coherent" processing, a set of directional antennas is used with known beampatterns (as shown on the left). We also consider the DMC to model the interference effect of non-specular multipath components in a more realistic form in contrast to an AWGN model.

We significantly extend our initial error bound analysis provided in [32], in particular, a detailed analysis of AoA information has been included yielding guidelines for the design of antenna radiation patterns. Furthermore, we describe a positioning algorithm based on our previous work in [31, 37, 38] and analyze its performance in comparison to the CRLB, using synthetically generated data as well as measured data. Our specific contributions are:

- We analyze the CRLB for a multipath signal model, considering non-coherent antenna arrays with directional beampatterns in comparison to conventional coherently processed antenna arrays (Sections 3 & 4).

- We quantify the contributions of delay and angle information of SMCs to the position information, taking into account self-interference by the DMC (Section 5).

- We develop and analyze positioning algorithms for the non-coherent directional antenna array (Section 6).

1.3. Notations

Boldface upper case letters represent matrices. Boldface lower case letters denote column vectors. Superscripts $^{\mathrm{T}}$, * and $^{\mathrm{H}}$ denote matrix transpose, complex conjugation and Hermitian transpose, respectively. The Kronecker product is denoted with $\otimes$. $\|\cdot\|$ is the Euclidean norm. $|\cdot|$ represents the absolute value. $\hat{\mathbf{A}}$ denotes an estimate of $\mathbf{A}$. $\boldsymbol{I}_{[\cdot]}$ represents the identity matrix with dimension denoted in the subscript $[\cdot]$. $\mathbb{E}\{\cdot\}$ denotes the expectation operator.

2. Problem Formulation

We consider the task of finding the position $\boldsymbol{p}$ of an agent node using radio signal measurements from one anchor node located at known position $\boldsymbol{a}_1$. We first examine the complete channel model and extract an approximation that contains position-related parameters. Then, we consider the received signal model to describe the recorded observations that will be used to determine the agent position. Finally, we describe how the channel parameters are related to the geometry of the environment.

2.1. Channel Model

The radio channel between the agent at position $\boldsymbol{p}$ and the anchor at position $\boldsymbol{a}_1$ is described with the spreading function [39] according to

$$h(\phi,\tau) = \sum_{k=1}^{K} \alpha_k e^{j\zeta_k}\,\delta(\phi-\phi_k)\,\delta(\tau-\tau_k) + \nu(\phi,\tau) \tag{1}$$

where $\delta(\cdot)$ denotes the Dirac delta function. This equation describes the superposition of MPCs that originate from reflections in the environment. For the sake of simplicity, we assume a two-dimensional scenario with horizontal-only propagation (in the azimuth plane).[1] The rational behind the selection of the model in (1) is that for radio measurements conducted with a finite observation aperture in space and frequency, not all MPCs can be resolved in distinct SMCs. Therefore, we assume that separated MPCs are collected into a set of $k = 1 \dots K$ SMCs and all unresolvable MPCs originating for example from diffuse scattering are described by a DMC [39, 40]. Each SMC is described by amplitude α_k, phase ζ_k, AoA ϕ_k and delay τ_k. The latter two parameters can be related to the agent position via the geometry of the environment as exemplified in Fig. 1 (for the delay, the corresponding path length d_k is shown). This will be described in detail in Sec. 2.4. The DMC $\nu(\phi,\tau) \in \mathbb{C}$ is modeled as a complex circular (i.e. zero-mean) Gaussian random process [40, 41]. Assuming uncorrelated scattering (US) in the delay and angular domains, the auto-correlation function of $\nu(\phi,\tau)$ is given by

$$R_{\nu\nu}(\phi,\phi';\tau,\tau') = S_\nu(\phi,\tau)\,\delta(\phi-\phi')\,\delta(\tau-\tau') \tag{2}$$

where $S_\nu(\phi,\tau)$ describes the azimuth-delay power spectrum [39] at the anchor position.

2.2. Received Signal Model

The anchor node employs an antenna array which consists of M antennas, each of which exhibits a beampattern $b_m(f,\phi)$. When referring to the general anchor position, we use $\boldsymbol{a}_1$ which is defined to be the mass point of the antenna array. On the other hand, the position of the mth antenna element at the anchor is denoted by $\boldsymbol{a}_1^{(m)}$. The agent transmits a lowpass-equivalent signal $s(t)$ modulated by carrier frequency f_c and the anchor receives signal $r_m(t)$ using antenna m.[2] We aim for a compact description and introduce the following assumptions.

- For the antennas at the anchor, in frequency domain, we assume identical beampatterns over all relevant frequencies, i.e., we use $b_m(f,\phi) = b_m(\phi)$ for the complex-valued azimuth antenna gains.
- For the time-domain description of radio waves impinging at the antenna elements, we make use of the far-field *plane-wave assumption*, i.e., we assume planar wave fronts instead of spherical ones.

---

[1] An extension to three dimensional scenarios with horizontal and vertical propagation is straightforward, but it would lead to cumbersome notations without bringing significant additional insights.

[2] Note that we assume that the anchor and the agent are synchronized. This can be achieved by using a two-way transmission protocol [42]. However, the proposed model can be extended to non-synchronized anchor-agent links along the lines of [15] (based on the fact that the relevant geometric information is also contained in the time differences of the SMCs).

- Introduced time delays at antenna elements in relation to the mass point will be only considered in terms of a phase change, i.e., the time delay of the signal envelope will be neglected. This is usually referred to as the *narrowband/wideband assumption*[3] and it is fair to use since the envelope information is negligible with respect to the phase information, especially in practical situations [11,13,14].

We apply these assumptions to obtain the received signal at antenna m via convolution of the spreading function in (1) with the transmitted signal $s(t)$ and antenna response $b_m(\phi)e^{j\zeta^{(m)}(\phi)}$ resulting in

$$\begin{aligned} r_m(t) &= \iint b_m(\phi)e^{j\zeta^{(m)}(\phi)} s\big(t-\tau\big)\, h(\phi,\tau)\,\mathrm{d}\phi\,\mathrm{d}\tau + w_m(t) \\ &= \sum_{k=1}^{K} b_m(\phi_k)\alpha_k e^{j\zeta_{k,m}}\, s(t-\tau_k) + r_m^{\mathrm{DM}}(t) + w_m(t) \end{aligned} \tag{3}$$

which can be separated in three distinct parts: The first part contains the position-related SMC parameters $\{\phi_k\}$ and $\{\tau_k\}$ which shift and scale the transmitted signal. The second part $r_m^{\mathrm{DM}}(t)$ is a stochastic process characterizing the self-interference due to the DMC. Finally, measurement noise $w_m(t)$ is modeled as additive white Gaussian noise (AWGN) with double-sided power spectral density of $\frac{N_0}{2}$. The SMC-related phase shifts are given as

$$\zeta_{k,m} = \zeta^{(m)}(\phi_k) + \zeta_k \tag{4}$$

where $\zeta^{(m)}(\phi)$ captures the antenna related phase shift and ζ_k the radio channel related one.

In the case of coherent array processing, only the K radio channel related phase shifts ζ_k are unknown in (4) and the systematic phase-offset introduced by the placement of antenna m w.r.t. reference position $\boldsymbol{a}_1$ is given as

$$\begin{aligned} \zeta^{(m)}(\phi) &= 2\pi f_{\mathrm{c}} \tau^{(m)}(\phi) \\ &= 2\pi \tfrac{d^{(m)}}{\lambda} \cos\big(\phi - \phi^{(m)}\big) \end{aligned} \tag{5}$$

where $\tau^{(m)}(\phi)$ is the time delay due to the distance of the antenna elements (situated at $\boldsymbol{a}_1^{(m)}$) relative to the phase center at $\boldsymbol{a}_1$, $d^{(m)}$ and $\phi^{(m)}$ denote the distance and angle of the mth antenna w.r.t. $\boldsymbol{a}_1$ (cf. Fig. 1), and λ is the wavelength at f_c. In the case of non-coherent processing, all measurements at the M antennas have unknown phase-offsets meaning that all $K \cdot M$ phase shifts $\zeta_{k,m}$ given by (4) are unknown.

The second part of (3) characterizes self-interference caused by the DMC and it is given as

$$r_m^{\mathrm{DM}}(t) = \iint b_m(\phi)e^{j\zeta^{(m)}(\phi)} s(t-\tau)\, \nu(\phi,\tau)\,\mathrm{d}\phi\,\mathrm{d}\tau.$$

We look at correlation properties of this signal for a pair of antennas

$$\begin{aligned} \mathbb{E}\big\{r_m^{\mathrm{DM}}(t)(r_{m'}^{\mathrm{DM}}(t'))^*\big\} = \iint & S_\nu(\phi,\tau) b_m(\phi)\, b_{m'}^*(\phi) \\ & \times e^{j(\zeta^{(m)}(\phi) - \zeta^{(m')}(\phi'))} s(t-\tau)\, s(t'-\tau)\,\mathrm{d}\phi\,\mathrm{d}\tau \end{aligned} \tag{6}$$

---

[3] With the narrowband/wideband model, it is assumed that delay and angle domains are separated, i.e., space-frequency cross-product terms are zero [43, Ch. 4.2].

where we applied the US assumption from (2). It should be noted that this assumption also allows us to use the same stochastic process $\nu(\phi,\tau)$ for all antenna elements, because the assumption implies homogeneity in the spatial domain [44, Ch. 2.4].

2.3. Discrete-Time Signal Model

In a practical system, the anchor acquires N samples of the received signal sampled with frequency $f_\mathrm{s} = 1/T_\mathrm{s}$ such that $[\boldsymbol{r}_m]_i = r_m([i-1]\cdot T_\mathrm{s})$, $i = 1 \dots N$ and stacks them into the observation vector $\boldsymbol{r} = [\boldsymbol{r}_1^T, \dots, \boldsymbol{r}_M^T]^T \in \mathbb{C}^{MN\times 1}$, given as

$$\boldsymbol{r} = \boldsymbol{x}(\boldsymbol{\theta}) + \boldsymbol{n}. \tag{7}$$

Here, we have on the one hand the SMC-related term $\boldsymbol{x}(\boldsymbol{\theta})$ as a function of the SMC parameters $\boldsymbol{\theta}$, and on the other hand the DMC and noise related term $\boldsymbol{n}$. In the following, we will describe these two terms in detail.

2.3.1. SMCs

The SMC part of the observation in (7) is described by

$$\boldsymbol{x}(\boldsymbol{\theta}) = [\boldsymbol{b}(\phi_1)\otimes\boldsymbol{s}(\tau_1), \dots, \boldsymbol{b}(\phi_K)\otimes\boldsymbol{s}(\tau_K)]\,\boldsymbol{\alpha} \tag{8}$$

with

$$\begin{aligned}\boldsymbol{s}(\tau_k) &= \left[s(0\cdot T_\mathrm{s}-\tau_k), \dots, s([N-1]\cdot T_\mathrm{s}-\tau_k)\right]^\mathrm{T} \ \in \mathbb{R}^{N\times 1}\\ \boldsymbol{\alpha} &= \left[\alpha_1, \dots \alpha_K\right]^\mathrm{T} \ \in \mathbb{R}^{K\times 1}\\ \boldsymbol{b}(\phi_k) &= \left[b_1(\phi_k)e^{j\zeta_{k,1}}, \dots, b_M(\phi_k)e^{j\zeta_{k,M}}\right]^\mathrm{T} \in \mathbb{C}^{M\times 1}.\end{aligned}$$

The parameter vector $\boldsymbol{\theta}$ contains the SMC parameters

$$\boldsymbol{\theta} = \left[\boldsymbol{\phi}^\mathrm{T}, \boldsymbol{\tau}^\mathrm{T}, \boldsymbol{\alpha}^\mathrm{T}, \boldsymbol{\zeta}^\mathrm{T}\right]^\mathrm{T} \tag{9}$$

where its components are of dimension $\mathbb{R}^{K\times 1}$. Of special mention is the phase parameter $\boldsymbol{\zeta}$, which is only of the same dimension if coherent processing is performed, i.e., if the antenna phases are determined by (5). However, our focus will be on the non-coherent case where $\boldsymbol{\zeta} \in \mathbb{R}^{(KM)\times 1}$ contains all phase shifts $\zeta_{k,m}$, since they are all unknowns. Hence, in this case, the stacked parameter vector $\boldsymbol{\theta}$ is of dimension $\mathbb{R}^{(3K+KM)\times 1}$.

2.3.2. DMC and Noise

The vector $\boldsymbol{n} = \boldsymbol{n}_\nu + \boldsymbol{w} \ \in \mathbb{C}^{MN\times 1}$ represents the DMC process and the measurement noise as a Gaussian process with covariance matrices

$$\boldsymbol{C}_{\boldsymbol{n}} = \boldsymbol{C}_{\boldsymbol{\nu}} + \sigma_w^2 \boldsymbol{I}_{MN} \ \in \mathbb{C}^{MN\times MN} \tag{10}$$

where $\sigma_w^2 = N_0/T_s$ is the measurement noise variance and $\boldsymbol{C}_{\boldsymbol{\nu}}$ is the DMC covariance matrix. For the DMC covariance matrix we need to take correlations between antenna elements into account. To this end, we can separate $\boldsymbol{C}_{\boldsymbol{\nu}}$ into blocks of size $N \times N$, each describing the correlations between one pair of antennas indexed as, e.g., (m, m'). We may use (6) to write one block of the DMC covariance matrix as

$$\begin{aligned}\boldsymbol{C}_{\boldsymbol{\nu}}^{(m,m')} = \iint & S_\nu(\phi,\tau)\, b_m(\phi)\, b_{m'}^*(\phi)\, e^{j(\zeta^{(m)}(\phi)-\zeta^{(m')}(\phi))}\\ & \times \boldsymbol{s}(\tau)\boldsymbol{s}(\tau)^\mathrm{H}\,\mathrm{d}\phi\,\mathrm{d}\tau.\end{aligned} \tag{11}$$

2.4. Relating SMCs to geometry

We describe the SMC parameters contained in $\boldsymbol{\theta}$ in more detail, considering their relation to the agent position. It should be emphasized that we will use the environment geometry, that is, we assume that each SMC involves the reflection on flat surfaces such as wall segments, as shown in Fig. 1. These segments can be described by a surface normal, or rather in the case of azimuth plane operation, by a single segment angle as will be described later. We aim for a compact and efficient computation of the parameters when anchor and surface positions are known. The SMC delay (time-of-flight) τ_k is related to the path length d_k by

$$\tau_k = \tfrac{1}{c} d_k = \tfrac{1}{c} \|\boldsymbol{a}_k - \boldsymbol{p}\| \tag{12}$$

where c is the propagation velocity. Here, $\boldsymbol{a}_k$ is the position of a VA [8, 45] that results from mirroring the anchor position on a known reflective surface in the environment, as exemplified in Fig. 1 by $\boldsymbol{a}_2$ and $\boldsymbol{a}_3$. Note that Fig. 7.10 in [19, Chapter 7.5] provides a detailed description of this operation called the image-source principle. For higher-order reflections, the mirroring process is repeated in the sequence of reflecting surfaces along the propagation path.

Considering the angle domain, the AoD φ_k at the agent is given by $\varphi_k = \measuredangle(\boldsymbol{a}_k - \boldsymbol{p})$. Using the angles of all involved wall segments, the AoD φ_k at the agent can be related to the AoA at the anchor node by

$$\phi_k = (-1)^{\mathcal{O}(k)} \big(\varphi_k - \pi\big) - 2 \sum_{j=1}^{\mathcal{O}(k)} (-1)^j \, \phi_{\mathrm{seg}_j}^{(k)} \tag{13}$$

where $\mathcal{O}(k)$ denotes the order of the reflection associated with MPC k, and $\phi_{\mathrm{seg}_j}^{(k)}$ denotes the angle of the jth involved reflective segment in the propagation path with $j = 1, \ldots, \mathcal{O}(k)$ ordered according to the sequence of bounced surfaces. As an example, see Fig. 1 for the segment angle related to VA $\boldsymbol{a}_3$.

What remains is the amplitude α_k and phase $\zeta_{k,m}$. The amplitude incorporates effects such as path-loss and reflection losses, whereas the phase incorporates the influence of reflections depending on the involved materials. These parameters are not easily related to the geometry and are thus treated as nuisance parameters in the position estimation problem.

3. Fisher information of channel parameters

On the basis of the signal model in (7) and (8), we can examine the useful information present in observed signals. To this end, we will determine the Fisher information matrix (FIM). The elements of this matrix quantify the amount of information that the observable vector $\boldsymbol{r}$ carries about the unknown parameters $\boldsymbol{\theta}$.

3.1. Fisher information matrix

The FIM $\boldsymbol{\mathcal{I}_\theta}$ on the parameter vector $\boldsymbol{\theta}$ is used to obtain the Cramér-Rao lower bound (CRLB) [46, 47] for an estimated parameter vector of $\hat{\boldsymbol{\theta}}$ via

$$\mathbb{E}\big\{\|\boldsymbol{\theta} - \hat{\boldsymbol{\theta}}\|^2\big\} \geq \mathrm{tr}\left(\boldsymbol{\mathcal{I}}_{\boldsymbol{\theta}}^{-1}\right). \tag{14}$$

The CRLB provides a lower bound on the variance of any unbiased estimator for the model parameters. The FIM, considering the Gaussian model with known covariance matrix $\boldsymbol{C_n}$, is defined as [47, Chapter 15.7]

$$\boldsymbol{\mathcal{I}_\theta} = 2\,\Re\left\{\boldsymbol{J}_{\boldsymbol{\theta}}^{\mathrm{H}}\boldsymbol{C}_{\boldsymbol{n}}^{-1}\boldsymbol{J}_{\boldsymbol{\theta}}\right\} \tag{15}$$

where $\boldsymbol{J_\theta}$ denotes the Jacobian of the signal model with respect to the elements of a length-L_θ parameter vector

$$\boldsymbol{J_\theta} = \left[\left(\frac{\partial}{\partial\theta_1}\boldsymbol{x}(\boldsymbol{\theta})\right), \ldots, \left(\frac{\partial}{\partial\theta_{L_\theta}}\boldsymbol{x}(\boldsymbol{\theta})\right)\right] \in \mathbb{R}^{MN\times L_\theta}. \tag{16}$$

In our case, using non-coherent processing, the number of parameters is $L_\theta = K(3+M)$. We define sub-matrices $\boldsymbol{\mathcal{I}_{\vartheta\vartheta'}}$ [15], where $\boldsymbol{\vartheta}, \boldsymbol{\vartheta}' \in \{\boldsymbol{\phi}, \boldsymbol{\tau}, \boldsymbol{\alpha}, \boldsymbol{\zeta}\}$. These sub-matrices cover all combinations of parameter types to assemble the full FIM from (15). The structure of the full FIM $\boldsymbol{\mathcal{I}_\theta}$ using these sub-matrices can be found in (50), whereas one element $[\cdot]_{k,k'}$ of $\boldsymbol{\mathcal{I}_{\vartheta\vartheta'}}$ is outlined in (51), both shown in Appendix A.

3.2. Towards CRLB: Equivalent FIM

Our main interest concerns the lower bound on the estimation of the delays τ_k and AoAs ϕ_k, and the resulting position estimation performance. Hence, we want to determine sub-matrices of the inverse FIM, in particular the respective block matrices on the main diagonal related to one type of parameter. For this purpose, it is beneficial to define the equivalent FIM (EFIM) [10] as

$$\widetilde{\boldsymbol{\mathcal{I}_\vartheta}} = \boldsymbol{\mathcal{I}_{\vartheta\vartheta}} - \boldsymbol{\mathcal{I}}_{\boldsymbol{\vartheta}\overline{\boldsymbol{\vartheta}}}\boldsymbol{\mathcal{I}}_{\overline{\boldsymbol{\vartheta}}\,\overline{\boldsymbol{\vartheta}}}^{-1}\boldsymbol{\mathcal{I}}_{\boldsymbol{\vartheta}\overline{\boldsymbol{\vartheta}}}^{\mathrm{H}} \tag{17}$$

where $\overline{\boldsymbol{\vartheta}}$ stacks the vectors of all remaining parameters, i.e. $\overline{\boldsymbol{\vartheta}} = \boldsymbol{\theta} \setminus \boldsymbol{\vartheta}$. The CRLB on the corresponding parameter can be obtained by computing the inverse of the respective EFIM. It should be noted that we rearrange the sub-matrices in (50) such that any desired parameter type is in the top left to make use of this inversion lemma. Numeric evaluation of (17) will allow for the evaluation of the CRLB for the respective parameter vector. The benefit of the EFIM definition is that the cross-dependence of the estimation of the parameters in $\boldsymbol{\vartheta}$ on any other parameters, described by the matrix $\boldsymbol{\mathcal{I}}_{\boldsymbol{\vartheta}\overline{\boldsymbol{\vartheta}}}$, turns approximately to $\mathbf{0}$ in many cases. Thus, it becomes sufficient to derive the inverse of the sub-matrix $\boldsymbol{\mathcal{I}_{\vartheta\vartheta}}$, yielding far more insightful formulations. In the following, we will present the derivations of the EFIM for the SMC delay and angle estimation using the assumptions given in Appendix B that allow further insightful discussions in terms of contributions to position information. Note that in general (17) can be used to compute the CRLB on the position error numerically without using the assumptions given in (65), (66) and (69). However, to gain more insights into the structure of the CRLB, we use these assumptions in what follows.

3.3. EFIM for SMC delay estimation

Based on the assumptions (65), (66) and (69) in Appendix B, the EFIM for delay estimation can be derived as (62) given in Appendix A. It can be rearranged in the following form

$$\left[\widetilde{\boldsymbol{\mathcal{I}_\tau}}\right]_{k,k} = 8\,\pi^2\,\beta_k^2\,\|\boldsymbol{b}(\phi_k)\|^2\,\mathrm{SINR}_k\,\xi_k^{\mathrm{delay}} \tag{18}$$

where

$$\beta_k^2 = \frac{\|\dot{\boldsymbol{s}}(\tau_k)\|_{\mathcal{H}}^2}{4\,\pi^2\,\|\boldsymbol{s}(\tau_k)\|_{\mathcal{H}}^2} \tag{19}$$

is the (mean-square) bandwidth of the *whitened* signal $\boldsymbol{s}(\tau_k)$ and $\dot{\boldsymbol{s}}(\tau) = \partial \boldsymbol{s}/\partial \tau$ denotes the derivative of the signal $\boldsymbol{s}(\tau)$ w.r.t. the delay τ, and

$$\mathrm{SINR}_k = \frac{|\alpha_k|^2}{N_0} \, \|\boldsymbol{s}(\tau_k)\|^2_{\mathcal{H}} \, T_{\mathrm{s}} \tag{20}$$

is the signal-to-interference-plus-noise-ratio (SINR), quantifying the level of DMC plus noise interference in one SMC. We use $\| \cdot \|^2_{\mathcal{H}}$ to denote the squared weighted norm (taking the noise model into account) which is described by (68) in Appendix B. The factor $\xi_k^{\mathrm{delay}} \in [0, 1]$ can be interpreted as the information loss on the SMC delay estimation induced by the complex amplitude estimation in the DMC [12,15], and it is given in (62) in Appendix A. We introduce the whitening gain $\gamma_k = \beta_k^2/\beta_0^2$, where $\beta_0^2 = \|\dot{\boldsymbol{s}}(\tau)\|^2/(4\pi^2\|\boldsymbol{s}(\tau)\|^2)$ is the mean-square bandwidth of signal $\boldsymbol{s}(\tau)$, and the *effective SINR*, $\widetilde{\mathrm{SINR}}_k = \mathrm{SINR}_k \, \gamma_k \, \xi_k^{\mathrm{delay}}$. Then, the EFIM for delay estimation in (18) can be rewritten as

$$\big[\widetilde{\boldsymbol{\mathcal{I}}_{\boldsymbol{\tau}}}\big]_{k,k} = 8\,\pi^2\,\beta_0^2 \sum_{m=1}^{M} |b_m(\phi_k)|^2 \, \widetilde{\mathrm{SINR}}_k \tag{21}$$

which is equivalent to what was shown in [12], with the difference that there is a weighting by the squared beampattern values, hence a gain dependent on the directionality.

3.4. EFIM for SMC AoA Estimation

We follow an analogous approach for the EFIM of the AoA estimation, i.e., we use the assumptions (65), (66) and (69) in Appendix B. The EFIM for AoA estimation in (63), in Appendix A, can be rearranged in the following form

$$\begin{aligned}\big[\widetilde{\boldsymbol{\mathcal{I}}_{\boldsymbol{\phi}}}\big]_{k,k} &= 2\,\mathrm{SINR}_k \, \|\dot{\boldsymbol{b}}(\phi_k)\|^2 \, \xi_k^{\mathrm{angle}} \\ &= 2\,\mathrm{SINR}_k \, \xi_k^{\mathrm{angle}} \sum_{m=1}^{M} |\dot{b}_m(\phi_k)|^2 \end{aligned} \tag{22}$$

where $\dot{\boldsymbol{b}}(\phi) = \partial \boldsymbol{b}/\partial \phi$ with $\dot{b}_m(\phi) = \partial b/\partial \phi$ denoting the derivative of the mth antenna's beampattern w.r.t. ϕ. The factor $\xi_k^{\mathrm{angle}} \in [0, 1]$ can be interpreted as the information loss on the SMC AoA estimation induced by the complex amplitude estimation in the DMC, and it is given in (63) in Appendix A.

A common property of antenna characteristics is an approximately symmetric beampattern, i.e., the beampattern can be described by an even function. In this case, due to the property of even functions exhibiting an odd function as derivative, there is orthogonality between the function and its derivative amounting to $\big\langle \dot{\boldsymbol{b}}(\phi_k), \boldsymbol{b}(\phi_k) \big\rangle \approx 0$. Therefore, we have $\xi_k^{\mathrm{angle}} \approx 1$ in (63) neglecting the information loss related to the angles in the upcoming derivations. Introducing the non-coherent normalized square array aperture

$$D_b^2(\phi) = \frac{1}{4\pi^2 M} \sum_{m=1}^{M} |\dot{b}_m(\phi)|^2 \tag{23}$$

the EFIM for AoA estimation in (22) can be rewritten as

$$\big[\widetilde{\boldsymbol{\mathcal{I}}_{\boldsymbol{\phi}}}\big]_{k,k} = 8\,\pi^2\,\mathrm{SINR}_k \, M \, D_b^2(\phi_k)\,. \tag{24}$$

3.5. Comparison to Coherent Processing

For a conventional antenna array with coherent processing, we obtain (cf. [11, 13])

$$\left[\widetilde{\mathcal{I}_{\boldsymbol{\phi}}}\right]_{k,k} = 8\pi^2 \mathrm{SINR}_k \, M \, D_\lambda^2(\phi_k) \tag{25}$$

with

$$D_\lambda^2(\phi) = \frac{1}{M} \sum_{m=1}^{M} \left(\frac{d^{(m)}}{\lambda} \right)^2 \sin^2\left(\phi - \phi^{(m)}\right) \tag{26}$$

which will serve as a reference result. The factor (26) has been interpreted as a coherent normalized squared aperture that scales the amount of angle information available. (Note the similarity to the scaling of delay information by the squared bandwidth.) The accompanying array response beampattern using (5) is given by

$$b_\lambda(\phi) = \frac{1}{M} \sum_{m=1}^{M} \exp\left(j2\pi \tfrac{d^{(m)}}{\lambda} \cos\left(\phi - \phi^{(m)}\right) \right). \tag{27}$$

For a numeric comparison of the squared apertures from (23) and (26), it is convenient to write the beampattern of antenna m as a Fourier series,

$$b_m(\phi) = b(\phi + m\tfrac{2\pi}{M}) = \sum_{\ell=-\infty}^{\infty} c_\ell e^{j\ell m \frac{2\pi}{M}} e^{j\ell\phi} \tag{28}$$

where coefficients c_ℓ describe the generic beam pattern $b(\phi)$ which is rotated by $m\frac{2\pi}{M}$ for antenna m. For non-coherent processing, a real-valued beampattern is assumed, hence $c_\ell = c_{-\ell}^*$. Straightforward manipulations yield

$$\|\boldsymbol{b}(\phi)\|^2 = M \sum_{\eta=-\infty}^{\infty} \sum_{\ell=-\infty}^{\infty} c_\ell c_{\ell-\eta M}^* e^{j\eta M\phi} \tag{29}$$

where the inner sum is the autocorrelation of the Fourier coefficients, c_ℓ, at lags ηM. For $\eta = 0$, this expression corresponds to a constant squared norm, whereas for $|\eta| \geq 1$, deviations from this constant are quantified. The deviations have a periodicity of $\frac{2\pi}{M}$, obviously.

We can use this insight to design antenna patterns that minimize or avoid fluctuations of $\|\boldsymbol{b}(\phi)\|^2$ as a function of ϕ, which is important to yield uniform delay information, independent of ϕ_k, cf. (18). Such constant delay information will be obtained when only coefficients $c_\ell \neq 0$ for $|\ell| \leq (M-1)/2$, yielding $\|\boldsymbol{b}(\phi)\|^2 = M \sum_\ell |c_\ell|^2$. Normalizing the energy of the beam pattern to one, i.e. $\|b(\phi)\|^2 = \sum_\ell |c_\ell|^2 = 1$, we get $\|\boldsymbol{b}(\phi)\|^2 = M$. It is seen that an SINR gain by a factor of M is obtained, which is identical to the SINR gain obtained with conventional coherent processing [12, 13].

To gain insight in the *equivalent* aperture value of the non-coherent antenna configuration, we analyze the expression (23). We re-use the Fourier series representation of $b_m(\phi)$ from (28), to reformulate (23) as

$$D_b^2(\phi) = \frac{1}{4\pi^2} \sum_{\eta=-\infty}^{\infty} \sum_{\ell=-\infty}^{\infty} \ell c_\ell (\ell - \eta M) c_{\ell-\eta M}^* e^{j\eta M\phi} \tag{30}$$

where the inner sum is the autocorrelation of the Fourier coefficients of the beampattern derivative, ℓc_ℓ, at lags ηM. Again, this expression corresponds to a

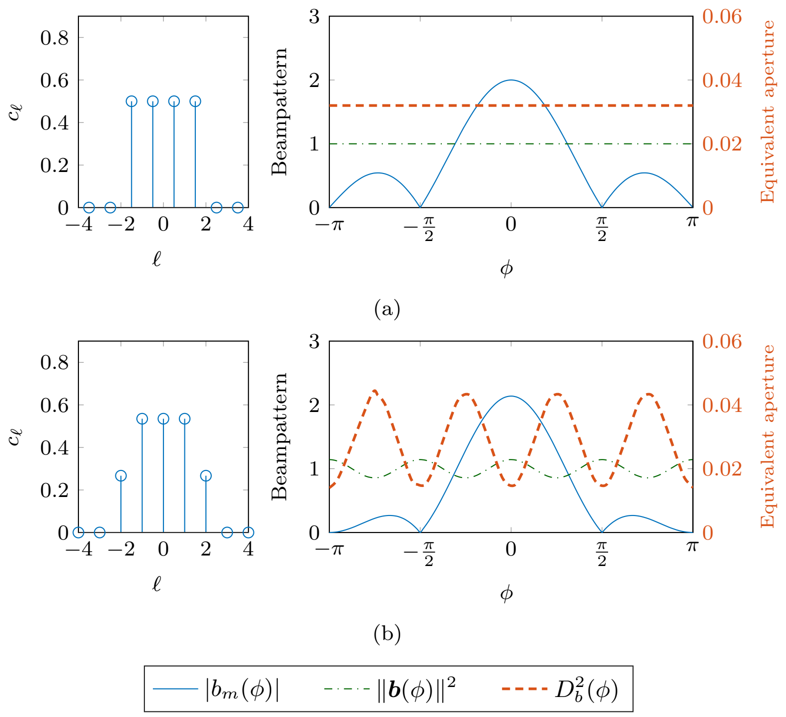

(a)

(b)

Figure 2: Beampattern design using $M = 4$ antennas to generate (a) a Dirichlet shape and (b) a raised-cosine shape. The left plots show the choice of Fourier coefficients c_ℓ for (a) $\ell = \{-1.5, -0.5, 0.5, 1.5\}$ and (b) $\ell = -2 \dots 2$ (where $c_\ell = 0$ for $|\ell| > 2$); the right plots show the resulting beampatterns and the equivalent apertures obtained via (28)-(30).

constant for $\eta = 0$, whereas for $|\eta| \geq 1$, deviations from this constant are quantified, which are periodic with $\frac{2\pi}{M}$. We can use this insight to design antenna patterns that minimize or avoid fluctuations of the angle information as a function of ϕ. In particular, constant angle information will be obtained when only coefficients $c_\ell \neq 0$ for $|\ell| \leq (M-1)/2$, yielding

$$\widetilde{D_b}^2(\phi) = \frac{1}{4\pi^2} \sum_{\ell=-(M-1)/2}^{(M-1)/2} \ell^2 |c_\ell|^2. \tag{31}$$

Choice of a constant $c_\ell = 1/\sqrt{M}$ for $|\ell| \leq (M-1)/2$ yields a Dirichlet kernel for the beam pattern with normalized energy $\|b(\phi)\| = 1$. It will have an equivalent squared aperture

$$\widetilde{D_b}^2(\phi) = \frac{1}{4\pi^2} \frac{M^2 - 1}{12} \tag{32}$$

which scales quadratically in the number of array elements. Fig. 2 exemplifies beampattern designs for a setup of $M = 4$ antennas. On the one hand, we have the previously described choice of uniform Fourier coefficients, shown on the left of Fig. 2a and the accompanying shape shown on the right, where a constant equivalent aperture is achieved. For comparison, in Fig. 2b we show a choice of coefficients that results in a raised-cosine shape, which means reduced sidelobes

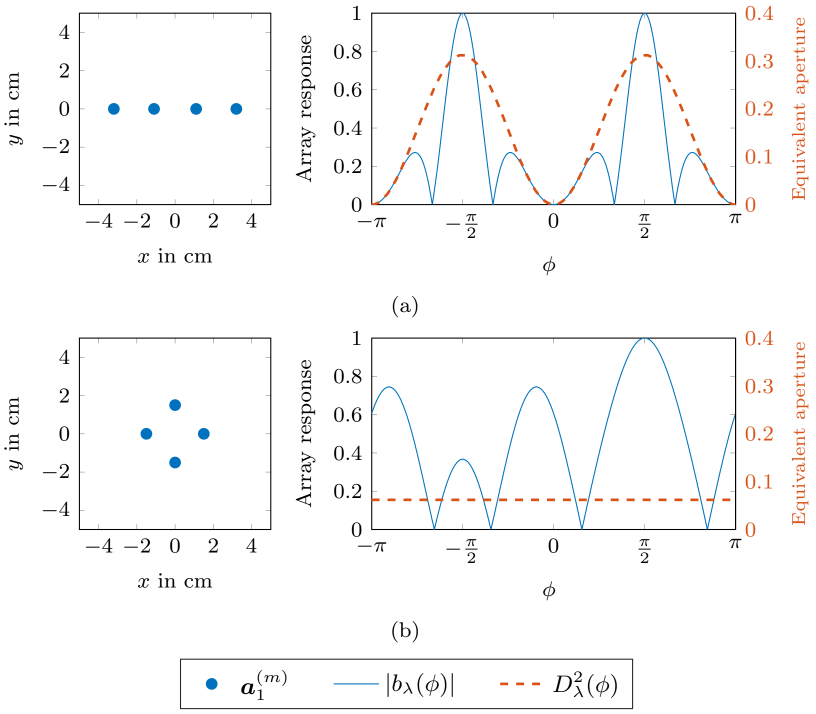

(a)

(b)

Figure 3: Array responses of coherent antenna arrays using $M = 4$ antennas, steered towards an angle of $\frac{\pi}{2}$ for (a) a uniform linear array and (b) a rectangular array. The left plots show the array geometry (anchor antenna positions) and the right plots show the resulting array responses and equivalent apertures obtained via (26) and (27).

for the beampattern shape at the cost of a ripple in the equivalent aperture, i.e., varying delay and AoA information for different directions.

Comparison to a uniform linear array with coherent processing and $\lambda/2$-spacing [13, Eq. (33)] reveals the same scaling with M and an increase by a factor of π^2 in broadside direction. The improvement is apparently at the cost of information in end-fire direction. In a uniform circular array, a constant $D^2_\lambda(\phi) \approx M^2/(16\pi^2)$ is obtained (for $M \gg 1$) which differs from (32) by a factor of 3. Fig. 3 shows illustrations of these array geometries with accompanying array responses (see [48, Sec.3]) and information gains for a steering in direction $\frac{\pi}{2}$. These results demonstrate the close correspondence between the angle information retrieved from the non-coherent antenna setup and a conventional, coherent array. The root-EFIM of the angle parameter will be reduced by a factor of $\sqrt{3}$ for the non-coherent case. We will further evaluate and compare the two antenna configurations in Section 5 by means of numerical results.

4. Error bound for positioning

This far, we derived the full FIM and EFIMs for our parameter vector $\boldsymbol{\theta}$. In the following, we evaluate the obtainable position accuracy for our measurement model. For that matter, we determine the CRLB for the agent position, termed *position error bound* (PEB) [10]. The PEB acts as a comprehensible quality measure that can be used as a benchmark for practical estimators.

4.1. General PEB

When the FIM is available for the observation model parameters, we can relate it to the PEB via a parameter transformation [10]. As a first step, we introduce a new parameter vector

$$\boldsymbol{\psi} = \left[\boldsymbol{p}^{\mathrm{T}}, \boldsymbol{\alpha}^{\mathrm{T}}, \boldsymbol{\zeta}^{\mathrm{T}}\right]^{\mathrm{T}} \in \mathbb{R}^{L_\psi \times 1}. \tag{33}$$

Here, we have the actual desired quantity, the agent position $\boldsymbol{p}$, but we still have to include the SMC amplitudes and phases as nuisance parameters. Since we have $D = 2$ dimensional positions and again phases $\zeta_{k,m}$, we obtain $L_\psi = D + K(M+1)$ for the respective number of parameters. We relate the original parameter vector to the new one via the Jacobian

$$\boldsymbol{J}_{\boldsymbol{\psi}} = \begin{bmatrix} \boldsymbol{J}_{\boldsymbol{p}} & \begin{matrix} \boldsymbol{0}_{2K \times K(M+1)} \\ \boldsymbol{I}_{K(M+1)} \end{matrix} \end{bmatrix} \tag{34}$$

where matrix $\boldsymbol{J}_{\boldsymbol{p}}$ describes the spatial gradients defined by

$$\boldsymbol{J}_{\boldsymbol{p}} = \tfrac{\partial}{\partial \boldsymbol{p}^{\mathrm{T}}} \boldsymbol{\theta} = \left[\left(\tfrac{\partial}{\partial p_1} \boldsymbol{\theta} \right), \ldots, \left(\tfrac{\partial}{\partial p_D} \boldsymbol{\theta} \right) \right] \in \mathbb{R}^{L_\theta \times D}. \tag{35}$$

Together with the parameter FIM from (50), we obtain the FIM for the new parameters

$$\boldsymbol{\mathcal{I}}_{\boldsymbol{\psi}} = \boldsymbol{J}_{\boldsymbol{\psi}}^{\mathrm{T}} \boldsymbol{\mathcal{I}}_{\boldsymbol{\theta}} \boldsymbol{J}_{\boldsymbol{\psi}} \in \mathbb{R}^{L_\psi \times L_\psi}. \tag{36}$$

The CRLB for $\boldsymbol{\psi}$ is related to the inverse of this matrix (cf. (14)). However, we are interested in the positions only, hence we look at the trace of the top left of the inverse that defines the PEB with

$$\mathrm{PEB}_{\boldsymbol{p}} = \sqrt{\mathrm{tr}\left(\left[\boldsymbol{\mathcal{I}}_{\boldsymbol{\psi}}^{-1} \right]_{D \times D} \right)}. \tag{37}$$

Taking the square of the right-hand side results in what is commonly known as the squared PEB, which quantifies the lower bound on the variance of the absolute position error.

4.2. Spatial gradients

For the spatial gradients (35), we apply the derivative with respect to the agent position to the parameter definitions in (12) and (13), resulting in

$$\begin{aligned}
&\tfrac{\partial}{\partial \boldsymbol{p}}(\tau_k) = \tfrac{1}{c}\, \boldsymbol{e}(\varphi_k) \\
&\tfrac{\partial}{\partial \boldsymbol{p}}(\phi_k) = \tfrac{1}{d_k}(-1)^{\mathcal{O}(k)} \boldsymbol{e}(\varphi_k - \tfrac{\pi}{2}) \\
&\tfrac{\partial}{\partial \boldsymbol{p}}(\alpha_k) = 0 \;;\; \tfrac{\partial}{\partial \boldsymbol{p}}(\zeta_{k,m}) = 0
\end{aligned}$$

where $\boldsymbol{e}(\varphi)$ denotes a unit vector pointing in the direction of the AoD φ. Furthermore, we assume that the amplitudes $\boldsymbol{\alpha}$ do not depend on the agent position $\boldsymbol{p}$. Since the phases $\boldsymbol{\zeta}$ stem from reflection properties and the measurement device, it is evident that they are also unrelated to the agent position. With this, we can assemble the Jacobian from (34) and follow the derivations until (37) to obtain the PEB.

4.3. PEB using EFIM

We use the EFIMs (21) and (24) to get a closed-form solution for (37), in order to obtain an insightful formulation. To make use of the EFIMs, it is beneficial to define subsets of the Jacobian from (35) that contain only the position-related parameters described by

$$\boldsymbol{J}_{\boldsymbol{\tau}} = \tfrac{\partial}{\partial \boldsymbol{p}^{\mathrm{T}}}\boldsymbol{\tau},\ \boldsymbol{J}_{\boldsymbol{\phi}} = \tfrac{\partial}{\partial \boldsymbol{p}^{\mathrm{T}}}\boldsymbol{\phi} \qquad\qquad \in \mathbb{R}^{K\times 2}.$$

The parameter transformation (36) enables the use of the inversion lemma (17) to compactly obtain the EFIM for the agent position via

$$\widetilde{\boldsymbol{\mathcal{I}}_{\boldsymbol{p}}} = [\boldsymbol{\mathcal{I}}_{\boldsymbol{\psi}}]_{2\times 2} = \boldsymbol{J}_{\boldsymbol{\tau}}^{\mathrm{T}}\widetilde{\boldsymbol{\mathcal{I}}_{\boldsymbol{\tau}}}\boldsymbol{J}_{\boldsymbol{\tau}} + \boldsymbol{J}_{\boldsymbol{\phi}}^{\mathrm{T}}\widetilde{\boldsymbol{\mathcal{I}}_{\boldsymbol{\phi}}}\boldsymbol{J}_{\boldsymbol{\phi}}.$$

With this, the full EFIM for the agent position is described by

$$\begin{aligned}\widetilde{\boldsymbol{\mathcal{I}}_{\boldsymbol{p}}} = 8\pi^2 \sum_{k=1}^{K} \Bigg(& \frac{\beta_k^2}{c^2}\|\boldsymbol{b}(\phi_k)\|^2\, \widetilde{\mathrm{SINR}}_k\, \boldsymbol{D}_r\left(\varphi_k\right) \\ & + \frac{D_b^2(\phi_k)}{d_k^2} M\, \mathrm{SINR}_k\, \boldsymbol{D}_r\left(\varphi_k - \tfrac{\pi}{2}\right)\Bigg) \qquad (38)\end{aligned}$$

where $\boldsymbol{D}_r\left(\varphi\right) = \boldsymbol{e}(\varphi)\boldsymbol{e}^{\mathrm{T}}(\varphi)$ is the *ranging direction matrix* [10]. For each SMC, we can see an information gain in radial direction via delay information (quantified by the squared bandwidth and the speed of light, i.e., β_k^2/c^2) and in tangential direction via angle information (quantified by the non-coherent squared antenna aperture and the SMC distance, i.e., $D_b^2(\phi_k)/d_k^2$).

5. Numerical results

This section aims at a numeric validation of the potential of the beampattern-enhanced, non-coherent positioning system. We evaluate the PEB for specific scenarios in indoor environments. Three setups are used to compare the performance obtained by the proposed non-coherent array with a conventional coherent array and a reference setup with a single antenna.

5.1. Evaluation setup

We assume given wall segments that form rooms with simple geometries and a given anchor position $\boldsymbol{a}_1$. The number of dedicated wall segments is denoted by K_{seg}. The anchor position is used together with the wall segments to determine VAs via mirroring operations, as described in Section 2.4. With the VA positions, the parameters τ_k and ϕ_k are determined as described by (12) and (13), respectively. We consider up to second-order reflections, which means the number of considered SMCs is given by $K \leq K_{\mathrm{seg}}(K_{\mathrm{seg}} - 1) + 1$. Note that for each agent position, VA visibility tests are performed, which may reduce this number on an individual basis [49]. The real-valued amplitudes α_k are simulated using the free space path-loss model, whereas each reflection results in a loss of 3 dB. Additionally, phases are applied to the amplitudes according to $e^{j2\pi f_c \tau_k}$. For the agent positions, a uniformly sampled grid is spanned over the floorplan of the room with a spacing of 2 cm.

To provide a context to previous work, we consider an "L-shaped" room, as shown in Fig. 5, which was also used in [15]. Hence, with $K_{\mathrm{seg}} = 6$ wall segments present, the number of usable SMCs amounts to $K \leq 31$. We also consider the same pulse signal for $s(t)$ as in [15], using a root-raised-cosine waveform with roll-off $\beta = 0.6$ and bandwidth $1/T_{\mathrm{p}} = 1$ GHz at a carrier frequency of $f_{\mathrm{c}} = 7$ GHz. For the DMC, we use the assumptions in (65) and (69), resulting in a block diagonal covariance matrix $\boldsymbol{C_n}$ with identical blocks for each antenna. We use a delay power spectrum $S_\nu(\tau)$ which exhibits a double-exponential shape as defined in [41] by Eq. (9) and illustrated in Figs. 4a and 4b. The used parameters are $\gamma_1 = 20$ ns, $\gamma_{\mathrm{rise}} = 5$ ns and $\chi = 0.98$, representing the decay and rise exponents and the relative power at excess delay zero, respectively. The power parameter Ω_1 is chosen such that we reach a Ricean K-factor of $|\alpha_1^{(1\mathrm{m})}|^2/\Omega_1 = 10$ dB for the line-of-sight (LOS) component energy, where $\alpha_1^{(1\mathrm{m})}$ is the complex amplitude of the LOS component at a distance of 1 m from the anchor. The power spectrum was aligned in time with the LOS component, i.e., it was shifted by τ_1. To define the signal-to-noise ratio (SNR) of the synthetically generated measurements, we introduce the SNR at 1 m, i.e.,

$$\mathrm{SNR}^{(1\mathrm{m})} = \frac{|\alpha_1^{(1\mathrm{m})}|^2}{N_0} \tag{39}$$

which relates the received LOS component energy at a distance of 1 m from the anchor to the noise power spectral density. Additionally, we define the receiver SNR as

$$\mathrm{SNR}^{\mathrm{r}} = \frac{\left\| \sum_{k=1}^{K} \alpha_k \boldsymbol{s}(\tau_k) \right\|^2 T_{\mathrm{s}}}{N_0} \tag{40}$$

where the parameters α_k and τ_k are determined for a specific agent ("receiver") position. This quantity takes distance and visibility conditions of the SMCs into account (e.g., K might be reduced due to non-visible SMCs) and thus relates to the impact of the propagation channel for a selected measurement noise level.

Fig. 4 illustrates the channel parameters (SMC and DMC) for two example agent positions, in Fig. 4a for an agent position where the LOS and four SMCs are visible, and in Fig. 4b for an agent position where the LOS is blocked and only two SMCs are visible. For visualization purposes, only first-order SMCs are considered, i.e., we have $K \leq 7$. The AWGN level is shown for two N_0 values where $\mathrm{SNR}^{(1\mathrm{m})} = 30$ dB and $\mathrm{SNR}^{(1\mathrm{m})} = 50$ dB. In Sec. 6, a positioning algorithm will be presented and evaluated on these simulated data.

5.2. PEB results for different setups

We evaluate the PEB described in (37) for each agent position, where we use both the full FIM, whose elements were computed using (50) (the respective sub-matrices are given in (52)-(57)), as well as the simplified, canonical EFIM from (38). We also select representative agent positions to show the respective scaled error ellipses that illustrate the components of the PEB in 2D-space. Throughout this section, we choose N_0 (and in turn σ_w^2) such that we get $\mathrm{SNR}^{(1\mathrm{m})} = 29.5$ dB as a reference value.

Setup 1: Single omni. First, we recreate the results from [15], examining the PEB for the multipath model considering only a single omni-directional antenna at the anchor. Hence, we set $M = 1$ and $b_m(\phi) = \frac{1}{\sqrt{2\pi}}$. The resulting PEB values are shown in Fig. 5a. While the setup allows for overall low PEB values due to the good resolution in delay domain, we can clearly see regions where the bound sharply decreases, caused by non-resolvable SMC path overlap.

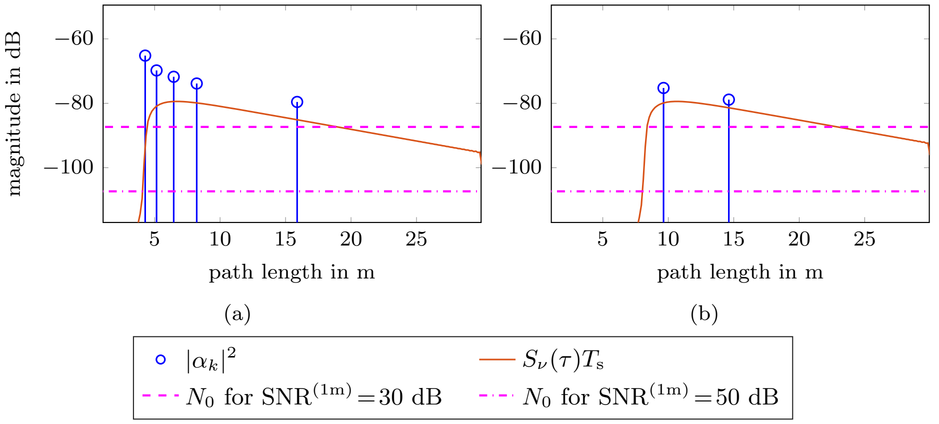

(a)

(b)

Figure 4: Visualization of the synthetic data: the power of used SMCs, DMC and AWGN is illustrated in log-scale (dB) for (a) a LOS case at agent position $\boldsymbol{p} = [6, 6]^\mathrm{T}$ and (b) a non-LOS case at agent position $\boldsymbol{p} = [3.7, 1.8]^\mathrm{T}$. Two reference AWGN levels are shown using (39) with the given $\mathrm{SNR}^{(1\mathrm{m})}$ values. The respective SNR^r values obtained using (40) are (a) $\mathrm{SNR}^\mathrm{r} = 20$ dB / 40 dB; and (b) $\mathrm{SNR}^\mathrm{r} = 9$ dB / 29 dB.

Fig. 8 shows the cumulative frequency of PEB values over the agent positions to quantitatively compare the positioning performance for the results illustrated in Fig. 5. The degradation in positioning accuracy due to path overlap is visible when considering the 90 percentile and above, where the error increases to multiple decimeter.

Setup 2: Array processing (coherent). We increase the antenna number to $M = 4$ and assume a conventional array with coherent phase processing. The antennas are on a circle with a constant radius $d^{(m)}$ and $\phi^{(m)} = \frac{\pi}{2} \cdot m$, such that an inter-antenna spacing of $\lambda/2$ is achieved, as illustrated in Fig. 3b. To use phase coherent processing, this setup requires the antenna phases $\zeta_m(\phi)$ to be determined by the respective AoA ϕ. Hence, for this setup, we change the vector $\boldsymbol{\zeta}$ to only include the K random SMC phases ζ_k, cf. (1).

The PEB for this constellation is shown in Fig. 5b. This time, the angle information helps resolving SMC path overlap while also increasing the overall accuracy, leading to a PEB that is dominated by SMC visibility properties. Non-resolvable path overlap remains only in a few regions, due to a smaller set of visible SMCs.

These performance improvements compared to the single omni setup are quantified in the cumulative frequency plot shown in Fig. 8, specifically when regarding the 90 percentile where sub-decimeter levels are achieved.

Setup 3: Directional beampatterns (non-coherent). Finally, we apply the proposed non-coherent array of $M = 4$ directional antennas. We use a Dirichlet kernel as defined in (28), described with M non-zero Fourier coefficients $c_\ell = 1/\sqrt{M}$ for $\ell \in \{-1.5, -0.5, 0.5, 1.5\}$, which is illustrated in Fig. 2a. Each antenna uses the same pattern but is pointed towards one of the four cardinal directions. For this setup we consider the full vector of $K \cdot M$ unknown phases $\zeta_{k,m}$. The resulting PEB is shown in Fig. 5c. The achieved accuracy comes close to Setup 2, i.e., directional antennas show a similar capability of resolving the path overlap, only slightly worse than the coherent omni-array setup. This observation is also confirmed when regarding the quantitative evaluation shown in Fig. 8, where we note the resemblance between the results of the coherent and non-coherent setups.

Additionally, in Fig. 5d, the PEB is shown for the simplified, canonical EFIM (38). It can be seen that the simplified PEB follows closely the full form, justifying the assumption in (66). The only significant differences are present in selected regions where SMC path overlap occurs. For the top left position, it is shown how the Fisher information from (38) affects both the radial and tangential position error via the information gains from delay and angle information, respectively.

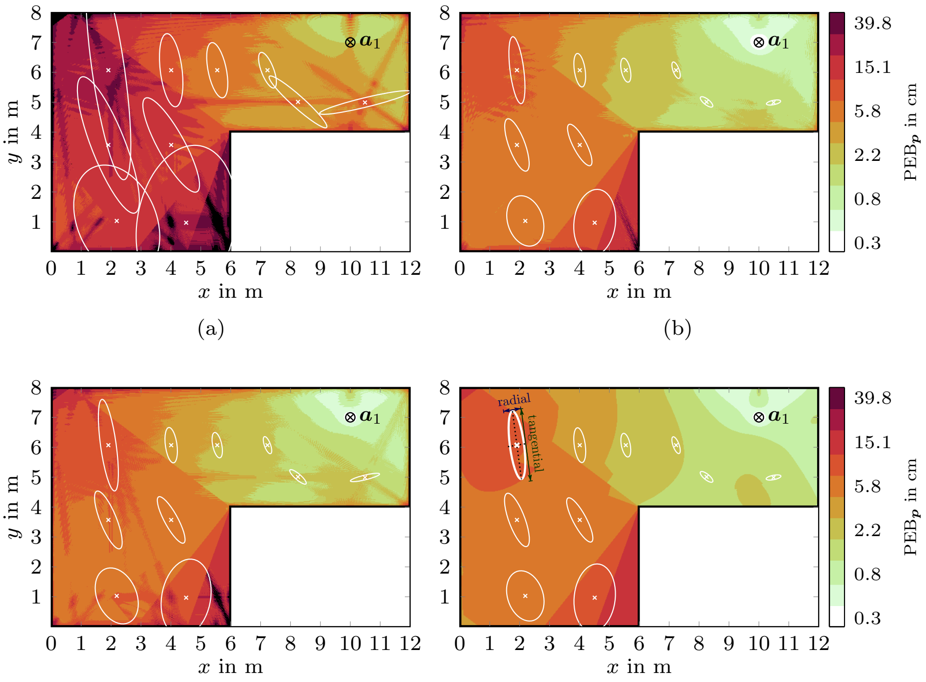

(a) (b)

(c) (d)

Figure 5: Position error bound using (a) $M = 1$ omni-directional antenna coherently, (b) $M = 4$ omni-directional antennas (spaced by $\lambda/2$) coherently, (c) $M = 4$ directional antennas non-coherently, and (d) $M = 4$ directional antennas non-coherently with the canonical FIM according to (38). At sample positions, 20-fold standard deviation error ellipses are shown.

Time vs. angle information. With the good achievable accuracy of the non-coherent setup, we want to determine the main contributor to the bounds in terms of position-related parameters. Specifically, we aim to show how much information the SMC delays add compared to the SMC angles. Also, we are interested in the effect of an increased number of antennas at the anchor, which puts the system in the context of mm-wave pencil-beam setups. We use the full FIM of the non-coherent model with $M = 4$ and $M = 16$ antennas to evaluate the PEB using only delays or angles, respectively, where the respective unused parameter (either τ_k or ϕ_k) is treated as another nuisance parameter.

The PEB results, considering delay information only, are shown in Fig. 6. From Fig. 6a, it is evident that the SMC delays carry the main contribution to the achieved accuracy, because the results come close to what was achieved with the

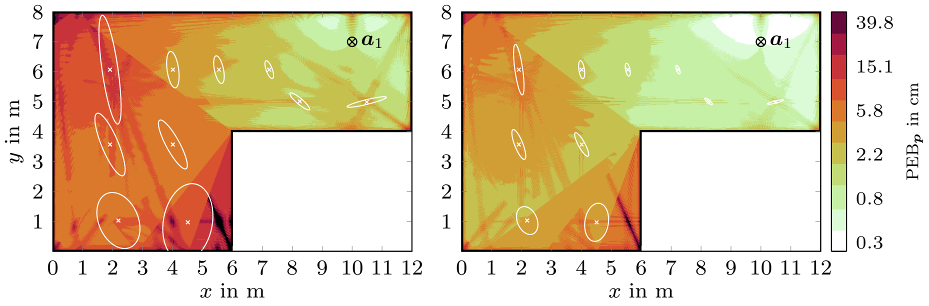

(a) (b)

Figure 6: Position error bound for the non-coherent case using only delay information with (a) $M = 4$ and (b) $M = 16$ antennas. At sample positions, 20-fold standard deviation error ellipses are shown.

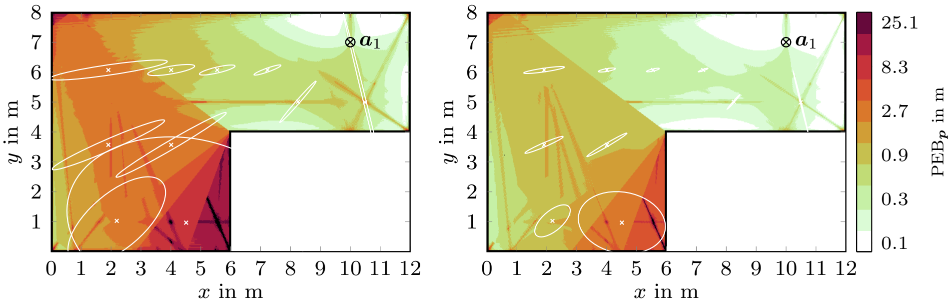

(a) (b)

Figure 7: Position error bound for the non-coherent case using only angle information with (a) $M = 4$ and (b) $M = 16$ antennas. At sample positions, standard deviation error ellipses are shown, 1-fold in (a) and 3-fold in (b).

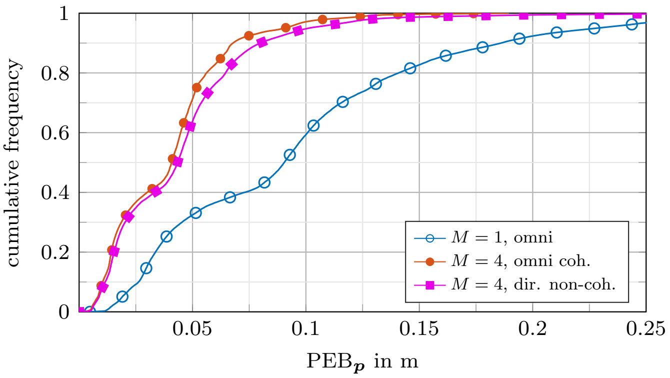

Figure 8: Cumulative frequency of the PEB values evaluated over the agent position grid for different antenna setups at the anchor (quantifying the results shown in Fig. 5).

full parameter set (cf. Fig 5c). Fig. 6b shows the same evaluation using $M = 16$ antennas, which achieves overall slightly better results, however the improvement is not significant.

In contrast, Fig. 7 shows the PEB results considering angle information only. Please note that the PEB is now shown in meter, due to the significanty higher error values compared to the delay information case. The error ellipses show that, predominantly, tangential information is provided. Furthermore, a large degradation is evident with an increased distance from the anchor. This is a well-known drawback of angle measurements, which can be seen mathematically from the inverse distance-scaling of the angle term in (38). Using $M = 16$ antennas greatly increases the positioning performance, which stands in stark contrast to the delay information improvements. The 3-fold standard deviation ellipses show that, for positions in LOS conditions, the tangential deviation is minimized. Note that, for visualization purposes, these ellipses are scaled by a larger factor for $M = 16$, due to the significantly lower PEB values.

Fig. 9 shows again a quantitative evaluation in terms of cumulative frequency for the PEB values of the described setups using delay and angle information respectively (cf. Figs. 6 and 7). With delay information, a significantly better performance is achieved. This confirms the observations from the qualitative PEB analysis, which identifies the delay information as the main contributor to accurate position estimates, justified by the large bandwidth. Increasing the number of used antennas to $M = 16$ decreases the error consistently. For the delay information case the accuracy scales by a factor of about 2. Considering the angle information case, the number of antennas has a higher impact. Here, using $M = 16$, the error decreases by a factor of 10. It is expected that the angle information will surpass the delay information when M is increased by a factor of 8 to $M = 128$. However, this result also depends on the room geometry, since angle information drops with d_k^2.

6. Positioning algorithm

In this section, we leverage the gained insights and present a positioning algorithm capable of estimating the agent position $\boldsymbol{p}$ given a measurement $\boldsymbol{r}$. We derive

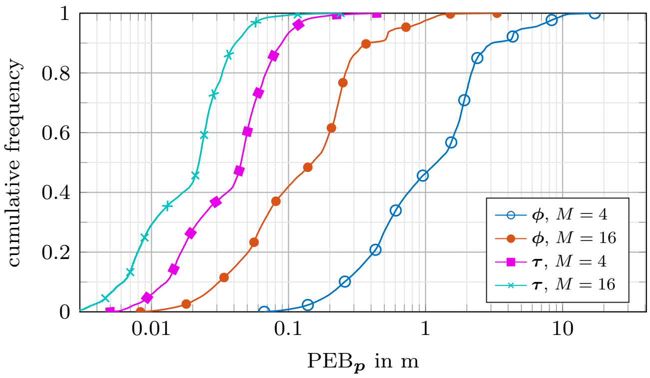

Figure 9: Cumulative frequency of the PEB values evaluated over the agent position grid for the non-coherent antenna setup at the anchor with varying number of antennas M, considering only information gained from the angles $\boldsymbol{\phi}$ or delays $\boldsymbol{\tau}$ (quantifying the results shown in Figs. 6 and 7).

the algorithm based on the received signal model (7) where we identify $\boldsymbol{\tau}$, $\boldsymbol{\phi}$, $\boldsymbol{\alpha}$ and $\boldsymbol{\zeta}$ as unknown variables. While $\boldsymbol{\tau}$ and $\boldsymbol{\phi}$ can be expressed as function of $\boldsymbol{p}$ (see Section 2.4), we need to estimate the nuisance parameters $\hat{\boldsymbol{\alpha}} \equiv \hat{\boldsymbol{\alpha}}(\boldsymbol{r}, \boldsymbol{p})$ and $\hat{\boldsymbol{\zeta}} \equiv \hat{\boldsymbol{\zeta}}(\boldsymbol{r}, \boldsymbol{p})$ jointly with $\hat{\boldsymbol{p}}$.

The positioning is performed by a maximum likelihood (ML) approach, on the basis of the log likelihood function $L(\boldsymbol{r}|\boldsymbol{p}, \boldsymbol{\alpha}, \boldsymbol{\zeta})$ derived from (7), which will be formulated later. Two algorithm variants will be given that vary in the noise model. The ML optimization problem can be formulated as

$$\hat{\boldsymbol{p}} = \underset{\bar{\boldsymbol{p}} \in \mathcal{P}}{\operatorname{argmax}} \, L(\boldsymbol{r}|\bar{\boldsymbol{p}}, \hat{\boldsymbol{\alpha}}, \hat{\boldsymbol{\zeta}}) \tag{42}$$

where the estimates $(\hat{\boldsymbol{\alpha}}, \hat{\boldsymbol{\zeta}})$ result from

$$(\hat{\boldsymbol{\alpha}}, \hat{\boldsymbol{\zeta}}) = \underset{(\boldsymbol{\alpha}, \boldsymbol{\zeta})}{\operatorname{argmax}} \, L(\boldsymbol{r}|\bar{\boldsymbol{p}}, \boldsymbol{\alpha}, \boldsymbol{\zeta}) \tag{43}$$

evaluated for one specific position $\bar{\boldsymbol{p}}$. The non-linear relations in (42) prevent a closed-form solution for $\hat{\boldsymbol{p}}$. Moreover, an independent estimation of $\hat{\boldsymbol{\alpha}}, \hat{\boldsymbol{\zeta}}$ is infeasible which sacrifices computational efficiency. As a remedy, we propose to evaluate the log likelihood function in (42) numerically for positions $\bar{\boldsymbol{p}} \in \mathcal{P}$ within the communication range. A straight-forward choice for the set of evaluation positions $\mathcal{P}$ is a reasonably dense position grid spanned over the floorplan of the considered environment, whereas the granularity of this grid poses a lower limit on the position error. Alternatively, prior range estimates can be used to reduce the set to a sphere around the anchor as proposed in [37] and evaluated in [31]. Then, to obtain the position estimate via (42), the likelihood is evaluated for all the chosen agent positions. To further enhance the feasibility of the algorithm, we relax the joint estimation in (43), as shown in the following.

6.1. Derivation of the positioning algorithm

An independent estimation of $\boldsymbol{\alpha}$ and $\boldsymbol{\zeta}$ is intractable for the original optimization problem, but possible by assuming that the measurements $\boldsymbol{r}_m$ are independent across m and by assuming the absence of overlapping SMCs. Following the derivations from [38], we start by factorizing $L(\boldsymbol{r}|\boldsymbol{p},\boldsymbol{\alpha},\boldsymbol{\zeta})$ using assumption (64), resulting in

$$L(\boldsymbol{r}|\boldsymbol{p},\boldsymbol{\alpha},\boldsymbol{\zeta}) = \sum_m L_m(\boldsymbol{r}_m|\boldsymbol{p},\boldsymbol{\alpha},\boldsymbol{\zeta}) \tag{44}$$

with

$$L_m(\boldsymbol{r}_m|\boldsymbol{p},\boldsymbol{\alpha},\boldsymbol{\zeta}) = -\det\{\boldsymbol{C}_{\boldsymbol{n}}^{(m)}\} - \sigma_w^{-2}\|\boldsymbol{r}_m - \mathbf{x}_m(\boldsymbol{p},\boldsymbol{\alpha},\boldsymbol{\zeta})\|^2_{\mathcal{H}_m}. \tag{45}$$

The covariance $\boldsymbol{C}_{\boldsymbol{n}}^{(m)}$ of the mth antenna is defined in (65) and the vector $\mathbf{x}_m(\boldsymbol{p},\boldsymbol{\alpha},\boldsymbol{\zeta}) \in \mathbb{C}^N$ is

$$\mathbf{x}_m(\boldsymbol{p},\boldsymbol{\alpha},\boldsymbol{\zeta}) = \sum_{k=1}^{K} \alpha_{k,m} b_m(\phi_k)\boldsymbol{s}(\tau_k) \tag{46}$$

where we introduced an auxiliary variable $\alpha_{k,m} = \alpha_k e^{j\zeta_{k,m}}$.

For an independent estimate of the parameters in $\boldsymbol{\alpha}$ and $\boldsymbol{\zeta}$, we assume that specular reflections do not overlap in the delay domain as stated in assumption (66). Then, maximizing (45) w.r.t. $\alpha_{k,m}$ yields

$$\hat{\alpha}_{k,m} = \frac{1}{b_m(\phi_k)} \frac{\langle \boldsymbol{s}(\tau_k), \boldsymbol{r}_m\rangle_{\mathcal{H}_m}}{\|\boldsymbol{s}(\tau_k)\|_{\mathcal{H}_m}}. \tag{47}$$

Subsequently, we maximize (44) w.r.t. $\hat{\zeta}_{k,m}$, contained in $\hat{\boldsymbol{\zeta}}$, and the results can be expressed as

$$\hat{\zeta}_{k,m} = \angle\hat{\alpha}_{k,m} \tag{48}$$

using $\hat{\alpha}_{k,m}$ obtained from (47). The SMC amplitudes $\hat{\alpha}_k$ result from maximizing (44) w.r.t α_k. Again, we assume no SMC path overlap, and obtain after some derivations

$$\hat{\alpha}_k = \frac{\sum_{m=1}^{M} |b_m(\phi_k)|^2 |\hat{\alpha}_{k,m}|}{\sum_{m=1}^{M} |b_m(\phi_k)|^2}. \tag{49}$$

The steps performed by the position estimator can be summarized as follows. To evaluate $L(\boldsymbol{r}|\bar{\boldsymbol{p}},\hat{\boldsymbol{\alpha}},\hat{\boldsymbol{\zeta}})$ from (42) for a specific $\bar{\boldsymbol{p}} \in \mathcal{P}$, first, SMC parameters $\boldsymbol{\tau}$ and $\boldsymbol{\phi}$ are calculated using (12) and (13) respectively, followed by estimating $\hat{\alpha}_{k,m}$ via (47). Subsequently, $\hat{\boldsymbol{\zeta}}$ and $\hat{\boldsymbol{\alpha}}$ result from (48) and (49), respectively. Finally, these estimates are plugged into (44) to calculate $L(\boldsymbol{r}|\bar{\boldsymbol{p}},\hat{\boldsymbol{\alpha}},\hat{\boldsymbol{\zeta}})$. This procedure is repeated for all $\bar{\boldsymbol{p}} \in \mathcal{P}$ and $\bar{\boldsymbol{p}}$ with the highest associated likelihood is chosen as position estimate $\hat{\boldsymbol{p}}$ (cf. (42)).

6.2. Evaluation of the Positioning Algorithm

We assess the performance of the presented positioning algorithm by comparing the mean-squared error (MSE)

$$\epsilon = \sqrt{\frac{1}{N_{\mathrm{MC}}} \sum_{i=1}^{N_{\mathrm{MC}}} \|\hat{\boldsymbol{p}}_i - \boldsymbol{p}\|^2}$$

between the true $\boldsymbol{p}$ and estimated position $\hat{\boldsymbol{p}}_i$, on the basis of observation data taken from N_{MC} realizations of $\boldsymbol{r}_m$, where we use both synthetically created data and measurement data. We compare the performance using two kinds of estimators which vary depending on the used noised model: First, we follow the derivations in Section 6.1 where we assumed knowledge regarding the noise covariance, described by $\boldsymbol{C}_{\boldsymbol{n}}^{(m)}$ (see (45)), resulting in an algorithm that makes use of the DMC statistics, hence we refer to this algorithm as *DMC-based* (note that the AWGN is also included in the covariance matrix).[4] Second, as a simpler alternative, we use an estimator with non-accessible $\boldsymbol{C}_{\boldsymbol{n}}^{(m)}$ where no DMC is used (this follows the algorithm described in [38]), which can be accomplished by replacing $\boldsymbol{C}_{\boldsymbol{n}}^{(m)}$ in (45) and (47) with an identity matrix $\mathbf{I}_N$. We refer to this variant of the algorithm as *AWGN-based*.

6.2.1. Synthetically Generated Data

In the first evaluation, we obtain observations by performing $N_{\mathrm{MC}} = 1000$ Monte-Carlo runs. We focus on the potential to estimate positions in LOS as well as in non-LOS conditions, located in the L-shaped room from Section 5 where agent positions $[6, 6]^{\mathrm{T}}$ and $[3.7, 1.8]^{\mathrm{T}}$ correspond to the LOS and non-LOS case. The signal parameters and beampatterns are identical to Section 5. For the SMCs, we use only first-order reflections, hence, we have $K \leq 7$. The observations are created using (7). In the first experiment, we keep the DMC power constant. The experiment is performed for varying AWGN levels, whereas the noise variance $\sigma_w^2 = N_0/T_{\mathrm{s}}$ is set using (39) such that $\mathrm{SNR}^{(1\mathrm{m})}$ values in the range of 10 to 60 dB are obtained. Fig. 4a illustrates the used SMCs in comparison with DMC and AWGN for the two agent positions and two AWGN levels.

Fig. 10 presents the MSE achieved comparing the DMC-based (solid blue) and AWGN-based (dashed cyan) estimators using $M = 3$ antennas for various AWGN levels. The corresponding PEB (black) from (37) is shown for comparison. In general, we can observe that the PEB for the LOS case is lower, showing the vital position information contained in the LOS component. In non-LOS conditions the achievable accuracy is decreased and moreover, the PEB is approached at a higher $\mathrm{SNR}^{(1\mathrm{m})}$ value of 45 dB ($\mathrm{SNR}^{\mathrm{r}} = 24$ dB) in comparison to LOS conditions where the PEB is approached at $\mathrm{SNR}^{(1\mathrm{m})} = 25$ dB ($\mathrm{SNR}^{\mathrm{r}} = 15$ dB).

A comparison between the two proposed estimators illustrates the importance of considering the DMC power in the estimation procedure. At $\mathrm{SNR}^{(1\mathrm{m})}$ values above 50 dB, the position error of the AWGN-based estimator saturates and diverges from the PEB. At these high $\mathrm{SNR}^{(1\mathrm{m})}$ values, the AWGN level is very low, hence the DMC is clearly the limiting factor and only the DMC-based estimator is able to approach the PEB.

To illustrate the impact of the DMC on the achievable performance, we calculate a position error bound $\mathrm{PEB}_{\boldsymbol{p}}^{\mathrm{AWGN}}$ assuming presence of AWGN only (replacing $\boldsymbol{C}_{\boldsymbol{n}}^{(m)}$ in (65) with $\sigma_w^2 \boldsymbol{I}_N$). Fig. 10 presents $\mathrm{PEB}_{\boldsymbol{p}}^{\mathrm{AWGN}}$ (gray) showing that at low $\mathrm{SNR}^{(1\mathrm{m})}$ values both $\mathrm{PEB}_{\boldsymbol{p}}$ and $\mathrm{PEB}_{\boldsymbol{p}}^{\mathrm{AWGN}}$ approach similar values. Increasing $\mathrm{SNR}^{(1\mathrm{m})}$ (and thus $\mathrm{SNR}^{\mathrm{r}}$), both PEBs decrease but $\mathrm{PEB}_{\boldsymbol{p}}$ saturates due to the constant DMC power. This saturation demonstrates again that dense multipath effectively limits the achievable accuracy regardless of the AWGN levels of the observations. It has to be emphasized that this unavoidable effect of the radio channel itself cannot be reduced by increasing $\mathrm{SNR}^{(1\mathrm{m})}$. However, the insight from the theoretical results shows how it can be eased by increasing the signal bandwidth and the number of the antennas or by using directional antennas.

In the second experiment, we evaluate the impact of number of antennas M. The beampattern is obtained using (28) with M non-zero Fourier-coefficients

---

[4] The proposed *DMC-based* algorithm can be extended in line with [40, 50] to jointly estimate the DMC statistics.

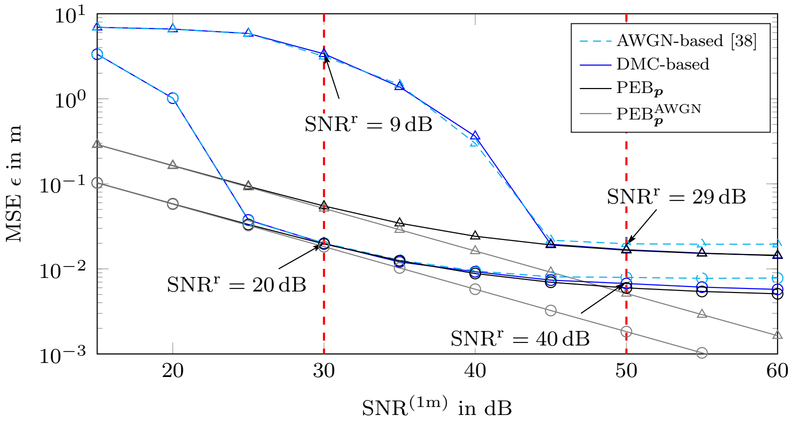

Figure 10: Mean-squared error ϵ achieved by the proposed position estimators in LOS (indicated by -○-) and non-LOS (indicated by -△-) conditions using $M = 3$ antennas. The position error bounds considering dense multipath and AWGN ($\mathrm{PEB}_{\boldsymbol{p}}$) as well as AWGN only ($\mathrm{PEB}_{\boldsymbol{p}}^{\mathrm{AWGN}}$) are shown for comparison. The AWGN level N_0 is set using the $\mathrm{SNR}^{(1\mathrm{m})}$ values from the x-axis in (39). $\mathrm{SNR}^{\mathrm{r}}$ values obtained using (40) are shown for both the LOS and non-LOS case at representative points.

$c_\ell = 1/\sqrt{M}$ with $\ell \in [-\frac{M-1}{2}, \dots, \frac{M-1}{2}]$. Fig. 11 illustrates the MSE for LOS and non-LOS conditions achieved by the DMC-based (solid blue) and AWGN-based (dashed cyan) estimators. For the AWGN, we set N_0 such that $\mathrm{SNR}^{(1\mathrm{m})} = 40$ dB, whereas the remaining parameters are equal to the first experiment. In general, we can observe that the PEB is less sensitive to M, e.g. increasing M by a factor of four accompanies with a reduction of the PEB by a factor of two, as anticipated in Section 3. However, at large M the position estimator has more independent observations which enhances the suppression of the DMC, as demonstrated in the non-LOS case.

6.2.2. Measured Data

The second evaluation is performed on the basis of a measurement campaign described in [32] and [38], which was conducted in a 6×8 m laboratory room with a single anchor at position $\boldsymbol{a}_1$ and an agent at position $\boldsymbol{p}$ as illustrated in Fig. 12. We consider again first-order reflections only, hence, for this room we have $K \leq 5$. Four directive antennas were used at the anchor, whereas the complex-valued beampatterns $b_m(\phi)$ were available as a codebook with a resolution of 10°. Measurements to the agent were performed using an Ilmsens Correlative Channel Sounder [51]. Each measurement was convolved by a raised cosine pulse with a pulse width of $T_\mathrm{p} = 2.4$ ns, a roll-off factor of $\beta = 0.9$, and a carrier frequency of $f_\mathrm{c} = 5.4$ GHz. The agent was placed at positions $\boldsymbol{p}$ on a 15×14 grid with 5 cm spacing as shown in Fig. 12, resulting in 210 measurements in (unobstructed) LOS condition. Both, anchor and agent, were placed at a height of 1.5 m, leading to reduced floor and ceiling reflections, since all involved antennas exhibit narrow elevation patterns. For the DMC-based algorithm, we estimated $\hat{\boldsymbol{C}}_{\boldsymbol{n}}^{(m)}$ individually for each antenna using the 210 measurements to estimate the DPS $\hat{S}_\nu^{(m)}(\tau)$.

For each grid position, the algorithms are used analogously to the synthetic

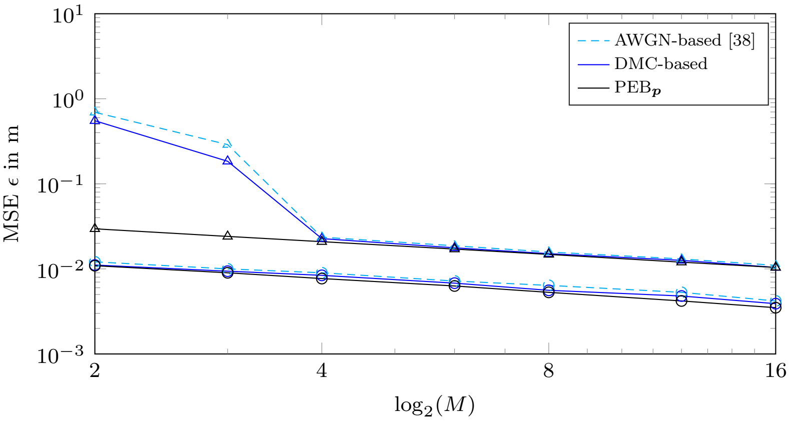

Figure 11: Impact of number of antennas M to the proposed position estimators in LOS (indicated by —○—) and non-LOS (indicated by —△—) conditions in comparison to $\mathrm{PEB}_{\boldsymbol{p}}$. The AWGN level N_0 was set such that $\mathrm{SNR}^{(1\mathrm{m})} = 40$ dB.

setup and the resulting cumulative frequency of the position error over the grid agent positions is shown in Fig. 13. For comparison, we include our previous results from [32], where this evaluation was performed using an omni-directional antenna at the anchor. We identify a significant improvement, especially regarding estimation outliers (i.e. errors of more than half a meter). By consideration of the DMC via $\hat{\boldsymbol{C}}_{\boldsymbol{n}}^{(m)}$ in the DMC-based method, the result can be improved even further. Specifically, the 80 % error is almost halved from 20 cm for the AWGN-based method down to 12 cm, and the amount of estimates to achieve an error of less than 10 cm goes up from 50 % to 72 %.

To gain further insight in the information provided by the SMCs and the beampatterns, we analyze $|b_m(\phi_k)|^2\,\mathrm{SINR}_k$, which is shown in Table 1. To obtain the SINRs, we apply (20) where we use the amplitude estimates obtained by (49). As seen in (38), these quantities indicate the quality of SMCs and highlight how each antenna can be used to focus on particular SMCs from different directions. E.g., we see that the SMC from the plasterboard east wall achieves a high SINR value from the east antenna measurement. For comparison, we include a sum of the weighted SINRs (similar to what is used in (38) to quantify the total information collected from each SMC with the multi-antenna system), as well as the SINRs of SMCs using a single omni-directional antenna at the anchor from [32] (the latter were obtained by method-of-moments estimation). The information gain of specific directional antennas is highlighted and the overall higher performance is justified. A variant of the AWGN-based algorithm was implemented on low-cost devices based on the DecaWave DWM1000 module as described in [31]. The system was evaluated in a field test and put in context with other indoor localization systems in terms of accuracy and required infrastructure.

7. Conclusions

In this article, we investigated a multipath-based, single-anchor positioning system for indoor environments, which exploits non-coherent angular measurements from a set of directive antennas. Such measurements can be obtained for example from

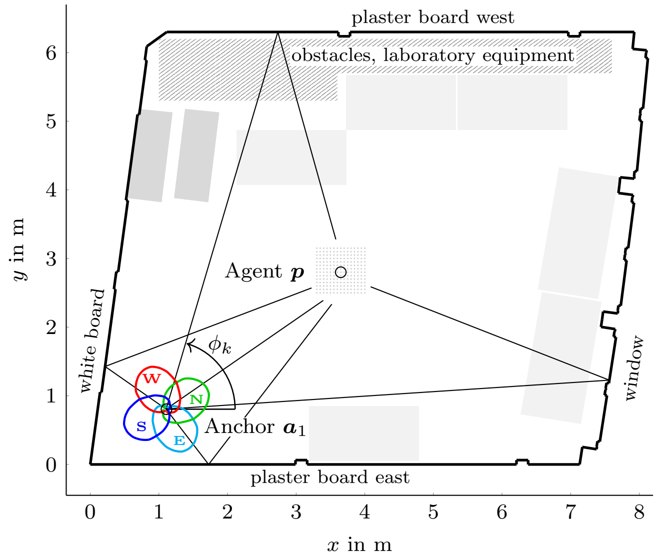

Figure 12: Floorplan of the used laboratory environment where the measurement campaign was conducted. The four reflective surfaces that yield specular reflections used by the algorithms are shown as well as the beampatterns of the antennas at the anchor, labelled according to the four cardinal directions by north (N), west (W), south (S) and east (E). The gray rectangles indicate tables and cupboards, which have negligible effect onto the azimuth propagation of the SMCs.

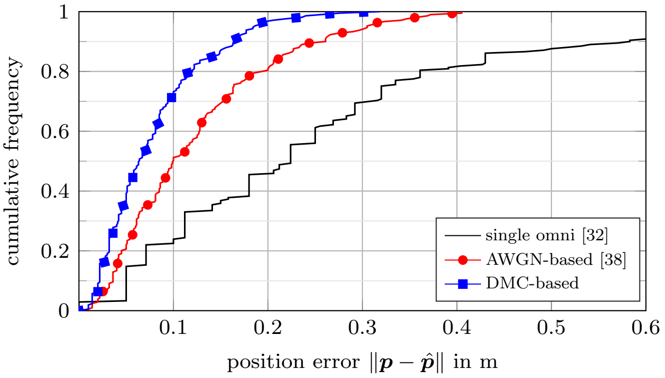

Figure 13: Cumulative frequency of the position error $\|\boldsymbol{p}-\hat{\boldsymbol{p}}\|$ for the algorithms described in Sec. 6.1 evaluated over grid agent positions with measurement data from the environment shown in Fig. 12.

a mm-wave radio system with analog beamforming or a UWB transceiver with switched directive antennas. We derived and analyzed the position error bound (PEB), the Cramér-Rao lower bound (CRLB) on the position estimation error, for the proposed measurement system to gain insight about the achievable performance in comparison to a conventional antenna array requiring fully coherent processing of the antenna signals. Analysis of the PEB showed that the main contribution to high-accuracy (centimeter-level) positioning lies in the delays of specular multipath components (SMCs), whereas the directional antennas allow overlapping SMCs

Table 1: $|b_m(\phi_k)|^2\,\mathrm{SINR}_k$ in dB of the respective SMCs and the four used antennas (cf. Fig. 12) obtained using (20) with the estimated amplitudes from (49). The column *added* contains the sum over all antennas, whereas the entry *omni* contains the results from [32] using an omni-directional antenna in the same setup.

SMC	*N*	*W*	*S*	*E*	added	omni [32]
LOS	23.2	16.7	12.6	11.9	24.6	17.2
plasterb east	7.0	−10.2	−15.6	16.3	16.8	3.1
plasterb west	3.6	5.7	−1.0	−12.5	8.4	−0.6
white board	−5.8	12.5	8.9	6.1	14.8	3.4
window	13.7	7.4	−4.2	8.0	15.5	$-\infty$

to be resolved, enhancing the robustness of the system. It was shown that non-coherent processing of directional measurements achieves a very similar performance compared to a fully coherent antenna array. Specifically, the bound on the RMS angle estimation error reduces by a factor of $\sqrt{3}$ when using the same number of antenna elements, whereas the delay estimation bound remains identical. This is a promising result, indicating that a high-accuracy, single-anchor positioning system exploiting angle information could be implemented efficiently with non-coherent (consecutive) measurements. Such measurements can be conducted with an adaptive, low-power analog antenna frontend, reducing the required number of radio chains to a minimum. In this regard, a position estimation algorithm was derived, showing the achievability of the PEB. Indeed, the performance is limited by dense multipath as self-interference, not by measurement noise.

Acknowledgments

This work was performed in part within the LEAD-Project "Dependable Internet of Things in Adverse Environments", funded by Graz University of Technology and in part by the Austrian Science Fund (FWF) under grants J 4027-N33.

Appendix

A. Derivation of EFIM

General FIM

The FIM for signal model (7) can be assembled by sub-matrices $\boldsymbol{\mathcal{I}}_{\boldsymbol{\vartheta}\boldsymbol{\vartheta}'}$ with $\boldsymbol{\vartheta}, \boldsymbol{\vartheta}' \in \{\boldsymbol{\phi}, \boldsymbol{\tau}, \boldsymbol{\alpha}, \boldsymbol{\zeta}\}$ as

$$\boldsymbol{\mathcal{I}}_{\boldsymbol{\theta}} = \begin{bmatrix} \boldsymbol{\mathcal{I}}_{\boldsymbol{\tau}\boldsymbol{\tau}} & \boldsymbol{\mathcal{I}}_{\boldsymbol{\tau}\boldsymbol{\phi}} & \boldsymbol{\mathcal{I}}_{\boldsymbol{\tau}\boldsymbol{\alpha}} & \boldsymbol{\mathcal{I}}_{\boldsymbol{\tau}\boldsymbol{\zeta}} \\ \boldsymbol{\mathcal{I}}_{\boldsymbol{\tau}\boldsymbol{\phi}}^{\mathrm{H}} & \boldsymbol{\mathcal{I}}_{\boldsymbol{\phi}\boldsymbol{\phi}} & \boldsymbol{\mathcal{I}}_{\boldsymbol{\phi}\boldsymbol{\alpha}} & \boldsymbol{\mathcal{I}}_{\boldsymbol{\phi}\boldsymbol{\zeta}} \\ \boldsymbol{\mathcal{I}}_{\boldsymbol{\tau}\boldsymbol{\alpha}}^{\mathrm{H}} & \boldsymbol{\mathcal{I}}_{\boldsymbol{\phi}\boldsymbol{\alpha}}^{\mathrm{H}} & \boldsymbol{\mathcal{I}}_{\boldsymbol{\alpha}\boldsymbol{\alpha}} & \boldsymbol{\mathcal{I}}_{\boldsymbol{\alpha}\boldsymbol{\zeta}} \\ \boldsymbol{\mathcal{I}}_{\boldsymbol{\tau}\boldsymbol{\zeta}}^{\mathrm{H}} & \boldsymbol{\mathcal{I}}_{\boldsymbol{\phi}\boldsymbol{\zeta}}^{\mathrm{H}} & \boldsymbol{\mathcal{I}}_{\boldsymbol{\alpha}\boldsymbol{\zeta}}^{\mathrm{H}} & \boldsymbol{\mathcal{I}}_{\boldsymbol{\zeta}\boldsymbol{\zeta}} \end{bmatrix}. \tag{50}$$

The main contributors to position information are the sub-matrices $\boldsymbol{\mathcal{I}}_{\boldsymbol{\tau}\boldsymbol{\tau}}$ and $\boldsymbol{\mathcal{I}}_{\boldsymbol{\phi}\boldsymbol{\phi}}$, which are described in detail in Sec. 3. In contrast, to characterize position information loss due to nuisance parameters, we examine the sub-matrices of the

FIM describing the cross-dependencies between the useful parameters and the nuisance parameters. The generic form of the sub-matrices $\boldsymbol{\mathcal{I}}_{\boldsymbol{\vartheta}\boldsymbol{\vartheta}'}$ is described by

$$[\boldsymbol{\mathcal{I}}_{\boldsymbol{\vartheta}\boldsymbol{\vartheta}'}]_{k,k'} = 2\,\Re\Big\{\tfrac{\partial}{\partial\vartheta_k}\left(\alpha_k \boldsymbol{b}(\phi_k)\otimes \boldsymbol{s}(\tau_k)\right)^{\mathrm{H}} \boldsymbol{C}_{\boldsymbol{n}}^{-1}\tfrac{\partial}{\partial\vartheta'_{k'}}\left(\alpha_{k'}\boldsymbol{b}(\phi_{k'})\otimes\boldsymbol{s}(\tau_{k'})\right)\Big\}. \tag{51}$$

EFIM for SMC Delay and Angle estimation

In the following derivations, we use the setup employing directional antennas with non-coherent processing, i.e., we use the parameters from (9), where we consider that all phase shifts $\zeta_{k,m}$ are unknown. In contrast, the FIM and resulting error bounds for a setup of coherent antenna arrays, including multipath resolved models, is well described in [11] in terms of array constellations and in [13] for models including a statistical description of the DMC.

To obtain more insightful expressions, we assume that the SMCs are orthogonal to each other, cf. (66), that the DMC is uncorrelated between antennas, cf. (65), and equal DMC statistics for each antenna, cf. (69), leading to the matrix elements

$$[\boldsymbol{\mathcal{I}}_{\boldsymbol{\tau}\boldsymbol{\tau}}]_{k,k} = 2\,|\alpha_k|^2\,\|\boldsymbol{b}(\phi_k)\|^2\,\|\dot{\boldsymbol{s}}(\tau_k)\|^2_{\mathcal{H}} \tag{52}$$

$$[\boldsymbol{\mathcal{I}}_{\boldsymbol{\phi}\boldsymbol{\phi}}]_{k,k} = 2\,|\alpha_k|^2\,\|\dot{\boldsymbol{b}}(\phi_k)\|^2\,\|\boldsymbol{s}(\tau_k)\|^2_{\mathcal{H}} \tag{53}$$

$$[\boldsymbol{\mathcal{I}}_{\boldsymbol{\alpha}\boldsymbol{\alpha}}]_{k,k} = 2\,\|\boldsymbol{b}(\phi_k)\|^2\|\boldsymbol{s}(\tau_k)\|^2_{\mathcal{H}} \tag{54}$$

$$[\boldsymbol{\mathcal{I}}_{\boldsymbol{\tau}\boldsymbol{\phi}}]_{k,k} = 2\,|\alpha_k|^2\,\Re\Big\{\big\langle\dot{\boldsymbol{b}}(\phi_k),\boldsymbol{b}(\phi_k)\big\rangle\,\big\langle\dot{\boldsymbol{s}}(\tau_k),\boldsymbol{s}(\tau_k)\big\rangle_{\mathcal{H}}\Big\} \tag{55}$$

$$[\boldsymbol{\mathcal{I}}_{\boldsymbol{\tau}\boldsymbol{\alpha}}]_{k,k} = 2\,\alpha_k\|\boldsymbol{b}(\phi_k)\|^2\,\Re\Big\{\big\langle\dot{\boldsymbol{s}}(\tau_k),\boldsymbol{s}(\tau_k)\big\rangle_{\mathcal{H}}\Big\} \tag{56}$$

$$[\boldsymbol{\mathcal{I}}_{\boldsymbol{\phi}\boldsymbol{\alpha}}]_{k,k} = 2\,\alpha_k\,\Re\Big\{\big\langle\dot{\boldsymbol{b}}(\phi_k),\boldsymbol{b}(\phi_k)\big\rangle\Big\}\,\|\boldsymbol{s}(\tau_k)\|^2_{\mathcal{H}} \tag{57}$$

where $\dot{\boldsymbol{s}}(\tau) = \partial\boldsymbol{s}/\partial\tau$ and $\dot{\boldsymbol{b}}(\phi) = \partial\boldsymbol{b}/\partial\phi$. We omit the phase related matrices, because each $\boldsymbol{\mathcal{I}}_{\boldsymbol{\zeta}\bar{\boldsymbol{\zeta}}}$ turns zero on the main diagonal due to the inner derivative of the phasor making the elements purely imaginary, which removes them via the $\Re\{\cdot\}$ operator. Only on the off-diagonals there can be non-zero values, hence the phase influences the estimation of other parameters only when the SMC orthogonality from (66) does not hold.

We observe that there is only an information loss due to the estimation of the amplitudes. More specifically, via the inversion lemma from (17), we obtain the full EFIM of position related parameters $\boldsymbol{\vartheta}\in\{\boldsymbol{\phi},\boldsymbol{\tau}\}$ as

$$\widetilde{\boldsymbol{\mathcal{I}}_{\boldsymbol{\vartheta}}} = \boldsymbol{\mathcal{I}}_{\boldsymbol{\vartheta}\boldsymbol{\vartheta}} - \mathrm{IL}_{\boldsymbol{\vartheta}} \tag{58}$$

where the second term can be interpreted as the information loss due to the estimation of the nuisance parameter given as

$$\mathrm{IL}_{\boldsymbol{\vartheta}} = \boldsymbol{\mathcal{I}}_{\boldsymbol{\vartheta}\boldsymbol{\alpha}}\boldsymbol{\mathcal{I}}^{-1}_{\boldsymbol{\alpha}\boldsymbol{\alpha}}\boldsymbol{\mathcal{I}}^{\mathrm{H}}_{\boldsymbol{\vartheta}\boldsymbol{\alpha}}. \tag{59}$$

Using the FIM sub-matrices (54) and (56), the information loss for the delay is given as

$$\big[\mathrm{IL}_{\boldsymbol{\tau}}\big]_{k,k} = 2\frac{|\alpha_k|^2}{\sigma_w^2}\,\frac{\|\boldsymbol{b}(\phi_k)\|^2\Re\big\{\big\langle\dot{\boldsymbol{s}}(\tau_k),\boldsymbol{s}(\tau_k)\big\rangle_{\mathcal{H}}\big\}^2}{\|\boldsymbol{s}(\tau_k)\|^2_{\mathcal{H}}}. \tag{60}$$

Using the FIM sub-matrices (54) and (57), the information loss for the angle is given as

$$\big[\mathrm{IL}_{\boldsymbol{\phi}}\big]_{k,k} = 2\frac{|\alpha_k|^2}{\sigma_w^2}\,\frac{\Re\big\{\big\langle\dot{\boldsymbol{b}}(\phi_k),\boldsymbol{b}(\phi_k)\big\rangle\big\}^2\|\boldsymbol{s}(\tau_k)\|^2_{\mathcal{H}}}{\|\boldsymbol{b}(\phi_k)\|^2}. \tag{61}$$

Inserting (60), and (52) into (58), results in the EFIM for delay estimation, given as

$$\begin{aligned}\left[\widetilde{\boldsymbol{\mathcal{I}}_{\boldsymbol{\tau}}}\right]_{k,k} &= 2\frac{|\alpha_k|^2}{\sigma_w^2}\|\boldsymbol{b}(\phi_k)\|^2\|\dot{\boldsymbol{s}}(\tau_k)\|^2_{\mathcal{H}}\left(1-\frac{\Re\left\{\left\langle \dot{\boldsymbol{s}}(\tau_k),\boldsymbol{s}(\tau_k)\right\rangle_{\mathcal{H}}\right\}^2}{\|\dot{\boldsymbol{s}}(\tau_k)\|^2_{\mathcal{H}}\|\boldsymbol{s}(\tau_k)\|^2_{\mathcal{H}}}\right)\\ &= 2\frac{|\alpha_k|^2}{\sigma_w^2}\|\boldsymbol{b}(\phi_k)\|^2\|\dot{\boldsymbol{s}}(\tau_k)\|^2_{\mathcal{H}}\xi_k^{\text{delay}} \end{aligned} \tag{62}$$

where $\xi_k^{\text{delay}} \in [0,1]$ can be interpreted as the information loss on the SMC delay estimation induced by the estimation of the complex amplitude α_k in the DMC. Inserting (61), and (53) into (58), results in the EFIM for AoA estimation, given as

$$\begin{aligned}\left[\widetilde{\boldsymbol{\mathcal{I}}_{\boldsymbol{\phi}}}\right]_{k,k} &= 2\frac{|\alpha_k|^2}{\sigma_w^2}\|\dot{\boldsymbol{b}}(\phi_k)\|^2\|\boldsymbol{s}(\tau_k)\|^2_{\mathcal{H}}\left(1-\frac{\Re\left\{\left\langle \dot{\boldsymbol{b}}(\phi_k),\boldsymbol{b}(\phi_k)\right\rangle\right\}^2}{\|\dot{\boldsymbol{b}}(\phi_k)\|^2\|\boldsymbol{b}(\phi_k)\|^2}\right)\\ &= 2\frac{|\alpha_k|^2}{\sigma_w^2}\|\dot{\boldsymbol{b}}(\phi_k)\|^2\|\boldsymbol{s}(\tau_k)\|^2_{\mathcal{H}}\xi_k^{\text{angle}} \end{aligned} \tag{63}$$

where $\xi_k^{\text{angle}} \in [0,1]$ can be interpreted as the information loss on the SMC AoA estimation induced by the estimation of the complex amplitude α_k in the DMC.

B. Assumptions

In the following, we will introduce assumptions for the SMC and DMC model that allow further insightful discussion in terms of contributions to position information.

- The DMC is uncorrelated between antennas, i.e., $\boldsymbol{C}_{\boldsymbol{\nu}}$ is block-diagonal (cf. (11)) with

  $$\boldsymbol{C}_{\boldsymbol{\nu}}^{(m,m')} = \boldsymbol{0} \qquad\qquad \forall m \neq m'.$$

  For different antenna setups, there are different arguments supporting this assumption: For a conventional array consisting of omni-directional antennas, the DMC becomes approximately uncorrelated for an antenna-spacing of $\lambda/2$ and a uniform angular power spectrum [44].

  In our considered case using directional antennas, it can be argued that each antenna at the anchor covers one sector in the azimuth plane with differently aligned main beam directions. As a result, the shapes of the beampatterns are approximately orthogonal such that

  $$\int S_\nu(\phi,\tau)\, b_m(\phi)\, b_{m'}^*(\phi)\,\mathrm{d}\phi \ll \int S_\nu(\phi,\tau)\,|b_m(\phi)|^2\,\mathrm{d}\phi. \tag{64}$$

  With this, we may reduce the noise covariance matrix in (10) to block matrices on the main diagonal for which the mth matrix is given as

  $$\boldsymbol{C}_{\boldsymbol{n}}^{(m)} = \int S_\nu^{(m)}(\tau)\,\boldsymbol{s}(\tau)\boldsymbol{s}(\tau)^{\mathrm{H}}\,\mathrm{d}\tau + \sigma_w^2\boldsymbol{I}_N \tag{65}$$

  where $S_\nu^{(m)}(\tau) = \int S_\nu(\phi,\tau)|b_m(\phi)|^2\mathrm{d}\phi$ is the delay power spectrum (DPS) considering the mth antenna beampattern of the antenna array at the anchor node.

- We assume that SMCs are orthogonal to each other, i.e., there is no path-overlap in the resolvable angle and delay domain. Analogously to the previous assumption, this can be justified due to the directional antennas at the anchor which cover non-overlapping sectors in the azimuth plane. This means that for any two SMCs k and k', we have

$$\sum_{m=1}^{M} b_m^*(\phi_k) b_m(\phi_{k'}) \langle \boldsymbol{s}(\tau_k), \boldsymbol{s}(\tau_{k'}) \rangle_{\mathcal{H}_m} \ll \sum_{m=1}^{M} |b_m(\phi_k)|^2 \|\boldsymbol{s}(\tau_k)\|_{\mathcal{H}_m} \tag{66}$$

  where

$$\langle \boldsymbol{x}, \boldsymbol{y} \rangle_{\mathcal{H}_m} = \sigma_w^2 \, \boldsymbol{x}^{\mathrm{H}} \big(\boldsymbol{C}_{\boldsymbol{n}}^{(m)}\big)^{-1} \boldsymbol{y} \tag{67}$$

$$\|\boldsymbol{x}\|_{\mathcal{H}_m}^2 = \langle \boldsymbol{x}, \boldsymbol{x} \rangle_{\mathcal{H}_m} \tag{68}$$

  are the weighted inner product and weighted norm, respectively, accounting for the inverse of $\boldsymbol{C}_{\boldsymbol{n}}^{(m)}$ which is a whitening operation [12, 46]. Specifically, the left-hand side expression of (66) is always close to zero, except for the rare case of two SMCs that arrive at the same time while also having the same AoA.

- We further simplify the DMC statistics by saying that each antenna at the anchor exhibits the same DMC statistics, i.e.,

$$S_\nu(\tau) = S_\nu^{(1)}(\tau) = \cdots = S_\nu^{(M)}(\tau) \tag{69}$$

  resulting in

$$\langle \boldsymbol{x}, \boldsymbol{y} \rangle_{\mathcal{H}} = \langle \boldsymbol{x}, \boldsymbol{y} \rangle_{\mathcal{H}_1} = \cdots = \langle \boldsymbol{x}, \boldsymbol{y} \rangle_{\mathcal{H}_M} \tag{70}$$

$$\|\boldsymbol{x}\|_{\mathcal{H}}^2 = \|\boldsymbol{x}\|_{\mathcal{H}_1}^2 = \cdots = \|\boldsymbol{x}\|_{\mathcal{H}_M}^2 \, . \tag{71}$$

References

[1] W. H. Chin, Z. Fan, and R. Haines, “Emerging technologies and research challenges for 5G wireless networks,” *IEEE Wireless Commun.*, vol. 21, no. 2, pp. 106–112, Apr. 2014.

[2] J. G. Andrews, S. Buzzi, W. Choi, S. V. Hanly, A. Lozano, A. C. K. Soong, and J. C. Zhang, “What will 5G be?” *IEEE J. Sel. Areas Commun.*, vol. 32, no. 6, pp. 1065–1082, June 2014.

[3] F. Rusek, D. Persson, B. K. Lau, E. G. Larsson, T. L. Marzetta, O. Edfors, and F. Tufvesson, “Scaling up MIMO: Opportunities and challenges with very large arrays,” *IEEE Signal Process. Mag.*, vol. 30, no. 1, pp. 40–60, Jan. 2013.

[4] E. G. Larsson, O. Edfors, F. Tufvesson, and T. L. Marzetta, “Massive MIMO for next generation wireless systems,” *IEEE Wireless Commun. Mag.*, vol. 52, no. 2, pp. 186–195, Feb. 2014.

[5] E. Torkildson, U. Madhow, and M. Rodwell, “Indoor millimeter wave MIMO: Feasibility and performance,” *IEEE Trans. Wireless Commun.*, vol. 10, no. 12, pp. 4150–4160, Dec. 2011.

[6] T. S. Rappaport, S. Sun, R. Mayzus, H. Zhao, Y. Azar, K. Wang, G. N. Wong, J. K. Schulz, M. Samimi, and F. Gutierrez, “Millimeter wave mobile communications for 5G cellular: It will work!” *IEEE Access*, vol. 1, pp. 335–349, 2013.

[7] S. Rangan, T. S. Rappaport, and E. Erkip, "Millimeter-wave cellular wireless networks: Potentials and challenges," *Proc. IEEE*, vol. 102, no. 3, pp. 366–385, Mar. 2014.

[8] K. Witrisal, P. Meissner, E. Leitinger, Y. Shen, C. Gustafson, F. Tufvesson, K. Haneda, D. Dardari, A. F. Molisch, A. Conti, and M. Z. Win, "High-accuracy localization for assisted living: 5G systems will turn multipath channels from foe to friend," *IEEE Signal Process. Mag.*, vol. 33, no. 2, pp. 59–70, Mar. 2016.

[9] H. Wymeersch, G. Seco-Granados, G. Destino, D. Dardari, and F. Tufvesson, "5G mmwave positioning for vehicular networks," *IEEE Wireless Commun.*, vol. 24, no. 6, pp. 80–86, Dec. 2017.

[10] Y. Shen and M. Win, "Fundamental limits of wideband localization; Part I: A general framework," *IEEE Trans. Inf. Theory*, vol. 56, no. 10, pp. 4956–4980, Oct. 2010.

[11] Y. Han, Y. Shen, X. Zhang, M. Win, and H. Meng, "Performance limits and geometric properties of array localization," *IEEE Trans. Inf. Theory*, vol. 62, no. 2, pp. 1054–1075, Feb. 2016.

[12] K. Witrisal, E. Leitinger, S. Hinteregger, and P. Meissner, "Bandwidth scaling and diversity gain for ranging and positioning in dense multipath channels," *IEEE Wireless Commun. Lett.*, vol. 5, no. 4, pp. 396–399, 2016.

[13] T. Wilding, S. Grebien, U. Mühlmann, and K. Witrisal, "Accuracy bounds for array-based positioning in dense multipath channels," *Sensors*, vol. 18, no. 12, p. 4249, 2018.

[14] T. Wilding, S. Grebien, E. Leitinger, U. Mühlmann, and K. Witrisal, "Single-anchor, multipath-assisted indoor positioning with aliased antenna arrays," in *Proc. Asilomar-18*, Pacifc Grove, CA, USA, Oct. 2018.

[15] E. Leitinger, P. Meissner, C. Rudisser, G. Dumphart, and K. Witrisal, "Evaluation of position-related information in multipath components for indoor positioning," *IEEE J. Sel. Areas Commun.*, vol. 33, no. 11, pp. 2313–2328, Nov. 2015.

[16] A. Shahmansoori, G. E. Garcia, G. Destino, G. Seco-Granados, and H. Wymeersch, "Position and orientation estimation through millimeter-wave MIMO in 5G systems," *IEEE Trans. Wireless Commun.*, vol. 17, no. 3, pp. 1822–1835, Mar. 2018.

[17] R. Mendrzik, H. Wymeersch, G. Bauch, and Z. Abu-Shaban, "Harnessing NLOS components for position and orientation estimation in 5G millimeter wave MIMO," *IEEE Trans. Wireless Commun.*, vol. 18, no. 1, pp. 93–107, Jan. 2019.

[18] Z. Abu-Shaban, X. Zhou, T. Abhayapala, G. Seco-Granados, and H. Wymeersch, "Error bounds for uplink and downlink 3D localization in 5G millimeter wave systems," *IEEE Trans. Wireless Commun.*, vol. 17, no. 8, pp. 4939–4954, Aug. 2018.

[19] A. Molisch, *Wireless Communications.* Wiley, 2005.

[20] E. Leitinger, F. Meyer, F. Hlawatsch, K. Witrisal, F. Tufvesson, and M. Z. Win, "A belief propagation algorithm for multipath-based SLAM," *IEEE Trans. Wireless Commun.*, vol. 18, no. 12, pp. 5613–5629, Dec. 2019.

[21] E. Leitinger, F. Meyer, F. Tufvesson, and K. Witrisal, "Factor graph based simultaneous localization and mapping using multipath channel information," in *Proc. IEEE ICCW-17*, Paris, France, May 2017, pp. 652–658.

[22] C. Gentner, T. Jost, W. Wang, S. Zhang, A. Dammann, and U. C. Fiebig, "Multipath assisted positioning with simultaneous localization and mapping," *IEEE Trans. Wireless Commun.*, vol. 15, no. 9, pp. 6104–6117, Sep. 2016.

[23] Y. Kuang, K. Åström, and F. Tufvesson, "Single antenna anchor-free UWB positioning based on multipath propagation," in *Proc. IEEE ICC-13*, Budapest, Hungary, Jun. 2013, pp. 5814–5818.

[24] R. Mendrzik, F. Meyer, G. Bauch, and M. Z. Win, "Enabling situational awareness in millimeter wave massive MIMO systems," *IEEE J. Sel. Topics Signal Process.*, vol. 13, no. 5, pp. 1196–1211, Sep. 2019.

[25] A. Guerra, F. Guidi, and D. Dardari, "Single-anchor localization and orientation performance limits using massive arrays: MIMO vs. beamforming," *IEEE Trans. Wireless Commun.*, vol. 17, no. 8, pp. 5241–5255, Aug. 2018.

[26] V. V. Ratnam, A. F. Molisch, O. Y. Bursalioglu, and H. C. Papadopoulos, "Hybrid beamforming with selection for multiuser massive MIMO systems," *IEEE Trans. Signal Process.*, vol. 66, no. 15, pp. 4105–4120, Aug. 2018.

[27] S. S. Ioushua and Y. C. Eldar, "A family of hybrid analog-digital beamforming methods for massive MIMO systems," *IEEE Trans. Signal Process.*, vol. 67, no. 12, pp. 3243–3257, June 2019.

[28] A. Fascista, A. Coluccia, H. Wymeersch, and G. Seco-Granados, "Millimeter-wave downlink positioning with a single-antenna receiver," *IEEE Trans. Wireless Commun.*, vol. 18, no. 9, pp. 4479–4490, Sep. 2019.

[29] N. Garcia, H. Wymeersch, and E. G. Larsson, "MIMO with more users than RF chains," 2017.

[30] J. Chen, D. Steinmetzer, J. Classen, E. Knightly, and M. Hollick, "Pseudo lateration: Millimeter-wave localization using a single RF chain," in *Proc. IEEE WCNC-17*, Mar. 2017, pp. 1–6.

[31] B. Großwindhager, M. Rath, J. Kulmer, M. S. Bakr, C. A. Boano, K. Witrisal, and K. Römer, "SALMA: UWB-based single-anchor localization system using multipath assistance," in *Proceedings of the 16th ACM Conference on Embedded Networked Sensor Systems*, ser. SenSys '18. New York, NY, USA: ACM, 2018, pp. 132–144. [Online]. Available: http://doi.acm.org/10.1145/3274783.3274844

[32] M. Rath, J. Kulmer, M. S. Bakr, B. Großwindhager, and K. Witrisal, "Multipath-assisted indoor positioning enabled by directional UWB sector antennas," in *Proc. IEEE SPAWC-17*, July 2017, pp. 1–5.

[33] P. Zand, J. Romme, J. Govers, F. Pasveer, and G. Dolmans, "A high-accuracy phase-based ranging solution with Bluetooth Low Energy (BLE)," in *Proc. IEEE WCNC-19*, 04 2019.

[34] G. Giorgetti, A. Cidronali, S. K. S. Gupta, and G. Manes, "Single-anchor indoor localization using a switched-beam antenna," *IEEE Commun. Lett.*, vol. 13, no. 1, pp. 58–60, Jan. 2009.

[35] A. Cidronali, S. Maddio, G. Giorgetti, and G. Manes, "Analysis and performance of a smart antenna for 2.45-GHz single-anchor indoor positioning," *IEEE Trans. Microw. Theory Tech.*, vol. 58, no. 1, pp. 21–31, Jan. 2010.

[36] G. Giorgetti, S. Maddio, A. Cidronali, S. K. S. Gupta, and G. Manes, "Switched beam antenna design principles for angle of arrival estimation," in *Proc. European Wireless Technology Conference 2009*, Sep. 2009, pp. 5–8.

[37] J. Kulmer, S. Hinteregger, B. Großwindhager, M. Rath, M. S. Bakr, E. Leitinger, and K. Witrisal, "Using DecaWave UWB transceivers for high-accuracy multipath-assisted indoor positioning," in *Proc. IEEE ICCW-17*, Paris, France, May 2017, pp. 1239–1245.

[38] J. Kulmer, S. Grebien, M. Rath, and K. Witrisal, "On the unimportance of phase-coherent measurements for beampattern-assisted positioning," in *Proc. IEEE WCNC-18*, Apr. 2018, pp. 1–6.

[39] B. H. Fleury, "First- and second-order characterization of direction dispersion and space selectivity in the radio channel," *IEEE Trans. Inf. Theory*, vol. 46, no. 6, pp. 2027–2044, Sept. 2000.

[40] A. Richter, "Estimation of Radio Channel Parameters: Models and Algorithms," Ph.D. dissertation, Ilmenau University of Technology, 2005.

[41] J. Karedal, S. Wyne, P. Almers, F. Tufvesson, and A. Molisch, "A measurement-based statistical model for industrial ultra-wideband channels," *IEEE Trans. Wireless Commun.*, vol. 6, no. 8, pp. 3028–3037, Aug. 2007.

[42] H. Kim, "Double-sided two-way ranging algorithm to reduce ranging time," *IEEE Commun. Lett.*, vol. 13, no. 7, pp. 486–488, July 2009.

[43] G. Durgin, *Space-time Wireless Channels*, 1st ed. Upper Saddle River, NJ, USA: Prentice Hall Press, 2002.

[44] A. Paulraj, R. Nabar, and D. Gore, *Introduction to space-time wireless communications.* Cambridge university press, 2003.

[45] J. Kunisch and J. Pamp, "An ultra-wideband space-variant multipath indoor radio channel model," in *Proc. IEEE ICUWB-03*, Nov. 2003, pp. 290–294.

[46] H. L. Van Trees, *Detection, Estimation and Modulation, Part I.* Wiley Press, 1968.

[47] S. Kay, *Fundamentals of Statistical Signal Processing: Estimation Theory.* Prentice Hall Signal Processing Series, 1993.

[48] H. L. Van Trees, *Optimum array processing: Part IV of detection, estimation, and modulation theory.* John Wiley & Sons, 2004.

[49] P. Meissner, E. Leitinger, and K. Witrisal, "UWB for robust indoor tracking: Weighting of multipath components for efficient estimation," *IEEE Wireless Comm. Lett.*, vol. 3, no. 5, pp. 501–504, Oct. 2014.

[50] J. Kulmer, S. Grebien, E. Leitinger, and K. Witrisal, “Delay estimation in presence of dense multipath,” *IEEE Wireless Commun. Lett.*, vol. 8, no. 5, pp. 1481–1484, Oct. 2019.

[51] R. Zetik, J. Sachs, and R. S. Thomä, “UWB short-range radar sensing - The architecture of a baseband, pseudo-noise UWB radar sensor,” *IEEE Instrum. Meas. Mag.*, vol. 10, no. 2, pp. 39–45, Apr. 2007.

Multipath-assisted Indoor Positioning Enabled by Directional UWB Sector Antennas

Michael Rath, Josef Kulmer, Mustafa S. Bakr, Bernhard Großwindhager,
and Klaus Witrisal

published in the 18th International Workshop on Signal Processing Advances in Wireless Communications (SPAWC 2017)

Abstract

High-accuracy indoor radio positioning can be achieved by using high signal bandwidths to increase the time resolution. Multiple fixed anchor nodes are needed to compute the position or alternatively, reflected multipath components can be exploited with a single anchor. In this work, we propose a method that explores the time and angular domains with a single anchor. This is enabled by switching between multiple directional ultra-wideband (UWB) antennas. The UWB transmission allows to perform multipath resolved indoor positioning, while the directionality increases the robustness to undesired, interfering multipath propagation with the benefit that the required bandwidth is drastically reduced. The positioning accuracy and performance bounds of the switched antenna are compared to an omni-directional antenna. Two positioning algorithms are presented based on different prior knowledge available, one using floorplan information only and the other using additionally the beampatterns of the antennas. We show that the accuracy of the position estimate is significantly improved, especially in tangential direction to the anchor.

1 Introduction

Accurate radio positioning for indoor environments can be achieved with time-of-flight methods based on (ultra-) wideband signals. In harsh scenarios, the dense multipath propagation can significantly deteriorate the probing signals. To tackle this issue, one can increase the signal bandwidth, allowing for an increased time resolution such that the interfering multipath is resolved in time from the useful line-of-sight (LOS) component [1]. At ultra-wide bandwidth (UWB), one can even exploit multipath, turning a foe into a friend [2]. This makes it possible to reduce infrastructure and to gain robustness in non-line-of-sight situations.

Alternatively, multiple measurements can be combined to resolve the multipath in the angular domain, which reduces the bandwidth required to achieve a desired accuracy. This can be achieved by combining signals originating from different transmitters distributed over the environment, or by using array processing techniques where the measurements of many omni-directional antennas are used. The latter case, using wideband antennas, is well known to yield highly accurate position measurements [3, 4], [5, Chapter 18]. However, both approaches require a lot of infrastructure and coherent processing of the received signals.

We propose employing multiple switched directional antennas which are capable of UWB transmissions [6]. The antennas are connected to a single transceiver, which will be used as an anchor, for instance. Each employed antenna covers (e.g.) a part of the azimuth plane. Due to the UWB transmission, their measurements can be used to perform multipath-resolved positioning where detectable multipath components (MPC) are associated with the environment. The directional antenna reduces interfering multipath and thus the required bandwidth to be able to resolve MPCs. We analyze the achieved positioning accuracy using directional antennas in comparison with an omni-directional one. We also derive algorithms for this new type of radio frontend. Both results are validated using experimental data from a measurement campaign. Directive antennas were also proposed for indoor positioning in [7, 8], however received signal strength measurements are used from narrowband antenna elements to augment angle-of-arrival estimation.

The paper is organized as follows: Section 2 discusses the basic signal model. Section 3 provides a description of the statistical error bounds for positioning taking the directive antennas into account. Section 4 describes the developed positioning algorithms based on the signal model. In Section 5 we evaluate the performance bounds, likelihood functions and achieved position accuracy with the algorithms based on measurement data. Section 6 summarizes the work and presents concluding remarks.

2 Signal Model

We consider an agent node aiming at finding its position $\boldsymbol{p}$ using radio frequency measurements from one anchor node, located at known position $\boldsymbol{a}$. The agent node is equipped with a single omni-directional antenna. The anchor node employs a sector antenna which consists of M directional antennas as illustrated in Fig. 1. Two anchors are shown, equipped with $M = 4$ antennas, each covering one sector of the azimuth angle plane with a half-power beamwidth of about 90°. Antenna m transmits the signal $s(t)$ and the sampled signal $\boldsymbol{r}_m \in \mathbb{C}^{N\times 1}$ is observed at the agent. We model this received signal as a sum of deterministic MPCs plus contributions of diffuse multipath (DM) $\boldsymbol{\nu}_m$ and additive, white Gaussian noise

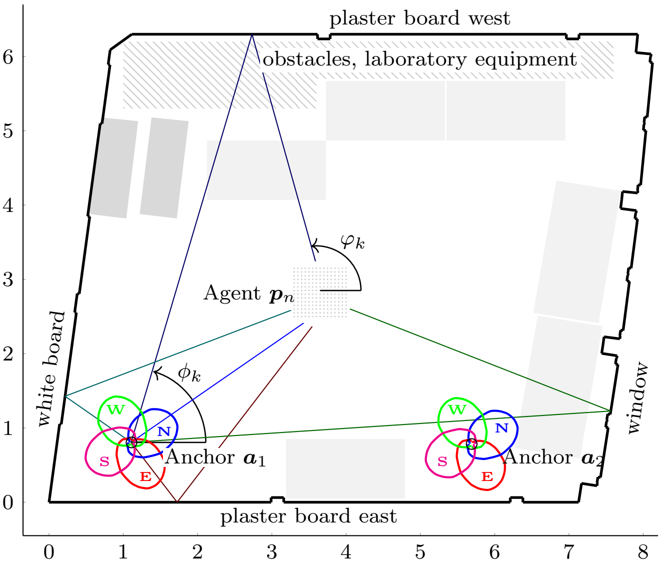

Figure 1: Floorplan of measurement environment. Tables (light-gray) and cupboards (dark-gray) are shown, as well as patterns of the used antennas at the anchors. The axis describes the distance in meters.

(AWGN) $\boldsymbol{w}_m$, according to

$$\boldsymbol{r}_m = \sum_{k=1}^{K} \alpha_k b_m(\phi_k) \boldsymbol{s}(\tau_k) + \boldsymbol{\nu}_m + \boldsymbol{w}_m. \tag{1}$$

The first term on the right-hand-side describes the deterministic MPCs as replicas of the transmitted signal $s(t)$. Each replica is delayed by τ_k which is determined by the length of the path between the agent and the anchor. Reflected paths can be modeled by virtual anchors whose positions are computed from the environment model [2, 9]. We use a vector notation with $\boldsymbol{s}(\tau_k) = [s(0 \cdot T_s - \tau_k), s(1 \cdot T_s - \tau_k), \ldots, s((N-1) \cdot T_s - \tau_k)]^{\mathrm{T}}$ where T_s is the sampling period and the signal is normalized according to $\|s(t)\|^2 = 1$. For each MPC, the environmental model is also used to determine the angle-of-departure at the anchor denoted by ϕ_k, as well as the angle-of-arrival at the agent denoted by φ_k. This is illustrated in Fig. 1, where both angles are shown for the MPC that comes from the “plaster board west” surface. The amplitude of each MPC is determined on the one hand by α_k which covers propagation effects, e.g. path loss or attenuation at the reflection point, and on the other hand by the complex-valued beampattern described by $b_m(\phi_k)$. For simplicity, we consider only the directional characteristics at the anchor side, assuming a uniform radiation pattern at the agent.

The second term of Equation (1) describes the DM which models interfering MPCs that cannot be associated to an environmental model. It is described as a zero-mean Gaussian random process, shaped by the transmitted signal $s(t)$. The AWGN exhibits a constant double-sided power spectral density of $N_0/2$.

3 Position error bound

We use the *position error bound* (PEB) [10] as derived in [2, 11] to analyze the performance gain of the sector antenna when used for multipath-assisted positioning. It is defined as

$$\mathbb{E}\{\|\boldsymbol{p}-\hat{\boldsymbol{p}}\|^2\} \geq \operatorname{tr}\{\boldsymbol{\mathcal{I}}_{\boldsymbol{p}}^{-1}\} \tag{2}$$

where $\mathbb{E}\{\cdot\}$ and $\operatorname{tr}\{\cdot\}$ denote the expectation and trace operators, respectively, and $\boldsymbol{\mathcal{I}}_{\boldsymbol{p}}$ is the Fisher information matrix of $\boldsymbol{p}$ written by

$$\boldsymbol{\mathcal{I}}_{\boldsymbol{p}} = \frac{8\pi^2\beta^2}{c^2}\sum_k\sum_m \mathrm{SINR}_{k,m}\boldsymbol{D}_r(\varphi_k). \tag{3}$$

Here, c is the speed of light, β is the mean-square bandwidth of the transmitted pulse and $\boldsymbol{D}_r(\varphi_k) = \boldsymbol{e}(\varphi_k)\boldsymbol{e}(\varphi_k)^{\mathrm{T}}$ is called the ranging direction matrix that is used to relate the ranging information intensity to the direction of φ_k, where $\boldsymbol{e}(\varphi_k) = [\cos\varphi_k \;\; \sin\varphi_k]^{\mathrm{T}}$ [10]. The contribution of each individual MPC is quantified by its signal-to-interference-plus-noise ratio (SINR) [11], here defined by

$$\mathrm{SINR}_{k,m} = \frac{|\alpha_k|^2|b_m(\phi_k)|^2}{N_0 + T_{\mathrm{p}}\int\limits_{\phi}|b_m(\phi)|^2 S_\nu(\tau_k,\phi)\,\mathrm{d}\phi}$$

where $S_\nu(\tau,\phi)$ describes the angle-delay power spectrum of the DM and T_{p} is a pulse duration parameter of waveform $s(t)$, see [11].

From (3), the gain of exploiting M measurements is seen to be expressed by $\sum_m \mathrm{SINR}_{k,m}$, because $\boldsymbol{D}_r(\varphi_k)$ is the same for all m. This result is based on the assumption that (i) only ranging information is exploited for solving the positioning problem (i.e. angle information is neglected because the angle resolution is assumed to be very coarse), and (ii) the DM and AWGN are independent for individual measurements m. To evaluate the potential performance gain, we assume a uniform angular power spectrum $S_\nu(\tau_k,\phi) = S_\nu(\tau_k)$. Furthermore, since the efficiency of the antenna is not related to its directivity, we assume that its total power gain is independent of the beam pattern, expressed as $\int_{-\pi}^{\pi}|b_m(\phi)|^2\,\mathrm{d}\phi = 1$. We thus get

$$\sum_m \mathrm{SINR}_{k,m} \approx \frac{|\alpha_k|^2}{N_0 + T_{\mathrm{p}}S_\nu(\tau_k)}\sum_m |b_m(\phi_k)|^2 \tag{4}$$

showing that the SINR gain is approximated as the sum of the antenna power gains at ϕ_k.

4 Derivation of the positioning algorithm

The previous section investigated the signal model and the expected position error using performance bounds. In the following, we derive an algorithm for multipath-assisted indoor localization using a single anchor only. We will exemplify two methods: Algorithm I treats the measurements as independent and Algorithm II incorporates the antenna gain patterns to get the agent's position.

In Algorithm I we assume that the path amplitudes, including the beam-patterns, $\alpha_{k,m} = \alpha_k b_m(\phi_k)$, are estimated independently from each measurement m as nuisance parameters. Stacking the signals $\boldsymbol{s}(\tau_k)$ in the signal matrix

$\boldsymbol{S}(\boldsymbol{\tau}) = [\boldsymbol{s}(\tau_1), \dots, \boldsymbol{s}(\tau_K)]$ with the delays $\boldsymbol{\tau} = [\tau_1, \dots, \tau_K]^{\mathrm{T}}$ and corresponding the amplitudes in $\boldsymbol{\alpha}_m = [\alpha_{1,m}, \dots, \alpha_{K,m}]^{\mathrm{T}}$, the signal model is

$$\boldsymbol{r}_m = \boldsymbol{S}(\boldsymbol{\tau})\boldsymbol{\alpha}_m + \boldsymbol{w}_m$$

where we neglect the contribution by the DM. With this AWGN noise model, the likelihood function of the received signal $\boldsymbol{r}_m$ conditioned on $\boldsymbol{\alpha}_m$ and $\boldsymbol{\tau}$ follows as

$$p(\boldsymbol{r}_m|\boldsymbol{\alpha}_m, \boldsymbol{\tau}) \propto \exp\big\{-\|\boldsymbol{r} - \boldsymbol{S}(\boldsymbol{\tau})\boldsymbol{\alpha}_m\|^2\big\}. \tag{5}$$

In order to estimate the agent's position, we express the delays $\boldsymbol{\tau}$ as a function of the agent's position $\boldsymbol{p}$ using the geometric model of the environment. With hypothesized $\boldsymbol{\tau}$, the amplitudes are estimated using least-squares [12]

$$\hat{\boldsymbol{\alpha}}_m = (\boldsymbol{S}^{\mathrm{H}}(\boldsymbol{\tau})\boldsymbol{S}(\boldsymbol{\tau}))^{-1}\boldsymbol{S}^{\mathrm{H}}(\boldsymbol{\tau})\boldsymbol{r}_m. \tag{6}$$

Stacking the measurements in $\boldsymbol{r} = [\boldsymbol{r}_1^{\mathrm{T}}, \cdots, \boldsymbol{r}_M^{\mathrm{T}}]^{\mathrm{T}}$ then the assumption of independent measurements and amplitudes yields

$$p(\boldsymbol{r}|\boldsymbol{p}) = \prod_m p(\boldsymbol{r}_m|\boldsymbol{p})$$

and the maximum likelihood estimation of the agent position $\hat{\boldsymbol{p}}_{\mathrm{Alg1}}$ follows as

$$\hat{\boldsymbol{p}}_{\mathrm{Alg1}} = \underset{\boldsymbol{p}\in\mathcal{P}}{\operatorname{argmax}} \prod_m p(\boldsymbol{r}_m|\boldsymbol{p}) \tag{7}$$

with the set $\mathcal{P}$ containing hypothesized agent positions within the communication range to the anchor.

Algorithm II explicitly employs the complex-valued beampatterns $\{b_m(\cdot)\}$ to estimate the MPC amplitudes α_k jointly from all measurements $m = 1 \dots, M$ using

$$\boldsymbol{r} = \boldsymbol{X}(\boldsymbol{\tau}, \{b_m(\phi_k)\})\boldsymbol{\alpha} + \boldsymbol{w}$$

where

$$\boldsymbol{X}(\boldsymbol{\tau}, \{b_m(\phi_k)\}) = \begin{bmatrix} b_1(\phi_1)\boldsymbol{s}(\tau_1) & \dots & b_1(\phi_K)\boldsymbol{s}(\tau_K) \\ \vdots & & \vdots \\ b_M(\phi_1)\boldsymbol{s}(\tau_1) & \dots & b_M(\phi_K)\boldsymbol{s}(\tau_K) \end{bmatrix}$$

and $\boldsymbol{\alpha} = [\alpha_1, \dots, \alpha_K]^{\mathrm{T}}$ and $\boldsymbol{w}$ as AWGN. The likelihood function follows in an equivalent fashion as (5) with the ML solution of $\hat{\boldsymbol{p}}_{\mathrm{Alg2}}$ according to

$$\hat{\boldsymbol{p}}_{\mathrm{Alg2}} = \underset{\boldsymbol{p}\in\mathcal{P}}{\operatorname{argmax}}\, p(\boldsymbol{r}|\boldsymbol{p}) \tag{8}$$

where we expressed the conditionals $\boldsymbol{\tau}$ and $\{b_m(\phi_k)\}$ by the agent's position $\boldsymbol{p}$. The amplitudes $\boldsymbol{\alpha}$ result equivalent to (6). Assuming non-overlapping MPCs the amplitudes are

$$\hat{\alpha}_k = \frac{\sum\limits_{m=1}^{M} b_m^*(\phi_k)\boldsymbol{s}^{\mathrm{H}}(\tau_k)\boldsymbol{r}_m}{\sum\limits_{m=1}^{M} |b_m(\phi_k)|^2} = \frac{\sum\limits_{m=1}^{M} b_m^*(\phi_k)\hat{\alpha}_{k,m}}{\sum\limits_{m=1}^{M} |b_m(\phi_k)|^2} \tag{9}$$

with $\hat{\alpha}_{k,m} = \boldsymbol{s}^{\mathrm{H}}(\tau_k)\boldsymbol{r}_m$ at the right-hand-side of (9). It shows that the estimated amplitudes $\{\hat{\alpha}_k\}$ of Algorithm II are a weighted average of the individual amplitudes $\{\hat{\alpha}_{k,m}\}$ in Algorithm I.

5 Evaluation

In this section, we evaluate the derived position performance bound in Section 3 and the achieved accuracy of the multipath-assisted indoor localization algorithms.

5.1 Measurement setup

We placed one agent at $\boldsymbol{p}_n$ and two anchors at $\boldsymbol{a}_1$ and $\boldsymbol{a}_2$ as illustrated in Fig. 1. The anchors were equipped with $M = 4$ directive antennas, equally spaced on a circle with radius of 2 cm at center $\boldsymbol{a}$. The antennas were aligned such that their mainlobes point at different directions, named *North* (N), *West* (W), *South* (S) and *East* (E), each 90° apart as illustrated in Fig. 1. The measurements between the agent and each directive antenna were performed using an Ilmsens Correlative Channel Sounder [13]. Subsequently, each measurement was convolved by a raised cosine pulse using a carrier frequency of $f_\mathrm{c} = 5.4\,\mathrm{GHz}$. For a comparison of the impact of bandwidth on the estimated SINRs, we used (i) a pulse duration of $T_\mathrm{p} = 0.5\,\mathrm{ns}$ (equivalent to a bandwidth of 2 GHz) with a roll-off factor of $R = 0.5$ and (ii) a pulse duration of $T_\mathrm{p} = 2.4\,\mathrm{ns}$ (bandwidth of 500 MHz) with a roll-off factor of $R = 0.9$ which has been found to model Channels 2 and 5 of the recently available DecaWave DW1000 UWB transceiver [14]. We placed the agent at $n \in \{1, \dots, 210\}$ different positions on a 15×14 grid with 5 cm spacing, resulting in 420 channel measurements. For a comparison, we repeated the experiment using omni-directional antennas on both anchor and agent nodes.

The complex-valued beampattern $b_m(\cdot)$ was available as a codebook in a resolution of 10°. We used linear interpolation to evaluate the beampattern, given a specific angle. The spatial offset between the directive antennas results in a phase shift of the carrier frequency as a function of the MPC angle-of-departure. For simplicity, we considered this phase shift already in the beampattern.

5.2 Evaluation of performance bounds

We evaluate the SINR values of individual MPCs which quantify their contributions to the PEB in (2) via (3). Tables 1 and 2 report the estimated SINR values for selected MPCs for the two anchor positions and the pulse durations of $T_\mathrm{p} = 0.5\,\mathrm{ns}$ and $T_\mathrm{p} = 2\,\mathrm{ns}$. The SINRs are reported for each directive antenna based on the estimated amplitudes $\hat{\alpha}_{k,m}$. The SINR of *Sec* is based on amplitude estimation considering the overall amplitude in (9) while *Added* denotes the (not weighted) sum of SINRs of $N+W+S+E$ as modeled by (4). For comparison we also show the SINRs for an omni-directional antenna at the anchor (*Omni*).

Comparison of Tables 1 and 2 demonstrates that, in general, the SINR increases with higher signal bandwidth, justified by the improved separation of MPCs along the delay domain. Further, we can observe that the SINR of an individual directive antenna (N, W, S or E) is strongly dependent on the angle-of-departure of the MPC (see Fig. 1 which exemplifies the beampatterns of the directional antennas in addition to the angle-of-departure of the MPCs).

Consideration of a joint amplitude estimation is highly beneficial in terms of SINR as shown in the *Sec* column. The SINR is clearly improved since it takes information obtained at M measurements into account. The sum of individual SINRs (*Added*) is seen to be an upper limit on the achievable performance. Hereby independent measurements of the DM of each antenna are required.

The tremendous advantage of the directional antennas is the potential to resolve MPCs in the spatial domain. This is justified by Tables 1 and 2 by comparison

Table 1: SINR in dB of deterministic MPCs for $T_\mathrm{p} = 0.5$ ns, $R = 0.5$ at anchor position $\boldsymbol{a}_1$ (top) and $\boldsymbol{a}_2$ (bottom) of sector antenna *North* (N), *West* (W), *South* (S), *East* (E). The omni-directional antenna (*Omni*) is shown for comparison.

anchor position $\boldsymbol{a}_1$

MPC	N	W	S	E	*Sec*	*Added*	*Omni*
LOS	30.6	16.4	17.9	11.7	33.0	31.0	25.4
plasterb east	6.3	$-\infty$	$-\infty$	12.1	12.8	13.1	11.0
plasterb west	-1.1	3.4	-5.4	$-\infty$	3.2	5.1	0.3
white board	-1.1	18.3	15.9	-0.4	19.4	20.3	11.1
window	1.2	$-\infty$	-3.3	-1.1	1.1	4.1	0.9
$\mathrm{PEB_r}$ / cm	0.2	0.6	0.6	1.1	0.1	0.2	0.3
$\mathrm{PEB_t}$ / cm	4.4	2.3	3.2	4.6	1.8	1.6	3.2

anchor position $\boldsymbol{a}_2$

MPC	N	W	S	E	*Sec*	*Added*	*Omni*
LOS	9.0	21.5	23.6	18.3	27.7	26.5	24.8
plasterb east	-9.3	0.3	1.9	1.8	$-\infty$	6.3	2.6
plasterb west	-5.1	-0.8	$-\infty$	$-\infty$	$-\infty$	0.6	$-\infty$
window	15.2	7.8	-0.1	4.3	15.8	16.3	10.0
$\mathrm{PEB_r}$ / cm	1.0	0.5	0.4	0.7	0.3	0.3	0.4
$\mathrm{PEB_t}$ / cm	3.0	5.3	13.0	9.4	2.8	2.4	5.3

of the SINR values. Consider e.g. the MPCs *plasterb east* and *white board* using anchor position $\boldsymbol{a}_1$. At a high bandwidth of $T_\mathrm{p} = 0.5\,\mathrm{ns}$ (Table 1), both MPCs are well separated in the delay domain and subsequently reasonably high SINR values ($> 10\,\mathrm{dB}$) are obtained. The omni-directional antenna reaches similar values compared to the combined sector antennas *Sec*. As soon as the bandwidth is reduced (Table 2), both MPCs overlap and the SINRs using the omni-directional antenna suffer. Still, the sector antenna is able to gain additional spatial information, verified by the formidable improvement of *Sec* and *Added*.

Finally, we report the evaluated PEB, radial ($\mathrm{PEB_r}$) and tangential ($\mathrm{PEB_t}$) to the angle-of-arrival of the LOS. In general, the PEB is lower in direction of the LOS because the LOS is usually equipped with the highest SINR. Using the sector antennas, the tangential PEB is reduced by up to a factor of three, still employing only one anchor node.

We conclude that the SINR is strongly dependent on the beampattern as well as the bandwidth. MPCs having an angle-of-departure within the antenna's mainlobe reach high SINRs. The combination of the antennas is superior since more channel measurements are used in combination with angular diversity.

5.3 Evaluation of the likelihood functions

Fig. 2 illustrates the likelihood functions in log-domain using $\boldsymbol{a}_1$ and pulse parameters of $s(t)$ with high bandwidth $(T_\mathrm{p}, R) = (0.5\,\mathrm{ns}, 0.5)$ and low bandwidth $(2.4\,\mathrm{ns}, 0.9)$ for positions within the communication range (compare to floorplan in Fig. 1). Brighter areas indicate a better model fit. We can observe that increased bandwidth (left) yields a steeper likelihood. The angular diversity of the sector antenna using Eq. (7) (Fig. 2b) and (8) (Fig. 2c) reduces some of the local maxima and thus the probability for outliers (Fig. 2a). The estimation of $\{\alpha_k\}$ in (8)

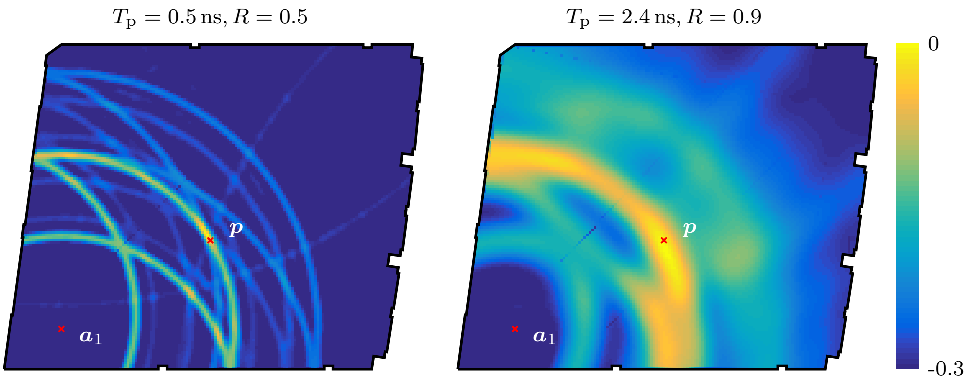

(a) Illustration of log-likelihood in (7) using the omni-directional antenna.

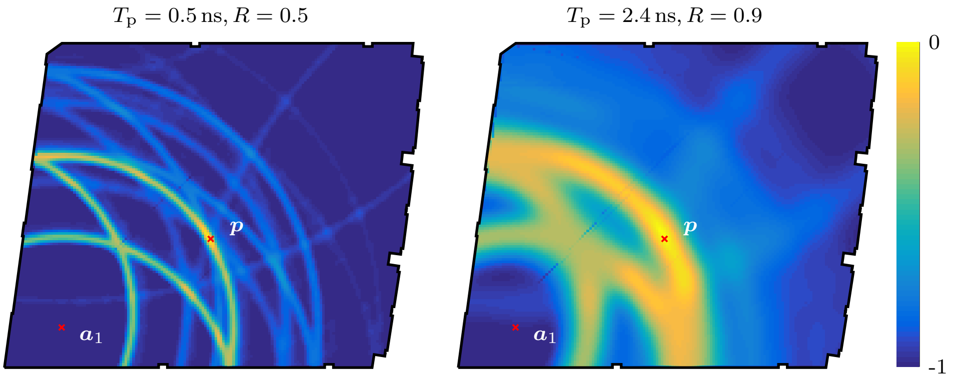

(b) Illustration of log-likelihood in (7) using the sector antenna.

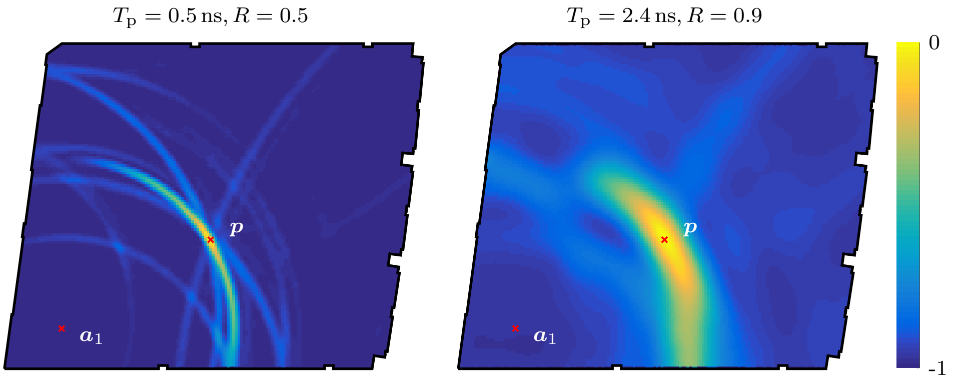

(c) Illustration of log-likelihood in (8) using the sector antenna.

Figure 2: Illustration of likelihood in log-domain using the sector antenna as function of agent position evaluated for points within the communication range (see Fig. 1). The anchor and *true* agent position are indicated by $\boldsymbol{a}_1$ and $\boldsymbol{p}$.

Table 2: SINR in dB of deterministic MPCs for $T_\mathrm{p} = 2.4$ ns, $R = 0.9$ at anchor position $\boldsymbol{a}_1$ (top) and $\boldsymbol{a}_2$ (bottom) of sector antenna *North* (N), *West* (W), *South* (S), *East* (E). The omni-directional antenna (*Omni*) is shown for comparison.

anchor position $\boldsymbol{a}_1$

MPC	N	W	S	E	*Sec*	*Added*	*Omni*
LOS	16.1	11.4	11.5	7.4	14.9	18.7	17.2
plasterb east	3.3	5.6	8.8	9.4	8.4	13.5	3.1
plasterb west	3.2	2.0	$-\infty$	-6.5	3.0	5.9	-0.6
white board	0.5	9.5	8.9	3.5	9.4	13.0	3.4
window	$-\infty$	$-\infty$	-1.1	3.0	$-\infty$	4.5	$-\infty$
$\mathrm{PEB_r}$ / cm	4.4	5.8	5.5	7.3	4.3	2.7	3.9
$\mathrm{PEB_t}$ / cm	20.5	18.9	21.5	18.2	16.9	9.8	28.1

anchor position $\boldsymbol{a}_2$

MPC	N	W	S	E	*Sec*	*Added*	*Omni*
LOS	3.8	19.3	18.2	16.2	23.5	22.9	19.4
plasterb east	-2.8	-0.1	1.9	3.4	3.5	7.2	1.4
plasterb west	$-\infty$	-0.4	$-\infty$	-4.4	-0.8	1.0	$-\infty$
window	10.8	2.2	-5.3	3.1	11.6	12.1	4.4
$\mathrm{PEB_r}$ / cm	8.0	3.1	3.6	4.3	1.9	2.0	3.0
$\mathrm{PEB_t}$ / cm	23.2	30.3	76.0	28.0	18.2	15.1	43.6

(Fig. 2c) results in a more distinct likelihood function compared to the independent estimation of $\{\alpha_{k,m}\}$ in (7) (Fig. 2a). Especially for $T_\mathrm{p} = 2.4$ ns the application of the directional antennas results in a distinct global maximum that is well separated from the local maxima as shown in Fig. 2c.

5.4 Evaluation of the position accuracy

Finally, we investigate the performance of both position estimators using anchor $\boldsymbol{a}_1$ and 210 measurements of $\{\boldsymbol{r}_m\}$ each at a different position of $\boldsymbol{p}$. All measurements were performed in LOS conditions, considering the MPCs evaluated in Tables 1 and 2. The cumulative distribution functions of the distance between the *true* and estimated positions $\epsilon = \|\boldsymbol{p}_\mathrm{true} - \hat{\boldsymbol{p}}\|$ are shown in Fig. 3. It confirms that a high bandwidth (Fig. 3 left) is favorable for indoor positioning, with 90% of ϵ below 10 cm. This reveals that the high bandwidth suffices to separate and utilize the multipath propagation.

Using a lower bandwidth (Fig. 3 right) exemplifies the gain due to the directional antennas compared to the omni-directional antenna. The omni-directional antenna is not able to separate the MPCs well enough (compare the likelihood function in Fig. 2a right) which results in a poor position error where the 90% limit of ϵ is only at 50 cm. Using the sector antenna drastically reduces the position error. Algorithm I gathers additional information due to angular diversity. The incorporation of the beampattern by Algorithm II enables highly accurate indoor localization where the 90% limit of the position error is reduced to 20 cm.

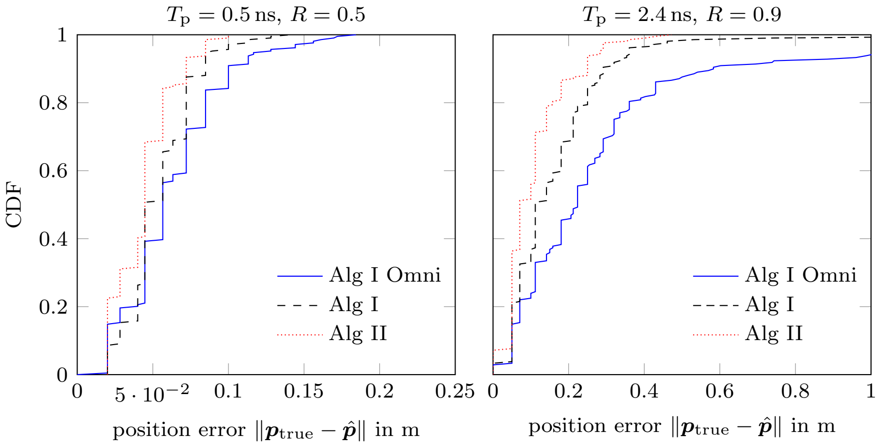

Figure 3: Cumulative distribution function (CDF) of the position error using pulse parameters $(T_\mathrm{p}, R) = (0.5\,\mathrm{ns}, 0.5)$ (left) and $(2.4\,\mathrm{ns}, 0.9)$ (right) of Algorithm I and II. Algorithm I Omni incorporates a single omni-directional antenna and is shown for comparison.

6 Conclusions

In this paper, we have evaluated a UWB indoor positioning system using multiple directive UWB sector antennas at the anchor side. We included the antenna patterns into theoretical performance bounds for positioning and, based on that, we analyzed the reliability of deterministic MPCs in comparison with the performance of an omni-directional antenna. Two positioning algorithms were presented, both described by ML estimators using the measurements of the directive antennas and the floorplan information. The second algorithm also made use of the directive antenna patterns. The accuracy of both algorithms was evaluated by examining the likelihood functions and the cumulative distribution function of the position error. It was shown that the directive antennas achieve overall better results, especially considering the tangential information of the MPC directions.

References

[1] K. Witrisal, E. Leitinger, S. Hinteregger, and P. Meissner, “Bandwidth scaling and diversity gain for ranging and positioning in dense multipath channels,” *IEEE Wireless Communications Letters*, vol. 5, no. 4, pp. 396–399, Aug 2016.

[2] K. Witrisal, P. Meissner, E. Leitinger, Y. Shen, C. Gustafson, F. Tufvesson, K. Haneda, D. Dardari, A. F. Molisch, A. Conti, and M. Z. Win, “High-accuracy localization for assisted living,” *IEEE Signal Processing Magazine*, 2016.

[3] Y. Shen and M. Z. Win, “On the accuracy of localization systems using wideband antenna arrays,” *IEEE Transactions on Communications*, vol. 58, no. 1, pp. 270–280, January 2010.

[4] Y. Han, Y. Shen, X. P. Zhang, M. Z. Win, and H. Meng, “Performance limits and geometric properties of array localization,” *IEEE Transactions on Information Theory*, vol. 62, no. 2, pp. 1054–1075, Feb 2016.

[5] B. Allen, M. Dohler, E. Okon, W. Malik, A. Brown, and D. Edwards, *Ultra wideband antennas and propagation for communications, radar and imaging.* John Wiley & Sons, 2006.

[6] B. Großwindhager, M. S. Bakr, M. Rath, F. Gentili, W. Bösch, K. Witrisal, C. A. Boano, and K. Römer, “Switchable Directional Antenna System for UWB-based Internet of Things Applications,” in *International Conference on Embedded Wireless Systems and Networks (EWSN)*, 2017.

[7] A. Cidronali, S. Maddio, G. Giorgetti, and G. Manes, “Analysis and performance of a smart antenna for 2.45-ghz single-anchor indoor positioning,” *IEEE Transactions on Microwave Theory and Techniques*, vol. 58, no. 1, pp. 21–31, 2010.

[8] G. Giorgetti, S. Maddio, A. Cidronali, S. Gupta, and G. Manes, “Switched beam antenna design principles for angle of arrival estimation,” in *Wireless Technology Conference, 2009. EuWIT 2009. European.* IEEE, 2009, pp. 5–8.

[9] J. Kunisch and J. Pamp, “An ultra-wideband space-variant multipath indoor radio channel model,” in *IEEE Conference on Ultra Wideband Systems and Technologies*, 2003.

[10] Y. Shen and M. Win, “Fundamental limits of wideband localization; part I: a general framework,” *IEEE Transactions on Information Theory*, 2010.

[11] E. Leitinger, P. Meissner, C. Ruedisser, G. Dumphart, and K. Witrisal, “Evaluation of position-related information in multipath components for indoor positioning,” *IEEE Journal on Selected Areas in Communications*, 2015.

[12] G. H. Golub and V. Pereyra, “The differentiation of pseudo-inverses and nonlinear least squares problems whose variables separate,” *SIAM Journal on numerical analysis*, vol. 10, no. 2, pp. 413–432, 1973.

[13] R. Zetik, J. Sachs, and R. S. Thoma, “Uwb short-range radar sensing - the architecture of a baseband, pseudo-noise uwb radar sensor,” *IEEE Instrumentation Measurement Magazine*, vol. 10, no. 2, pp. 39–45, April 2007.

[14] J. Kulmer, S. Hinteregger, B. Großwindhager, M. Rath, M. Bakr, E. Leitinger, and K. Witrisal, “Using DecaWave UWB Transceivers for High-accuracy Multipath-assisted Indoor Positioning,” in *IEEE ICC 2017 Workshop on Advances in Network Localization and Navigation (ANLN)*, 2017.

Indoor Localization and Communication Enhanced by Directional UWB Antennas

Michael Rath, Josef Kulmer, Mustafa S. Bakr, Bernhard Großwindhager,
and Klaus Witrisal

published in the COST Action CA15104 Workshop “Dependable Wireless
Communications and Localization for the IoT” (2017)

Abstract

In this paper, we demonstrate the advantage of using directive ultra-wideband antennas for time-of-flight positioning methods. We show how the employment of a switched sector antenna system assists in multipath-resolved indoor positioning with a single anchor. The antenna system improves the joint time and angle resolution which enables resolving multipath components even in unfavorable situations to increase the robustness of positioning methods.

1 Motivation

In indoor environments, radio signals are affected by dense multipath propagation. Accurate positioning methods are based on time-of-flight (ToF) estimation of probing signals. To estimate the ToF accurately, high bandwidths are needed to achieve high time resolution where the multipath deterioration is reduced. With ultra-wideband (UWB) signals, one can even exploit the multipath, because the line-of-sight (LOS) component and the interfering multipath components (MPC) can be resolved in time domain. This enables robust positioning using a single anchor by associating the MPCs with an environment model [1].

Path overlap is an issue that may arise for these methods in unfavorable positions. It occurs when one or more MPCs arrive shortly after each other making it impossible to resolve them in time domain. To tackle this issue, one can explore additionally the angle domain. One way to achieve this is with multiple (array) measurements from antennas distributed over a small region in the environment. The measurements can be coherently combined which improves the angular resolution and thus the positioning accuracy [2]. However, this comes at the cost of an expensive (multi-antenna) infrastructure and implementation issues with the coherent processing of the measurement signals. Alternatively, the angle domain can be explored using multiple directional antennas, each covering a subspace of the angle domain, thereby enabling indoor positioning methods based on received signal strength [3, 4].

In our approach, we stick with measurements from a single anchor position using a switchable system that employs a set of directional UWB antennas. Each antenna thus “shouts” towards one sector around it. Fig. 1 shows the used scenario with four sector antennas [5, 6]. The switching system is indicated by the beam patterns on top of the anchor position $\boldsymbol{a}$, labeled according to the cardinal directions (North, West, South, East). Measurements with this setup were performed with the shown agent at position $\boldsymbol{p}$. To estimate channel statistics, a measurement grid was used around the agent position which is also shown in Fig. 1.

In this work, we investigate the received signals for each antenna and compare them to measurements from an omni-directional antenna in terms of the capability to resolve MPCs. We will also report the positioning performance of a simple positioning algorithm using the sector antennas compared to an omni-directional antenna. The performance is represented by the cumulative distribution function of the position error.

An additional motivation for this switching system is a possible application for UWB PHY communication systems, where we expect an improvement in link quality by making use of the gained location awareness [7]. Also, an application in multi-user interference scenarios could be considered [5].

2 Signal model

The agent at position $\boldsymbol{p}$ records radio frequency measurements originating from one anchor located at position $\boldsymbol{a}$ (or vice versa). The agent is equipped with a single omni-directional antenna, while the anchor employs the described switching system with $M = 4$ antennas, referred to by $m = 1 \dots M$. Antenna m transmits the signal $s(t)$ and the signal $r_m(t)$ is observed at the agent. Based on our previous work [1], we model this received signal as a sum of deterministic MPCs, described by amplitudes α_k and path delays τ_k, plus contributions of diffuse multipath (DM)

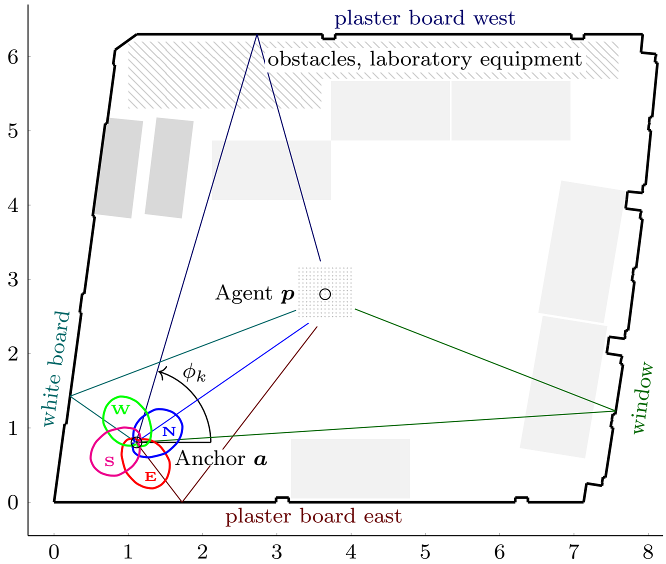

Figure 1: Floorplan of measurement environment. Tables (light-gray) and cupboards (dark-gray) are shown, as well as patterns of the used antennas at the anchors. The axis describes the distance in meters.

$\nu_m(t)$, and additive, white Gaussian noise (AWGN) $w(t)$, according to

$$r_m(t) = \sum_{k=1}^{K} \alpha_k b_m(\phi_k) s(t - \tau_k) + s(t) * \nu_m(t) + w(t).$$

An addition for this work is the influence of the beampattern $b_m(\cdot)$ which affects on the one hand the amplitude of the MPCs and on the other hand the DM $\nu_m(t)$ that has been spatially filtered by the antenna. The angle ϕ_k denotes the angle-of-departure at the anchor (see Fig. 1).

The same signal model was used in [6] where we evaluated position error bounds, outlined simple positioning algorithms and investigated the resulting position likelihood and error statistics.

3 Measurement setup

The measurement setup follows the one described in [6]; a short summary follows.

The directional antennas were mounted at the anchor position $\boldsymbol{a}$, rotated 90° apart such that they point in the four cardinal directions as shown on Fig. 1. Each antenna exhibits a half-power beamwidth of approximately 90°, hence the whole azimuth plane is covered. In an additional measurement, an omni-directional antenna was used at the same anchor position. The agent employed an omni-directional antenna for all measurements. The measurements between agent and anchor were performed using an Ilmsens Correlative Channel Sounder [8]. The measured signals were convolved by a raised cosine pulse with pulse duration of $T_\mathrm{p} = 2.4\,\mathrm{ns}$ (equivalent to a bandwidth of about 500 MHz), roll-off factor of $R = 0.9$ at a carrier frequency of $f_c = 5.2\,\mathrm{GHz}$. Multiple measurements were made by moving the agent on a 15×14 grid with 5 cm spacing.

4 Results

In this section, we examine the received signals for the center position of the grid, comparing the sector antennas at the anchor with an omni-directional setup. We also demonstrate the performance gain in terms of the position accuracy.

4.1 Capability to resolve MPCs

In Fig. 2 the amplitude as the absolute value of the received baseband-equivalent signal is shown over the path length (obtained by multiplying the delay time by the speed of light c). The amplitude is normalized to the maximum value among all the shown signals to make them comparable. The vertical dashed lines indicate the expected arrival times of the MPCs resulting from reflections on the surfaces stated at the top of the figure (compare with Fig. 1).

Comparing the signals of the directional sector antennas in Fig. 2b to the signals from the omni-directional antenna in 2a, we can see that the directivity increases the strength of the MPCs that are in the respective directions of the antennas, while also decreasing the DM between the MPC peaks. Moreover, a large benefit can be seen when examining the *plaster board east* and *white board* MPCs. These MPCs arrive very close after each other which results in path overlap that causes a single peak between the MPC positions as shown in Fig. 2a. In Fig. 2b we can see that the directive antennas can clearly resolve this issue, where the *West* and *South* antennas can focus on the *white board* MPC and the *East* antenna can focus on the *plaster board east* MPC.

4.2 Positioning accuracy

As a closure, we present one result based on [6] where we evaluated the position accuracy using the switching system compared to an omni-directional antenna. An approximate maximum likelihood algorithm was used to estimate agent position $\hat{\boldsymbol{p}}$ for each grid point (see Fig. 1) based on the measurements described above. The resulting cumulative distribution function of the position error is shown in Fig. 3.

It can be seen that an accuracy gain is achieved, where 90% of the estimations using the sector antennas exhibit an error of only 25 cm, whereas the omni-directional antenna measurements result in an error of 60 cm (c.f. the horizontal arrow in Fig. 3). Moreover, a robustness gain is observable when we examine how many of the measurements can reach a low error of 25 cm (55% with the omni-directional antenna, against 90% with the sector antennas, c.f. the vertical arrow in Fig. 3). Lastly, the highest error occurring with the switching system is around 40 cm, while with the omni-directional antenna there are points where the error is above one meter (about 5% of the points).

5 Conclusions

In this paper, we investigated the application of multiple directive UWB sector antennas for ToF positioning. We showed that the switched antenna system can significantly enhance a single-anchor-based multipath-resolved indoor positioning system. The combined time and angle resolution makes MPCs resolvable even in unfavorable positions and thus increases the robustness and / or reduces the required bandwidth. These capabilities enable practical implementations with commercially available devices such as the DW1000 transceiver front-end. In

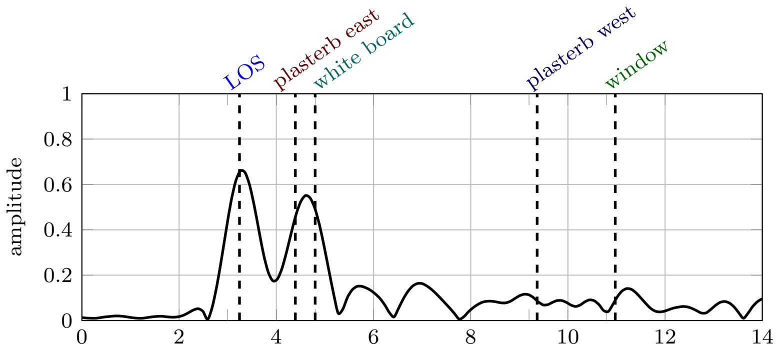

(a) omni-directional antenna

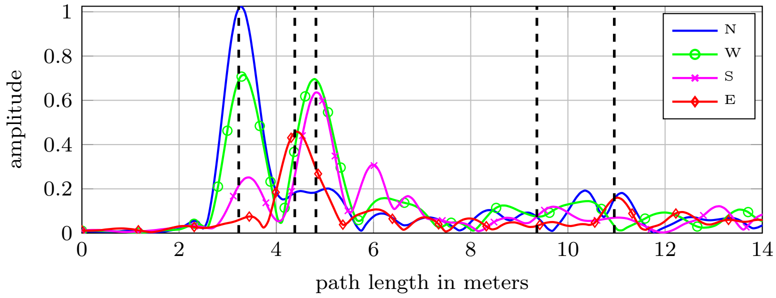

(b) sector antennas

Figure 2: Received signal of agent at $\boldsymbol{p}$ transmitted from anchor at $\boldsymbol{a}$ which uses an omni-directional antenna (a) and the directional sector antennas (b). Specific MPCs are indicated by the dashed vertical lines (compare with Fig. 1).

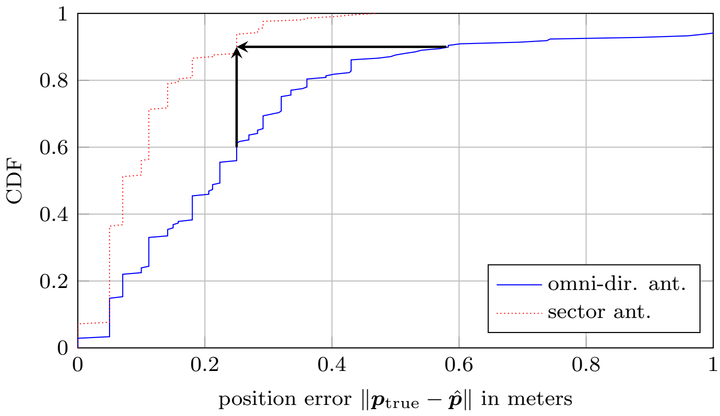

Figure 3: Cumulative distribution function (CDF) of the position error using an approximate maximum likelihood algorithm as described in [6].

the future, we will investigate the application of the antenna system for UWB communications.

References

[1] K. Witrisal, P. Meissner, E. Leitinger, Y. Shen, C. Gustafson, F. Tufvesson, K. Haneda, D. Dardari, A. F. Molisch, A. Conti, and M. Z. Win, "High-accuracy localization for assisted living," *IEEE Signal Processing Magazine*, 2016.

[2] Y. Han, Y. Shen, X. P. Zhang, M. Z. Win, and H. Meng, "Performance limits and geometric properties of array localization," *IEEE Transactions on Information Theory*, vol. 62, no. 2, pp. 1054–1075, Feb 2016.

[3] A. Cidronali, S. Maddio, G. Giorgetti, and G. Manes, "Analysis and performance of a smart antenna for 2.45-ghz single-anchor indoor positioning," *IEEE Transactions on Microwave Theory and Techniques*, vol. 58, no. 1, pp. 21–31, 2010.

[4] G. Giorgetti, S. Maddio, A. Cidronali, S. Gupta, and G. Manes, "Switched beam antenna design principles for angle of arrival estimation," in *Wireless Technology Conference, 2009. EuWIT 2009. European.* IEEE, 2009, pp. 5–8.

[5] B. Großwindhager, M. S. Bakr, M. Rath, F. Gentili, W. Bösch, K. Witrisal, C. A. Boano, and K. Römer, "Switchable Directional Antenna System for UWB-based Internet of Things Applications," in *International Conference on Embedded Wireless Systems and Networks (EWSN)*, 2017.

[6] M. Rath, J. Kulmer, M. S. Bakr, B. Großwindhager, and K. Witrisal, "Multipath-assisted indoor positioning enabled by directional UWB sector antennas," in *18th IEEE International Workshop on Signal Processing Advances in Wireless Communications, SPAWC*, 2017.

[7] R. D. Taranto, S. Muppirisetty, R. Raulefs, D. Slock, T. Svensson, and H. Wymeersch, "Location-aware communications for 5G networks: How location information can improve scalability, latency, and robustness of 5G," *IEEE Signal Processing Magazine*, vol. 31, no. 6, pp. 102–112, Nov 2014.

[8] R. Zetik, J. Sachs, and R. S. Thoma, "UWB short-range radar sensing - the architecture of a baseband, pseudo-noise UWB radar sensor," *IEEE Instrumentation Measurement Magazine*, vol. 10, no. 2, pp. 39–45, April 2007.

Directionally Resolved UWB Channel Modeling for Environment-Aware Positioning

Michael Rath, Erik Leitinger, Anh Nguyen, and Klaus Witrisal

published in the 14th European Conference on Antennas and Propagation (EuCAP 2020)

Abstract

In this paper, we formulate a radio channel model for directionally resolved ultra-wideband radio measurements, which takes the directionality of a steerable antenna frontend into account. We outline a figure of merit to assess the quality of specular multipath components (SMCs) for positioning applications, the signal-to-noise-and-interference-ratio (SINR), and perform an analysis thereof for a practical environment on the basis of a measurement campaign conducted in a parking house. The angle resolved analysis of the SINRs of various SMCs establishes a site specific model of the radio environment that can be leveraged for location-aware radio positioning and communication systems.

1 Introduction

Many applications of radio networks require knowledge about the environment in some form, desirably via a radio map that assigns each position in the environment a quality measure about a specific radio link. Previously, these maps would describe the received signal strength (RSS) or power spectral density from a particular transmitter (base station), which is a main performance indicator for narrowband systems, e.g., Wi-Fi. With the increasing bandwidth of upcoming radio systems, for example with millimeter-wave (mm-wave) systems or ultra-wideband (UWB) radio nodes, a high delay resolution becomes available, and with massive multiple-input multiple-output (MIMO) systems also a high angle resolution. These properties allow to resolve multipath propagation such that one can describe (a main component of) the radio channel by a superposition of specular multipath components (SMCs). The parameters of these SMCs (delay, angle) are related to the position of the agent node. It becomes possible to describe each SMC with its delay and angle, relating both to geometric properties of the environment and the locations of the transceivers, and therefore to map and predict these channel parameters across an environment, yielding far superior channel state information in comparison to an RSS model. For instance for positioning, this information translates directly to the expected performance, because each SMC carries useful position information [1].

In this work, we propose to describe UWB radio channels with a directionally resolved SMC amplitude model, relating the amplitudes of SMCs to the position of a mobile agent, as an extension of the purely geometric delay/angle model. We evaluate the proposed model using radio channel response measurements acquired in a parking deck by means of low-cost UWB transceivers. At the anchor side the transceiver was equipped with a switched array of directional antennas. We perform a qualitative analysis on the basis of the channel measurements themselves and a quantitative analysis on the basis of the signal-to-interference-and-noise-ratios (SINRs) of the SMC amplitudes, which quantify their useful position information. Our analysis intends to outline the applicability of such a multipath-resolved, directional environment model for (ultra)-wideband radio systems equipped with steerable antennas.

2 Problem Formulation

We consider radio systems operating at ultra-wide bandwidth and employing switchable directional antenna arrays. On the basis of these systems, we may build a multipath resolved radio channel model that has a close relation to geometric properties of the environment. A single physical anchor at position $\boldsymbol{a}_1$ is considered, that communicates with a mobile agent at position $\boldsymbol{p}$. We intend to formulate a model for multipath component amplitudes in relation to the agent position. To this end, we first establish a model for the measured channel response and then outline the extraction of MPC parameters in relation to the environment.

2.1 Measurement Model

The anchor node employs an antenna array which consists of M directional antennas, each of which exhibits a beampattern $b_m(\phi)$, where we operate in the azimuth plane with angle-of-departure (AoD) ϕ. When referring to the general anchor position, we use $\boldsymbol{a}_1$ which is defined to be the mass point of the antenna array. The agent transmits a lowpass-equivalent signal $s(t)$ modulated by carrier frequency f_c and the anchor receives the channel response signal $r_m(t)$ using antenna m.

The anchor acquires N samples of the received signal sampled with frequency $f_\mathrm{s} = 1/T_\mathrm{s}$ at antenna m such that $[\boldsymbol{r}_m]_i = r_m([i-1] \cdot T_\mathrm{s}), i = 1 \dots N$ and stacks them into the observation vector $\boldsymbol{r}_m$.

We describe this observation vector by the superposition of $k = 1 \dots K$ specular multipath components (SMCs) and use the sampled transmitted signal

$$\boldsymbol{s}(\tau_k) = [s(0 \cdot T_\mathrm{s} - \tau_k), \dots, s([N-1] \cdot T_\mathrm{s} - \tau_k)]^\mathrm{T} \ \in \mathbb{R}^{N \times 1}$$

to write

$$\boldsymbol{r}_m = \sum_{k=1}^{K} b_m(\phi_k) \alpha_{k,m}\, \boldsymbol{s}(\tau_k) + \boldsymbol{n}_{\nu,m} + \boldsymbol{w}_m \ \in \mathbb{C}^{N \times 1} \tag{1}$$

which can be separated in three distinct parts: The first part contains the position-related SMC parameters ϕ_k and $\tau_k = 1/c \cdot d_k$, where c is the speed of light. The according complex amplitudes $\alpha_{k,m} = \alpha_k \mathrm{e}^{j\zeta_{k,m}}$ also contain phase offsets $\zeta_{k,m}$ introduced by the measurement equipment between measurements $m = 1, \dots, M$. The second part $\boldsymbol{n}_{\nu,m}$ are samples of a stochastic process characterizing the self-interference due to the dense multipath component (DMC). Finally, measurement noise $\boldsymbol{w}_m$ is modeled as additive white Gaussian noise (AWGN) with variance $\sigma_w = N_0/T_\mathrm{s}$, where $N_0/2$ is the double-sided power spectral density.

To describe the DMC and AWGN, the (m, m')th block of the noise covariance matrix $\boldsymbol{C_n} \in \mathbb{C}^{MN \times MN}$ reads

$$[\boldsymbol{C_n}]_{m,m'} = [\boldsymbol{C_\nu}]_{m,m'} + \sigma_w^2 \boldsymbol{I}_N \qquad \in \mathbb{C}^{N \times N}.$$

where $\boldsymbol{C_\nu}$ is the DMC covariance matrix. The (m, m')th block of the DMC covariance matrix is given as

$$[\boldsymbol{C_\nu}]_{m,m'} = \iint S_\nu(\phi, \tau)\, b_m(\phi)\, b_{m'}^*(\phi) \boldsymbol{s}(\tau) \boldsymbol{s}(\tau)^\mathrm{H} \,\mathrm{d}\phi \,\mathrm{d}\tau. \tag{2}$$

To simplify this covariance matrix, we assume the DMC to be uncorrelated between antennas, i.e., $\boldsymbol{C_\nu}$ is block-diagonal, which can be argued since each antenna at the anchor covers one sector in the azimuth plane with differently aligned main beam directions. As a result, the shapes of the beampatterns are approximately orthogonal such that

$$\int S_\nu(\phi, \tau)\, b_m(\phi)\, b_{m'}^*(\phi) \,\mathrm{d}\phi \ll \int S_\nu(\phi, \tau)\, |b_m(\phi)|^2 \,\mathrm{d}\phi$$

which shows that the angle-delay power spectrum has to be considered for this assumption to be fulfilled exactly. With this, the noise covariance matrix $\boldsymbol{C_n}$ becomes a block-diagonal matrix with the mth block matrix $\boldsymbol{C}_{\boldsymbol{n}}^{(m)} = [\boldsymbol{C_n}]_{m,m}$ given as

$$\boldsymbol{C}_{\boldsymbol{n}}^{(m)} = \int S_\nu^{(m)}(\tau)\, \boldsymbol{s}(\tau) \boldsymbol{s}(\tau)^\mathrm{H} \,\mathrm{d}\tau + \sigma_w^2 \boldsymbol{I}_N \qquad \in \mathbb{C}^{N \times N} \tag{3}$$

where $S_\nu^{(m)}(\tau) = \int S_\nu(\phi, \tau) |b_m(\phi)|^2 \mathrm{d}\phi$ is the delay power spectrum (DPS) considering the mth antenna beampattern of the antenna array at the anchor node.

2.2 Geometric Model

In the following, we aim at modelling the SMC parameters from (1) in relation to the geometry of the environment. The SMCs result from reflections on flat surfaces in the considered environment, where the number of bounced surfaces defines the order of the SMC denoted by $\mathcal{O}(k)$.[1] The number of useful SMCs K is determined by designation of significantly large flat surfaces ($> 1\ \mathrm{m}^2$) whose number we denote by K_{seg} and then setting $K = (K_{\mathrm{seg}} - 1)^{\max\{\mathcal{O}(k)\}}$, where we used the maximum operator $\max\{\cdot\}$ to find the SMC with the highest number of bounced surfaces. With the SMC set at hand, we define the virtual anchor set $\mathcal{A}$ which consists of the physical anchor $\boldsymbol{a}_1$ as well as $K-1$ virtual anchors (VAs) $\boldsymbol{a}_k$ that are determined by mirroring $\boldsymbol{a}_1$ on the respective reflective surfaces. Depending on the SMC order, this mirroring operation has to be performed multiple times at each surface in the propagation path.

Now we have the tools to describe the kth SMC in relation to the geometry of the environment. We first have the SMC delay described by

$$\tau_k(\boldsymbol{p}) = \tfrac{1}{c}\|\boldsymbol{p} - \boldsymbol{a}_k\| \tag{4}$$

and the angle-of-arrival (AoA) with respect to the VA described by

$$\phi_k^{\mathrm{VA}}(\boldsymbol{p}) = \angle(\boldsymbol{p} - \boldsymbol{a}_k). \tag{5}$$

This angle is used to determine the AoD with respect to the physical anchor described by

$$\phi_k(\boldsymbol{p}) = (-1)^{\mathcal{O}(k)}\phi_k^{\mathrm{VA}}(\boldsymbol{p}) - 2\sum_{j=1}^{\mathcal{O}(k)}(-1)^j\ \phi_{\mathrm{seg}_j}^{(k)} \tag{6}$$

where $\phi_{\mathrm{seg}_j}^{(k)}$ denotes the angle of the jth involved reflective segment in the propagation path with $j = 1, \ldots, \mathcal{O}(k)$ ordered according to the sequence of bounced surfaces.

We use this angle in our model, since the antenna configuration is situated at the physical anchor. With these position-related delay and angle models the complex amplitudes of the SMCs can be modeled as

$$\alpha_{k,m}(\boldsymbol{p}) = \mathrm{PL}\big(\tau_k(\boldsymbol{p})\big)\Gamma_k\big(\phi_k(\boldsymbol{p})\big)\mathrm{e}^{j(2\pi f_{\mathrm{c}}\tau_k(\boldsymbol{p})+\zeta_{k,m})} \tag{7}$$

where we have the pathloss (PL) for the respective propagation delay and the complex-valued reflection coefficient Γ_k, which covers reflection losses and carrier phase rotations, both related to the materials of the involved surfaces and the incidence angle of each bounced surface, hence we have the AoD dependence. The phasor accounts for the phase rotation depending on the carrier frequency f_{c} and the phase offset $\zeta_{k,m}$ that combines hardware and array effects. Since measurements of different antennas are only combined non-coherently, we do not exploit the phase related to the carrier frequency.

2.3 Amplitude Quality Model

We are interested in the quality of SMC amplitudes for applications such as positioning systems, hence, for each SMC k at antenna m, we define the signal-to-

---

[1] In most considerations, only first and second order reflections are regarded due to the high reflection losses.

interference-and-noise-ratio (SINR) as [2]

$$\begin{aligned}\mathrm{SINR}_k(\boldsymbol{p}) &= \sum_{m=1}^{M} |b_m(\phi_k)|^2 |\alpha_{k,m}(\boldsymbol{p})|^2 \\ &\quad \times \boldsymbol{s}^{\mathrm{H}}\big(\tau_k(\boldsymbol{p})\big)\big[\boldsymbol{C}_{\boldsymbol{n}}^{(m)}\big]^{-1}\boldsymbol{s}\big(\tau_k(\boldsymbol{p})\big) \\ &= \sum_{m=1}^{M} |b_m(\phi_k)|^2 \mathrm{SINR}_{k,m}(\boldsymbol{p}),\end{aligned} \tag{8}$$

which describes the non-coherently combined SINR for all antennas. A detailed derivation can be found in [2]. This quantity was previously evaluated in regards of contributions to position estimate accuracy [3] and contributions to communication channel capacity [4].

When using low-cost devices to acquire channel response measurements, it is a challenging task to obtain reliable SMC amplitude estimates $\hat{\alpha}_{k,m}$ to be used for SINR evaluation. We follow the approach outlined in [5, 6] to obtain

$$\hat{\alpha}_{k,m} = \frac{1}{b_m(\phi_k)} \frac{\boldsymbol{s}^{\mathrm{H}}(\tau_k)\big[\boldsymbol{C}_{\boldsymbol{n}}^{(m)}\big]^{-1}\boldsymbol{r}_m}{\boldsymbol{s}^{\mathrm{H}}(\tau_k)\big[\boldsymbol{C}_{\boldsymbol{n}}^{(m)}\big]^{-1}\boldsymbol{s}(\tau_k)} \tag{9}$$

where we omitted the agent position dependence for brevity. These individual amplitude estimates can then in turn be combined, weighted by the respective beampatterns, to obtain the estimate of one SMC via

$$\hat{\alpha}_k = \frac{\sum_{m=1}^{M} |b_m(\phi_k)|^2 |\hat{\alpha}_{k,m}|}{\sum_{m=1}^{M} |b_m(\phi_k)|^2}. \tag{10}$$

With the amplitudes given in (10), the SINR of the kth SMC used in (8) is estimated using a Method-of-Moments estimator as in [7].

3 Results

A measurement campaign was performed in a parking deck as illustrated in Fig. 1. Fig. 2 shows an overview photo of the parking spaces around the physical anchor position $\boldsymbol{a}_1$.

3.1 Involved Hardware

For both anchor and agent, a modified hardware platform based on the DecaWave DWM1000 module [8] was used with a self-built directional UWB antenna at the anchor and an omni-directional UWB antenna at the agent. Photos of the hardware modules are shown in Fig. 3. The system is capable of measuring channel responses at a carrier of 6.5 GHz with a bandwidth of 900 MHz (Channel 7 of the IEEE 802.15.4 UWB standard [9]) between the agent and one of the four directional antennas at intervals of approximately 15 milliseconds. Each directional antenna has a half-power beamwidth of about 100° and the antennas are pointed towards the four cardinal directions to cover the whole azimuth plane. For a more detailed description of this system, please refer to [6], where the system was evaluated for indoor positioning in office environments.

The agent device was mounted on top of a car at a height of 1.8 m. This car was equipped with a highly accurate IMU which provided a ground truth position

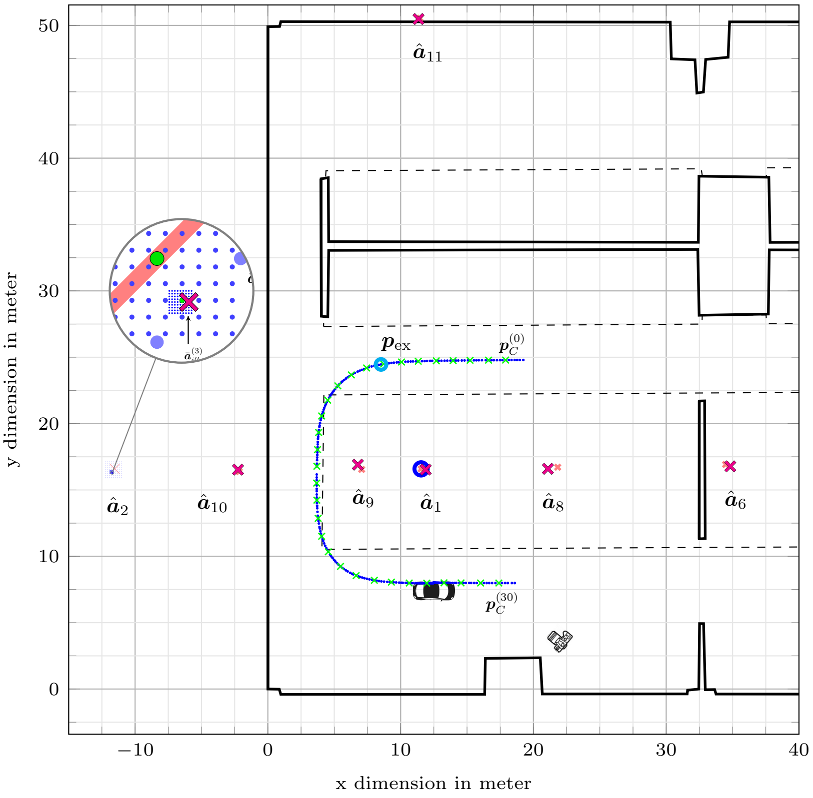

Figure 1: Floorplan of used environment. The physical anchor at position $\boldsymbol{a}_1$ is indicated with a blue circle and the calibrated virtual anchors $\hat{\boldsymbol{a}}_k$ are indicated with magenta crosses (initial VA positions are shown in light red crosses). For the anchor $\boldsymbol{a}_2$ the 3 stage grid points to calibrate the anchor position are shown (see Sec. 3.2). The trajectory ground truth positions of the agent are shown as a line of blue dots between the parking spaces. Green crosses along the trajectory indicate the positions of the cluster centers $\boldsymbol{p}_C^{(i)}$ for the SINR analysis from Sec. 3.3. The starting pose of the used car is shown by the respective icon (the agent was mounted on the center left side of the car). On the bottom right, the camera icon shows the orientation of the camera used to obtain the photo seen in Fig. 2.

Figure 2: A photo showing the parking deck where the measurements were conducted. The position from where this photo was shot is indicated in Fig. 1 with a camera icon.

(a) anchor

(b) agent

Figure 3: Photos showing the modified DecaWave DWM1000 hardware platform to perform the measurements at the anchor and agent respectively.

estimate of the agent with millimeter accuracy at a significantly higher rate than the channel response measurements. These position estimates were synchronized with the channel response measurements via a GPS responder, recording a common time estimate at the start and end of the measurement run. The car traveled around the parking spaces for three rounds. For one round the relevant ground truth positions of the traveled trajectory are shown in Fig. 1. The trajectory shown is a subset of all recorded positions that we will consider in the following.

Channel response measurements between the agent and the antenna pointing towards the "left" (cf. Fig. 1) are shown in Fig. 4. In Fig. 5, the recorded channel responses of each antenna are shown for one example trajectory position $\boldsymbol{p}_{\mathrm{ex}}$. In both plots, it is easily possible to make out the SMCs associated with the environment, which can be formulated via the VA model. A detailed analysis thereof is given in the following.

3.2 VA Processing

The initial steps to analyze the measured channel responses, i.e., to process SMC amplitudes, involve the establishment of the VA model as described in Sec. 2.1. In a first step, the position of the physical anchor is mirrored at known surfaces to

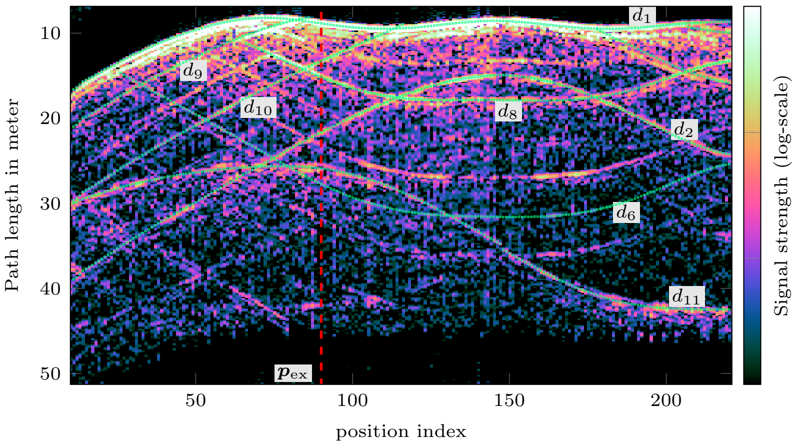

Figure 4: Channel responses for the antenna pointing towards the left. Shown in log-scale for one round. The ranges d_k to the respective VAs are superimposed in light green dots. The red dashed line indicates the channel response that is shown in Fig. 5d.

obtain initial VA positions $\tilde{\boldsymbol{a}}_k$ (see Fig. 1). This results in the anchor positions $\tilde{\boldsymbol{a}}_2$ and $\tilde{\boldsymbol{a}}_{11}$ belonging to the western and northern wall, respectively. Additional mirroring operations are carried out for potential reflecting materials such as the ceiling metal beams (see Fig. 2) to obtain anchor positions $\tilde{\boldsymbol{a}}_9$ and $\tilde{\boldsymbol{a}}_{10}$ for the metal beams in the west and $\tilde{\boldsymbol{a}}_6$ and $\tilde{\boldsymbol{a}}_8$ for the metal beams in the east. We want to note that there are additional VAs representing the remaining metal beam reflections which are omitted from our further analysis (and thus not shown in Fig. 1) due to minor insights gained.

The second pre-processing step involves the calibration of each VA position. This is accomplished iteratively for $l = 1 \dots L$ by spanning a grid around a VA basis position (initially $\tilde{\boldsymbol{a}}_k$ is used) obtaining candidate positions and sets $\bar{\boldsymbol{a}}_i^{(l)} \in \bar{\mathcal{A}}^{(l)}$. Additionally, for each VA, a suitable subset of the trajectory positions $\mathcal{P}^{(k)}$ is chosen where the initial VA $\tilde{\boldsymbol{a}}_k$ exhibits good visibility conditions, i.e., a significantly strong reflection is possible at the respective surface. The best candidate VA $\boldsymbol{a}_{\mathrm{best}}^{(l)}$ is chosen based on a maximum likelihood approach. This procedure is performed for $L = 3$ times, each time using finer grid spacing and the previously determined VA as a basis to obtain the finalized VA positions $\hat{\boldsymbol{a}}_k \in \hat{\mathcal{A}}$. The calibration procedure is illustrated in Fig. 1 for $\boldsymbol{a}_2$. The set of calibrated VAs allows us already to perform a qualitative analysis of the CIRs. In Fig. 4, on top of the CIRs, the distances d_k between VAs and agent positions are shown as green dots. A qualitative examination of the distance trajectories shows a good fit to the progress of the SMC delays along the agent position trajectory. The shown channel responses for the selected position $\boldsymbol{p}_{\mathrm{ex}}$ alongside the dotted distance lines of each SMC confirm this observation. However, we take the next step and examine the strength of these SMCs for antennas pointing towards different directions to study the evident angle-relation of the amplitudes. Hence, in the following, we apply the geometric model to estimate SMC amplitudes and examine the position/angle resolved statistics.

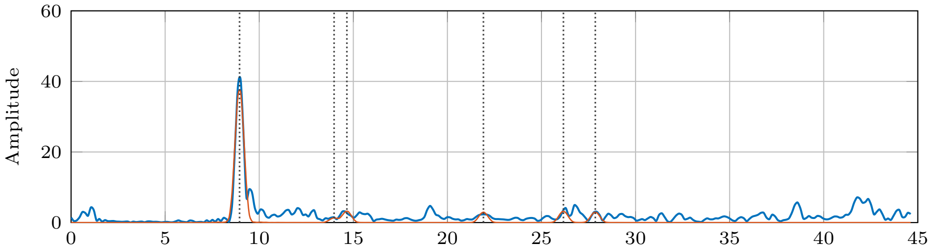

(a) right

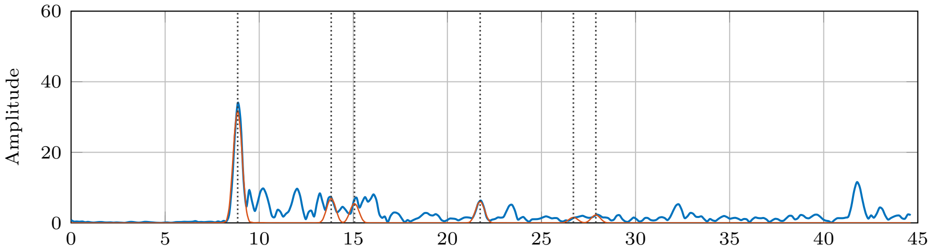

(b) down

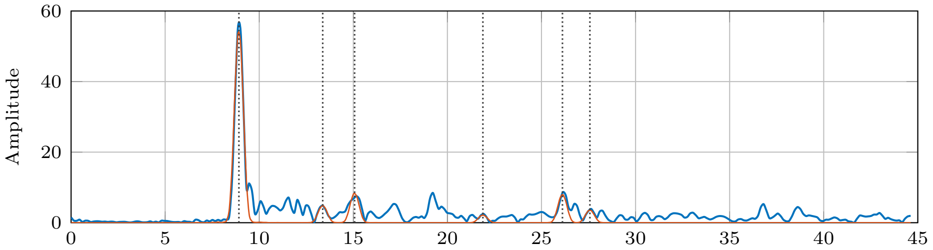

(c) up

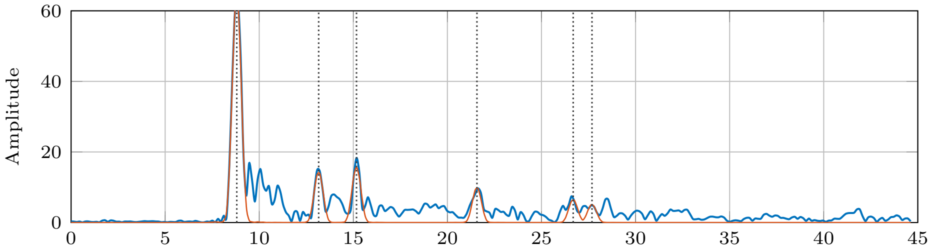

(d) left

Figure 5: Example of channel responses for each antennas pointing in one of the cardinal direction. The used position is indicated in Fig. 1 as $\boldsymbol{p}_{\mathrm{ex}}$, and in Fig. 4 the respective channel response is indicated. Hypothesized pulses shifted according to the delays from (4) and weighted with amplitudes from (10) are also plotted in red.

3.3 SINR Analysis

We aim for a further quantitative analysis of the SMC amplitudes and use the SINR estimated via (8) as a figure of merit for selected positions along the trajectory. To this end, we choose representative positions along the trajectory to form position clusters. We use a spacing of 1.25 meter to designate cluster centers denoted by $\boldsymbol{p}_C^{(i)}$, resulting in $i = 0, \ldots, 30$ representative trajectory positions as shown in Fig. 1, where the first and last cluster centers (i.e., $\boldsymbol{p}_C^{(0)}$ and $\boldsymbol{p}_C^{(30)}$) are shown for reference. Each channel response measurement is assigned to the cluster that is closest to the respective ground truth position. We use the calibrated VA positions $\hat{\boldsymbol{a}}_k$ to estimate the SMC amplitude values $\hat{\alpha}_{k,m}$ using (9) and in turn $\hat{\alpha}_k$ using (10) for each measured channel response. The collected SMC amplitudes of one cluster are used with a Method-of-Moments estimator [7, 10] to obtain the respective SINR given in (8).

The SINRs of each SMC at each cluster point are shown in Fig. 6, on the one hand over the positions along the trajectory and on the other hand over the respective AoD. While the line-of-sight component (α_1) unsurprisingly achieves generally high values approaching 20 dB, we see specific regions where SMCs achieve an SINR of more than 10 dB, which characterizes a reflection strong enough to be of use for positioning and location-aware systems. As specific examples, we note the west wall reflection α_2, which achieves high values towards the U-turn beginning (around cluster 8, close to $\boldsymbol{p}_{\mathrm{ex}}$) as well as the starting position, highlighting the potential for multipath-assistance in these regions. Another remarkable example is seen for the northern wall reflection α_{11}, which even surpasses the LOS strength at around cluster 15. This is due to the obstruction of the LOS component at the peak of the U-turn.

We turn our attention to the angular distribution of the SMC SINRs seen in 6b. While the LOS component covers most of the angle region, it is evident that each SMC is focused around one specific angle. For instance, when we consider angles around 0° (i.e., towards the "right" of the anchor), we have the SMCs α_6 and α_8, on the opposite side we have α_2, α_9 and α_{10}. With SINR values approaching or even surpassing 10 dB, a multi-antenna system can steer towards these directions to collect useful location information and therefore enhance the robustness of a positioning system.

4 Conclusion

In this article, we established a directional model for radio channel responses operating at ultra-wide bandwidths. We formulated this model as a superposition of specular multipath components impinging from different directions and a dense multipath component resulting from diffuse scattering from the environment. Each specular component is characterized by delay and angle related to the geometry of the environment. With this relation, the strengths of the specular reflections were modeled and the Signal-to-noise-and-interference ratio (SINR) was introduced as a figure of merit. We outlined a measurement campaign in a parking house and presented an angle and delay-resolved analysis of the reflection SINRs, motivating the application of multi-antenna systems to harvest these reflections for localization and communication systems.

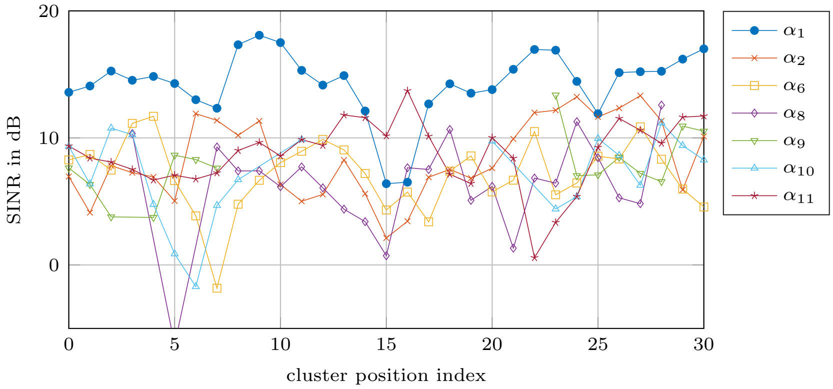

(a) Over position.

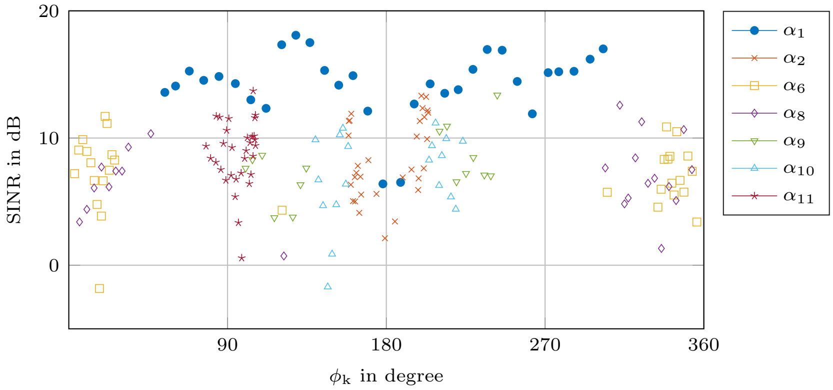

(b) Over AoD.

Figure 6: Amplitude SINR estimates using method-of-moments over clusters of positions along the trajectory (from all three rounds).

Acknowledgments

We would like to thank the navigation group of the institute of geodesy at TU Graz for assisting in the measurement campaign and providing the position ground truth. We would also like to thank MAGNA Steyr Engineering for access to the parking house environment and for providing the vehicle used in the measurement campaign.

References

[1] K. Witrisal, P. Meissner, E. Leitinger, Y. Shen, C. Gustafson, F. Tufvesson, K. Haneda, D. Dardari, A. F. Molisch, A. Conti, and M. Z. Win, “High-accuracy localization for assisted living,” *IEEE Signal Processing Magazine*, 2016.

[2] M. Rath, J. Kulmer, E. Leitinger, and K. Witrisal, “Single-anchor positioning: Multipath processing with non-coherent directional measurements,” 2020, in preparation.

[3] E. Leitinger, P. Meissner, C. Ruedisser, G. Dumphart, and K. Witrisal, “Evaluation of position-related information in multipath components for indoor positioning,” *IEEE Journal on Selected Areas in Communications*, 2015.

[4] A. N. Hong, M. Rath, E. Leitinger, S. Hinteregger, K. N. Van, and K. Witrisal, “Channel capacity analysis of indoor environments for location-aware communications,” in *2016 IEEE Globecom Workshops (GC Wkshps)*. IEEE, 2016, pp. 1–6.

[5] J. Kulmer, S. Grebien, M. Rath, and K. Witrisal, “On the unimportance of phase-coherent measurements for beampattern-assisted positioning,” in *2018 IEEE Wireless Communications and Networking Conference (WCNC)*, April 2018, pp. 1–6.

[6] B. Großwindhager, M. Rath, J. Kulmer, M. S. Bakr, C. A. Boano, K. Witrisal, and K. Römer, “SALMA: UWB-based single-anchor localization system using multipath assistance,” in *Proceedings of the 16th ACM Conference on Embedded Networked Sensor Systems*, ser. SenSys ’18. New York, NY, USA: ACM, 2018, pp. 132–144. [Online]. Available: http://doi.acm.org/10.1145/3274783.3274844

[7] P. Meissner, E. Leitinger, and K. Witrisal, “UWB for robust indoor tracking: weighting of multipath components for efficient estimation,” *IEEE Wireless Communications Letters*, vol. 3, no. 5, pp. 501–504, Oct. 2014.

[8] Decawave Ltd., *DW1000 Datasheet. Version 2.12*, 2016.

[9] I. C. Society, *Standard for Low-Rate Wireless Networks*, Std. 802.15.4, 2015.

[10] L. J. Greenstein, D. G. Michelson, and V. Erceg, “Moment-method estimation of the Ricean K-factor,” *IEEE Communications Letters*, vol. 3, no. 6, pp. 175–176, 1999.